



The  
University  
Of  
Sheffield.

## **Flame Instabilities in Open Ended Tubes**

Nazrein Adrian **Amaludin**

A thesis submitted in partial fulfilment of the requirements for the degree of  
Doctor of Philosophy

The University of Sheffield  
Faculty of Engineering  
Department of Mechanical Engineering

June 2020

## DECLARATION

I, Nazrein Adrian bin Amaludin, confirm that the Thesis is my own work. I am aware of the University's Guidance on the Use of Unfair Means ([www.sheffield.ac.uk/ssid/unfair-means](http://www.sheffield.ac.uk/ssid/unfair-means)). This work has not been previously been presented for an award at this, or any other, university.

To Izreen and Izeleia

## **ACKNOWLEDGEMENTS**

I would like to thank my supervisor, Dr. Robert Woolley of the University of Sheffield for all the guidance and his patience during the period of this research, my colleagues, Celestine Ebieto, Houshi Jiang, Abdullah Alsharif, and Oliver Cooper for the countless fruitful discussions on combustion instabilities.

Thanks are due to my father, Amaludin bin Sagi, my mother, Latifah binti Yacob, as well as my siblings, Adriana Erica binti Amaludin and Hassanel Zachary bin Amaludin, and my in-laws, Ismail bin Ibrahim and Salmah binti Ahmad for their endless moral support.

I would also like to extend my appreciation to the Ministry of Higher Education Malaysia and also Universiti Malaysia Sabah for the financial support, and members of the Sheffield Students' Union, particularly Daniel Capewell and Genevieve Gardner for their support, advice and encouragement during the difficult times in Sheffield.

Finally, my thanks go to my wife, Izreen Yasmi binti Ismail and our lovely daughter, Izeleia Jasmine binti Nazrein to whom I dedicate this work. Their ability to keep me distracted from doing combustion related mental gymnastics during the writing-up period were very much appreciated.



## ABSTRACT

Premixed flame propagation in an open-ended horizontal tube has been investigated. Methane-air flames with equivalence ratio ranging between  $\phi = 0.8 - 1.5$  and hydrogen addition,  $R_H = 0 - 0.8$ , were filmed with a high-speed camera and the pressure captured. Two-thirds along the tube, the flames encountered an acoustic field and were subjected to longitudinal oscillations.

Depending on the hydrogen content, significant differences were observed in the behaviour of the flames, which were categorized into 3 different categories, a steady flame, a pulsating flame and an oscillating flame. A steady flame propagated steadily, while a pulsating flame was shortened and elongated due to the oscillating pressure.

For oscillated flames, the flame speed initially decreased as it entered the field, and was then subjected to violent oscillations, resulting in a high acceleration and speed. The accelerations were attributed by the formation of Rayleigh-Taylor instabilities, which existed in the form of spikes of unburned mixture into the burned gasses that coupled with the pressure oscillations.

This satisfied the Rayleigh criteria that the acoustically driven instabilities require the heat release and pressure waves to be in phase. When the hydrogen content was increased, as the flame passed through the acoustic field, the flame speed decreased, and no Rayleigh-Taylor instabilities were observed. This difference in behaviour with hydrogen content was attributed to the higher flame speeds with higher hydrogen concentrations.

# TABLE OF CONTENTS

Declaration.....	ii
Acknowledgements .....	iv
Abstract .....	v
Table of Contents.....	vi
List of Tables.....	ix
List of Figures.....	xi
Nomenclature .....	xxii
1 Introduction .....	1
2 Literature review .....	3
2.1 Premixed Flame Instabilities .....	3
2.2 Types of Premixed Flame Instabilities.....	14
2.2.1 Body-force Instability.....	14
2.2.2 Thermodiffusive Instability.....	19
2.2.3 Hydrodynamic Instability.....	22
2.3 Effect of Tube Configuration on Instabilities.....	23
2.3.1 Flame in Tubes Closed at Both Ends .....	23
2.3.2 Flame in Tubes Open at Ignition End.....	24
2.3.3 Flame in Tubes Open at Non-Ignition End.....	26
2.3.4 Flame in Tubes Open at Both Ends .....	27
2.4 Fuel Composition.....	28
2.4.1 Fuel Composition Effect on Flame Instabilities.....	28
2.4.2 Equivalence Ratio .....	32
2.4.3 Hydrogen Addition.....	33
2.5 Spectral Analysis.....	35
2.5.1 Fast Fourier Transform.....	37
2.5.2 Synchrosqueezed Wavelet Transform.....	42
2.5.3 Phase Study.....	47
2.6 Research Gap .....	50
3 Experimental Methodologies .....	51
3.1 Experimental Apparatus .....	51
3.2 Data Acquisition .....	53
3.2.1 Optical Measurements.....	53
3.2.2 Pressure Measurement .....	55
3.2.3 Optical and Pressure Data Synchronization.....	56
3.3 Fuel .....	60
3.3.1 Fuel Related Apparatus.....	60

3.3.2	Rig Volume Calculation .....	60
3.3.3	Fuel Volume Calculation .....	60
3.4	Experimental Errors .....	63
3.4.1	Systematic Error .....	63
3.4.2	Random Error .....	64
4	Post-Processing.....	65
4.1	Introduction.....	65
4.2	Flame Classifications.....	65
4.3	Raw Video Preparation.....	68
4.3.1	Video Cropping and Conversion .....	68
4.3.2	Image Denoising.....	68
4.4	Flame Front, Tail, Mean, Thickness and Size Tracking .....	72
4.4.1	Flame Front Analysis .....	76
4.5	MATLAB Frequency Analysis.....	79
4.5.1	Fast Fourier Transform (FFT) .....	80
4.5.2	Synchrosqueezed Wavelet Transform (SST).....	81
4.5.3	Phase Study .....	90
5	Experimental Results.....	93
5.1	Introduction.....	93
5.2	Equivalence Ratio Effect .....	104
5.2.1	Initial Study .....	104
5.2.2	Frequency Analysis .....	109
5.2.3	Phase Analysis.....	116
5.2.4	Non-steady Flame Shape Analysis .....	120
5.3	Hydrogen Addition Effect .....	123
5.3.1	Initial Study .....	123
5.3.2	Frequency Analysis .....	127
5.3.3	Phase Analysis.....	134
5.3.4	Non-steady Flame Shape Analysis .....	139
5.4	Constant Laminar Burning Velocity Comparison .....	143
5.4.1	Initial Study .....	143
5.4.2	Frequency Analysis .....	145
5.4.3	Phase Analysis.....	148
5.4.4	Non-steady Flame Shape Analysis .....	151
5.5	Overall Flame Analysis.....	153
5.5.1	Overall Flame Propagation Analysis .....	153
5.5.2	Overall Tube End Pressure Analysis .....	161
6	Discussions.....	165
6.1	Discussions on Equivalence Ratio Effect .....	165

6.2	Discussions on Hydrogen Addition Effect.....	167
6.3	Discussions on Constant Laminar Burning Velocity .....	169
6.4	Overall Discussion .....	171
7	Conclusions.....	179
7.1	Future Work .....	180
	References .....	182
	Appendices.....	192

## LIST OF TABLES

Table 2.1 Lewis number of pure methane flames [54].

Table 2.2 Reactive mixtures laminar flame velocity, expansion ratio, and laminar spatial velocity, reproduced from [64].

Table 2.3 Hydrogen mole fraction range for  $R_H$  method and mole fraction mixing method.

Table 2.4 Parameters for three different waves.

Table 3.1 Tabulated results of the synchronisation workflow test.

Table 3.2 Tabulated laminar burning velocity, mole fraction, volume, and the standard deviation (based on maximum pressure) for all mixtures tested in the present work.

Table 4.1 Low pass Finite Impulse Response filter properties.

Table 4.2 Resulting frequency penalty for different penalty levels.

Table 5.1 Impact of pressure components on the underlying acceleration of a flame.

Table 5.2 Flame sequence at point B (white line) for methane flames at constant hydrogen addition,  $R_H = 0.1$ , with increasing equivalence ratio,  $\phi = 0.9 - 1.3$ . Interval of 1/1500 seconds increment for every frame upwards.

Table 5.3 Flame sequence at point C (white line) for methane flames at constant hydrogen addition,  $R_H = 0.1$ , with increasing equivalence ratio,  $\phi = 0.9 - 1.3$ . Interval of 1/1500 seconds increment for every frame upwards.

Table 5.4 Flame sequence at point B (white line) for methane flames at constant equivalence ratio,  $\phi = 1.1$ , with increasing hydrogen addition,  $R_H = 0 - 0.4$ . Interval of 1/1500 seconds increment for every frame upwards.

Table 5.5 Flame sequence at point B (white line) for methane flames at constant equivalence ratio,  $\phi = 1.1$ , with increasing hydrogen addition,  $R_H = 0.5 - 0.8$ . Interval of 1/1500 seconds increment for every frame upwards.

Table 5.6 Flame sequence at point C (white line) for methane flames at constant equivalence ratio,  $\phi = 1.1$ , with increasing hydrogen addition,  $R_H = 0 - 0.4$ . Interval of 1/1500 seconds increment for every frame upwards.

Table 5.7 Flame sequence at point B (white line) for methane flames with constant burning velocity,  $\phi = 0.8$ ,  $R_H = 0.3$ ,  $\phi = 1.0$ ,  $R_H = 0.2$ , and  $\phi = 1.4$ ,  $R_H = 0.4$ . Interval of 1/1500 seconds increment for every frame upwards.

Table 5.8 Flame sequence at point C (white line) for methane flames with constant burning velocity,  $\phi = 0.8$ ,  $R_H = 0.3$ ,  $\phi = 1.0$ ,  $R_H = 0.2$ , and  $\phi = 1.4$ ,  $R_H = 0.4$ . Interval of 1/1500 seconds increment for every frame upwards.

Table 6.1 Mixtures tested for studying the effect of equivalence ratio.

Table 6.2 Mixtures tested for studying the effect of hydrogen addition.

Table 6.3 Mixtures tested for studying the effect of equal laminar burning velocity.

## LIST OF FIGURES

Figure 2.1 Effect of different phase of heat supply relative to phase of pressure, i) in phase, ii) out of phase, iii) quarter period before, and iv) quarter period after. Reproduced from [17].

Figure 2.2 First three harmonics of an open-ended tube, a) first harmonic, b) second harmonic, c) third harmonic, where A signifies the velocity antinodes whereas N represents velocity nodes. Reproduced from [19].

Figure 2.3 Feedback mechanism of thermoacoustic instabilities.

Figure 2.4 Initiation and propagation of a tulip flame. Reproduced from [21].

Figure 2.5 Formation of (a) distorted tulip flame and (b) classic tulip flame. Solid lines indicate the initial flame shape; dashed lines indicate the subsequent flame shape. Arrows indicate the characteristic flow velocity field. Reproduced from [23].

Figure 2.6 Sequence of numerical schlieren images representing the evolution from a normal flame to a distorted tulip flame. Reproduced from [26].

Figure 2.7 Pulsating and oscillating flame structure induced by vibration of gas column. Reproduced from [5].

Figure 2.8 Regions of unstable oscillation and pulsation induced by vibrations for different dimensionless frequency,  $\Omega$ , at varying dimensionless velocity amplitude,  $W$ , and dimensionless wavelength,  $\lambda$ . Reproduced from [5].

Figure 2.9 Five different combustion states categorized based on normalized permutation entropy,  $H_{PE}$  and equivalence ratio,  $\phi$  [31].

Figure 2.10 Schematic flow patterns in the evolution of RT unstable two-dimensional flows. The light fluid penetrates the heavy fluid under acceleration directed towards the heavy fluid in all conditions where a) normal mode perturbation, b) free-surface bubble, c) falling spike in negligible density medium, d) falling spike in a medium with finite density, and e) advanced stage of intermixing. Reproduced from [42].

Figure 2.11 Before and after schematics of a shock passing through a fluid interface, producing the Richtmyer-Meshkov instability. Initial shock was planar, while the transmitted and reflected shocks were corrugated. Reproduced from [40].

Figure 2.12 Two types of Rayleigh-Taylor instability, a) gravity driven and b) pressure driven, divided into three stages, i) undisturbed interface, ii) disturbed interface, and iii) interface at time  $t$ . Reproduced from [46].

Figure 2.13 Schematic diagram of thermodiffusive instability for Lewis number more than 1, equal to 1 and less than 1. A and B represent the concave and convex surface of the flame respectively.

Figure 2.14 Development of a hydrodynamic instability. Reproduced from [56].

Figure 2.15 Example of a flame distortion cycle in a closed tube propagation. Reproduced from [4].

Figure 2.16 Propagation pressure and flame position of a  $\phi = 0.77$  propane mixture, with a laminar flame speed,  $U_L = 0.27$  m/s. Propagation fell under type (iii), acoustic frequency was 122 Hz. Reproduced from [8]

Figure 2.17 High speed tomographic cuts of premixed flames in open ended ignition tubes at different stages, a) curved flame during onset of primary instability, b) flat flame during saturation of primary instability, c) cellular structures during onset of secondary instability, and d) high amplitude cells during secondary instability. Reproduced from [62] based on [8].

Figure 2.18 Fluctuation of the mean B/G ratio and the flame front position, reproduced from [63].

Figure 2.19 Maximum peak-to-peak pressure amplitudes for n-butane-methane-air mixtures, oscillating at the fundamental mode ( $\sim 260$  Hz) in a 0.6 m tube, reproduced from [28].

Figure 2.20 Maximum peak-to-peak pressure amplitudes for n-butane-methane-air mixtures, oscillating at the first harmonic ( $\sim 260$  Hz) in a 1.2 m tube, reproduced from [28]

Figure 2.21 Laminar burning velocity of methane.



Figure 2.22 Effect of hydrogen addition on laminar burning velocity of methane.

Figure 2.23 Three waves,  $y_1$ ,  $y_2$  and  $y_3$  plotted in (a) and the combined wave,  $y_{total}$  in (b).

Figure 2.24 Example of a discrete Fourier Transform from a) randomly generated time signal, producing b) the 3-dimensional representation of the time-series signal, c) the power spectrum, and finally d) the phase spectrum. Reproduced from [72].

Figure 2.25 Acoustic pressure records decane flame spray in a 1.2 m tube. a)  $\phi = 0.9$ , showing a short silence before a frequency transition in the instability whereas b)  $\phi = 1.1$  showing three consecutive instabilities appearing at different frequencies. Reproduced from [6].

Figure 2.26 Fast Fourier transform of position (solid blue line) and pressure signal (dotted red line) of a  $\phi = 0.8$  propane flame divided into 3 sections according to flame structure. Reproduced from [74].

Figure 2.27 Fast Fourier Transform of  $y_{total}$ .

Figure 2.28 Fourier spectrogram of a) flame position and b) flame pressure of a  $\phi = 0.8$  propane flame. Reproduced from [74].

Figure 2.29 Comparison between a Continuous Wavelet Transform (CWT) and a synchrosqueezed wavelet transform (SST). Reproduced from [80].

Figure 2.30 Synchrosqueezed transform plot for  $y_{total}$ , clearly showing the existence of 2 different dominant frequencies.

Figure 2.31 Plots of a) instantaneous phase of  $y_2$  and  $y_3$ , followed by b) phase difference between both signals.

Figure 2.32 Phase difference between flame chemiluminescence and combustor pressure against normalized instability intensity for 4,950 operating conditions. Reproduced from [93].

Figure 3.1 Picture of the flame tube rig.

Figure 3.2 The flame tube rig diagram, I – Ignition Port, FI – Fuel Injection Port.

Figure 3.3 Flame sequence of a  $\phi = 0.8$ ,  $R_H = 0.3$  flame, recorded at 1,500 fps, suffers low light intensity.

Figure 3.4 Flame sequence of a  $\phi = 1.0$ ,  $R_H = 0.2$  flame, recorded at 1,500 fps.

Figure 3.5 Example of a) flame front position plot produced from flame tracking of b) flame sequence.

Figure 3.6 Example of a) trigger signal with pressure signal, b) zoomed in pressure signal, both before cropping.

Figure 3.7 Video recording to trigger signal synchronisation in the present work.

Figure 3.8 Reversing motion of the tracked metal plate edge (green line) after hitting the tube.

Figure 3.9 Example of a synchronised pressure and flame front position signal.

Figure 4.1 Typical flame propagation sequence with time increment of 0.00067 seconds for each frame upwards.

Figure 4.2 Sequential flame images for three types of flame behaviour: a) steady flame, b) pulsating flame and c) oscillating flame. The images are from a  $\phi = 1.2$  methane flame with  $R_H = 0.2$  hydrogen addition. Yellow lines were used to show the flame sequence, with a 1/1500 s increment between them upwards the column.

Figure 4.3 Image denoising flowchart.

Figure 4.4 Background subtraction. (a) Current image, (b) First image of the sequence, (c) Subtracted image.

Figure 4.5 Intensity enhancement. (a) 5x intensity. (b) 10x intensity. (c) 15x intensity and (d) 20x intensity.

Figure 4.6 Image thresholding. (a) Grayscale image. (b) 0.6 threshold. (c) 0.7 threshold. (d) 0.8 threshold.

Figure 4.7 Small objects removal. (a) Original image. (b) 5 pixels object removal. (c) 10 pixels object removal. (d) 15 pixels object removal.

Figure 4.8 Image dilation. (a) Original image. (b) 3 pixels disk dilation. (c) 6 pixels disk dilation. (d) 9 pixels disk dilation.

Figure 4.9 Region filling. (a) Original image. (b) Filled image.

Figure 4.10 Large objects removal. (a) Original image. (b) 50 pixels object removal.

Figure 4.11 Coordinate based noise removal. (a) Original image) (b) Noise removed beyond 30% of the rightmost pixel.

Figure 4.12 Initial and final white pixel count per row.

Figure 4.13 Flame front, tail, mean and thickness definition based on white pixel count per column.

Figure 4.14 a) Flame positions, b) Flame thickness and c) Flame size plotted against time.

Figure 4.15 Effects of different passband frequency on a) flame position and b) flame distance amplitude and c) underlying flame velocity.

Figure 4.16 Flame front positions and their respective derivatives.

Figure 4.17 Artificial signal original composition.

Figure 4.18 Fast Fourier Transform on artificial signal.

Figure 4.19 Fast Fourier Transform of a  $\phi = 1.2$  methane flame with  $R_H = 0.2$  hydrogen addition, exhibiting spectral broadening.

Figure 4.20 Four main steps of oscillatory modes extraction via synchrosqueezed wavelet transform.

Figure 4.21 Synchrosqueezed transform contour plot of artificial signal.

Figure 4.22 Effect of penalty levels on the formation of frequency ridges formed from a) no penalty, b) penalty = 1, and c) penalty =20.

Figure 4.23 Comparison between original and reconstructed components.

Figure 4.24 SST contour plot of a  $\phi = 1.2$  methane flame with  $R_H = 0.2$  hydrogen addition pressure signal.

Figure 4.25 Frequency ridges formed from an SST penalty of 20 on a  $\phi = 1.2$  methane flame with  $R_H = 0.2$  hydrogen addition pressure signal.

Figure 4.26 Reconstruction of a) the original pressure signal into b) ~200 Hz pressure component, and c) ~400 Hz pressure component of a  $\phi = 1.2$  methane flame with  $R_H = 0.2$  hydrogen addition. Two parameters collected, i) maximum ~200 Hz pressure and ii) maximum ~400 Hz pressure component.

Figure 4.27 Instantaneous phase plots for a) 200 Hz flame size component, b) 200 Hz pressure component, c) 400 Hz flame size component, and d) 400 Hz pressure component.

Figure 4.28 Phase difference of a) 200 Hz components and b) 400 Hz components.

Figure 4.29 Phase difference vs pressure of oscillation for a) 200 Hz components and b) 400 Hz components.

Figure 5.1 Sequence of flame behaviours, 1) steady flames, 2) pulsating flames, and 3) oscillating flames.

Figure 5.2 Comparison between real flame images with flame structures described by Markstein[5] in Figure 2.7, for a) oscillating flames and b) pulsating flames.

Figure 5.3 Image sequence of the propagation of an oscillating  $R_H$  0.2, 1.2 equivalence ratio flame along with pressure and flame front position.

Figure 5.4 Image sequence, pressure signal and flame front position of a steady flame.

Figure 5.5 Image sequence, pressure signal and flame front position of a pulsating flame.

Figure 5.6 Image sequence, pressure signal and flame front position of an oscillating flame.

Figure 5.7 Propagation of a  $R_H = 0.1$ ,  $\phi = 1.2$  methane flame with a) underlying acceleration, b) decomposed velocity, c) decomposed pressure and d) flame sequence.

Figure 5.8 Flame propagation at point A, where a) flame underlying acceleration, b) flame sequence.

Figure 5.9 Flame propagation at point B, where a) flame underlying acceleration, b) flame sequence.

Figure 5.10 Flame propagation at point C, where a) flame underlying acceleration, b) flame sequence.

Figure 5.11 Flame propagation at point D, where a) flame underlying acceleration, b) flame sequence.

Figure 5.12 Range of flames analysed based on the theoretical laminar burning velocity contour plot, where a) flames with increasing equivalence ratio,  $\phi$  at constant hydrogen addition  $R_H = 0.1$ , b) flames with increasing hydrogen addition,  $R_H$  at constant equivalence ratio,  $\phi = 1.1$ , and finally 3 flames of approximately similar laminar burning velocity at points (c), (d), and (e).

Figure 5.13 Effect of equivalence ratio on  $R_H$  0.1 flames on a) flame front position, b) flame front position amplitude, c) flame front speed, d) tube end pressure, e) flame size, and finally f) flame length for equivalence ratios,  $\phi = 0.8 - 1.1$ .

Figure 5.14 Effect of equivalence ratio on  $R_H$  0.1 flames on a) flame front position, b) flame front position amplitude, c) flame front speed, d) tube end pressure, e) flame size, and finally f) flame length for equivalence ratios,  $\phi = 1.2 - 1.5$ .

Figure 5.15 SST plots for a) pressure signal and b) distance amplitude signal of methane flames with constant hydrogen addition,  $R_H = 0.1$ , and increasing equivalence ratio,  $\phi = 0.8 - 1.1$ .

Figure 5.16 Frequency analysis of a) raw flame speed, broken down into b) underlying flame speed, c) 200 Hz flame speed component, and d) 400 Hz speed component for,  $\phi = 0.8 - 1.1$ . Analysis continued with e) raw pressure signal, broken down into f) 200 Hz pressure signal component and g) 400 Hz pressure signal component.

Figure 5.17 SST plots for a) pressure signal and b) distance amplitude signal of methane flames with constant hydrogen addition,  $R_H = 0.1$ , and increasing equivalence ratio  $\phi = 1.2 - 1.5$ .

Figure 5.18 Frequency analysis of a) raw flame speed, broken down into b) underlying flame speed, c) 200 Hz flame speed component, and d) 400 Hz speed component for  $\phi = 1.2 - 1.5$ . Analysis continued with e) raw pressure signal, broken down into f) 200 Hz pressure signal component and g) 400 Hz pressure signal component.

Figure 5.19 Phase study between tube end pressure and flame size for  $\phi = 0.8 - 1.1$ . Raw signals broken down into 200 Hz component of a) flame pressure, b) flame size, c) phase difference between a) and b). 400 Hz component of d) flame pressure, e) flame size and f) phase difference between d) and e).

Figure 5.20 Phase study between tube end pressure and flame size for  $\phi = 1.2 - 1.5$ . Raw signals broken down into 200 Hz component of a) flame pressure, b) flame size, c) phase difference between a) and b). 400 Hz component of d) flame pressure, e) flame size and f) phase difference between d) and e).

Figure 5.21 Phase difference for a) 200 Hz component and b) 400 Hz component plotted against tube end pressure signal for flames  $\phi = 0.8 - 1.1$ .

Figure 5.22 Phase difference for a) 200 Hz component and b) 400 Hz component plotted against tube end pressure signal for flames  $\phi = 1.2 - 1.5$ .

Figure 5.23 Effect of hydrogen addition on  $\phi = 1.1$ ,  $R_H = 0 - 0.4$  flames, on a) flame front position, b) flame front position amplitude, c) flame front speed, d) tube end pressure, e) flame size, and f) flame length.

Figure 5.24 Effect of hydrogen addition on constant equivalence ratio,  $\phi = 1.1$ , and increasing hydrogen addition,  $R_H = 0.5 - 0.8$  flames on a) flame front position, b) flame front position amplitude, c) flame front speed, d) tube end pressure, e) flame size, and f) flame length.

Figure 5.25 SST plots for a) pressure signal and b) distance amplitude signal of methane flames with constant equivalence ratio,  $\phi = 1.1$  and increasing hydrogen addition,  $R_H = 0 - 0.4$ .

Figure 5.26 Frequency analysis of a) raw flame speed, broken down into b) underlying flame speed, c) 200 Hz flame speed component, and d) 400 Hz speed

component for  $\phi = 1.1$  flames,  $R_H = 0 - 0.4$ . Analysis continued with e) raw pressure signal, broken down into f) 200 Hz pressure signal component and g) 400 Hz pressure signal component.

Figure 5.27 SST plots for a) pressure signal and b) distance amplitude signal of methane flames with constant equivalence ratio,  $\phi = 1.1$  and increasing hydrogen addition,  $R_H = 0.5 - 0.8$ .

Figure 5.28 Frequency analysis of a) raw flame speed, broken down into b) underlying flame speed, c) 200 Hz flame speed component, and d) 400 Hz speed component for  $\phi = 1.1$  flames,  $R_H = 0.5 - 0.8$ . Analysis continued with e) raw pressure signal, broken down into f) 200 Hz pressure signal component and g) 400 Hz pressure signal component.

Figure 5.29 Phase study between tube end pressure and flame size for  $\phi = 1.1$  flames,  $R_H = 0 - 0.4$ . Raw signals broken down into 200 Hz component of a) flame pressure, b) flame size, c) phase difference between a) and b). 400 Hz component of d) flame pressure, e) flame size and f) phase difference between d) and e).

Figure 5.30 Phase study between tube end pressure and flame size for  $\phi = 1.1$  flames,  $R_H = 0.5 - 0.8$ . Raw signals broken down into 200 Hz component of a) flame pressure, b) flame size, c) phase difference between a) and b). 400 Hz component of d) flame pressure, e) flame size and f) phase difference between d) and e).

Figure 5.31 Phase difference for a) 200 Hz component and b) 400 Hz component plotted against tube end pressure signal for  $\phi = 1.1$  flames,  $R_H = 0 - 0.4$ .

Figure 5.32 Phase difference for a) 200 Hz component and b) 400 Hz component plotted against tube end pressure signal for  $\phi = 1.1$  flames,  $R_H = 0.5 - 0.8$ .

Figure 5.33 Comparison between  $\phi = 0.8$ ,  $R_H = 0.3$ ,  $\phi = 1.0$ ,  $R_H = 0.2$  and  $\phi = 1.4$ ,  $R_H = 0.4$  flames, where a) flame front position, b) flame front position amplitude, c) flame front speed, d) tube end pressure, e) flame size, and f) flame length.

Figure 5.34 SST plots for a) pressure signal and b) distance amplitude signal of methane flames with approximately similar laminar burning velocity,  $\phi = 0.8$ ,  $R_H = 0.3$ ,  $\phi = 1.0$ ,  $R_H = 0.2$  and  $\phi = 1.4$ ,  $R_H = 0.4$ .

Figure 5.35 Frequency analysis of a) raw flame speed, broken down into b) underlying flame speed, c) 200 Hz flame speed component, and d) 400 Hz speed component for  $\phi = 0.8$ ,  $R_H = 0.3$ ,  $\phi = 1.0$ ,  $R_H = 0.2$  and  $\phi = 1.4$ ,  $R_H = 0.4$  flames. Analysis continued with e) raw pressure signal, broken down into f) 200 Hz pressure signal component and g) 400 Hz pressure signal component.

Figure 5.36 Phase study between tube end pressure and flame size for  $\phi = 0.8$ ,  $R_H = 0.3$ ,  $\phi = 1.0$ ,  $R_H = 0.2$  and  $\phi = 1.4$ ,  $R_H = 0.4$  flames. Raw signals broken down into 200 Hz component of a) flame pressure, b) flame size, c) phase difference between a) and b). 400 Hz component of d) flame pressure, e) flame size and f) phase difference between d) and e).

Figure 5.37 Phase difference for a) 200 Hz component and b) 400 Hz component plotted against tube end pressure signal for  $\phi = 0.8$ ,  $R_H = 0.3$ ,  $\phi = 1.0$ ,  $R_H = 0.2$  and  $\phi = 1.4$ ,  $R_H = 0.4$  flames.

Figure 5.38 Contour plot of maximum raw flame front distance amplitude.

Figure 5.39 Contour plot of maximum 200 Hz flame front distance amplitude.

Figure 5.40 Contour plot of maximum 400 Hz flame front distance amplitude.

Figure 5.41 Contour plot of initial underlying flame velocity.

Figure 5.42 Contour plot of maximum underlying flame velocity.

Figure 5.43 Contour plot of maximum 200 Hz flame velocity.

Figure 5.44 Contour plot of maximum 400 Hz flame velocity.

Figure 5.45 Contour plot of maximum raw tube end pressure signal.

Figure 5.46 Contour plot of maximum 200 Hz tube end pressure signal.

Figure 5.47 Contour plot of maximum 400 Hz tube end pressure signal.

Figure 6.1 Maximum raw pressure contour plot with theoretical laminar burning velocity contour lines.

Figure 6.2 Peak distance amplitude against peak pressure scatter plot for ~200 Hz and ~400 Hz components for all unsteady flames.



Figure 6.3 Peak velocity against peak pressure scatter plot for ~200 Hz and ~400 Hz components for all unsteady flames.

Figure 6.4 Peak underlying velocity against peak pressure scatter plot for ~200 Hz and ~400 Hz components of oscillating flames.

## NOMENCLATURE

$\phi$	Equivalence ratio
$C$	Mole concentration
$R_H$	Hydrogen addition
$R$	Rayleigh Index
$p'$	Fluctuating pressure
$q'$	Fluctuating heat release
$T$	Period of instability
$\lambda$	Wavelength
$v$	Velocity
$g$	Gravitational acceleration
$Le$	Lewis number
$\alpha$	Thermal diffusivity
$D$	Molecular diffusivity
$k$	Wave number of perturbation
$U_L$	Laminar burning velocity
$\sigma$	Growth rate of hydrodynamic instability
$\rho$	Density
$\bar{x}_F$	Fuel mole fraction
$\bar{x}$	Mole fraction of constituent
$a_s$	Air-fuel ratio
$X_f$	Fourier coefficient
$f$	Frequency
$n$	Number of data points
$x$	Inverse Fourier transform
$A$	Instantaneous amplitude
$t$	Instantaneous time

$\theta$	Instantaneous phase
$\eta$	Additive noise
$W_s$	Wavelet transform
$\psi^*$	Mother wavelet in time domain
$a$	Scale of mother wavelet
$b$	Time shift of mother wavelet
$\xi$	Angular frequency
$\hat{\psi}^*$	Mother wavelet in frequency domain
$\omega_s$	Instantaneous frequency
$\omega_l$	Central frequency
$T_s$	Sychrosqueezed transform

#### Subscripts

$F$	Fuel constituent of the mixture
$H$	Hydrogen constituent of the mixture
$m$	Methane constituent of the mixture
$A$	Air constituent of the mixture
$st$	Stoichiometric
$o$	Unburned gas
$b$	Burned gas
$i$	$i^{\text{th}}$ constituent of fuel mixture
$j$	$j^{\text{th}}$ constituent of fuel mixture
$n$	Number of data points
$k$	Number of iterations / $k^{\text{th}}$ component
$K$	Maximum number of components in signal
$s$	Instantaneous component of frequency

# 1 INTRODUCTION

The impact of acoustically driven oscillations on flames remains a continual problem in combustion. It was evident at the beginning of combustion research when Mallard and Le Chatelier [1] investigated the propagation of flames in tubes, and it has been reinvestigated over the subsequent years, usually as a result of the need to better understand combustion hazards or when there is a requirement to increase the specific power of combustion driven engines. The propagation of premixed flames in tubes is a convenient method of observing acoustically driven oscillations. Investigations in tubes date back many years with notable contributions by Mallard and Le Chatelier [1], Mason and Wheeler [2], Coward and Hartwell [3], Guénoche [4], Markstein [5] and Clanet et al. [6] to name a few. However, despite these studies, there remain uncertainties concerning the main features associated with the propagation of flames in tubes. A key problem is that the way the flame propagates is sensitive to the rig configuration and boundary conditions, these include propagation direction (horizontal or vertical), ends closed or open, tube diameter and ignition source.

The description of premixed flame propagation in open-ended horizontal tubes has been provided by Markstein [5] and Guénoche [4]. Following ignition, the flame shape becomes convex towards the unburned gas and propagates steadily down the tube significantly faster than the laminar burning velocity. At around half of the distance along the tube, the flame enters a longitudinal acoustic field created by itself. The frequency of the oscillations depends on the dimensions of the tube. The initial impact of the oscillations on the flame is to flatten its shape resulting in a decrease in its velocity due to the reduced surface area. After a few acoustic cycles, the flame can suddenly start to accelerate and this is associated with violent flame oscillations and an increase in the amplitude of the pressure oscillations. As the flame continues down the tube, the amplitude of the oscillations within the field dampens and ultimately the flame propagates steadily at the end of the tube.

Flames can spontaneously produce acoustic oscillations in tubes or any other confined space [4]. The oscillations are attributed to a feedback process where the acoustic wave modulates the heat release as described by Rayleigh's criterion [7]. This states that the acoustic wave will be amplified if the fluctuations in the heat release and the acoustic pressure are in phase. Following on from the work of Markstein, in particular, Searby proposed the existence of two acoustic instabilities in tubes: primary and secondary [8], [9]. The primary instability (flame flattening) does not feature here as it only appears within a very short period in the

configuration tested. The secondary instability (the subject of this study) is much more violent and is associated with pulsating cellular flames and has the characteristics of a parametric instability. In a parametric instability, the resonance is driven by modulation of the natural frequency. Despite the long and distinguished history of the study of flames propagating in tubes, it is probably not possible to predict how a flame might behave without performing a measurement.

Here we have observed the behaviour of premixed methane/hydrogen/air flames propagating horizontally in a 1.2m long tube (internal diameter 0.02m) open at both ends. Methane with equivalence ratio,  $\phi$ , ranging from 0.8 – 1.5 with 0.1 increment was tested. Adapting a hydrogen addition method,  $R_H$ , by Yu et al.[10], each equivalence ratio was added with hydrogen up to  $R_H = 0.8$ , with 0.1 increment. A total of 72 different mixtures were burnt and observed using a high-speed camera. Increasing the hydrogen addition increased the laminar burning velocity and the primary objective of this work was to observe the impact on the oscillatory propagation of the flame.

## 2 LITERATURE REVIEW

In this section, the history and definitions of flame propagation instabilities in tubes were covered to provide some background of the present work which includes flame tube configuration, fuel composition, flame stability and spectral analysis of flame propagations, which will ultimately highlight the research gap covered by the present work.

### 2.1 Premixed Flame Instabilities

The discovery of singing flames by Higgins[11] back in 1777 initiated the interest in thermoacoustic instabilities. He describes how he discovered the phenomenon, which was simply by placing a diffusion hydrogen flame into a tube with the intention to show formation of water droplets from hydrogen combustion, and discovered a humming sound during the process. He did further investigations on the phenomenon by burning hydrogen flames in tubes of different geometries and materials, getting different tones for different configurations.

In 1878, Lord Rayleigh characterized the occurrence of thermoacoustic instabilities scientifically, associating heat release with pressure oscillations. He describes it as a vibration maintained by heat, in which heat release excites pressure oscillations [7]. He concludes that vibration is encouraged in two conditions, when heat is applied to air in high pressure or when heat is taken away from air in low pressure, whereas the vibration is dampened when heat is applied to air in low pressure or heat is taken away from air in high pressure [12].

Putnam and Dennis [13] published a very detailed survey paper on organ-pipe oscillations, known as thermoacoustic interactions presently, covering 53 different papers in total. They classified the references based on the combustion system used to study the interaction which are singing diffusion flames, flash tubes, gauze tone burners, rocket shaped burners, secondary air burners, and ram jet type burners. It would be lengthy to cover all of the combustion systems mentioned, so the present work will only cover flash tubes, which is the setup used in this study, and gauze tone burners, which will be helpful in understanding the Rayleigh's criterion mentioned in the introduction. If the reader wishes to do further reading on the different combustion systems for studying thermoacoustic interactions, this paper is very useful in understanding the combustion systems mentioned.

Flash tubes were first discovered by Mallard and Le Chatelier[1] in 1883, stating that a flame propagating from an open to a closed end will start oscillating as it progresses along the tube. They performed photographic studies on the

propagating flames and later concluded that oscillation and detonation depend on the composition of the mixture and the tube configuration. This was left for quite a while until Coward [3] conducted a study to investigate the oscillations in 10 and 20 cm diameter tubes. One of the important findings that they discovered was the fact that oscillations occur when the flame moves from the pressure node towards a velocity node within a tube.

Later in 1951, Schimdt [14] utilized schlieren photography to study the oscillations in tubes of different configurations. A description of how the interaction evolves starts from an oscillating flame which sets off a series of waves, and accumulates energy, leading to detonation in some cases. They proposed that the following sequence of tube configurations with increasing possibility of oscillation, open to closed, closed to open and finally closed to closed. However, there was no theory presented for the source of initial energy driving the oscillations.

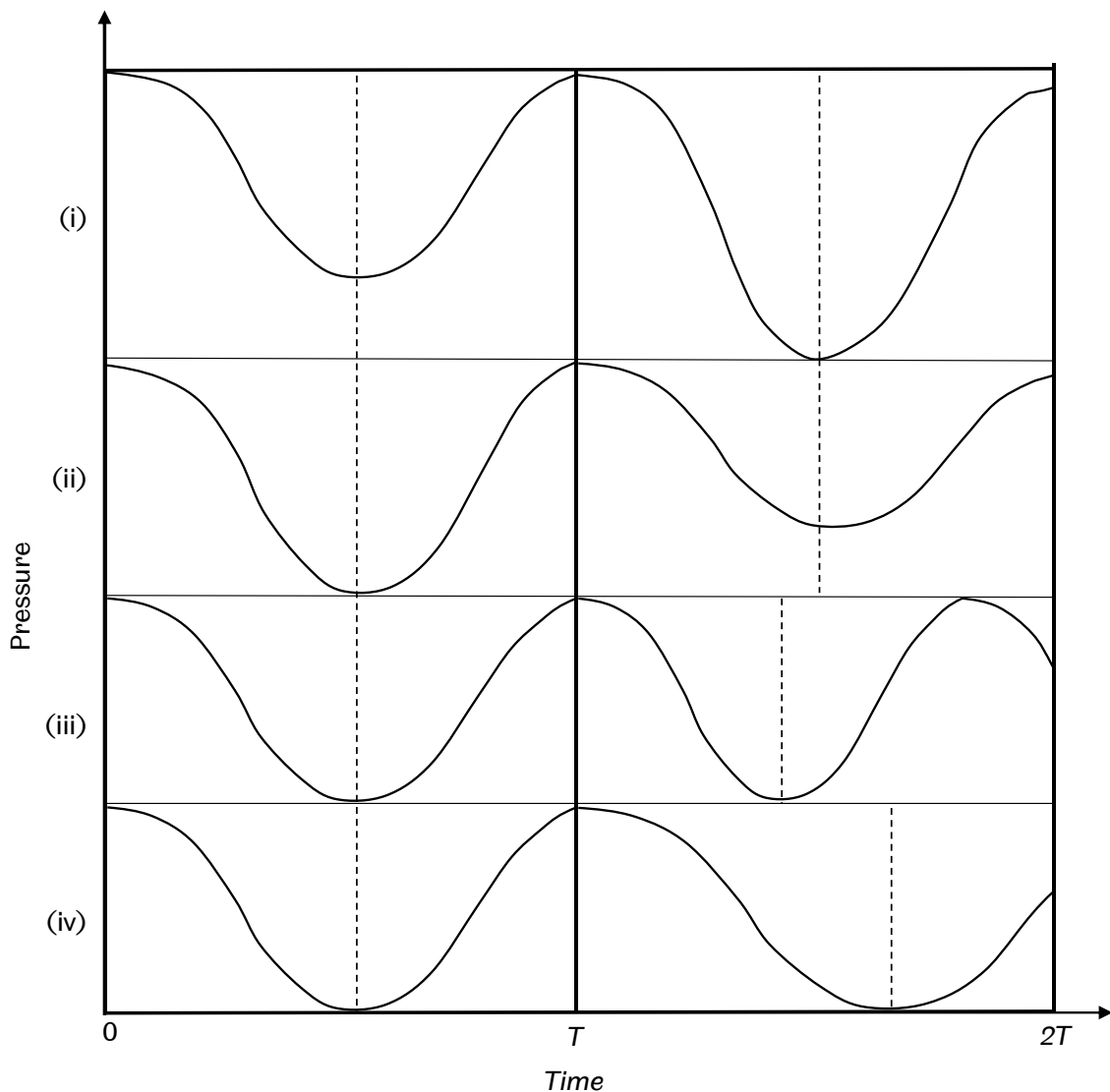
Kaskan[15] used methane air mixtures in most of his experiments. He conducted experiments with tubes of 0.75 and 1.5 inch in diameter, with an open to closed configuration. Instead of testing a wide range of fuel mixtures, he concentrated on mixtures that produces flat and disk-like flames during propagation, in order to study the cyclic addition of heat which drives the oscillations. Majority of the oscillations started oscillating in between  $1/3$  to  $1/2$  of the tube length and stops at  $5/6$  of the tube length. The study concluded 2 possible mechanisms responsible for the heat driven oscillation. The first conclusion was that flame speed fluctuates with the cyclic change in the temperature and pressure, which means the heat release rate periodically changes with pressure, satisfying Rayleigh's criterion.

The second mechanism proposed by Kaskan[15] was the periodic change in flame area. He described that within the acoustic boundary layer (defined as a thin region near the wall where viscosity effects exist [16] ), the flame will flatten out at its point of maximum recession and becomes cusped (cellular) during the point of maximum penetration, leading to an increased surface area of the flame. Since the point of maximum penetration is caused by an increase in pressure, the driving condition stated by Rayleigh is also satisfied. In addition to this, he also stated that during the early part of propagation, the pressure amplitude increases, driving the oscillation, and as the flame gets closer to the end, the velocity amplitude decreases, leading to a reduction in flame shape fluctuation which eventually stops the fluctuation.

Wood stated the effects of phase of heat supply relative to phase of pressure, shown in Figure 2.1. For simplicity, let us assume that the initial pressure wave (left side of the figure) has a frequency of 80 Hz at a phase of  $90^\circ$ , and an amplitude of 5 bars. If the heat supply component has a phase of  $90^\circ$  (in phase) and a frequency of 80 Hz,

the amplitude of pressure will increase to a value higher than 5 bars, while the frequency maintains at 80Hz, represented by (i). If the heat supply component has a phase of  $270^\circ$  (out of phase), and a frequency of 80 Hz, the pressure amplitude will decrease to a value lower than 5 bars, while maintaining a frequency of 80 Hz, represented by (ii).

If the phase of heat supply was  $0^\circ$  (quarter period before the phase of pressure), the amplitude of vibration will be maintained at 5 bars, but the frequency will increase to a value higher than 80 Hz, represented in (iii). Finally, if the phase of heat supply was  $180^\circ$ , (a quarter period after the phase of pressure), the amplitude remains constant at 5 bars, while the frequency decreases to a value lower than 80 Hz, represented in (iv) [17].



**Figure 2.1 Effect of different phase of heat supply relative to phase of pressure, i) in phase, ii) out of phase, iii) quarter period before, and iv) quarter period after.**

Reproduced from [17].



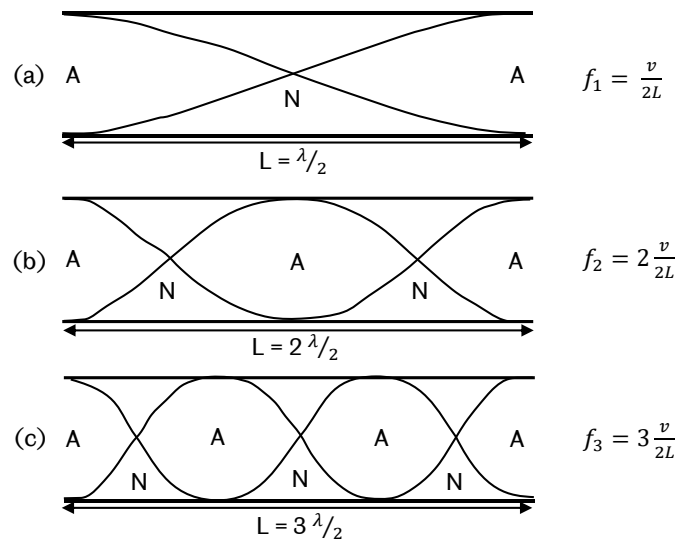
Lord Rayleigh stated that one aspect which needs to be considered for a heat driven oscillation is the phase relation between heat release and acoustic pressure oscillation. This criterion sparked the interest in Putnam and Dennis [13] to derive it mathematically and at the same time incorporates the phase relation suggested by Lord Rayleigh.  $R$  represents the Rayleigh Index,  $T$  represents the time taken for one cycle of instability (period), and finally,  $p'$  and  $q'$  represent the fluctuating pressure and heat release respectively:

$$R = \int_0^T p'(t)q'(t) dt \quad (2.1)$$

Based on equation (2.1), a positive valued Rayleigh Index indicates a transfer of energy from the heat release to the pressure oscillations, and a negative index indicates the damping of pressure oscillation. However, a positive index does not guarantee an amplification of the pressure oscillation, it must be sufficient to overcome the pressure dissipation losses in order to maintain a self-driven thermoacoustic instability, which could be achieved through the coupling between the heat release and pressure oscillation [13].

Thermoacoustic phenomenon described by the Rayleigh's criterion in the previous section was thoroughly investigated by Rijke [18] in 1859. He was able to prove the phenomenon experimentally and theoretically with a Rijke tube, which is a vertically open-ended tube with a heat source placed at the bottom quarter of the tube. Sound waves propagating within a tube will be reflected back into the tube when it reaches an open end, and when the reflected sound wave interferes another wave, this forms standing waves within a tube [19], which varies according to its wavelength as shown in Figure 2.2. The three different harmonics correspond to 3 different frequency of vibrations,  $f$  based on the wavelength, at a constant wave speed (normally assumed to be the speed of sound in the tube),  $v$ .

Based on Figure 2.2(a), the first harmonic of an open-ended tube has pressure nodes located at its open ends, which coexists with velocity fluctuation antinodes, indicating that the velocity fluctuation phase leads the pressure oscillation phase by  $90^\circ$  in the bottom half of the tube, and lags the same amount of phase in the top half. When a heat source is introduced to the tube, the flow across the tube will follow the direction of the heat, which is upwards, due to the buoyancy effect of the heat source.

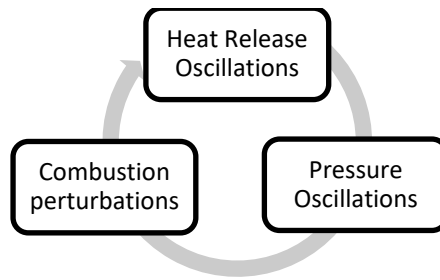


**Figure 2.2 First three harmonics of an open-ended tube, a) first harmonic, b) second harmonic, c) third harmonic, where A signifies the velocity antinodes whereas N represents velocity nodes. Reproduced from [19].**

Taking upward flow as a positive direction for velocity fluctuation, placing a heat source at the bottom half of the tube will excite the flow since heat transfer is directly coupled with flow velocity, and flow damping will occur if the heat source is in the top half. This is theoretically confirmed by the Rayleigh Index, which is positive for the bottom half of the tube, and negative for the top half. The excitation will produce a pressure fluctuation at its characteristic frequency which depends on different criteria for different configurations of a tube and start a feedback mechanism of thermoacoustic instability [18].

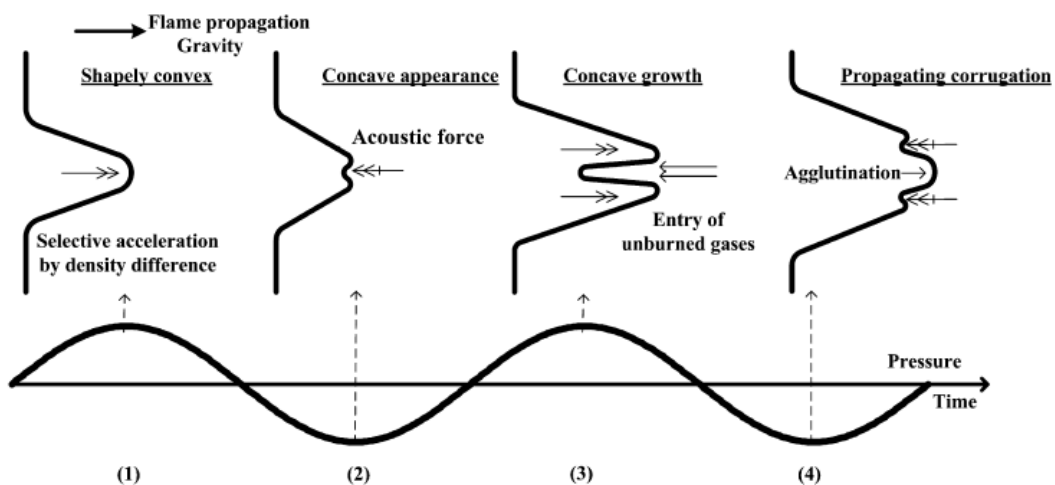
Studies have been conducted on the thermoacoustic coupling in lean premixed combustion systems, stating that fluctuation in the local volumetric heat release was due to perturbation in the flow field and reactant mixture composition caused by acoustic waves [20]. These fluctuations were often related with thermal diffusive instability and the Rayleigh-Taylor instability.

Thermal diffusive instabilities relate the difference in diffusion rate of mass and heat in the unburnt portion of a combustible mixture. The ratio of thermal to mass diffusivity of the deficit component in a mixture, Lewis number, is used to represent this instability[21]. The Rayleigh-Taylor instability in the other hand is caused by density difference between two fluids, leading to an acceleration of the boundary between two fluids accelerates towards the denser fluid. For a premixed flame, the reactive flame head acts as a boundary accelerating towards the denser unburnt portion [22].



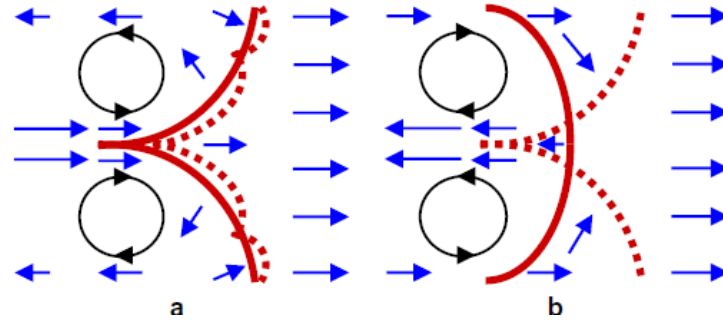
**Figure 2.3 Feedback mechanism of thermoacoustic instabilities.**

Confined propagating flames will generate acoustic waves, causing oscillation of the flame front, taking the shape of a tulip. Taniyama [21] described the initiation and propagation of a tulip flame, relating this phenomenon with the fluctuating pressure in a flame confinement as shown in Figure 2.4. Referring back to Rayleigh's criterion, self turbulization is possible when the heat release is in phase with the pressure fluctuation, forming the feedback loop in Figure 2.3.



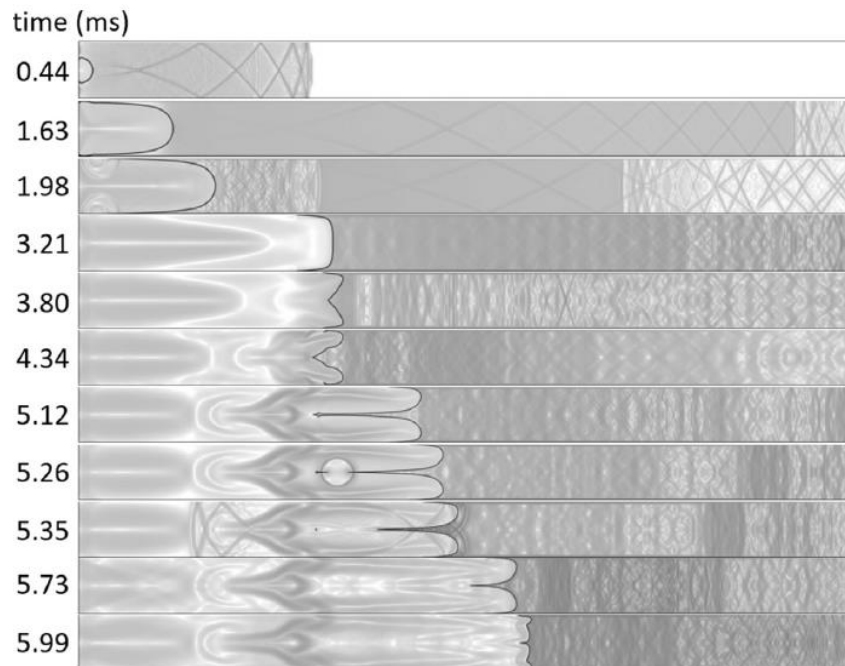
**Figure 2.4 Initiation and propagation of a tulip flame. Reproduced from [21].**

Xiao did an extensive study on the formation of a tulip flame computationally and experimentally. He proposed and explained in detail the formation of a distorted tulip flame due to vortex generation at the back of the tulip flame lips, as shown in Figure 2.5 [23]. The distorted tulip flame can only form following the formation of a classic tulip flame, which undergoes a force strong enough to cause the distortion, which is not the case in every propagating flame.



**Figure 2.5 Formation of (a) distorted tulip flame and (b) classic tulip flame. Solid lines indicate the initial flame shape; dashed lines indicate the subsequent flame shape. Arrows indicate the characteristic flow velocity field. Reproduced from [23].**

Viewing the formation of a tulip flame from a different aspect, both experimental and numerical studies suggests that tulip flame formation is a fluid dynamic phenomenon instead of an instability [23–25]. Xiao suggested the transition from a curved flame to a distorted tulip flame consists of five stages, 1) hemispherical flame expanding outward unaffected by sidewalls, 2) axially elongated finger shaped flame due to confinement and rapid increase of flame surface area, 3) elongated flame in contact with sides, causing surface area reduction, 4) tulip flame formation after flame inversion with a cusp pointing towards burnt gas, increasing surface area, 5) distorted tulip flame with secondary cusps superimposed on the primary tulip flame. This transition was depicted in Figure 2.6 by Xiao between 0.44-5.99 ms [26].



**Figure 2.6 Sequence of numerical schlieren images representing the evolution from a normal flame to a distorted tulip flame. Reproduced from [26].**

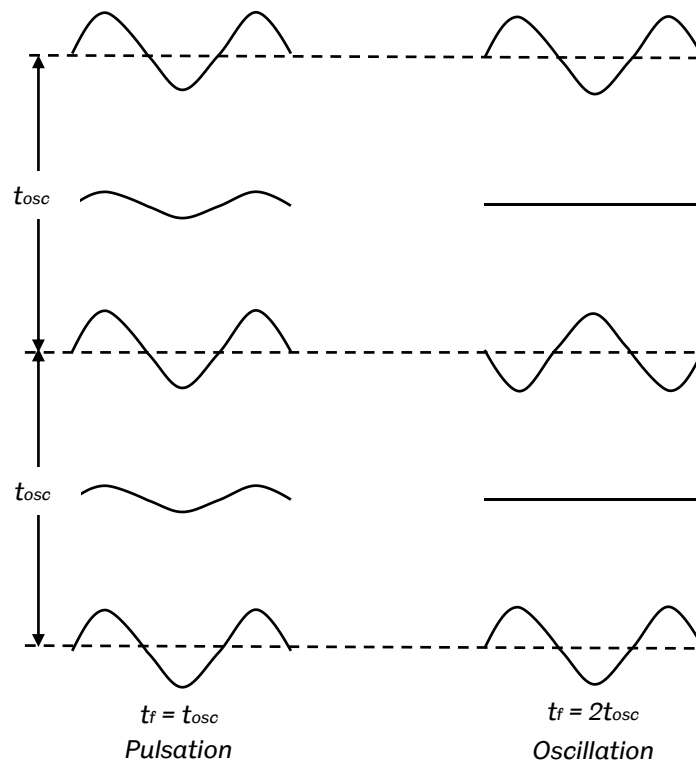
Markstein [27], [28] on the other hand, was more interested in the flame structure, which he believed to be overlooked by other researchers in the field. He conducted experiments that utilize n-butane and methane air mixtures as fuel. The working principle of his experiments was to get the flame ignited and stabilized with the aid of nitrogen for diluting the mixture if the propagation speed was too high. The study was separated into two parts.

The first part consisted of cellular structure of the flames tested. Upon completion of the first part, Markstein concluded that 20% methane/80% n-butane was the limit for a fully developed cellular flame structure, 50% leads to a non-cellular structure. The range between 20% and 50% methane produces non-cellular flames towards the richer region, and cellular flames close to stoichiometric. The fact that the difference in flame speed causes a variation in the flame structure made it a significant part of the findings. However, he had difficulty in testing lean mixtures due to the difficulty in stabilizing lean flames.

In the second part of his study, he focused on the vibratory flame movements, subjecting the flames to periodic acceleration, neglecting the impact of pressure waves. He discovered a complex sequence of frequency, amplitude, wave shape and flame speed during vibratory movements, and stated it was out the research scope. Towards the end of his study, there was a contradiction between the theoretical calculations and the experimental results. Theory suggests that excitation is proportional to the flame speed, meaning richer flames will have lower pressure maxima, but his experimental results stated the opposite. He concluded that the slower moving rich flames build up to larger values since they remain longer in the region prone to vibratory movements.

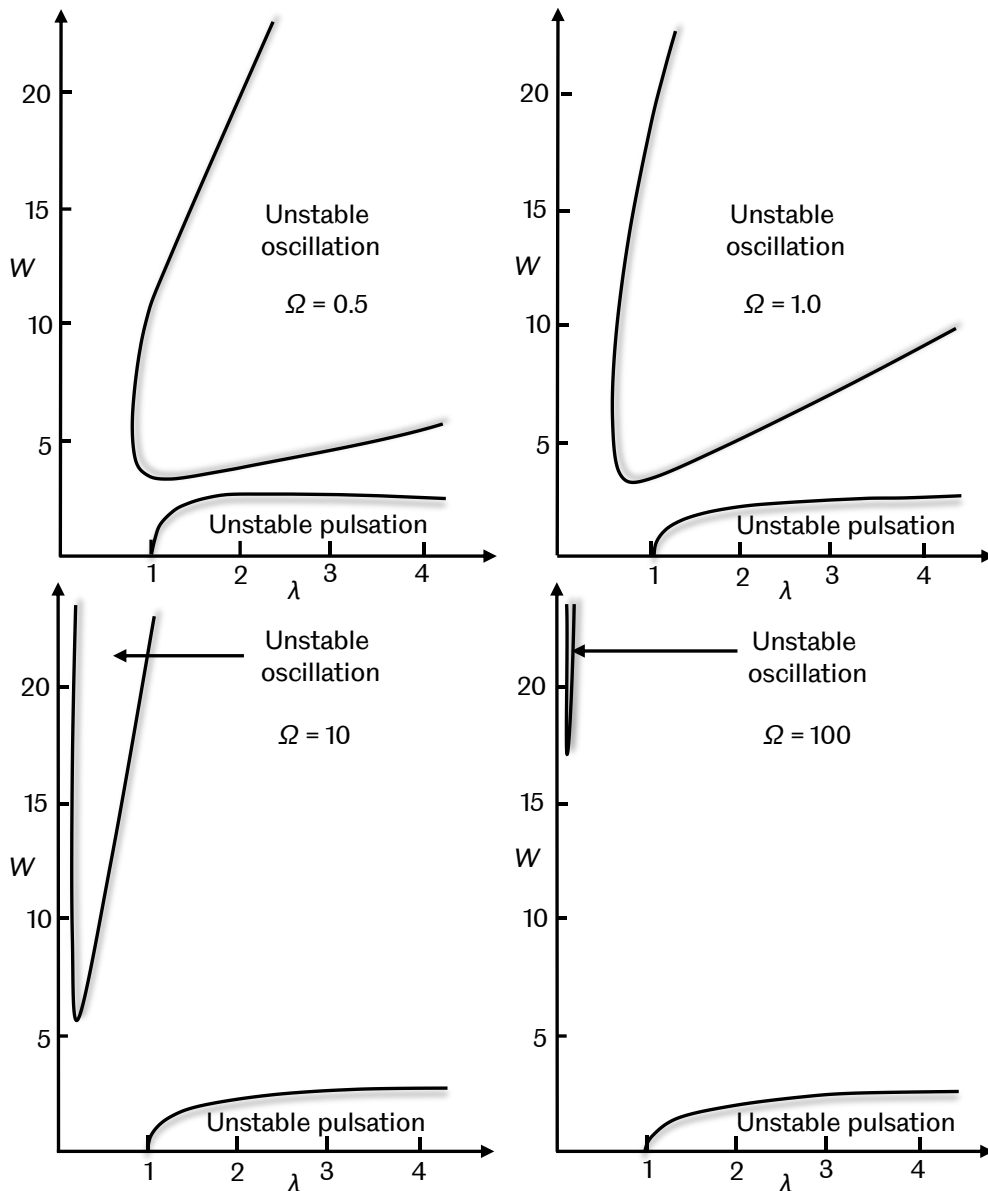
Markstein identified two unstable modes that occur in vibratory induced motion in flames, described graphically in Figure 2.7[5], which was exaggerated in terms of its shape to emphasize the difference between a pulsating and oscillating flame. The first mode was pulsation, which was observed to have the same period as the oscillation of the gas without inversion of the flame structure, which caused an insignificant change in the flame area. The minimal change in flame area may not provide the required feedback for the Rayleigh criterion[12]. The second mode described by Markstein was oscillation, where the flame was observed to experience structural inversion after turning flat, leading to an oscillatory period of twice the gas oscillation. The structural inversion mentioned was responsible for the change in flame structure from a sine wave to a straight line, providing more potential for interaction with the acceleration wave via the Rayleigh criterion.

Previously observed by Jost[29], he highlighted that the flame surface area of a pulsating flame did not fluctuate too much from an average value, whereas the oscillating flame undergoes a significant increase in flame surface area. This was thought to be related with the doubling of period experienced by oscillating flames shown in Figure 2.7. Markstein added that the unstable oscillation of a flame depends heavily on the frequency of the vibration, stating that the transition from a pulsating flame to an oscillating flame is easier for a low frequency vibration since a low velocity amplitude can trigger the unstable oscillation, whereas a high velocity amplitude is required to trigger the unstable oscillation for a high frequency vibration[5].



**Figure 2.7 Pulsating and oscillating flame structure induced by vibration of gas column. Reproduced from [5].**

It was further added by Markstein [5] that the flame is only subjected to one of these instabilities at any one time depending on the dimensionless velocity amplitude,  $W$ , and dimensionless wavelength,  $\lambda$ , of the periodic acceleration as shown in Figure 2.8. 4 plots were plotted in the figure, each tested at a different dimensionless frequency of oscillation,  $\Omega$ , a Strouhal number (dimensionless number describing the mechanism of an oscillating flow [30]), which depends on a characteristic length of a flame known today as the Markstein length,  $L$ . The Markstein length of a flame characterises the impact of flame curvature on the flame speed, and he further suggested that  $L$  was related to the flame thickness [5].



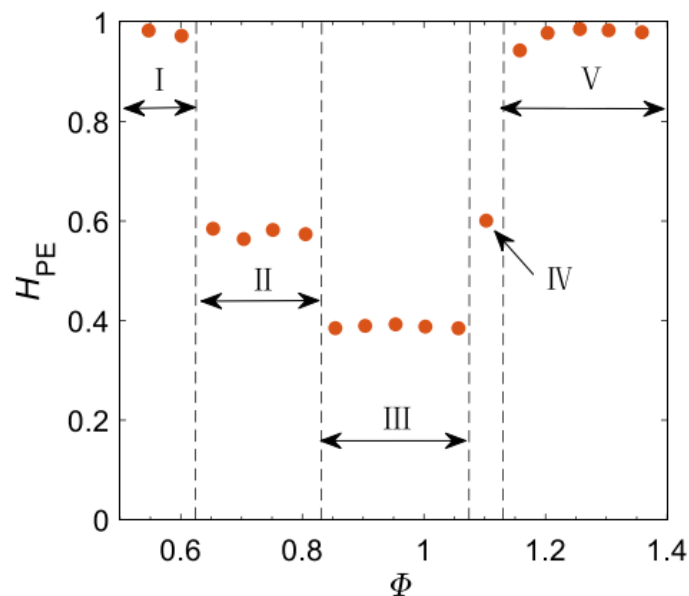
**Figure 2.8 Regions of unstable oscillation and pulsation induced by vibrations for different dimensionless frequency,  $\Omega$ , at varying dimensionless velocity amplitude,  $W$ , and dimensionless wavelength,  $\lambda$ . Reproduced from [5].**

Markstein went on to compare his theoretical results with experimental results from flame propagation in tubes, utilizing two studies in particular, simultaneous pressure and chemiluminescence measurements normal to the tube, and high speed shadowgraphy performed down a tube which clearly identified formation of 'cells'. During the early stages of flame propagation, the cells were observed to "fade away and appear periodically", which he stated occurs in all flames, and further added that the phenomenon should not be confused with flames that spontaneously produce cells [5].

During the unstable pulsation phase, Markstein observed that the flame propagation velocity was reduced with each pulsation of the flame structure, indicating a steady increase in the pressure amplitude. The transition from pulsation to oscillation depends on the Strouhal number,  $\Omega$ , which is influenced by the Markstein length of the flame,  $L$ . Change in the Strouhal number was observed to change the range of dimensionless velocity amplitude and dimensionless wavelength where the instability occurs.

The feedback between the pressure pulsations and flame according to Rayleigh's criterion was not accounted in the analysis by Markstein, but he did note changes in the phase difference between pressure and light intensity between the two instability modes. Another issue was mentioned in relating the pressure reading with the flame propagation as the pressure was measured at the end of the tube whilst the flame was located further up the tube [5].

In a recent study by Rao et al. [31], the relationship between pressure oscillations and flame behaviours were studied in a premixed swirl stabilized combustor of 0.7 m length and a bulk flow velocity of 10m/s. They were able to discover 5 different combustion states, specific to their swirl combustor which they named, i) lean stable combustion, ii) quasi-periodic oscillation mode, iii) limit-cycle oscillation mode, iv) dual-frequency oscillation mode, and v) rich stable combustion shown in Figure 2.9.



**Figure 2.9 Five different combustion states categorized based on normalized permutation entropy,  $H_{PE}$  and equivalence ratio,  $\phi$  [31].**

They were able to distinguish the 5 states in Figure 2.9 according to the normalized permutation entropy (PE), which was defined as the estimated degree of



randomness from the values of a time-series [32]. The main highlight of the work was regarding phase difference during unstable states, where they mentioned that a phase difference of less than  $60^\circ$  was observed when the flames were in an unstable state. It was further added that the lowest phase difference observed was at  $21^\circ$ , which caused the strongest thermoacoustic oscillation, categorized under the limit-cycle oscillation mode.

## 2.2 Types of Premixed Flame Instabilities

Williams outlined three distinct instabilities which may be responsible for a premixed flame instability (in the order of reducing size phenomena), which are body-force instabilities, hydrodynamic instabilities, and diffusive-thermal (thermodiffusive) instabilities [33], which causes the flame to propagate in a non-laminar manner. Each of the instability will be reviewed and their significance discussed with regards to the present work.

### 2.2.1 Body-force Instability

Placing a fluid of higher density at rest above a fluid of lower density at rest under the influence of gravity will result in a buoyantly unstable condition, better known as a body-force instability according to Taylor [22]. Gravity is technically a constant acceleration of  $9.80665 \text{ m/s}^2$  towards the earth [34], thus a perpendicular acceleration to the flame surface (which acts as the interface between the dense unburned gas and the less dense burned gas) will produce instabilities similar to a body-force instability described earlier.

Treating the flame as a discontinuity moving at a velocity of  $v_0$  (unburned gas/flame front) and  $v_b$  (burned gas/flame tail), under the influence of  $g$  (gravitational acceleration) [33], the characteristic transverse length and growth time of the body force instability can be estimated to be the order of:

$$\text{Characteristic transverse length} \propto \frac{v_0 v_b}{g} \quad (2.2)$$

$$\text{Growth time} \propto \frac{\sqrt{v_0 v_b}}{g} \quad (2.3)$$

The instability comes from the difference in the flame tail and flame front, the difference in propagation speed causes the flame to either shorten or elongate, thus producing a flame with varying length. Based on equation (2.3), the instability increases with a decrease in flame speed, making the growth time smaller, leading to a quicker development of the instability. This matter was discussed in detail by Williams[33], who concluded that a flame undergoing acceleration perpendicular to

its surface, in the direction of the flame propagation, will experience body-force instabilities, whereas a decelerating flame will be stabilized.

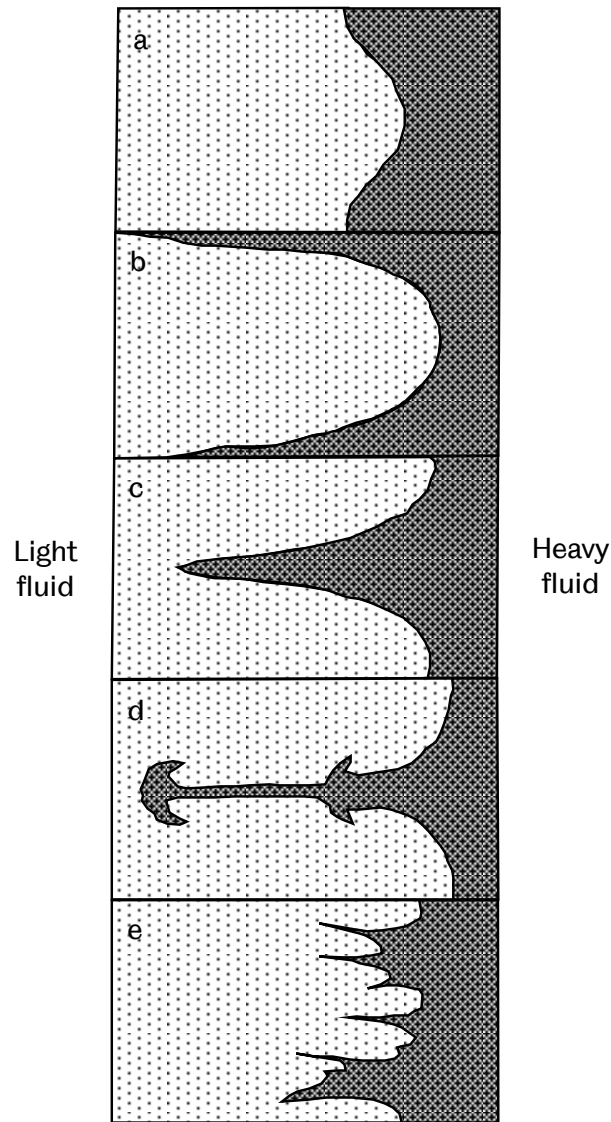
Two fluid instabilities which fall into the body-force category are the Rayleigh-Taylor (RT) instability and the Richtmyer-Meshkov (RM) instability, where the main mechanism producing these instabilities are the different acceleration induced by the same fluid force on regions with different density, which exists typically at the flame surface.

RT instability was theoretically analysed by Rayleigh [35] in 1882, only to be rediscovered by Taylor [22] in 1950, and experimentally validated by Lewis [36] in the same year. Lewis stated in his study that an unstable air-water interface under the constant acceleration of gravity consisted of three subsequent stages which were 1) exponential growth of instability, 2) transition phase of bubble formation and 3) an asymptotic stage of rising air columns. However, the instability was not observed if the lighter fluid is accelerated towards the heavier fluid.

Figure 2.10 shows an overview of characteristic flow patterns in the evolution of RT instabilities. In all patterns, the fluids were kinematically accelerated from the light fluid towards the heavy fluid. Figure 2.10(a) shows a sinusoidal surface modulation resulting from normal mode perturbations of a horizontal equilibrium surface based on theoretical calculations by Taylor [22], where the initially flat interface was accelerated from the left region towards the right, which produced the sinusoidal surface observed in Figure 2.10(a). The instability eventually grows to the shape in Figure 2.10(b), experimentally observed by Lewis [36] and Emmons et al. [37].

Baker et al. [38] performed numerical simulations on the effect of Atwood number on RT instability using the vortex method and concluded that the Atwood number calculated from the density interface plays a significant role in the formation of RT instability spikes. Formation of the spikes for density interface with Atwood number of 1 is shown in Figure 2.10(c), but for Atwood number less than 1, the spikes were followed with rolling of the spikes as shown in Figure 2.10(d). The rolling of the spikes were also theoretically observed by Gardner et al. [39] who described it as shedding of vortices at the tip of the spike.

On the other hand, RM instability was studied theoretically by Richtmyer [40] in 1960 and experimentally by Meshkov [41] in 1972. Richtmyer [40] considered the growth of the instabilities under an impulsive acceleration, which generally means the interface undergoes huge acceleration for a short period of time followed by a period of small/no acceleration beyond that, which was achievable by applying a pressure wave towards the fluid interface with different density.

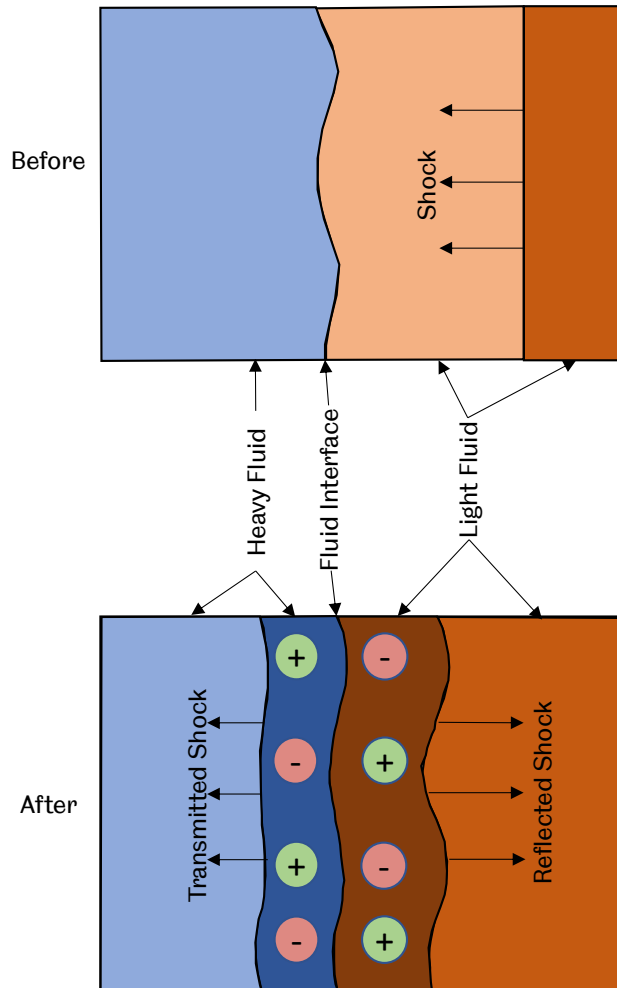


**Figure 2.10 Schematic flow patterns in the evolution of RT unstable two-dimensional flows. The light fluid penetrates the heavy fluid under acceleration directed towards the heavy fluid in all conditions where a) normal mode perturbation, b) free-surface bubble, c) falling spike in negligible density medium, d) falling spike in a medium with finite density, and e) advanced stage of intermixing. Reproduced from [42].**

In order for a pressure wave to be transmitted within the fluid, it needs to be a compressible fluid, leaving gas as the only option to study this type of instability. Meshkov [41] used different combinations of inert gasses such as carbon dioxide, freon, helium and air, separated by thin films, accelerated by a bursting diaphragm to create the shock wave. He concluded that the interface is unstable if impulsively accelerated from the lighter gas towards the heavier gas or vice versa.

Figure 2.11 shows the before and after schematics of a shock wave passing through a fluid interface reproduced from Richtmyer [40]. The difference between a shock

wave and a normal wave is that it propagates at supersonic speeds [43]. Before passing the fluid interface, the shock wave was assumed to be a plane, which produced two different corrugated shock, a transmitted shock, and a reflected shock. The corrugations in both resultant shocks played an important role in destabilizing the fluid interface.



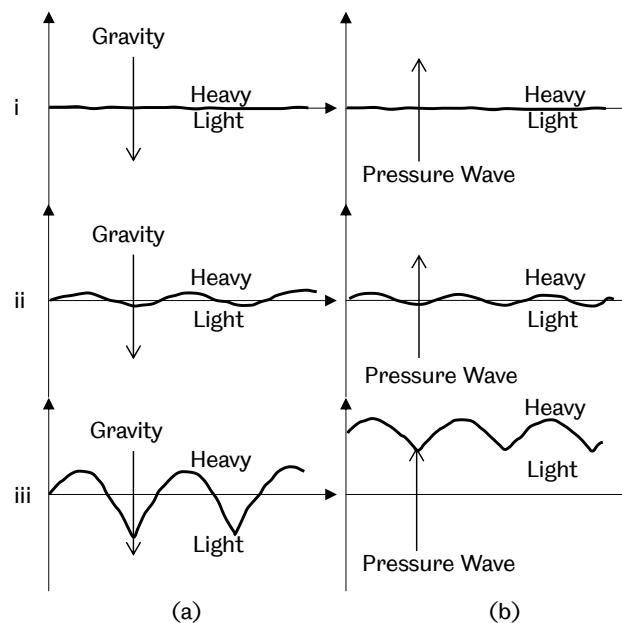
**Figure 2.11 Before and after schematics of a shock passing through a fluid interface, producing the Richtmyer-Meshkov instability. Initial shock was planar, while the transmitted and reflected shocks were corrugated. Reproduced from [40].**

Referring to Figure 2.11, the crest of the interface (where the heavy fluid protrudes into the light fluid) grows since the transmitted shock appeared less perturbed compared to the interface, producing a slight excess in pressure in the heavy fluid, whereas the reflected shock was more perturbed compared to the interface producing a slight pressure deficiency in the light fluid. This causes the original motion of the shock to be resisted, making the crest almost stationary. The opposite effect was produced at the trough of the interface, accelerating the troughs into the heavy fluid, following the original motion of the shock [40].

Both instabilities may appear similar to each other but according to Gardner et al. [44], the RT instability is usually associated with instabilities arising due to a constant acceleration, for example when honey is suspended above water under the constant acceleration of gravity, whereas the RM instability is associated with an acute gradient pressure (shock waves) at a shorter length scale (impulsive acceleration), thus generating instabilities at a larger scale compared to RT instability according to Cloutman [45].

To prevent confusion, it is worth noting that no shock waves were detected in the present work, but instead only normal pressure waves, leaving RT instability as the main body-force instability. The pressure waves may travel at the speed of sound, but they did not exceed the speed of sound (supersonic), which is required to form a shockwave needed for the formation of a RM instability.

Liu et al. [46] conducted a numerical study on pressure wave-flame front interaction to differentiate between a gravity driven RT instability with a pressure driven RT instability, shown in Figure 2.12. Both types were almost similar in nature, but the distinguishing difference they discovered was the growth rate of the magnitude of interface disturbance, which increases exponentially for the gravity driven case and sub-exponentially for the pressure driven one.



**Figure 2.12 Two types of Rayleigh-Taylor instability, a) gravity driven and b) pressure driven, divided into three stages, i) undisturbed interface, ii) disturbed interface, and iii) interface at time  $t$ . Reproduced from [46].**

Based on Figure 2.12, Liu et al. [46] made a thorough comparison between the gravity driven RT instability and the pressure driven RT instability. It was discovered that

acceleration from the burned gas towards the unburned gas causes the flame front disturbance to be unstable, while reversing this process would make the flame front disturbance stable for both cases. The difference was observed in the basic flow field, where the gravity driven interface was stationary since there was no basic flow velocity, while the pressure driven interface was accelerated by the pressure wave, which made the basic flow have a time dependent velocity.

In addition to the basic flow field difference, Liu et al. [46] also stated that both cases had different time of instability growth. For the gravity driven case, the instability growth started once gravity acts on the interface, while the pressure driven case started to grow after compressibility effects due to the pressure wave start to take place, producing differential accelerations in parts with different density.

The interface may look different based on Figure 2.12, but with time, both cases will develop similar looking spikes and bubbles. A different interaction was developed when flames were exposed to sinusoidal pressure disturbances. Sinusoidal pressure disturbance causes the flame front to oscillate, reducing the overall flame front turbulence level following an alternation between enhancement and suppression in the flame front disturbance, which was experimentally observed by Tsuruda et al. [47].

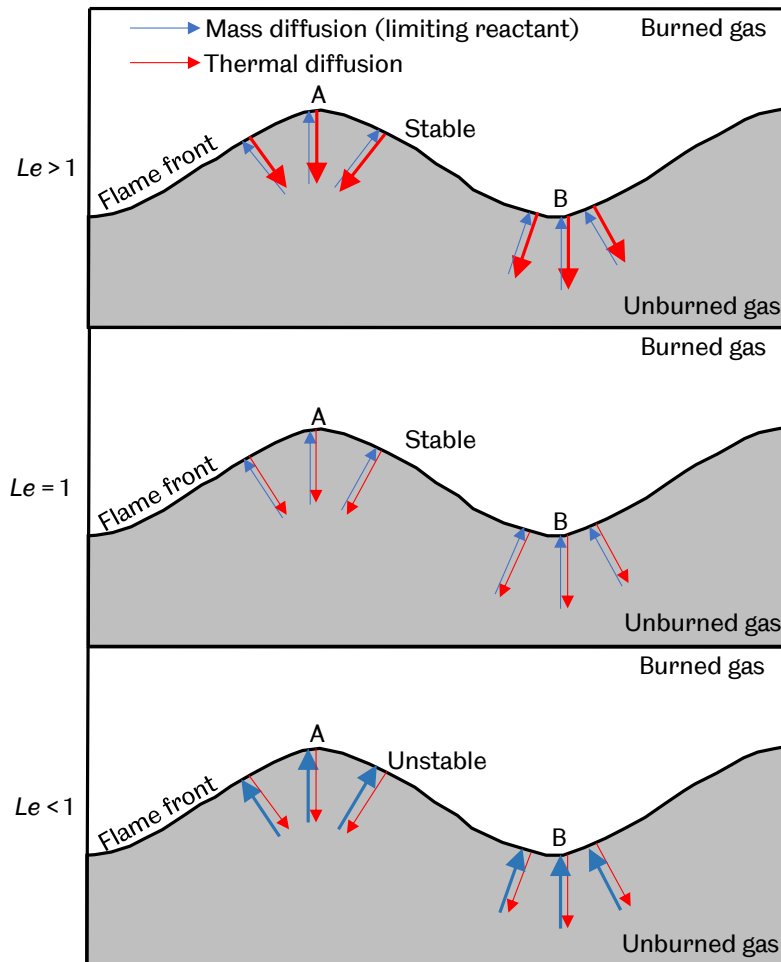
The relationship between the non-flame flow and the flame appears to be dependent on the flame shape. Ebierto [48] observed the reduction in flame size when flames were exposed to sinusoidal pressure, leading to a flat flame. The formation of a flat flame was accompanied by a steady growth of the sinusoidal pressure, which eventually led to a non-flame flow strong enough to form spikes of unburnt gas into the flame. Following the formation of unburnt gas spikes, the sinusoidal pressure disturbance was amplified to a significantly higher level.

### 2.2.2 Thermodiffusive Instability

The term thermodiffusive instability basically means instability from two competing processes which occurs at the perturbed preheat zone, thermal conduction and diffusion of the limiting component [49]. A few pioneering works regarding Lewis number were performed by Sivashinsky [50], Clavin [51] and Denet and Haldenwang [52], who attributed the formation of cellular cells to thermodiffusive instabilities. The Lewis number is used to define the ratio of thermal diffusivity ( $\alpha$ ) of the bulk mixture to the mass/molecular diffusivity ( $D$ ) of the deficient reactant [53], based on the equation:

$$Le = \frac{\alpha}{D} \quad (2.4)$$

Based on equation (2.4), it can be deduced that a  $Le = 1$  signifies an equidiffusive flame,  $Le > 1$  signifies a flame with a higher thermal diffusivity, and  $Le < 1$  signifies a flame with a higher mass diffusivity of the deficient reactant. Figure 2.13 shows the schematic diagram for all three conditions on a non-planar flame front, where A represents the concave part of the flame, and B represents the convex part of the flame.



**Figure 2.13 Schematic diagram of thermodiffusive instability for Lewis number more than 1, equal to 1 and less than 1. A and B represent the concave and convex surface of the flame respectively.**

For the  $Le > 1$  flame (thermal diffusion  $>$  mass diffusion), the thermal diffusion from the concave part of the flame (A) towards the unburnt gas is converged, increasing the temperature ahead of the concave part, thus increasing the flame speed. The opposite happens at the convex part of the flame (B), reducing the flame speed due to the diverging loss of heat from the flame surface. Combination of both processes causes the perturbation to be stabilized with time [54].

For the equidiffusive flame,  $Le = 1$  (thermal diffusion = mass diffusion), the thermal diffusion from the flame surface to the unburnt gas is compensated by the mass diffusion of deficient reactant, resulting in a constant flame temperature, leaving the perturbations unchanged [54]. It is worth noting that the diffusion of the deficient reactant towards the flame surface increases the flame temperature because the diffusion brings the flame closer to the stoichiometric equivalence ratio, which has an effectively higher adiabatic flame temperature. In the case of a rich (lean) flame, the deficient reactant would be the oxygen (fuel), and in the event of an increased rate of mass diffusion, both situations would lead to an increase in the flame temperature and speed.

Finally, for the  $Le < 1$  flame (thermal diffusion < mass diffusion), the increase in mass diffusion of the deficient reactant towards the flame surface causes the convex part of the flame (B) to increase in temperature, technically increasing the speed. The increase in speed causes the convex part to penetrate further into the unburnt gas, destabilizing the flame surface. Clarke [54] claimed that the process will continue until the flame becomes cellular, adding that the transition to cellular flames would be faster compared to a hydrodynamically unstable flame.

Lewis number calculations for the mixtures used in the present work was not done due to the difficulty in calculating the Lewis number of binary fuel mixtures. Clarke [54] did a systematic study on Lewis number of different hydrocarbons, using different Lewis number calculations, which included methane. Based on his findings, the Lewis number calculated based on the deficient species for pure methane ranged between 0.87 – 0.95 for equivalence ratios between 0.6 – 1.4, tabulated in Table 2.1.

**Table 2.1 Lewis number of pure methane flames [54].**

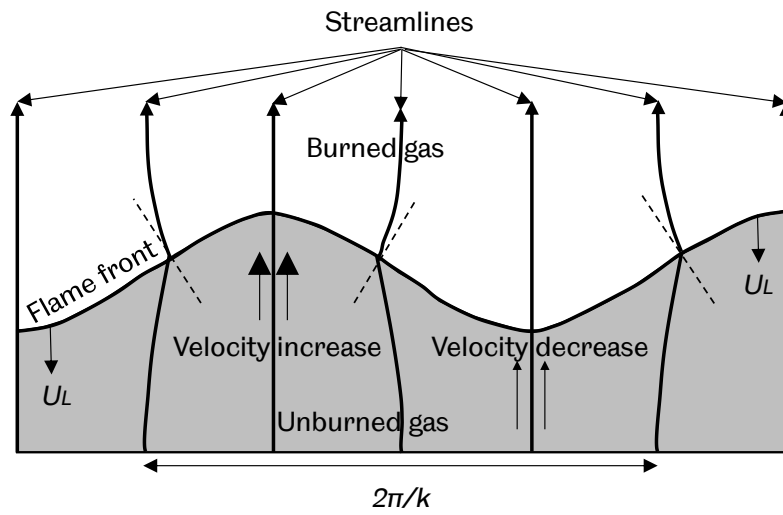
<b>Equivalence Ratio, <math>\phi</math></b>	0.6	0.7	0.8	0.9	1.0	1.1	1.2	1.3	1.4
<b>Lewis number, <math>Le</math></b>	0.95	0.94	0.93	0.92	0.91	0.87	0.87	0.87	0.88

Jackson et al. [55] did an extensive study on the impact of hydrogen addition on lean premixed methane towards high strained flows. Effective Lewis numbers were calculated for their fuel mixtures, and it was discovered that the Lewis number of hydrogen enriched methane mixtures were lower compared to pure methane mixtures, technically reducing flame sensitivity to strain rates. However, the mixing method utilized in the study was different from the method used in the present work, which will be discussed later in detail.



### 2.2.3 Hydrodynamic Instability

In 1938, Darrieus presented that the gas expansion due to the release of heat from a wrinkled premixed flame, travelling at a constant normal speed,  $U_L$ , will redirect the streamlines towards the normal of the wrinkled flame [56]. The streamlines here are defined as the path a particle would follow during the combustion process. The deviation of the streamlines as shown in Figure 2.14, are responsible for an increase in the wrinkling of the flame, where the converged parts of the flame will be accelerated, whereas the diverged parts will be decelerated.



**Figure 2.14 Development of a hydrodynamic instability. Reproduced from [56].**

Landau predicted this instability independently in 1944, stating that the instability growth rate varies with the wave number of the perturbation,  $k$ , the laminar burning velocity,  $U_L$ , and finally a positive function of order unity which disappears as the expansion ratio,  $\left(\frac{\rho_b}{\rho_u}\right)$  approaches 1,  $f\left(\frac{\rho_b}{\rho_u}\right)$ . The growth rate can be defined as [56]:

$$\sigma = k \cdot U_L \cdot f\left(\frac{\rho_b}{\rho_u}\right) \quad (2.5)$$

Hydrodynamic instabilities were since then known as Darrieus-Landau (DL) instability, which are inherent to any flame in a combustible gaseous mixture. If no perturbations exist at the flame surface, an initially planar flame would then be curved spontaneously towards the unburned gas, increasing the flame surface area, thus the flame speed. The velocity difference described in Figure 2.14 only exists in wrinkled flames.

## 2.3 Effect of Tube Configuration on Instabilities

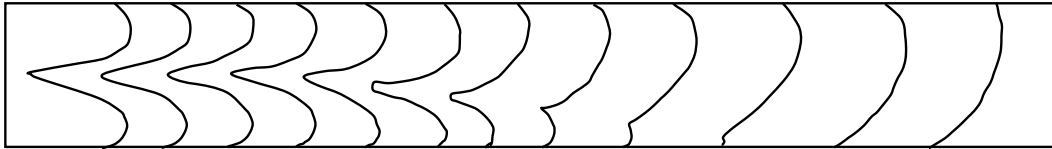
Premixed flames propagating in tubes have been studied for a significantly long time, where Mallard and Le Chatelier [1] were among the first ones dated back in 1883, motivated by the problems of exploding coal mines during that era. They discovered that a flame propagating in a tube from an open end towards a closed end started to oscillate. This discovery initiated many other researches regarding flame propagation instability in tubes, which were mostly reviewed and compiled by Markstein [5] and Guenoche [4] in 1964. Subsequently, Clavin [57] also reviewed and compiled the progress made on the theory of unsteady combustion waves propagating in premixed gases, which partly covered flame propagation instabilities in tubes. It was proposed by Guenoche [4] that there were 4 possible configurations for investigating flame propagation instabilities in tubes which were tubes closed at both ends, tubes open at the ignition end, tubes open at non-ignition end, and finally tubes open at both ends. These configurations were studied either horizontally or vertically, but recent researches were done more on flames propagating vertically downwards i.e. Searby [8] and Higuera [58], favoured due to the fact that downwards flame propagation stabilizes the flame from a body force instability point of view [33].

### 2.3.1 Flame in Tubes Closed at Both Ends

When a mixture of flammable gas is ignited inside a tube closed at both ends, both the exhaust and the fresh gas ahead of the flame are impeded. Guenoche [4] mentioned that propagation in a tube closed at both ends consisted of 2 stages, starting with the expansion of the flame, before it reaches the walls of the tube, followed by the flame reaching the walls of the tube. During the first phase, it was observed that longer tubes resulted in longer flames, thus a larger flame surface area. The increase in surface area directly affects the flame speed, which also increases, but eventually reaches a plateau speed after a certain length according to Popov [59].

In the second phase of propagation, indicated by the flame reaching the sidewalls, the cylindrical shape of the flame vanishes, thus a reduction in flame area was observed. The rapid decrease in flame surface area led to a reduction in flame speed. However, in short tubes, this reduction may not be observed, since the flame does not have enough time to elongate, thus appear as if it is propagating with an almost constant speed [4]. If the tube was longer, the flame would be longer, and a more abrupt change in speed will be observed, resulting in an inversion of the flame front, known as tulip flames by other researchers [24-26], [57].

In long tubes, the inverted centre of the flame will accelerate, as shown in Figure 2.15, making the flame normalize (convex towards fresh gas), and become inverted in the centre again, producing oscillations of a variable frequency. Guenoche [4] further added that the amplitude of flame oscillation decreases as it approaches the tube end, and the frequency could not be associated with the gas column acoustic vibration.



**Figure 2.15 Example of a flame distortion cycle in a closed tube propagation.**

Reproduced from [4].

### **2.3.2 Flame in Tubes Open at Ignition End**

Flames propagating in tubes open at the ignition end propagates with a uniform movement for the longest period of time compared to other configurations according to Mallard and Le Chatelier [1]. This gives an advantage since the burning velocity can be calculated during the uniform movement period.

Guenoche [4] stated that the initial phase was similar to that of a tube closed at both ends, but over a shorter distance due to the expansion of burnt gas towards the ignition end. It was further added that an auxiliary flame would ignite the whole cross section, minimizing the initial perturbation compared to a point ignition source. Once the flame reaches the tube wall, the second phase of propagation starts.

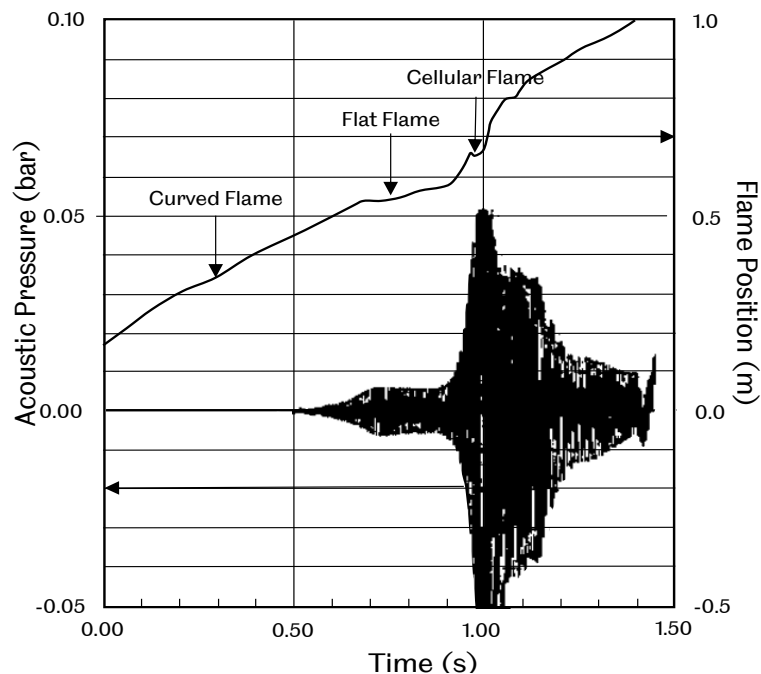
The flame propagates steadily at a constant velocity before the flame surface starts to vibrate around a mean position due to the vibration of the gas column. The vibratory transverse movement of the gas column led to a decrease in the flame surface area, which slows down the flame. The continuous vibration of the gas column accompanied by the reduction in flame speed led to the formation of cellular flame structures, which increases the flame surface area and flame speed. Amplitude of vibration increases which causes the frequency of vibration to be irregular. The amplitude of vibration continues to drive the flame with a mean propagating velocity which then decays rapidly to a uniform value.

For cases utilizing narrow tubes, most rich hydrocarbon mixtures tend to vibrate, except for methane, hydrogen and acetylene, which vibrates even at lean equivalence ratios [61]. If the same mixture was used while the diameter was decreased, the chances of a vibratory propagation to occur increases slightly [4]. The

absence of vibrations tends to produce steady propagating flames with minimal velocity fluctuations.

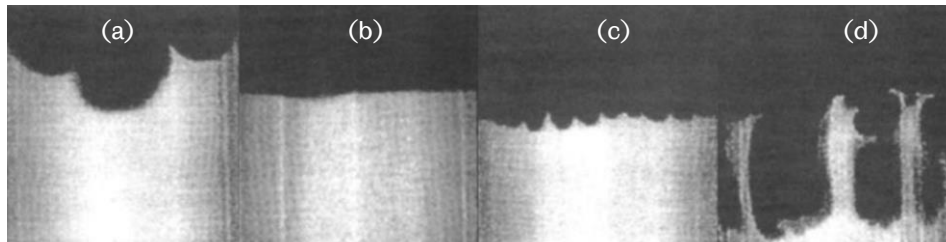
Coward et al. [3] stated that a flame propagating in a circular tube pulsates easier compared to a square tube, where the latter produced a slow humming sound which was not strong enough to change the speed or shape of the propagating flame. They further added that the material of the flame tube plays a role in damping the vibration induced instability where they replaced the glass tube with a rubber tube and heard minimal sound emitted from the tube, indicating a low amplitude instability.

In a study conducted by Searby [8], he classified the different propagation of flames in tube open at the ignition end towards a closed end into four types, which were roughly based on their laminar flame speeds, i) below 0.16 m/s, silent steady flame, ii) between 0.16-0.25 m/s, flame with primary acoustic instability in the lower half of the tube, iii) above 0.25 m/s, flame with secondary acoustic instability of higher amplitude following the primary acoustic instability, and finally iv) higher speed flames beyond 0.25 m/s, flame will undergo a secondary instability which reaches high acoustic level, which decays into turbulent motion, resulting in a drop in sound level. Figure 2.16 shows the propagation pressure and flame position of a type (iii) flame, and three different flame structures were observed, a curved flame, flat flame, and finally a cellular flame.



**Figure 2.16 Propagation pressure and flame position of a  $\phi = 0.77$  propane mixture, with a laminar flame speed,  $U_L = 0.27$  m/s. Propagation fell under type (iii), acoustic frequency was 122 Hz. Reproduced from [8]**

Based on Figure 2.16, it was observed that the curved flame corresponds to a very low level of acoustic pressure. Once the pressure starts to build up at  $\sim 0.6$  seconds, the curved flame becomes slightly distorted as seen in Figure 2.17(a). The saturation of the primary instability to  $\sim \pm 0.007$  bar at  $\sim 0.7$  seconds led to a flat flame shape shown in Figure 2.17(b). At the beginning of the onset of the secondary instability at  $\sim 0.9$  seconds, cellular structures in Figure 2.17(c) start to appear on the flat flame surface, which eventually start oscillating into a high amplitude cellular flame shown in Figure 2.17(d), which started decaying after reaching a maximum acoustic pressure of  $\sim \pm 0.05$  bar at  $\sim 1.00$  seconds.



**Figure 2.17 High speed tomographic cuts of premixed flames in open ended ignition tubes at different stages, a) curved flame during onset of primary instability, b) flat flame during saturation of primary instability, c) cellular structures during onset of secondary instability, and d) high amplitude cells during secondary instability.**

Reproduced from [62] based on [8].

### 2.3.3 Flame in Tubes Open at Non-Ignition End

According to Guenoche [4], the first phase of flame propagation in tubes open at the non-ignition end is similar to a long closed tube at both ends, since the open end allows expansion of fresh gas. However, the expansion of fresh gas resulted in a faster flame in the second phase of propagation, allowing the flame to turn unstable easier, making most of the flames burnt in this condition oscillatory. The oscillation of the flame was of similar nature to the one described in Figure 2.15.

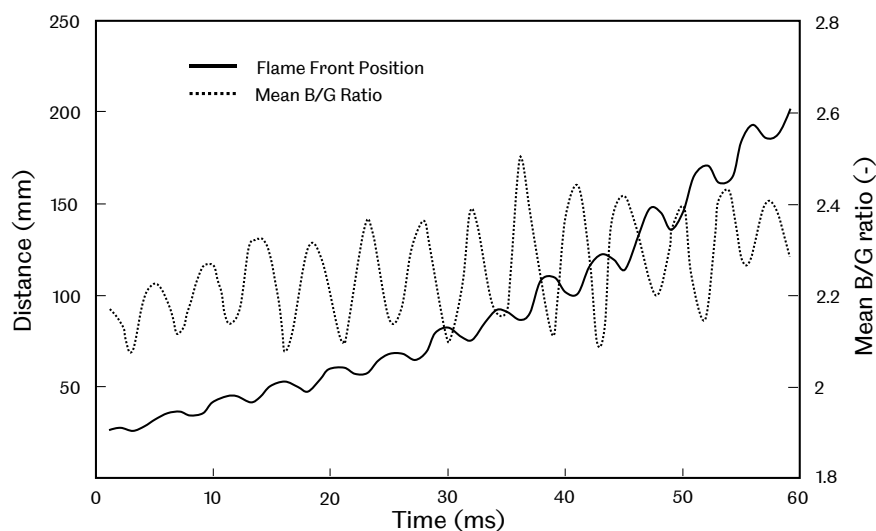
Following the first phase, Schmidt et al. [14] stated that the flame becomes indented in the centre with reducing velocity. This was followed by the indented centre taking over the edges, similar to the closed tube case, but over a longer distance due to unrestricted fresh gas. The flame eventually turns convex towards the fresh gas after the indented centre overtook the edges, simultaneously reducing the flame area and the thrust from exhaust gasses, accompanied by the cooling of hot gasses, the flame decelerates and becomes indented again. The process repeats until it reaches the end, where a steady increase in the mean propagation velocity was observed.

Schmidt et al. [14] further added that the increased velocity was not only from the open end, but also from the turbulence caused by the expansion of fresh gas, creating a flame oscillation with several instances of flame motion reversal. In one of their experiments, a stoichiometric propane-air mixture was burned, and turned turbulent, reaching a speed of 50 m/s, which they claimed to be 90% contributed by the motion of the moving column.

### 2.3.4 Flame in Tubes Open at Both Ends

It was stated by Guenoche [4] that the first phase of an open ended tube flame propagation is similar to that observed in a tube open at the ignition end. The expansion of fresh gas and exhaust gas sets the fresh gas into motion, slightly accelerating the flame, leading to a higher flame propagation velocity compared to other configurations. He further added that between 1/3 and 1/2 length of the tube, flame vibration starts, causing the initially curved flame to flatten, reducing the mean flame velocity, followed by an increasing amplitude in the gas mass, ultimately leading to a smooth acceleration or an oscillating flame, as observed by Mason and Wheeler [2].

Yang et al. [63] conducted an experimental study on rich propane-air mixtures propagation in open ended tubes. They observed that the self-induced fluctuations in pressure led to flame oscillations with a maximum amplitude of  $\pm 10$  mm at a recorded frequency of 220 Hz, which decayed as it progresses towards the end of the tube. Relating their findings with chemiluminescence, Yang et al. [63] described the fluctuation of the flame chemistry to be consistent with the flame oscillation as shown in Figure 2.18.



**Figure 2.18 Fluctuation of the mean B/G ratio and the flame front position, reproduced from [63].**

The flame propagation was observed to be similar to a flame propagating in a tube open at the ignition end, but without the presence of the flat flame. At low amplitude oscillations, instead of the flat flame, the flame was observed to propagate with a caterpillar-like movement, alternating between a stationary flame tail and advancing front, with a stationary front and advancing tail. The pressure eventually builds up and the flame centre was inverted, which they described as tongues of unburned reactant, pushed into the hot combustion products, leading to rapid acceleration into the fresh gas [63]. The inverted centre was found to be similar with the one described by Guenoche [4] in Figure 2.15.

## **2.4 Fuel Composition**

### **2.4.1 Fuel Composition Effect on Flame Instabilities**

Fuel composition is an important parameter of combustion research in order to understand the effects may inflict on any combustion system. Changing the composition of an air-fuel mixture changes the way it behaves during propagation which includes flame propagation speed and instabilities that may develop.

Varying the fuel composition had been performed by many researchers for decades to study instabilities in combustion rigs. Kerampran et al. [64] conducted a study on the instability induced acceleration inside a horizontal flame tube with varying length, using propane, ethylene and acetylene as their base fuel. The equivalence ratio was varied for each reactive mixture to obtain a group of mixture with a good amount of luminosity and increasing laminar burning velocity, ranging between 0.24 – 1.38 m/s, tabulated in Table 2.2, along with the laminar spatial velocity, the product of multiplication between the laminar burning velocity and the expansion ratio.

Kerampran et al. [64] concluded that the observed oscillating propagation were very dependent on two parameters, the gaseous composition and the tube length. If the laminar spatial velocity is low, the flame was found to be sensitive towards acoustic perturbations, making them prone to oscillations during propagation. It was also discovered that the average flame velocity did not increase with increasing tube length. On the other hand, flames with high laminar spatial velocity appears to be more resistant towards acoustic perturbations, indicated by a non-oscillating propagation with a slight reduction in speed. The average flame velocity increased with an increase in the tube length. They concluded that the flame behaviour was a product of the competition between the propagating flame and the oscillating column of gas within the tube.

**Table 2.2 Reactive mixtures laminar flame velocity, expansion ratio, and laminar spatial velocity, reproduced from [64].**

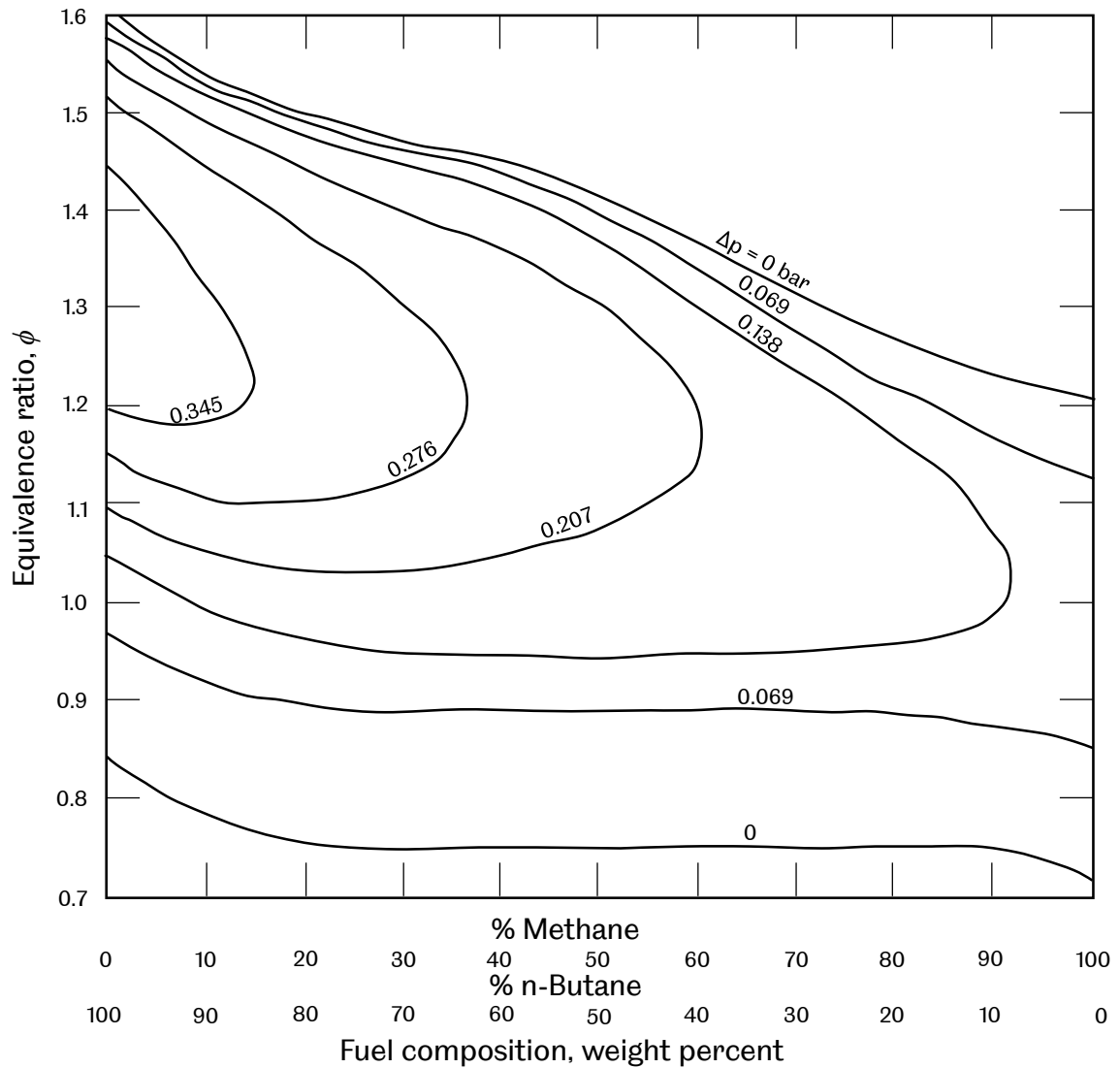
<b>Reactive Mixture</b>	<b>Equivalence ratio, <math>\phi</math></b>	<b>Laminar burning velocity, <math>S_u</math> (m/s)</b>	<b>Expansion ratio, <math>\alpha</math></b>	<b>Laminar spatial velocity, <math>V</math> (m/s)</b>
<b>Propane-air</b>	1.0	0.38	8.0	3.0
	1.2	0.39	8.0	3.1
	1.4	0.24	7.8	1.9
<b>Ethylene-air</b>	1.0	0.64	8.2	5.3
<b>Acetylene-air</b>	0.6	0.65	6.6	4.3
	0.8	1.08	7.9	8.5
	1.0	1.38	8.5	11.7

Markstein and Somers [28] conducted a study with binary fuel mixtures consisting of methane and n-butane, focussed more on the vibratory propagation in a vertical flame tube of 0.6 m and 1.2 m length, with inner diameter of 0.0915 m, propagating downwards to a closed end, where methane was added in 15% by weight increment to n-butane. In order to obtain steady propagation at the beginning of the tube, nitrogen was added to the mixture, making it possible to record the transition to vibratory propagation. However, this was only limited to rich fuels as they had a difficult time in stabilizing lean fuel mixtures. It was discovered that cellular structures disappeared when the fuel mixture exceeds 50% methane.

Following the formation of the cellular structures, the flame proceeds to a complicated vibratory propagation, which they stated to be out of the scope of the paper. They proceeded to only analyse the maximum pressure peak-to-peak amplitudes and the flame speed during uniform movement. The flame speed variation of methane with equivalence ratio was found to be displaced towards the lean side compared to its laminar burning velocity, while n-butane flame speed was displaced towards the rich side.

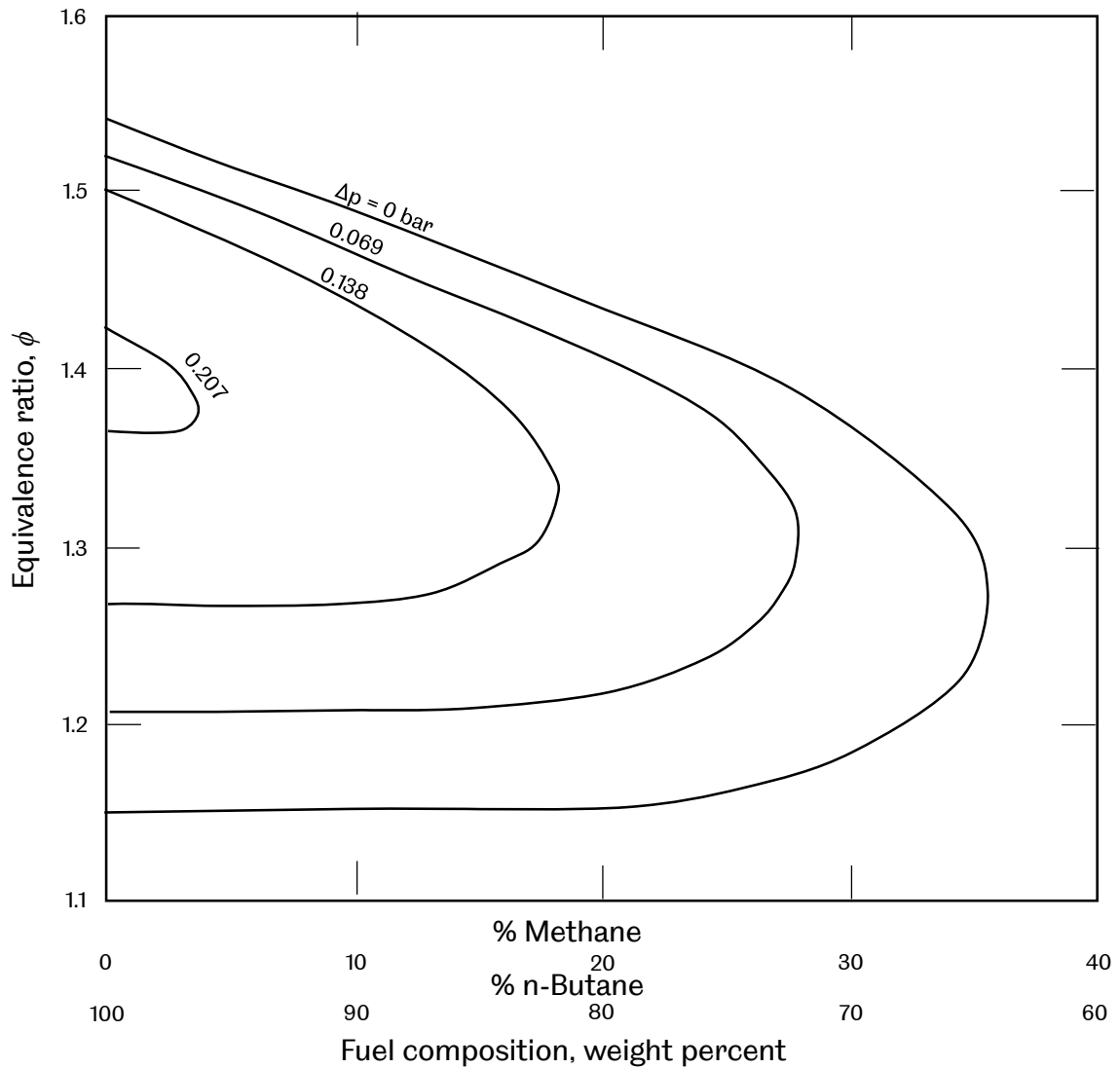
The maximum peak-to-peak amplitudes of pressure, which was found to be oscillating at the fundamental frequency (~270 Hz) for most of the mixtures in the 0.6 m tube was shown in Figure 2.19. Based on the contours, pure rich n-butane ( $\phi = 1.2 - 1.4$ ) created the highest peak pressure amplitudes (0.345 bar), which decreased steadily to 0.069 bar as methane concentration was increased towards lean pure methane ( $\phi = 0.9 - 1.1$ ).





**Figure 2.19 Maximum peak-to-peak pressure amplitudes for n-butane-methane-air mixtures, oscillating at the fundamental mode (~260 Hz) in a 0.6 m tube, reproduced from [28].**

The study was continued by increasing the tube length to 1.2 m, where they discovered that the fundamental mode in the 1.2 m tube was high but erratic, making it difficult to correlate with the equivalence ratio of the mixtures, unlike the first harmonic. The first harmonic of the tube was excited systematically with the equivalence ratio when the tube length was increased to 1.2 m, but only in mixtures ranging between  $\phi = 1.2 - 1.5$  and n-butane weight percentage between  $\sim 70 - 100\%$ , as shown in Figure 2.20. Despite the difference in length, both the 0.6 m and 1.2 m tube were excited systematically with the equivalence ratio at a frequency of  $\sim 260$  Hz.



**Figure 2.20 Maximum peak-to-peak pressure amplitudes for n-butane-methane-air mixtures, oscillating at the first harmonic (~260 Hz) in a 1.2 m tube, reproduced from [28]**

The excitation of the 1.2 m tube first harmonic was attributed to the cellular structures observed by Markstein and Somers [28]. This was found to be in agreement with the discovery made by Behrens [61], who correlated the excitation of vibration with flame structures, but the frequency of excitation was not stated. They concluded that the longer the flame stays within the oscillating gas region (slower flames) the pressure amplitudes may build up to a larger value compared to faster flames [28].

Mandilas et al. [65] conducted a study regarding the effect of hydrogen addition to methane and iso-octanes using spherical bombs in both laminar and turbulent conditions. Under laminar conditions, methane and iso-octane mixtures increased

in laminar burning velocity, except for rich methane mixtures beyond 1.2 equivalence ratio. They also discovered that hydrogen addition led to an earlier onset of laminar flame instabilities. Under turbulent conditions, the turbulent burning velocity was roughly twice at the lean limit, but the increase in velocity was reduced slowly until it reaches the rich ignition limit for methane, and buoyant limit for iso-octane.

In order for the present work to systematically study the effect of hydrogen addition, the equivalence ratio and hydrogen addition must be varied systematically in order to gain a useful insight of the effects that are taking place. The following sections cover both the effects of equivalence ratio and hydrogen addition.

#### 2.4.2 Equivalence Ratio

Equivalence ratio can be described as the fuel concentration of a premixed fuel-air mixture. This is an important parameter which determines the speed and the emission of a flame. Scientifically, equivalence ratio is the ratio of fuel to oxidizer present in the mixture over the quantity of fuel to oxidizer in a stoichiometric condition. The equation below describes the mathematical formula of equivalence ratio, where  $C_F$  represents mole concentration of fuel,  $C_A$  represents mole concentration of air, while the subscript  $st$  denotes the mole concentration at a stoichiometric condition:

$$\phi = \frac{C_F/C_A}{(C_F/C_A)_{st}} \quad (2.6)$$

Multiple researches have been done to study the relationship between the laminar burning velocity and equivalence ratio of a fuel mixture. These studies conducted obtained varying values of laminar burning velocity with varying experimental method. These experiments however depict a certain trend which can be described as a bell-shaped curve, with the maximum velocity being around an equivalence ratio of 1.0-1.1 and starts to go lower as the mixture gets leaner or richer.

Figure 2.21 shows a compiled set of laminar burning velocity from different papers. The different methods led to different values of laminar burning velocities, Gu [66], Edmonson [67] and C.K Law [68] adapted the constant volume spherical vessel method, Bunsen burner method, and the counter-flow method respectively. These values are useful for comparison with the speed contour plot later on to ensure that the corresponding values of equivalence ratio has a similar trend to the plot in Figure 2.21.

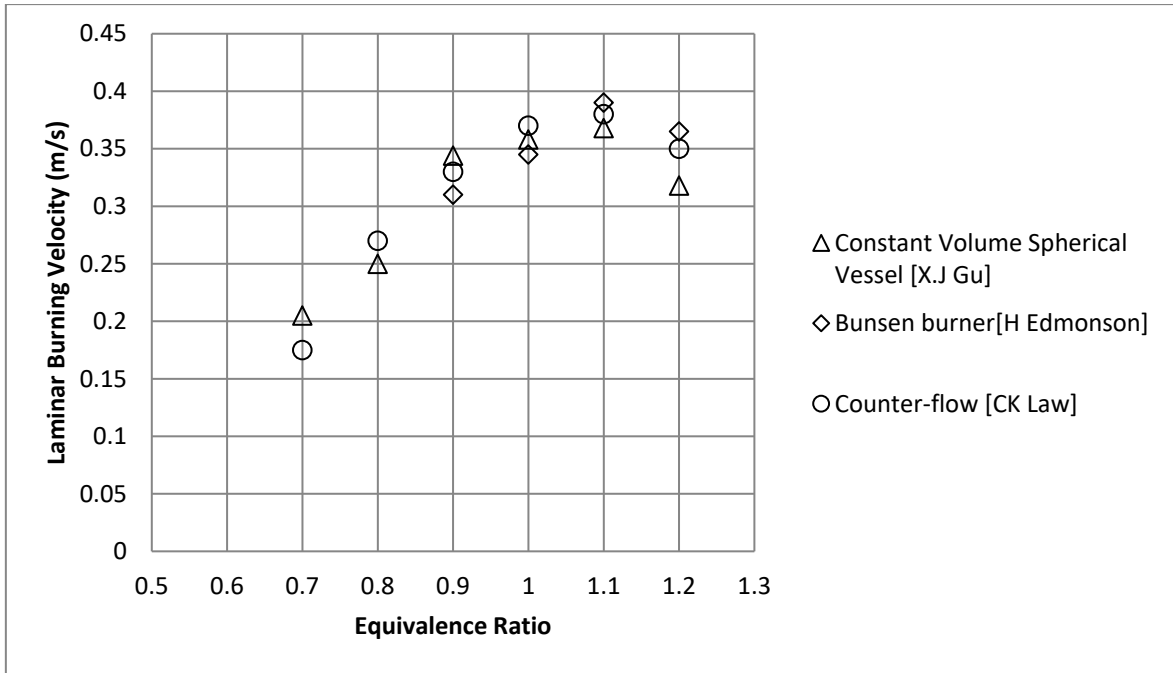


Figure 2.21 Laminar burning velocity of methane.

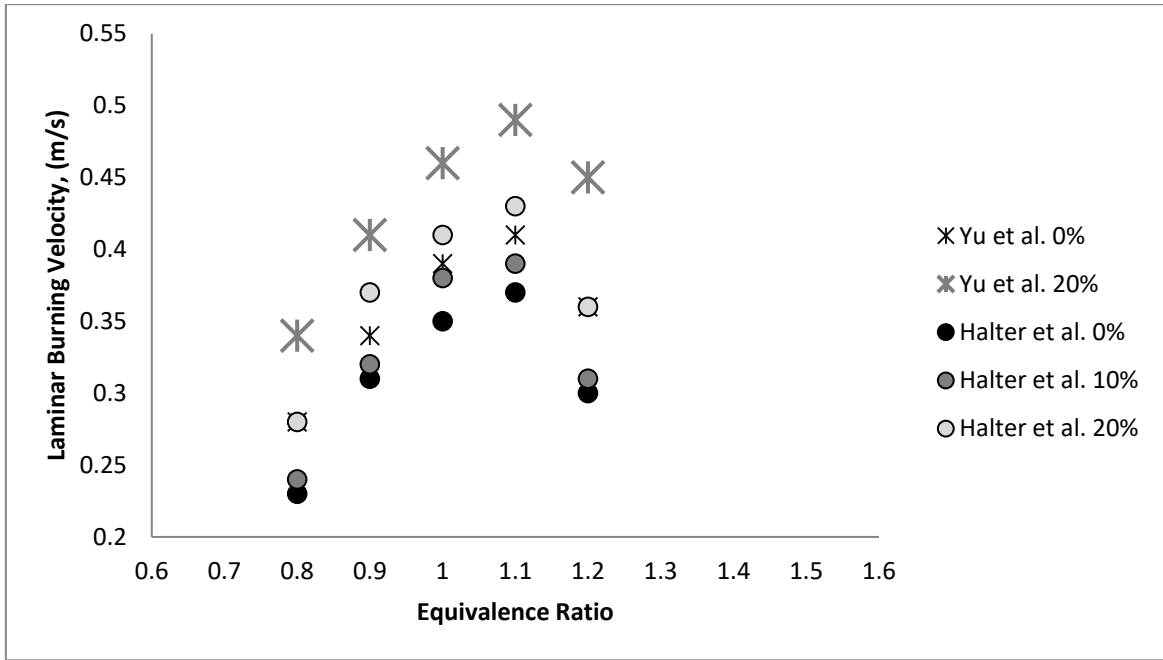
### 2.4.3 Hydrogen Addition

Hydrogen addition to a fuel mixture requires some additional calculations to incorporate both fuel into the equivalence ratio equation, since both the fuel and hydrogen are combustible. Yu et al. [10] proposed the following equation for hydrogen addition to a fuel mixture, where  $C_F$  represents mole concentration of fuel,  $C_A$  represents mole concentration of air, and  $C_H$  represents the mole concentration of hydrogen, and the subscript  $st$  denotes the mole concentration at stoichiometric conditions:

$$\phi_F = \frac{C_F / [C_A - C_H / (C_H / C_A)_{st}]}{(C_F / C_A)_{st}} \quad (2.7)$$

$$R_H = \frac{C_H + [C_H / (C_H / C_A)_{st}]}{C_F + (C_A - C_H / (C_H / C_A)_{st})} \quad (2.8)$$

Yu concluded that hydrogen addition increases the laminar burning velocity of pure methane by using the counter flow method. A similar research was done by Halter [69] using the constant volume spherical bomb method and a similar trend was observed in the laminar burning velocity of methane, but lower compared to Yu's findings. Figure 2.22 shows the speed comparison from both papers.



**Figure 2.22 Effect of hydrogen addition on laminar burning velocity of methane.**

Another method proposed by Bradley et al. [70] utilized the mole fraction mixing method by using a predetermined equivalence ratio and mole fractions of the combined fuels. Two fuels  $i$  and  $j$ , will have their mole fraction calculated based on the total fuel, obtaining  $\bar{x}_{Fi}$  and  $\bar{x}_{Fj}$ , i.e, for a 10% fuel  $j$  mixture,  $\bar{x}_{Fi} = 0.9$  and  $\bar{x}_{Fj} = 0.1$ . The stoichiometric air-fuel ratio for fuel  $i$  and  $j$ ,  $a_{si}$  and  $a_{sj}$  ( $a_{sm} = 9.547$  for methane and  $a_{sh} = 2.387$  for hydrogen), will also be used to calculate the mole fraction mole fraction for the air-fuel mixture,  $\bar{x}_i$  and  $\bar{x}_j$ , based on the equation:

$$\bar{x}_{Fi} = \frac{\left(\frac{\phi}{\phi + a_{si}}\right) \bar{x}_i}{\left[\left(\frac{\phi}{\phi + a_{si}}\right) \bar{x}_i + \left(\frac{\phi}{\phi + a_{sj}}\right) \bar{x}_j\right]} \quad (2.9)$$

Comparing the two method, the  $R_H$  method was chosen to be used in the present study to systematically add hydrogen across all equivalence ratios. Another advantage of this method is for making comparison with other fuels which may be tested in the future, since the  $R_H$  method basically calculates the hydrogen addition based on the total volume of the rig, making a side-by-side comparison between two hydrogen enriched fuels to be sensible. A comparison between the two methods was made for methane-hydrogen fuel mixture ranging between equivalence ratio 0.8-1.5, and the resulting hydrogen mole fraction was tabulated in Table 2.3. It was observed that despite the change in equivalence ratio, the hydrogen mole fraction was constant using the  $R_H$  method compared to the volumetric method.

**Table 2.3 Hydrogen mole fraction range for  $R_H$  method and mole fraction mixing method.**

Hydrogen Addition	Hydrogen Mole Fraction Range	
	$R_H$ Method	Mole Fraction Mixing Method
0	0	0
0.1	0.027	0.005-0.015
0.2	0.049	0.012-0.031
0.3	0.068	0.019-0.051
0.4	0.085	0.028-0.073
0.5	0.099	0.039-0.100
0.6	0.111	0.052-0.133
0.7	0.122	0.070-0.174
0.8	0.132	0.093-0.226

## 2.5 Spectral Analysis

Spectral analysis is an important part in signal processing to extract useful information from raw time domain signals. One of the widely used spectral analysis technique is the Fast Fourier transform (FFT), used to visualize the signal in the frequency domain and allowing the user to see the dominant frequency within the signal. Inversing the FFT product would reconstruct the frequency domain signal back to a time domain signal. The reconstruction howe

Another useful tool that recently gained interest of researchers is the Synchrosqueezed wavelet transform (SST). Unlike FFT, SST provides the user with information that is usually hidden in the Fourier spectrum [71]. The main advantage SST provides over FFT is the ability to reassign the time domain signal into a time-frequency domain, allowing the user to identify the instantaneous dominant frequency of the signal at any point of time.

The third spectral analysis technique is the Hilbert transform. It is commonly used in signal processing to extract complex signal from a signal that contains only a real part [72], for example a time domain pressure signal. Hilbert transform in the present work was used to extract the phase of time domain signals to perform a phase study. This phase study was required in order to understand the interaction between different raw data signals. All three techniques will be discussed in detail in the following section.

Three waves will be used to demonstrate the ability of each technique in analysing the waves. The waves were governed by the following equation:

$$y(t) = A \cos(\omega t + \phi) \quad (2.10)$$

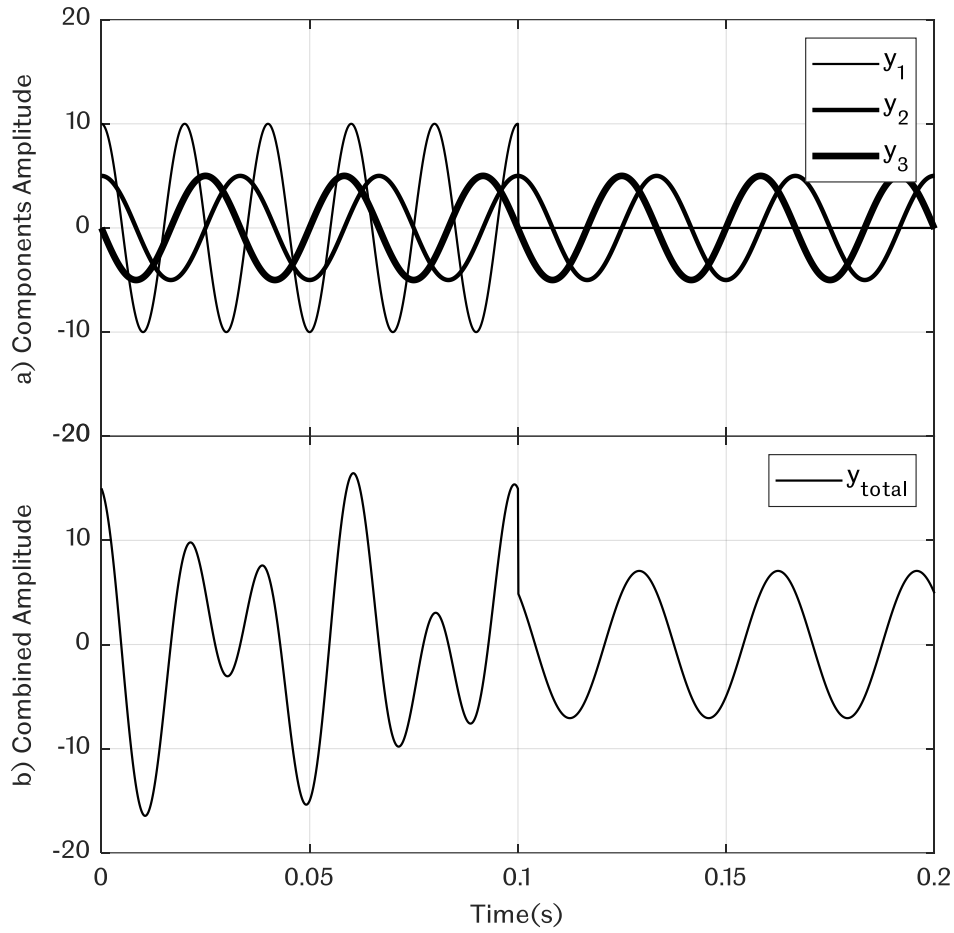
$$\omega = 2\pi f \quad (2.11)$$

In equation (2.10),  $y(t)$  represents the wave function with respect to time,  $A$  represents the amplitude, the angular frequency represented by  $\omega$ , and finally  $\phi$  represents the phase of the wave. The angular frequency,  $\omega$  is directly proportional to the frequency of the wave,  $f$ , defined by equation (2.11). The parameters of the three waves were tabulated in Table 2.4.

**Table 2.4 Parameters for three different waves.**

Wave	Amplitude, $A$	Frequency, $f$ (Hz)	Angular frequency, $\omega$ (rad/s)	Phase, $\phi$ (radians)	Duration, (seconds)
$y_1$	10	50	314.2	0	0.1
$y_2$	5	30	188.5	0	0.2
$y_3$	5	30	188.5	$\pi/2$	0.2

The waves will be combined to produce wave  $y_{total}$ , which will be used to test the effectiveness of the Fast Fourier Transform in detecting the dominant frequencies. Wave  $y_1$  has a duration of 0.1 seconds less compared to the other waves to test the capability of the Synchrosqueezed Transform in detecting the different frequencies in  $y_{total}$ . Waves  $y_2$  and  $y_3$  are identical in all parameters except for their phase, where  $y_3$  leads by  $\pi/2$  radians, equivalent to  $90^\circ$ . These two waves will be used to test the effectiveness of the Hilbert Transform in determining the phase difference between identical waves of different phase. The individual waves were plotted in Figure 2.23(a) and the combined wave,  $y_{total}$  in Figure 2.23(b).



**Figure 2.23** Three waves,  $y_1$ ,  $y_2$  and  $y_3$  plotted in (a) and the combined wave,  $y_{total}$  in (b).

### 2.5.1 Fast Fourier Transform

Fourier transform is obtained by calculating the dot product between a time signal and sine waves of different frequencies [72]. Sine waves have three characteristics that distinguish them from each other which are the frequency (the number of cycles completed per second), power or amplitude (power is obtained from squaring the amplitude), and finally the phase (the timing of the sine wave, measured in degrees or radians). The main function of a Fourier transform is to convert a time series signal into a three-dimensional representation which consists of the frequency, power, and phase.

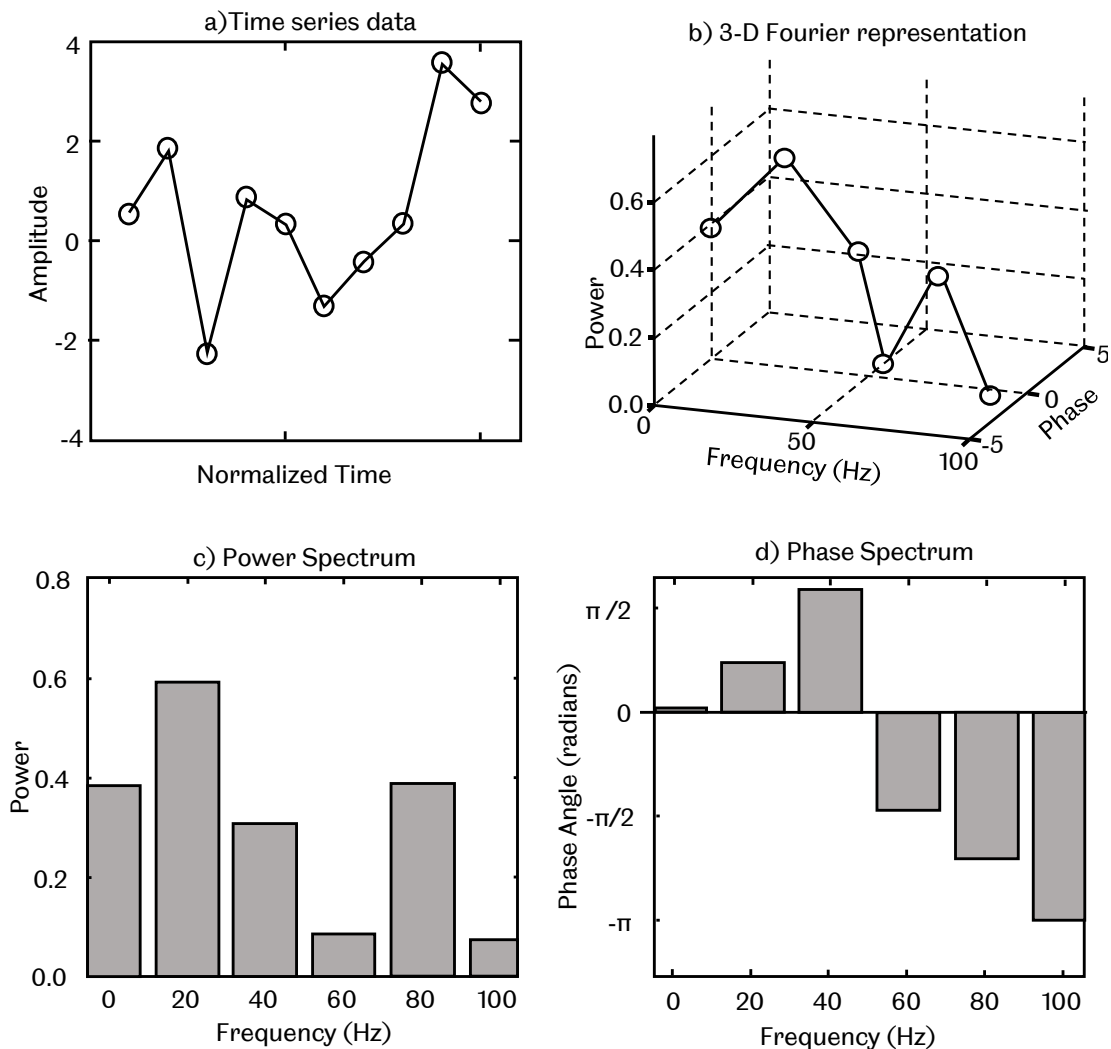
A discrete time Fourier transform is a type of Fourier transform which is limited by the time-series signal. The amount of data points in the time-series signal decides the amount and the frequency of sine waves created, defined by the following equation [72]:

$$X_f = \sum_{k=1}^n x_k e^{-i2\pi f(k-1)n^{-1}} \quad (2.12)$$



In equation (2.12),  $n$  refers to the number of data points in the time series signal  $x$ ,  $X_f$  represents the Fourier coefficient of the time series variable  $x$ , recorded at a frequency  $f$ , and finally  $k$  is the number of iterations in the summation. Figure 2.24(a) shows a randomly generated time-series signal with  $n = 10$ . Utilizing equation (2.12) on the signal will produce a summation of the Fourier coefficient, consisting of the frequency, power and phase, shown in Figure 2.24(b). Viewing the 3-dimensional graph from the power-frequency axis will produce the graph in Figure 2.24(c), while viewing the graph from the phase-frequency axis will produce the graph in Figure 2.24(d). The three-dimensional representation can be used to reconstruct the time signal by utilizing the inverse Fourier transform based on the following equation:

$$x_k = \sum_{k=1}^n X_k e^{i2\pi f(k-1)n^{-1}} \quad (2.13)$$



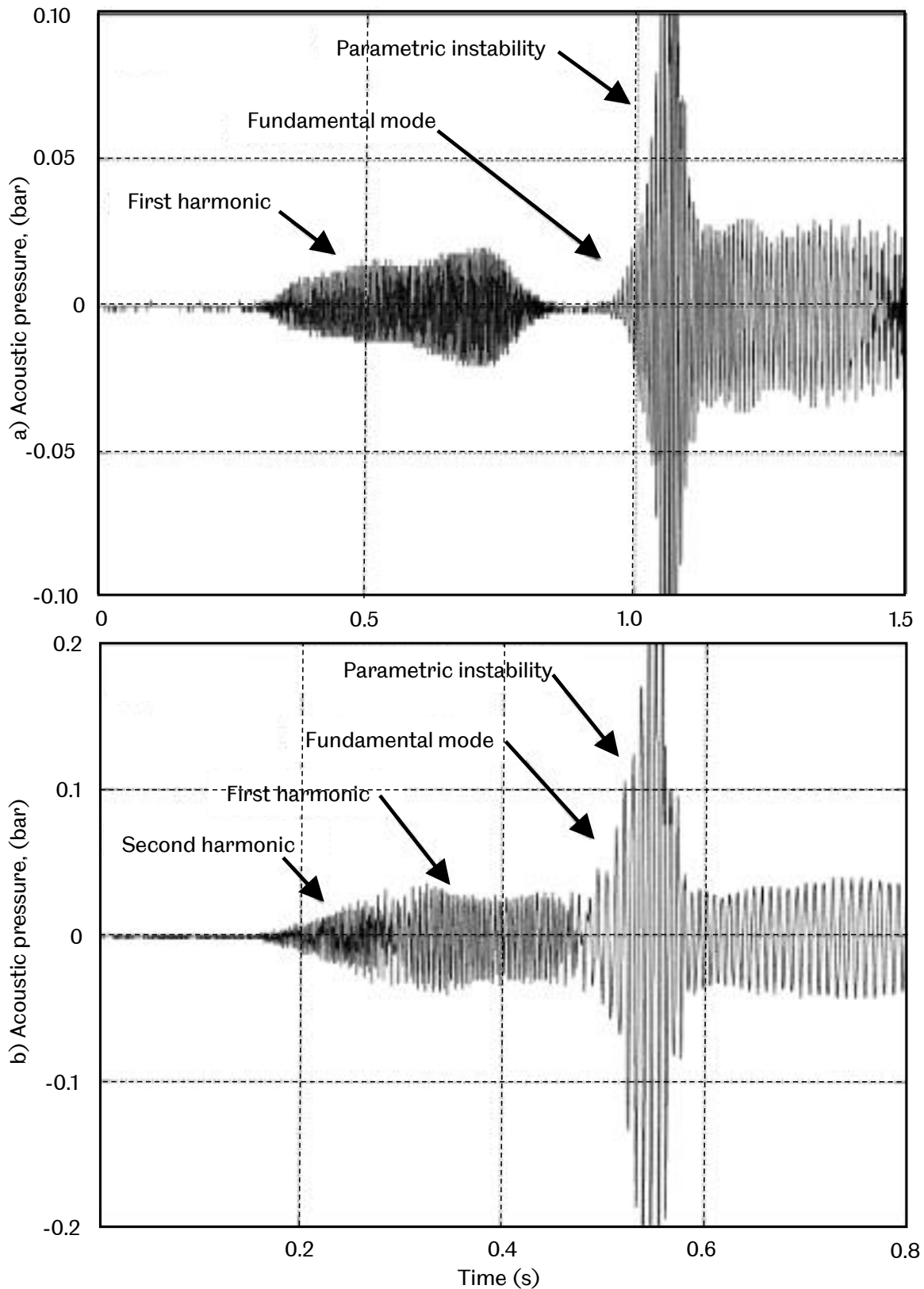
**Figure 2.24 Example of a discrete Fourier Transform from a) randomly generated time signal, producing b) the 3-dimensional representation of the time-series signal, c) the power spectrum, and finally d) the phase spectrum. Reproduced from [72].**

Fast Fourier Transform (FFT) is another way of computing the Fourier transform by eliminating elements that are redundant within the original calculation without losing any information [72]. If the reader wishes to gain a better understanding of the Fourier transform and its other forms, a textbook by Cohen [72] covers the vital parts regarding the matter.

FFT plays a huge role in the study of unstable combustion. Researchers often use FFT to quickly detect the frequency components of the flame oscillation based on the power-frequency graph of the Fourier transform, as shown in Figure 2.24(c). Ebieto et al. [73], utilized FFT to obtain the dominant frequency of the flame oscillations in their flame oscillation study, concluding that the ~240 Hz oscillations they observed were a characteristic of the tube, which changes slightly as the hydrogen content was increased.

In another study conducted by Clanet et al. [6], FFT was utilized to detect multiple frequency oscillations they attributed to resonant modes of the tube they used. Figure 2.25 shows two different flames at different equivalence ratio oscillating. Figure 2.25(a) is a  $\phi = 0.9$  decane flame, showing a clear silence after the first harmonic oscillation, before the start of the fundamental instability.

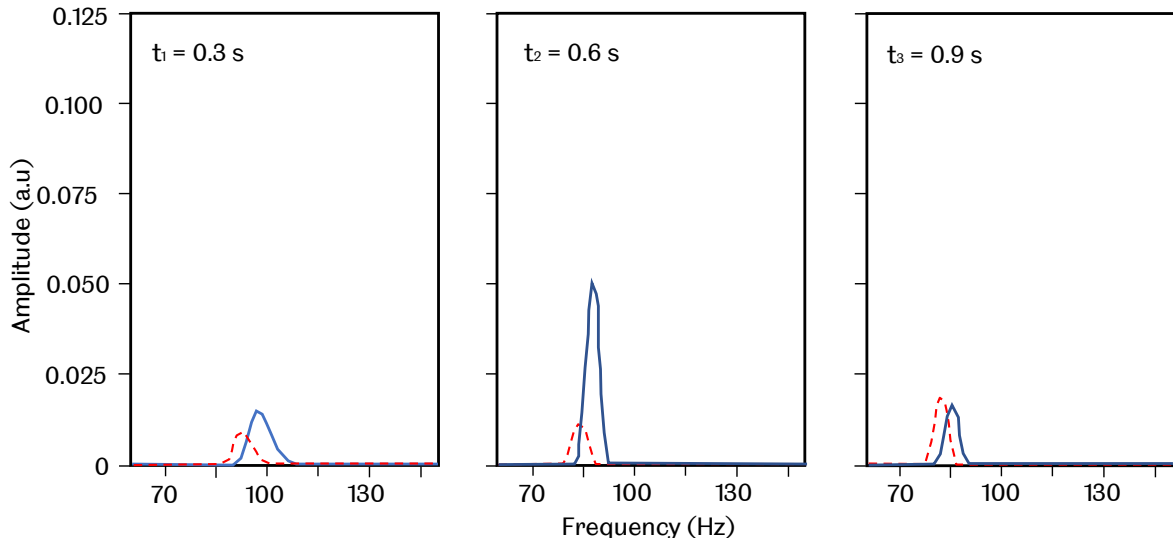
Increasing the equivalence ratio to 1.1 as shown in Figure 2.25(b), led to an onset of a different set of frequencies, which occurred consecutively with minimal drop in pressure. FFT seems to be useful in detecting the dominant frequency in the oscillations stated above, but in the event of an overlapping oscillation, it is quite difficult to distinguish the frequency, for example between the fundamental mode and the parametric instability in Figure 2.25(b). The signal would need to be cropped into separate sections in order to obtain the dominant frequency, and justifying where to crop would be another difficult task.



**Figure 2.25 Acoustic pressure records decane flame spray in a 1.2 m tube. a)  $\phi = 0.9$ , showing a short silence before a frequency transition in the instability whereas b)  $\phi = 1.1$  showing three consecutive instabilities appearing at different frequencies.**

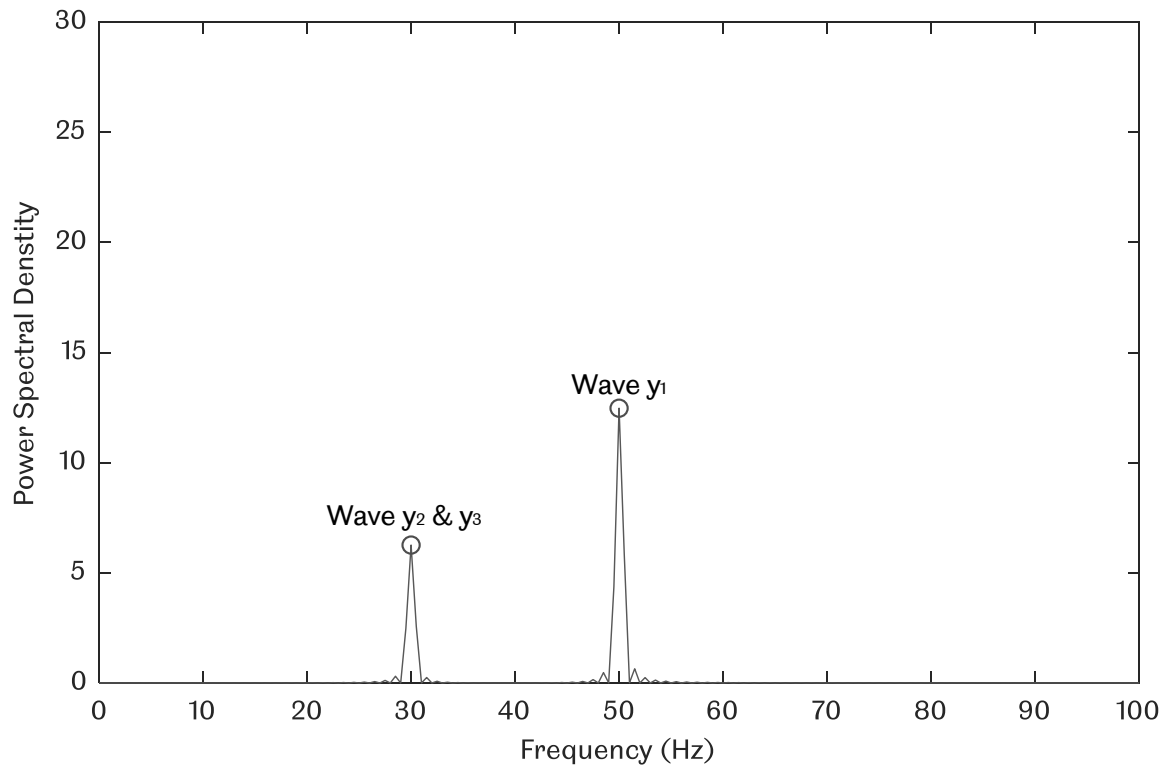
Reproduced from [6].

Veiga-López et al. [74] recently conducted a study regarding oscillatory premixed flames in a Hele-Shaw cell towards a closed end. In an attempt to dissect the oscillatory manner of the flames, they utilized FFT on the pressure and flame position signal, cropping them based on the appearance of flame structures. Figure 2.26 shows the Fast Fourier transform of flame position and the pressure signal for a lean  $\phi = 0.8$  propane flame, divided into 3 sections according to the flame shapes. If the signal was not divided into 3 sections, the FFT result would have multiple peaks unlike the ones shown in Figure 2.26.



**Figure 2.26 Fast Fourier transform of position (solid blue line) and pressure signal (dotted red line) of a  $\phi = 0.8$  propane flame divided into 3 sections according to flame structure. Reproduced from [74].**

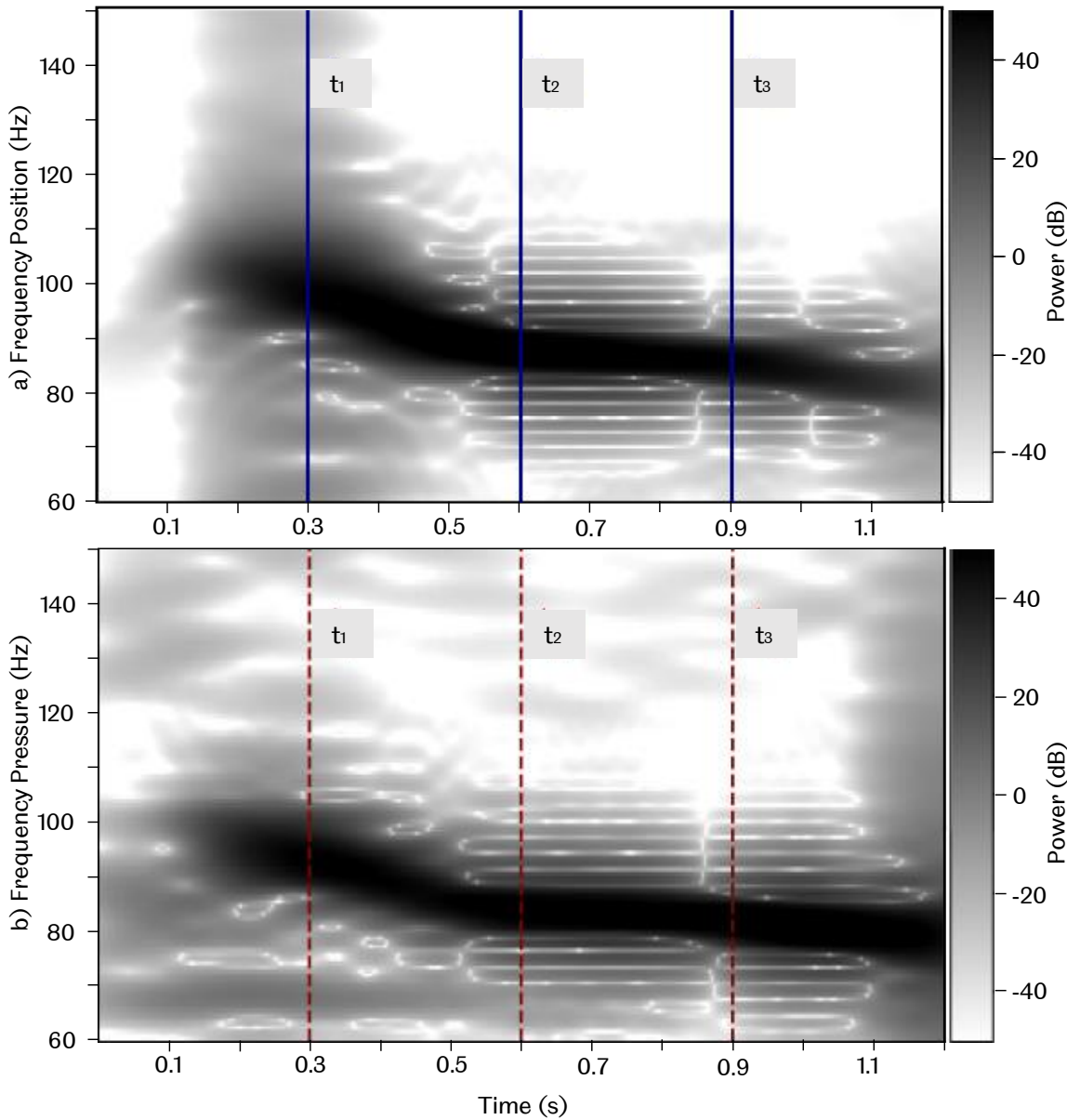
Performing FFT on the summation of the three waves from Table 2.4,  $y_{total}$ , produces two distinct peaks as shown in Figure 2.27. Wave  $y_1$  was responsible for the peak at 50 Hz, while wave  $y_2$  and  $y_3$  produced a single peak at 30 Hz, which corresponds to their respective frequency in Table 2.4. However, the disadvantage in using FFT is the absence of the time domain, leaving the time information hidden. It would be almost impossible to know when a certain frequency dominates, unless it is done on divided time-series sections as shown in Figure 2.26, but for cases with multiple overlapping components, it is rather tedious to perform. Another method that may overcome this problem is by producing a time-frequency plot, which will be explained in the next section.



**Figure 2.27 Fast Fourier Transform of  $y_{total}$**

### 2.5.2 Synchrosqueezed Wavelet Transform

Veiga-López et al. [74] attempted to produce a time-frequency plot using a Fourier spectrogram as shown in Figure 2.28, based on the same data used to produce the FFT plots in Figure 2.26. The shift in the dominant frequency can be observed in both the spectrogram plots of position and pressure. A Fourier spectrogram is useful for visualizing the shift in dominant frequency within the signal given that it only consists of one component. In the case of a multi component signal with different overlapping frequencies, the visualization would be difficult to interpret, and even more difficult to decompose into its individual components.



**Figure 2.28** Fourier spectrogram of a) flame position and b) flame pressure of a  $\phi = 0.8$  propane flame. Reproduced from [74].

Empirical mode decomposition (EMD) is a technique used to decompose a superposition of many signals into their individual signals, given that they are well separated both temporally and spectrally in the time-frequency plane. Daubechies et al. [75] made a thorough comparison of different EMD methods, which will not be covered here. They proposed a method called synchrosqueezed wavelet transform (SST) which aims to decompose time-series signals,  $s(t)$  into constituent components with time-varying harmonic behaviour, defined by [71] :

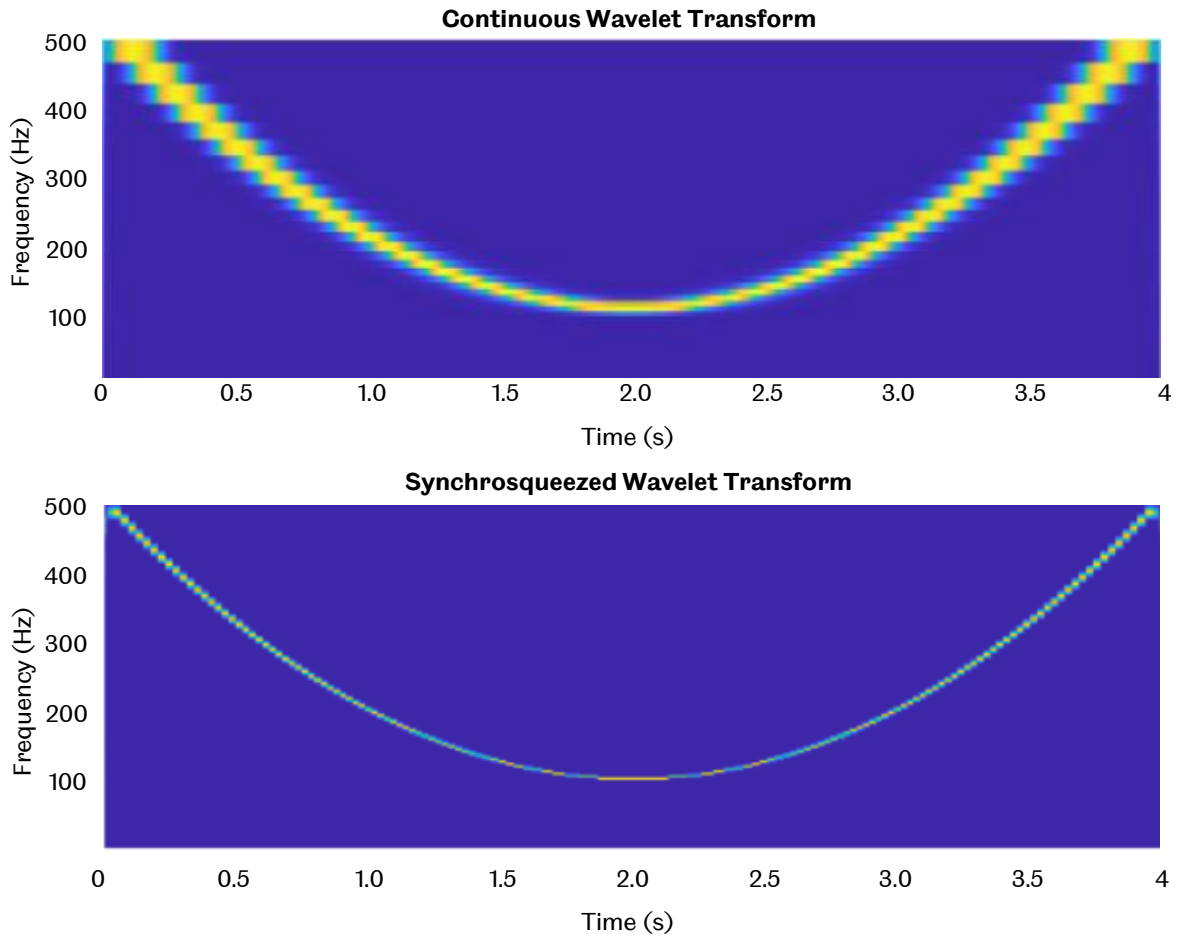
$$s(t) = \sum_{k=1}^K A_k(t) \cos[\theta_k(t)] + \eta(t) \quad (2.14)$$

In equation (2.14),  $A_k(t)$  represents the instantaneous amplitude,  $\eta(t)$  represents additive noise,  $K$  is the maximum number of components in one signal, and  $\theta_k(t)$  the instantaneous phase of the  $k$ th component. The instantaneous phase is used to estimate the instantaneous frequency  $f_k(t)$  of the  $k$ th component defined by [71]:

$$f_k(t) = \frac{1}{2\pi} \frac{d}{dt} \theta_k(t) \quad (2.15)$$

The main objective of using SST is to decompose a raw signal into  $K$  number components, each having an amplitude of  $A_k(t)$ , at their respective instantaneous frequency  $f_k(t)$ . Time-series signals in the form of equation (2.14) exists in many scientific applications [73-76] where the key to understanding the problem is by analysing the time varying spectral properties. Similar to FFT, reconstruction of the signals back into the time-domain is possible via SST with an added advantage of reconstructing the time signal into  $K$  number of signals, which becomes the original signal if summed together. Examples of SST implementation on artificial signals will be shown in the methodology chapter.

The working principle of a synchrosqueezed wavelet transform can be broken down into 3 steps. The first step is by obtaining the Continuous Wavelet Transform (CWT) of a signal using an analytical wavelet, in order to capture the instantaneous frequency information. The second step is to extract the instantaneous frequency from the CWT output, and the final step is by 'squeezing' the CWT over regions with constant phase transform. 'Squeezing' results in a concentrated instantaneous frequency in the time-frequency plane, unlike the smeared instantaneous frequency observed in the Fourier spectrogram utilized by Veiga-López et al. [74]. Another example was shown in Figure 2.29, comparing the CWT and SWT output of the same signal, showing significant sharpening of the smeared instantaneous frequency line when SWT was implemented.



**Figure 2.29 Comparison between a Continuous Wavelet Transform (CWT) and a synchrosqueezed wavelet transform (SST). Reproduced from [80].**

The steps in obtaining an SST plot from a CWT of a signal consists of a few steps. Daubechies [81] stated that the CWT of a signal  $s(t)$  consists of the complex conjugate of the mother wavelet,  $\psi^*$ , the time shift applied to the mother wavelet,  $b$ , and the scale applied to the mother wavelet,  $a$ , defined by equation (2.16):

$$W_s(a, b) = \frac{1}{\sqrt{a}} \int_{-\infty}^{\infty} s(t) \psi^* \left( \frac{t-b}{a} \right) dt \quad (2.16)$$

Based on equation (2.16), the CWT of the signal  $s(t)$ , can be defined as a cross correlation between the signal with several scaled and time shifted versions of the mother wavelet [71]. Using the coefficients obtained from equation (2.16), the instantaneous frequency can be obtained and a CWT plot similar to the plot in Figure 2.29 will be produced [75]. Rewriting equation (2.16) in the frequency domain using Plancherel's theorem (integral of a function's squared modulus frequency spectrum is equal to the integral of the function's squared modulus) produces equation (2.17), where  $j = \sqrt{-1}$ ,  $\xi$  is the angular frequency,  $\hat{\psi}^*(a\xi)$  is the scaled mother wavelet in frequency domain, and  $e^{jb\xi}$  is the time shift  $b$  in the frequency domain:



$$W_s(a, b) = \frac{1}{2\pi} \int_{-\infty}^{\infty} \frac{1}{\sqrt{a}} \hat{s}(\xi) \hat{\psi}^*(a\xi) e^{jb\xi} d\xi \quad (2.17)$$

Assuming a simple signal in the form of equation (2.10), applying to equation (2.17) could be simplified into equation (2.18):

$$W_s(a, b) = \frac{A}{2\sqrt{a}} \hat{\psi}^*(a\omega) e^{jb\omega} \quad (2.18)$$

Mapping the information obtained from equation (2.18) usually leads to blurred/smeared representation in the time-scale plane, which mainly occurs in the scale dimension,  $a$ , assuming a constant time shift,  $b$ . Daubechies and Maes [82] proposed that the derivative of equation (2.18) will minimize the effect of smearing. Computing the derivative of equation (2.18) for all  $W_s(a, b) \neq 0$ , the instantaneous frequency,  $\omega_s(a, b)$ , defined in equation (2.19) will be obtained:

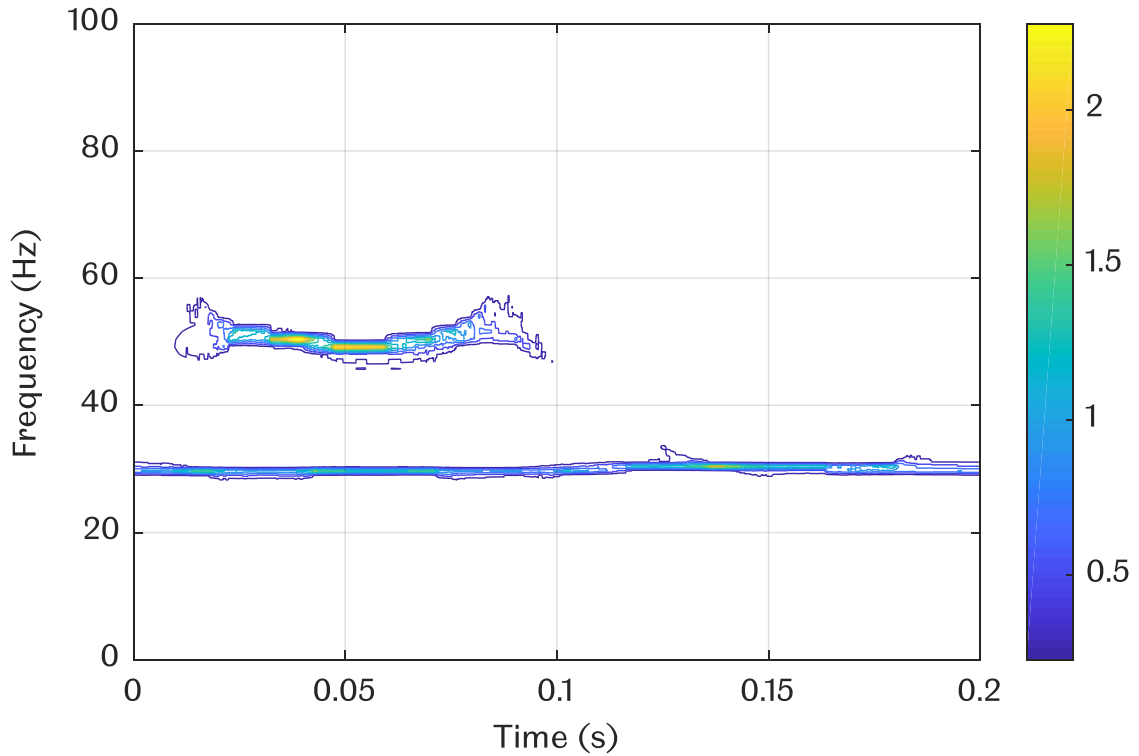
$$\omega_s(a, b) = \frac{-j}{W_s(a, b)} \frac{\partial}{\partial b} W_s(a, b) \quad (2.19)$$

In order to complete the process, the time-scale information ( $a - b$  plane) needs to be mapped to the time-frequency plane ( $\omega_l - b$  plane). This operation is defined as synchrosqueezing, where the information will be transferred from the form of  $(b, a)$  to  $(b, \omega_s(a, b))$ [75].  $a$  and  $b$  are distinctly different values, where a scaling step can be computed for each  $a_k$ , defined as  $\Delta a_k = a_{k-1} - a_k$ , for any value of  $W_s(a, b)$ .

Since  $a$  is defined as the scale, which technically changes the frequency of the mother wavelet, the scaling step for  $\omega$  is needed for computing the synchrosqueezed transform,  $T_s(\omega_l, b)$ , where only the centre of the instantaneous frequency,  $\omega_l$ , will be computed, within the range of  $(\omega_l - \frac{\Delta\omega}{2}, \omega_l + \frac{\Delta\omega}{2})$ , where  $\Delta\omega = \omega_l - \omega_{l-1}$ , producing equation (2.20):

$$T_s(\omega_l, b) = \frac{1}{\Delta\omega} \sum_{a_k: |\omega(a_k, b) - \omega_l| \leq \Delta\omega/2} W_s(a_k, b) a_k^{-\frac{3}{2}} (\Delta a)_k \quad (2.20)$$

Equation (2.20) shows that the output signal will be synchrosqueezed along the frequency axis only, without affecting the time shift [83]. The synchrosqueezed wavelet transform is available for use in MATLAB [84] along with a simple explanation of the execution of the wavelet synchrosqueezing algorithm in [80]. Implementing the Synchrosqueezed Transform on  $y_{total}$  produced Figure 2.30, which was able to detect the 30 Hz frequency that lasted for the whole 0.2 seconds, and also the 50 Hz frequency, which was abruptly stopped at 0.1 seconds.



**Figure 2.30 Synchrosqueezed transform plot for  $y_{total}$  clearly showing the existence of 2 different dominant frequencies.**

### 2.5.3 Phase Study

Phase study on flame signals is an important part in understanding the pressure amplification phenomena observed in combustion resonance [82–86]. In order to conduct a phase study, the phase of combustion related time-series signals must be extracted and computed to obtain their phase difference. According to Rayleigh [7], the amplification of a combustion occurs if the heat release and pressure are in phase, thus the best way to find this relation is by computing the phase difference between the heat release and pressure signal.

Mathematically, the Hilbert transform can be defined as a transform which changes a time domain function into a complex function using the following integral [90]:

$$U(s) = \int_{-\infty}^{\infty} \left[ \frac{1}{\pi(s-t)} \right] u(t) dt \quad (2.21)$$

where the time domain data,  $u(t)$ , is multiplied with the Hilbert Transform kernel, denoted in the square bracket, which were then integrated in terms of time,  $t$ , and obtaining the output in terms of  $s$ , a time dependent variable. Hahn [90] stated that the theory Hilbert Transform is closely tied to the Fourier Transform in the sense that both of them involve the use of integrals, but with different kernels.

The output of the Hilbert transform can be reversed back into its original form,  $u(t)$  via the following integral [90]:

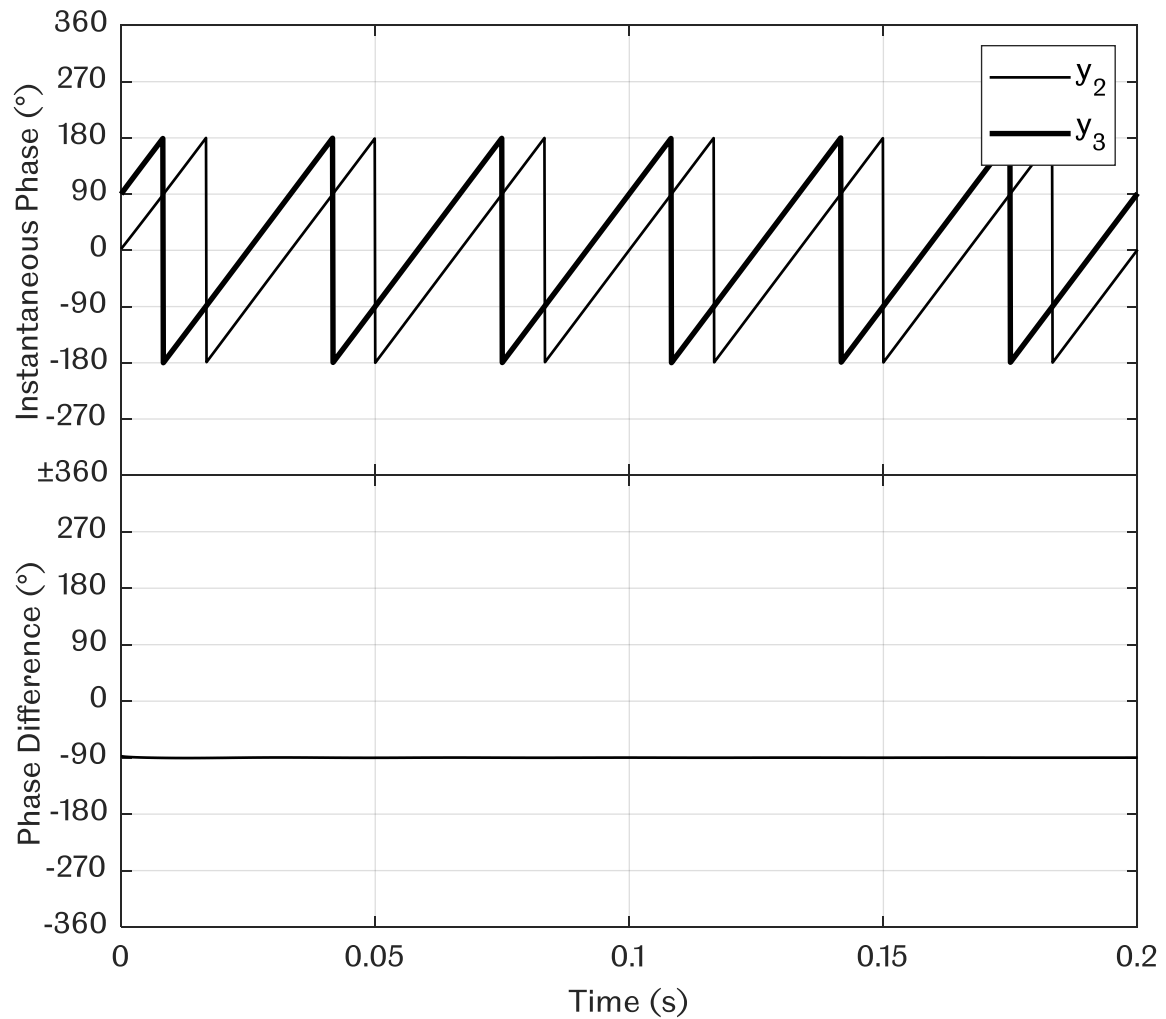
$$u(t) = \int_{-\infty}^{\infty} \left[ \frac{1}{\pi(t-s)} \right] U(s) ds \quad (2.22)$$

where the original transform,  $U(s)$ , obtained from equation (2.21) is multiplied with the conjugate Hilbert Transform kernel, denoted in the square bracket, and integrated in terms of the time dependent variable,  $s$ . If the reader wishes to understand further regarding Hilbert Transform, Hahn [90] explained the working principle of Hilbert Transform extensively.

In terms of applying the Hilbert Transform to the current work, the author utilized the Hilbert function in MATLAB on time domain data. However, it was noticed that the output of the function is not a purely imaginary signal defined by equation (2.21), but instead a combination between the real part (original signal) and the imaginary part (Hilbert Transform data) [91]. The output was then used by extracting the imaginary part only, which represents the phase of the signal, obtained by creating and adding the phase quadrature component to the real-valued signal, which basically means rotating the parts of the complex Fourier spectrum of a real valued signal [92].

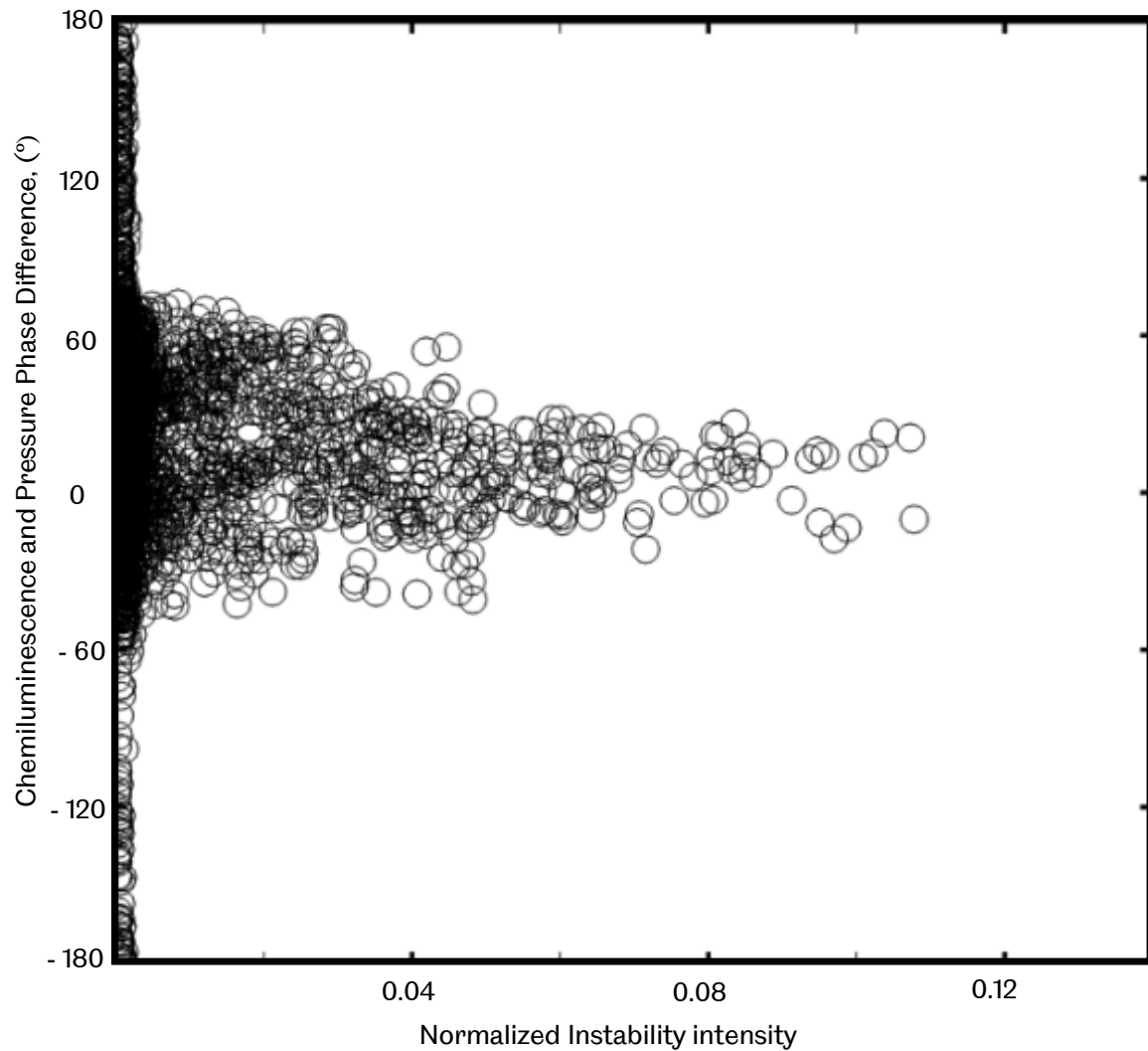
The function was tested on wave  $y_2$  and  $y_3$  to obtain their phase. Based on their information in Table 2.4, both waves were similar in frequency and amplitude, but with a different phase, where  $y_3$  leads  $y_2$  by  $90^\circ$ . Figure 2.31(a) shows the plot for their instantaneous phase, where it could be clearly seen that wave  $y_3$  started with an instantaneous phase of  $90^\circ$  whereas  $y_2$  started with  $0^\circ$ . The phase difference was calculated by subtracting the instantaneous phase of  $y_2$  with  $y_3$  for the whole duration in Figure 2.31(b), and it was found to be constant at  $-90^\circ$ .

In order to use the Hilbert Transform on a signal, it is important to apply a bandpass filter to obtain the phase of the desired frequency. Applying the Hilbert transform directly to an unfiltered signal would still give the phase information, but it would be the summation of phase information from other frequencies, making it difficult to understand. Similar to the example in Figure 2.31, wave  $y_2$  and  $y_3$  were used since they contain a similar single frequency of 50 Hz, but with a different phase. If  $y_1$  was used for this example, the phase difference would not be constant at  $-90^\circ$ .



**Figure 2.31 Plots of a) instantaneous phase of  $y_2$  and  $y_3$ , followed by b) phase difference between both signals.**

Lee et al.[93] performed a study on the coupling of combustion instability mechanisms in a lean premixed gas turbine combustor. Based on Figure 2.32, the amplification was the most obvious within the  $-90^\circ - 90^\circ$  phase difference range, indicating that the unsteady heat addition increases the energy of the system when in phase, and vice versa. It is worth noting that although in phase, some of the plotted points had low intensity, indicating a higher acoustic damping compared to gain [93].



**Figure 2.32 Phase difference between flame chemiluminescence and combustor pressure against normalized instability intensity for 4,950 operating conditions. Reproduced from [93].**

## 2.6 Research Gap

The current work aims to study the effect of fuel variation on the flame behaviour and shape. The implementation of SST on time-series signals obtained would then be used to associate the time-varying spectral contents to flame behaviours and flame shapes. The time-series signals would then be analysed further to study relationship between the flame heat release and the tube pressure using Hilbert transform to compute the phase difference.

## 3 EXPERIMENTAL METHODOLOGIES

### 3.1 Experimental Apparatus

The apparatus used in the present work consisted of 2 main parts, the flame tube rig and data acquisition tools, shown in Figure 3.1. The flame tube rig was a constant volume mixing loop fabricated from copper tubes, compression fittings, mixing fans, and a quartz tube, chamber pressure transducer, vacuum pump and valves. The rig was originally designed and fabricated by Pennington [94] for his undergraduate project and subsequently developed by two postgraduate students, Mossa [95] and Ebieta [48]. The rig was originally designed for studying the premixed flame propagation speed of fuels, but in this work the rig has been used to study thermoacoustic interactions with flames.



**Figure 3.1** Picture of the flame tube rig.

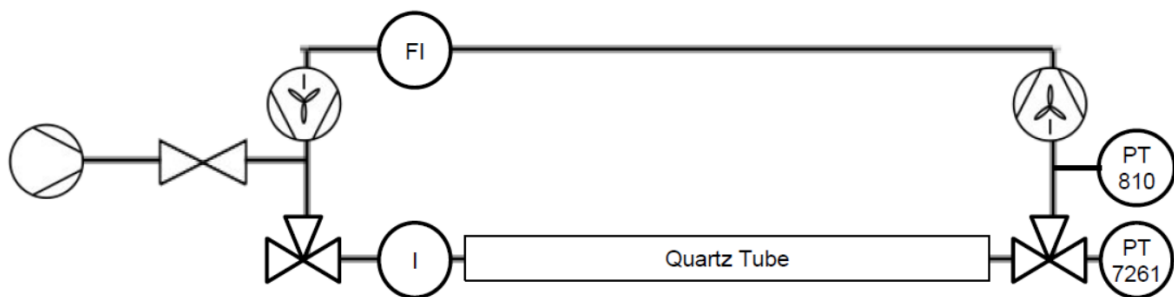
The working principle of the rig was based on a constant volume mixing loop. The vacuum pump was used to remove air and combustion products from the mixing loop after an experiment, creating a pressure of approximately  $-0.95$  bar. The mixing loop pressure was monitored with a pressure transducer. Fuel was then injected via the ignition port into the chamber using a syringe. Ambient air was then allowed to enter the loop by opening one of the 3-way valves.

Once the chamber pressure reached ambient pressure, the 3-way valve was closed, and the mixing fans turned on to mix the fuel and air. The mixture of fuel and air was mixed for 3 minutes to ensure a homogenous mixture. The quartz tube was then isolated from the mixing loop by turning the 3-way valves so that both ends of the tube were open to the atmosphere. and mixture was ignited using a pilot flame. The experiments were conducted under ambient temperature and pressure, which has

a typical value of 20 °C and 1.013 bar of atmospheric pressure, measured using a barometer and a room thermometer.

Copper tubes of 0.02m internal diameter (0.022m outer diameter) were used to construct the mixing loop. The quartz tube had the same inner diameter and a length of 0.65m for optical access. Brass compression fittings, elbows, and equal tees of the same diameter were used to connect the copper tubes, mount the pressure transducer, mixing fans, ignition port, and also the fuel injection port.

The pressure inside the loop was monitored with a Druck PDCR810 pressure transducer, with pressure reading range between -1 to 1 bar gauge pressure. This was only used to monitor the loop pressure during vacuuming and injection of fuel into the rig. A septum, a self-sealing plastic plug, was used on the injection port to prevent the mixture from leaking from the rig after injecting fuel into the rig. 3-way valves were used to isolate the quartz tube from the mixing loop before igniting the mixture. A one-way valve was used to connect the rig to the vacuum pump.



**Figure 3.2 The flame tube rig diagram, I – Ignition Port, FI – Fuel Injection Port.**

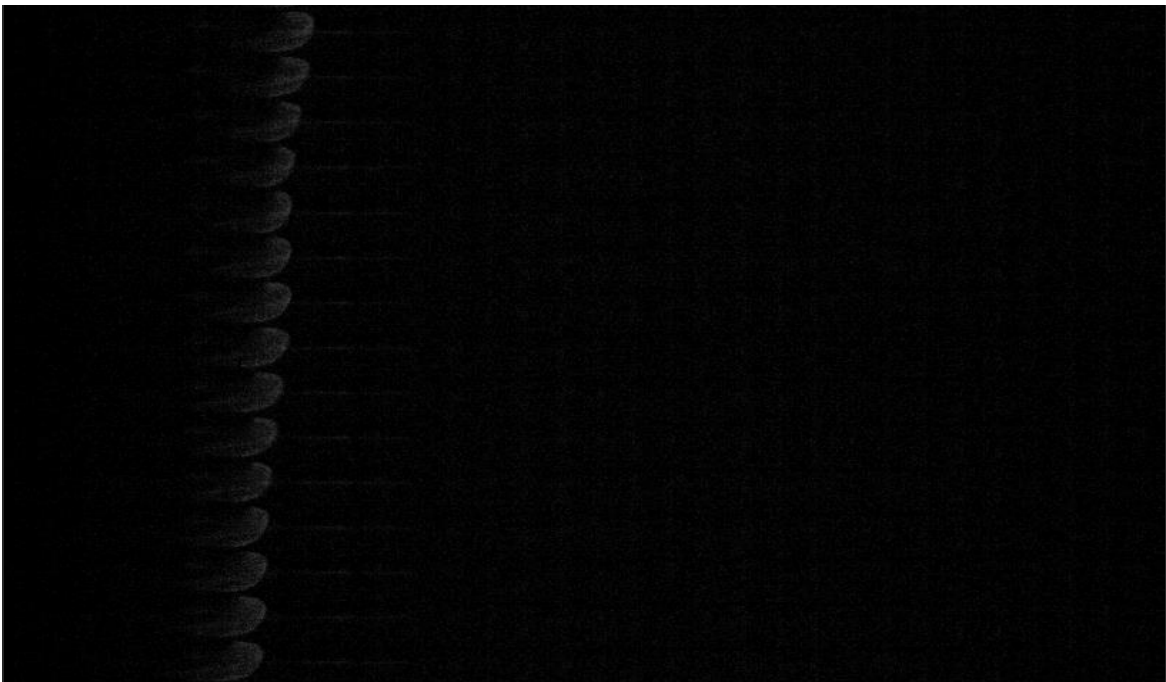
Figure 3.2 shows the schematic diagram of the flame tube rig observed in Figure 3.1. Notice how the pressure transducer locations are different for their respective functions. Ignition was performed using a pilot flame via the ignition port. This method of ignition was preferred compared to a spark ignition system, due to the extra energy provided by the system, causing flames to propagate faster based on a study conducted by Wu et al. [96]. The duration taken for a flame to propagate through the recorded part of the tube ranges between 0.059 - 0.653 seconds. The fuel collection procedure is available in Appendix B, whereas the complete experimental procedure is available in Appendix E.

## 3.2 Data Acquisition

### 3.2.1 Optical Measurements

In the present work a typical combustion event took place in less than a second, making high-speed imaging an essential component in capturing the movement of the flame. A typical everyday camera has a framing rate of 24-30 fps. and tend to suffer from motion blur due to their exposure time.

A Phantom V210 high-speed camera was used for all the experiments performed in the present work. The camera was fitted with a monochrome CMOS sensor and was able to record at a resolution of 1,280 x 800 pixels at 2000 fps, up to 300,000 fps at 128x8 pixels resolution [97]. Phantom Camera Control (PCC) was used to adjust the resolution, framing rate and triggering the camera. For natural light experiments, the camera was paired with a Nikon AF Zoom-NIKKOR 24-85mm f/2.8-4D IF lens. Whilst the high framing rate provided details of the flames, the images could be hard to observe due to the low light intensity, causing signal loss in the flame recording, as observed in Figure 3.3.

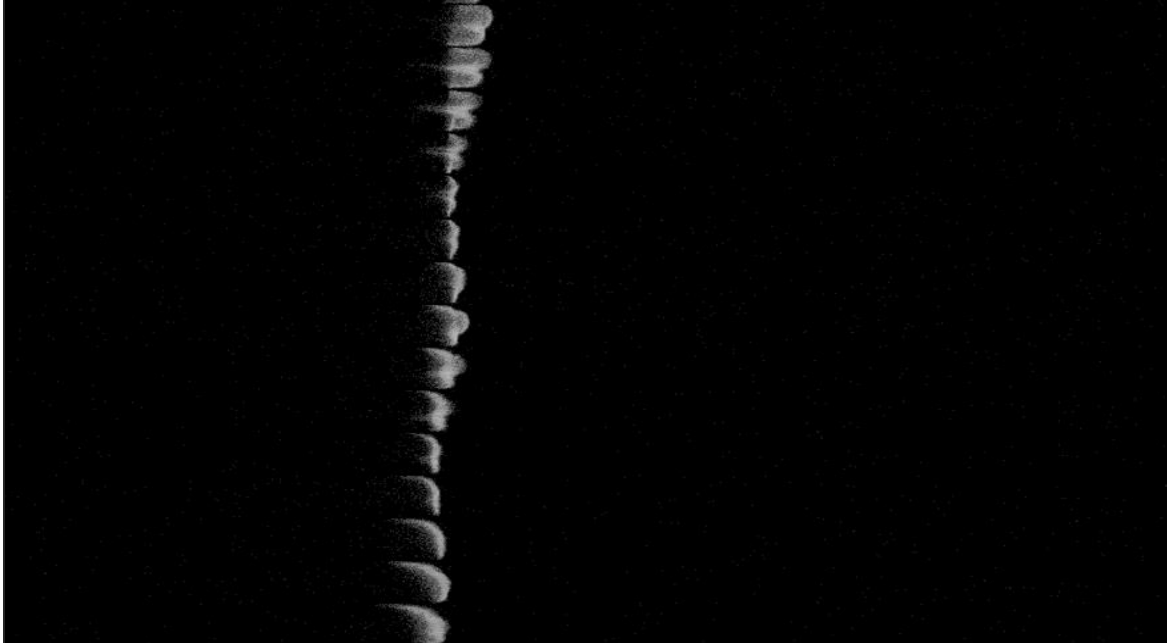


**Figure 3.3 Flame sequence of a  $\phi = 0.8$ ,  $R_H = 0.3$  flame, recorded at 1,500 fps, suffers low light intensity.**

In order to overcome this problem: the aperture of the lens was kept at f/2.8; the camera was placed as close as possible to the quartz tube maximizing the amount of light entering the lens and the experiments were performed in a darkened room



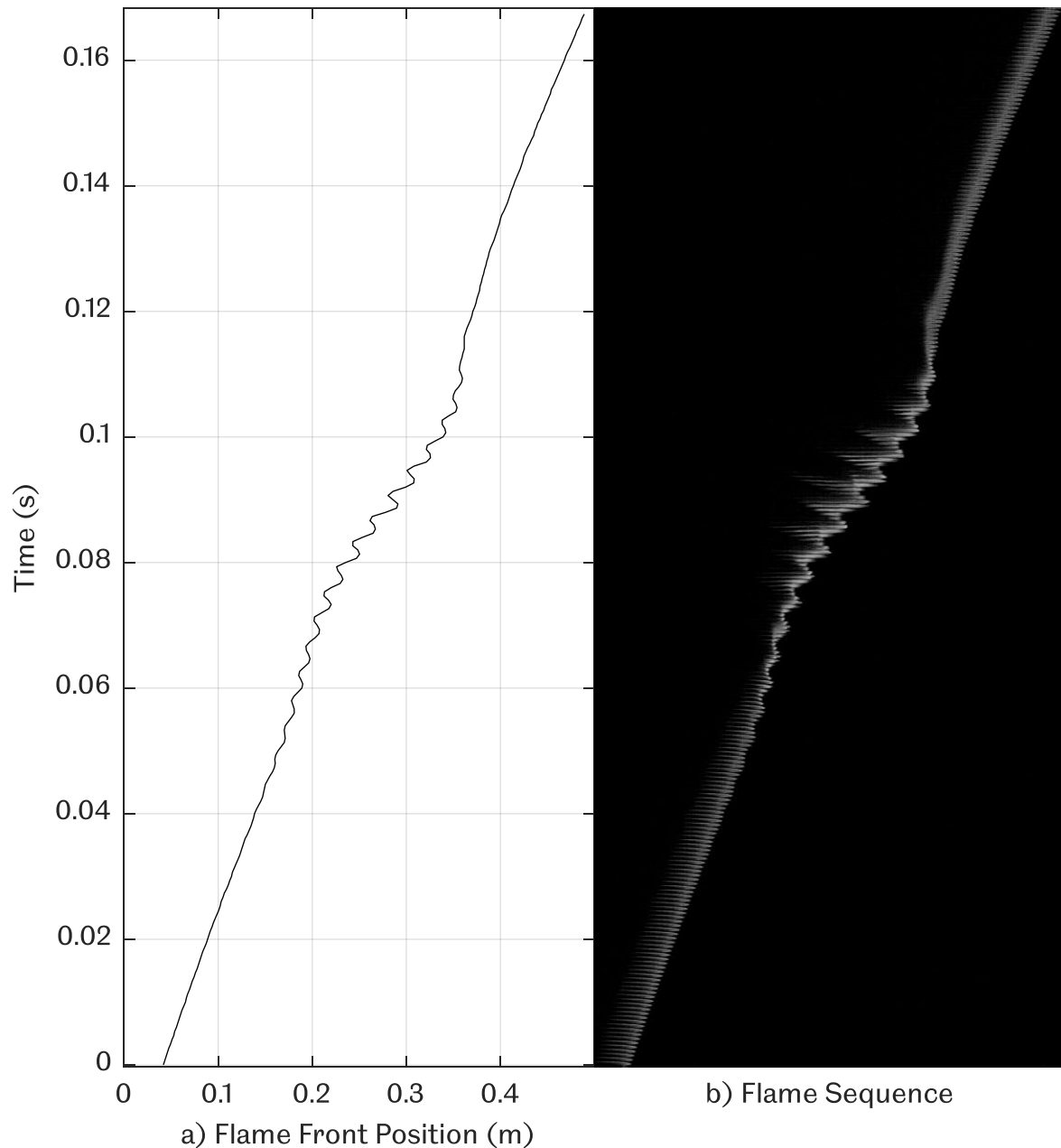
to remove extraneous light sources. A framing rate of 1,500 fps and an exposure time of 1/1500 seconds was used to ensure the widest possible range of fuel compositions could be recorded without changing the framing rate. Comparing Figure 3.3 to Figure 3.4, the stoichiometric flame appears to be clearer compared to the lean flame.



**Figure 3.4 Flame sequence of a  $\phi = 1.0$ ,  $R_H = 0.2$  flame, recorded at 1,500 fps.**

Light intensity was one of the limiting factors in the present work, limiting the lean side of the equivalence ratio to 0.8. Schmidt et al. [14] overcame this light intensity problem by utilizing Schlieren photography, which would be one of the future recommendations for the present work, but would require the fabrication of a square tube rig in order for Schlieren photography to work. They were able to reach an equivalence ratio,  $\phi = 0.6$  for propane flames.

A post-trigger method was implemented in the present work via the PCC software. The event was continuously recording to a buffer and images captured when the camera was triggered via a trigger button. The images before the trigger were recorded rather than those after the trigger. The post-trigger method was found to be more successful at capturing the event. The flame position was tracked using MATLAB, which will be discussed in detail in the next chapter. Flame tracking would usually produce a flame front position plot observed in Figure 3.5(a), which was produced from the flame sequence in Figure 3.5(b). The tracked flame position would then be synchronised with the flame pressure before being analysed further. The procedures for optical calibration are available in Appendix C.



**Figure 3.5 Example of a) flame front position plot produced from flame tracking of b) flame sequence.**

### 3.2.2 Pressure Measurement

Two pressure transducers were utilised, a Kistler Type 7261 and a Druck PCDR810. The Kistler Type 7261 low pressure transducer was used for recording the dynamic pressure during the combustion event. The transducer range was set to 1 bar. The Kistler transducer is a Piezoelectric quartz transducer [98], suitable for highly dynamic pressure measurements, which works by generating a charge when pressure is applied. The produced charge then gets amplified by the Kistler Type

5018 Charge Amplifier, which is connected to a computer, and gets logged by a LabView program.

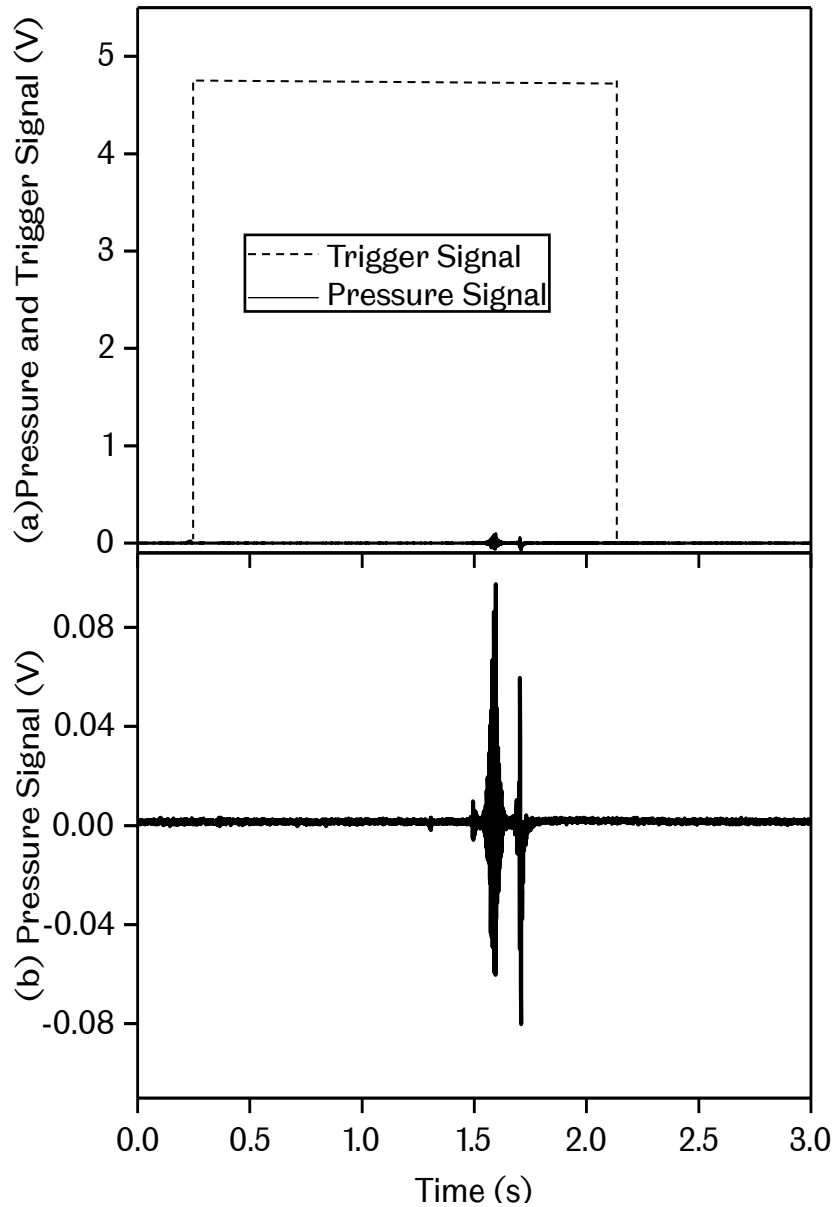
A Druck PCDR810 pressure transducer was used for monitoring the rig pressure during fuel mixing procedures and rig volume calculation. The pressure transducer was connected to a Druck Digital Pressure Indicator 260 to display the output pressure in bar. The Druck transducer is a strain-gauge based pressure transducer [99], with a silicon diaphragm and a titanium module, converting pressure into a measurable signal by calculating deformation of the strain gauge caused by the pressure. The pressure from this transducer not logged, but only used for monitoring the overall rig pressure during rig vacuuming and fuel injection. The procedure for pressure calibration is available in Appendix D.

### **3.2.3 Optical and Pressure Data Synchronization**

Synchronization between the pressure and optical data is important for the analysis of the data. The synchronization was achieved with a National Instruments myDAQ (Part No. 781326-01) data acquisition device, which has an ADC and DAC resolution of 16 bits [100]. The box was designed to send a Transistor-Transistor Logic (0 to ~5V) signal when the trigger button was pressed, which dropped back down when the button was released.

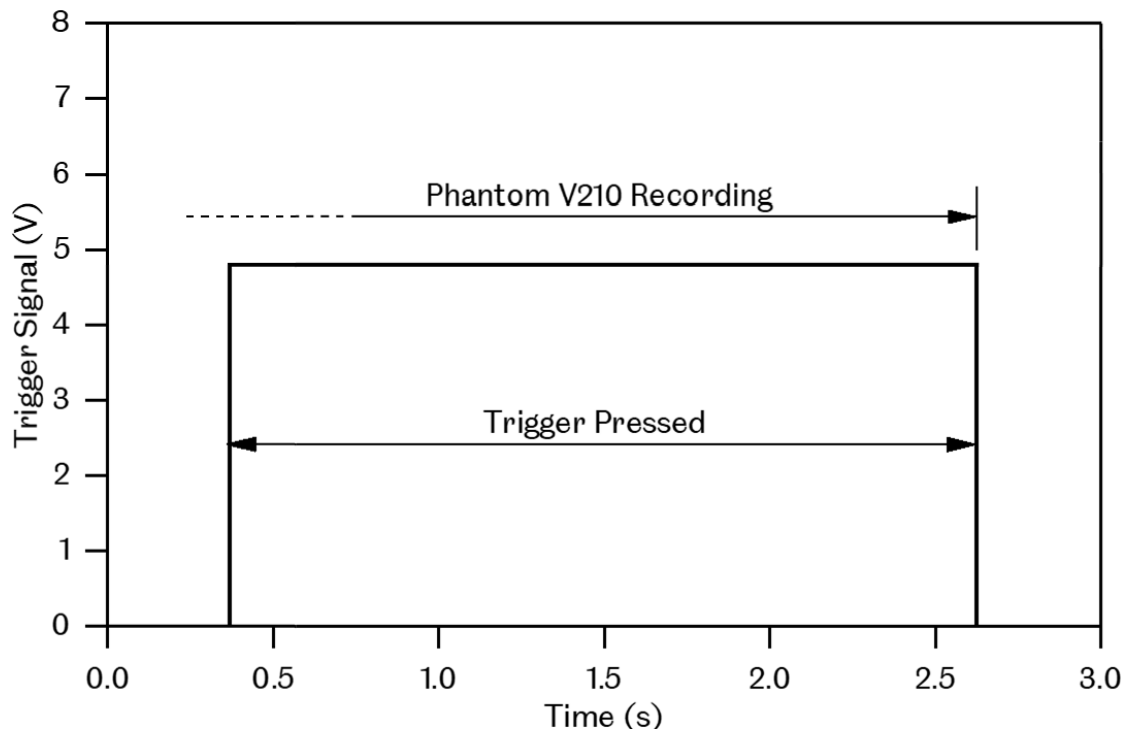
A LabVIEW program was used to log the pressure readings from the charge amplifier together with the trigger signal. Figure 3.6(a) shows an example of a trigger signal and a pressure signal obtained from an experiment, the difference in voltage was large, making the pressure signal unnoticeable. Zooming towards the pressure signal, a better view of the pressure signal was seen in Figure 3.6(b).

First step for the synchronization was to crop the pressure signal. The beginning is the rise of the trigger signal to 5 V and ends when it drops back to 0 V. Cropping of the pressure signal was rather direct, taking the rise of the trigger signal as the beginning, and the trigger signal drop as the ending. The cropped pressure signal needs to be converted from Voltage to bar, stated as 0.1 bar / V on the Kistler Type 5018 charge amplifier screen, shown in Appendix D. Once the conversion was done, the flame propagation in the video recording needs to be tracked. Detailed procedure of the flame tracking will be explained in the next chapter.



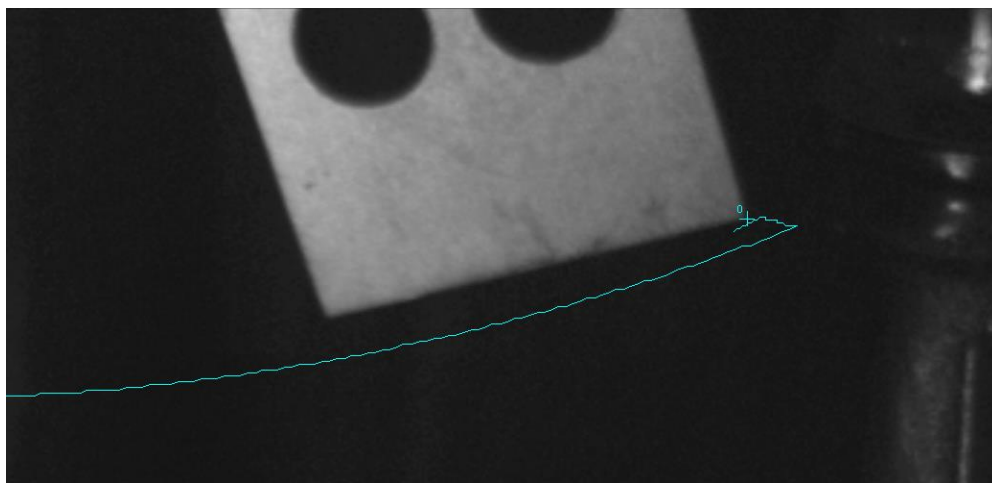
**Figure 3.6 Example of a) trigger signal with pressure signal, b) zoomed in pressure signal, both before cropping.**

Once the flame propagation was tracked in the video recording to obtain the flame position signal, it needs to be synchronised with the pressure signal. Since the Phantom camera operates based on a post-trigger system, it continuously records until the trigger is released, making the end of the video synchronised with the end of the trigger signal, which is technically the end of the cropped pressure signal, as shown in Figure 3.7.



**Figure 3.7 Video recording to trigger signal synchronisation in the present work.**

Prior to the synchronisation, the synchronisation process was tested by recording a metal plate hitting a fixed area of the flame tube, producing a sound which will be captured by the pressure transducer. The movement of the plate was tracked in a similar way as the flame was tracked. When the metal plate touches the tube, the motion of the tracked metal plate was usually reversed, as shown in Figure 3.5. The time of plate reversal was compared to the time of pressure rise captured and tabulated in Table 3.2. A standard deviation of  $3.266 \times 10^{-4}$  seconds was obtained for all 10 tests.

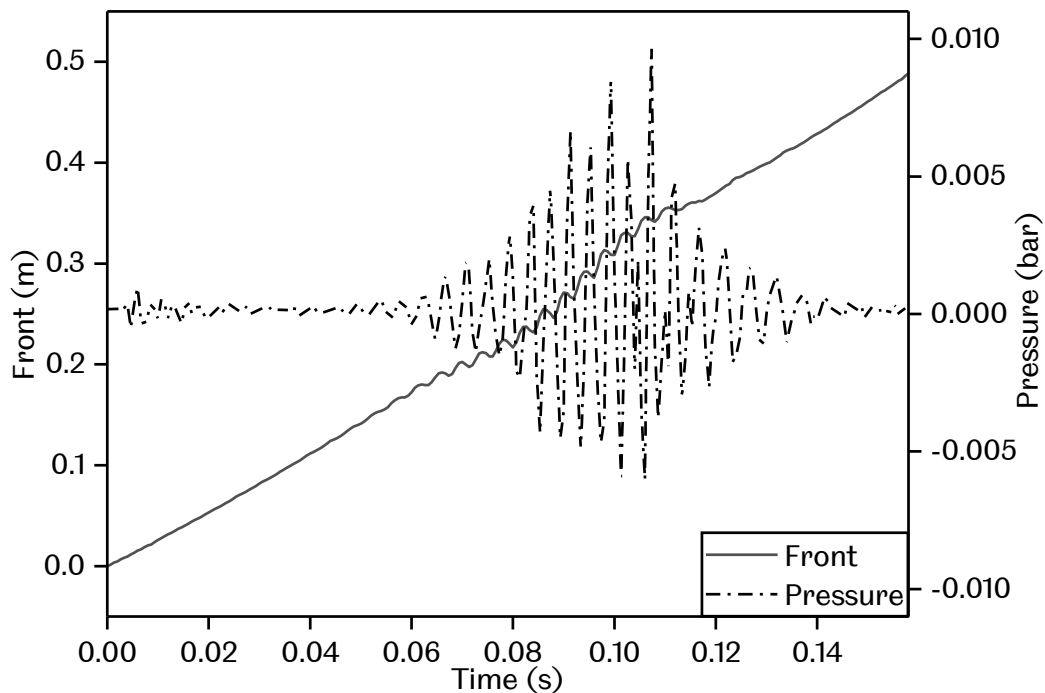


**Figure 3.8 Reversing motion of the tracked metal plate edge (green line) after hitting the tube.**

**Table 3.1 Tabulated results of the synchronisation workflow test.**

Run No.	Time of pressure rise, s	Time of plate reversal, s	Time difference, s	Standard deviation, s
1	2.3107	2.3107	0	3.266E-04
2	1.3080	1.3073	6.67E-04	
3	1.4567	1.4560	6.67E-04	
4	1.5973	1.5967	6.67E-04	
5	1.5193	1.5193	0	
6	1.7240	1.7233	6.67E-04	
7	1.6197	1.6190	6.67E-04	
8	1.4197	1.4197	0	
9	1.9247	1.9247	0	
10	1.9850	1.9843	6.67E-04	

The flame position signal will then be cropped according to the trigger signal, and aligned with the pressure signal as shown in Figure 3.6. Comparing the raw data obtained in Figure 3.6 to the work done by Searby [8], the pressure signal seems to be of the same quality, but the flame recordings appear to be better in terms of capturing the oscillatory motion. Referring back to Figure 2.16 reproduced from Searby [8], the flame front position appears to be smooth, leaving no opportunity to further study the oscillatory behaviour of the flame front performed in the present work.



**Figure 3.9 Example of a synchronised pressure and flame front position signal.**

## 3.3 Fuel

### 3.3.1 Fuel Related Apparatus

The fuels used in the present work were methane, propane, and hydrogen. These flammable gasses present a hazard and require proper handling. The storage cylinders were placed outside of the lab. Gas sampling bags were used to collect the required gasses for the experiments. The Kynar gas sampling bags were fitted with an on/off valve for filling the bag, and a septum valve. The septum valves which self-sealed allowing the fuel to be collected using a syringe [48], preventing air entering the fuel bag.

### 3.3.2 Rig Volume Calculation

Initial attempts in calculating the rig volume included geometrical calculation and a water displacement method [95]. The main problem for the geometrical calculation method was the internal structures of the compression fittings, mixing fans, three-way valves and other complicated shaped components resulted in significant uncertainty. A water displacement method was then used, where the whole rig was filled with water and calculated the volume by dividing the weight of water inside the rig with the density. This method was more accurate, but was inconvenient as the rig geometry was changed frequently.

A rig volume calculation method [48], based on the Boyle's Law was used in the present work. Boyle's Law states that for a certain mass of an ideal gas at constant temperature, the pressure is inversely proportional to the volume. Assuming the gas inside the rig has a constant temperature and behaves like an ideal gas. The rig volume was calculated before starting a batch of experiments using the Druck PDCR810 pressure transducer, a syringe of known volume. The procedure for rig volume calculation is available in Appendix A.

### 3.3.3 Fuel Volume Calculation

Fuel volume calculations were based on the equivalence ratio equation discussed in the previous chapter, equation (2.6). Equivalence ratio in this form is useful for single air-fuel mixtures, but cannot be used once two or more fuels are combined to form a mixture. In order to add hydrogen systematically to a fuel mixture the  $R_H$  method was used in the present work. The  $R_H$  method was proposed by Yu et al. [10], governed by equation (2.7) ( $\phi$ , equivalence ratio) and equation (2.8) ( $R_H$ , hydrogen addition). The main advantage of this method is the amount of hydrogen addition is independent of the main fuel and equivalence ratio.

The mixtures tested in the present work was tabulated in Table 3.2, showing the calculated laminar burning velocity (using CHEMKIN [101]), mole fraction(using Gaseq [102]) and volume of methane and hydrogen for each equivalence ratio at different levels of hydrogen addition,  $R_H$ . It is worth noting that the mole fraction and volume of hydrogen was constant for all equivalence ratios at each hydrogen addition levels.  $R_H$ , as shown previously in Table 2.3 in the previous chapter.

The total number of mixtures tested was 72, and each mixture was burnt and recorded 3 times, totalling up to 216 runs. The standard deviation of each mixture was calculated based on the maximum tube pressure and tabulated in Table 3.2, ranging from  $3.13 \times 10^{-20}$  –  $2.513 \times 10^{-3}$  bar. In the present work, the maximum tube pressure was preferred over the pressure growth rate since not all mixtures were observed to oscillate and have a growth rate, leading to an incomplete comparison of the whole range of mixtures tested.

**Table 3.2 Tabulated laminar burning velocity, mole fraction, volume, and the standard deviation (based on maximum pressure) for all mixtures tested in the present work.**

Hydrogen Addition, $R_H$	Equivalence Ratio, $\phi$	Laminar Burning Velocity, $S_U$ (m/s)	Mole Fraction		Volume (mL)		Standard Deviation, (bar)
			Methane	Hydrogen	Methane	Hydrogen	
0	0.8	0.2718	0.077	0	100.126	0	3.764E-06
	0.9	0.3270	0.086	0	111.563	0	3.073E-06
	1.0	0.3596	0.095	0	122.784	0	8.836E-04
	1.1	0.3599	0.103	0	133.793	0	7.107E-04
	1.2	0.3200	0.112	0	144.598	0	1.904E-03
	1.3	0.2338	0.120	0	155.204	0	1.408E-05
	1.4	0.1399	0.128	0	165.616	0	6.697E-06
	1.5	0.0928	0.136	0	175.839	0	6.146E-06
0.1	0.8	0.3353	0.070	0.027	91.257	34.829	4.527E-05
	0.9	0.3884	0.079	0.027	101.679	34.829	3.724E-04
	1.0	0.4184	0.086	0.027	111.903	34.829	6.628E-04
	1.1	0.4213	0.094	0.027	121.934	34.829	1.059E-03
	1.2	0.3887	0.102	0.027	131.778	34.829	6.387E-05
	1.3	0.3121	0.109	0.027	141.441	34.829	1.328E-03
	1.4	0.2108	0.117	0.027	150.926	34.829	1.339E-05
	1.5	0.1329	0.124	0.027	160.239	34.829	1.408E-05
0.2	0.8	0.3995	0.065	0.049	83.653	63.853	2.281E-03
	0.9	0.4485	0.072	0.049	93.206	63.853	1.302E-03
	1.0	0.4771	0.079	0.049	102.578	63.853	8.713E-04
	1.1	0.4824	0.086	0.049	111.773	63.853	4.840E-04



	1.2	0.4543	0.093	0.049	120.797	63.853	8.213E-04
	1.3	0.3877	0.100	0.049	129.654	63.853	1.018E-03
	1.4	0.2905	0.107	0.049	138.349	63.853	3.521E-04
	1.5	0.1881	0.113	0.049	146.885	63.853	1.483E-03
<b>0.3</b>	0.8	0.4604	0.060	0.068	77.218	88.412	1.190E-03
	0.9	0.508	0.066	0.068	86.036	88.412	1.238E-03
	1.0	0.5512	0.073	0.068	94.687	88.412	1.525E-03
	1.1	0.5582	0.080	0.068	103.175	88.412	2.958E-04
	1.2	0.5365	0.086	0.068	111.505	88.412	7.496E-05
	1.3	0.4813	0.092	0.068	119.680	88.412	1.235E-03
	1.4	0.387	0.099	0.068	127.706	88.412	3.297E-04
<b>0.4</b>	0.8	0.5267	0.055	0.085	71.702	109.463	3.045E-04
	0.9	0.5788	0.062	0.085	79.891	109.463	5.887E-05
	1.0	0.6103	0.068	0.085	87.924	109.463	2.634E-04
	1.1	0.6179	0.074	0.085	95.806	109.463	7.609E-04
	1.2	0.599	0.080	0.085	103.540	109.463	3.286E-04
	1.3	0.5506	0.086	0.085	111.132	109.463	5.807E-04
	1.4	0.4709	0.092	0.085	118.584	109.463	2.513E-03
	1.5	0.3581	0.097	0.085	125.902	109.463	1.085E-03
<b>0.5</b>	0.8	0.5874	0.052	0.099	66.922	127.706	4.391E-04
	0.9	0.638	0.058	0.099	74.565	127.706	1.240E-04
	1.0	0.6687	0.063	0.099	82.062	127.706	1.757E-04
	1.1	0.6768	0.069	0.099	89.418	127.706	4.232E-04
	1.2	0.6601	0.075	0.099	96.637	127.706	1.597E-04
	1.3	0.6162	0.080	0.099	103.723	127.706	8.927E-05
	1.4	0.545	0.085	0.099	110.679	127.706	6.687E-04
	1.5	0.4481	0.091	0.099	117.508	127.706	2.218E-04
<b>0.6</b>	0.8	0.647	0.048	0.111	62.739	143.670	2.917E-04
	0.9	0.6961	0.054	0.111	69.905	143.670	2.476E-04
	1.0	0.7261	0.059	0.111	76.933	143.670	2.853E-04
	1.1	0.7347	0.065	0.111	83.830	143.670	2.691E-04
	1.2	0.7198	0.070	0.111	90.598	143.670	7.533E-05
	1.3	0.6797	0.075	0.111	97.240	143.670	3.765E-04
	1.4	0.6144	0.080	0.111	103.761	143.670	2.807E-04
	1.5	0.5269	0.085	0.111	110.164	143.670	5.674E-04
<b>0.7</b>	0.8	0.7052	0.046	0.122	59.049	157.755	2.773E-04
	0.9	0.7531	0.051	0.122	65.792	157.755	1.629E-04
	1.0	0.7826	0.056	0.122	72.408	157.755	3.459E-04
	1.1	0.7915	0.061	0.122	78.899	157.755	2.530E-04
	1.2	0.7783	0.066	0.122	85.268	157.755	5.986E-04
	1.3	0.7414	0.071	0.122	91.520	157.755	1.283E-03
	1.4	0.6809	0.075	0.122	97.658	157.755	8.430E-04
	1.5	0.5994	0.080	0.122	103.684	157.755	7.294E-04

<b>0.8</b>	0.8	0.7619	0.043	0.132	55.768	170.275	3.602E-04
	0.9	0.8087	0.048	0.132	62.137	170.275	1.268E-03
	1.0	0.8377	0.053	0.132	68.385	170.275	9.878E-04
	1.1	0.8471	0.058	0.132	74.515	170.275	4.114E-04
	1.2	0.8352	0.062	0.132	80.531	170.275	4.709E-04
	1.3	0.8012	0.067	0.132	86.436	170.275	3.462E-04
	1.4	0.7452	0.071	0.132	92.232	170.275	8.955E-04
	1.5	0.6685	0.076	0.132	97.924	170.275	8.751E-04

### 3.4 Experimental Errors

Experimental errors are inevitable in any experiments performed. Errors are divided into two categories, systematic errors and random errors. Systematic errors refer to systematically occurring errors which are very likely associated with the data acquisition system. In the other hand, random errors do not happen systematically in all the experimental data. In order to minimize these errors, precautionary measures were taken.

#### 3.4.1 Systematic Error

Proper calibration of the data acquisition system was essential in preventing systematic errors. For the optical data acquisition system, a slight angle between the camera lens and the quartz/square tube will contribute to a systematic error on each and every one of the recordings if left uncorrected. These were prevented by aligning the tube with the horizontal grid display in the camera's software, and repeated after a few experimental runs. The high-speed camera also produces a high frequency noise in the recordings if it was used for too long. These noises contribute to systematic errors in the flame recordings. In order to prevent this from happening, a Current Session Referencing (CSR) was performed every 10 experiments recorded, which was explained in detail in Appendix C.

On the other hand, the pressure acquisition system was prevented from having systematic errors by selecting the correct setting via the charge amplifier interface, as shown in Appendix D. Incorrect settings were proven to cause the pressure signals to have incorrect values. Care should also be taken to not disconnect the pressure transducer from the charge amplifier while powered on, since it was found to cause an overload in the charge amplifier. An overloaded charge amplifier does not recover by simply restarting the unit, instead it takes a few hours to recover. An overloaded charge amplifier will have an 'Overload' button flashing red and negative pressure readings even at ambient pressure.

### 3.4.2 Random Error

The synchronisation error originating from the pressure-flame position synchronisation appears to be a random error as observed in Table 3.1. The maximum error produced in time was observed to be the same magnitude as 1 frame of picture, which was 1/1500 seconds. The error appears to be small, and may be considered negligible.

Cross-contamination of gasses was a major contributor to random errors in the present work. Cross-contamination occurs when gas sampling bags and syringes were used for different type of gasses. Sampling bags and syringes should be labelled and used for a specific gas only.

Dilution of gas was also one of the sources of random errors. The gas bags used has a septum valve for collecting gas, similar to the one used for the injection port in the rig. Septum will wear out over time, and lose its self-sealing ability, causing a leak leading to dilution of the gas. This was one of the commonly overlooked sources of error and should not be taken lightly. Septum was replaced on both the gas sampling bags and the rig whenever an obvious sign of wear was present.

Homogeneity of the fuel-air mixture is an important aspect of the research. Random errors can occur due to overmixing as well as undermixing. A fuel mixture should be mixed for 3 minutes, no longer (overmixing), nor shorter (undermixing) to ensure a consistent mixture was obtained in every experiment.

Pilot flame ignition gets its error from the different ignition timing once the ignition port was opened. One fuel-mixture may be ignited quicker compared to another, contributing to mixture dilution as well. The orientation of the pilot flame towards the ignition port also plays a role in random errors. A consistent pilot flame orientation was kept to minimize this error. Gas related random errors listed above contributes to the calculated standard deviation of the maximum pressure listed in Table 3.2.

Based on the current methodology, a more thorough error analysis could be performed if the crucial measurements were conducted, for example, the purity of the combustible gas kept in the gas bag, the amount of oxygen in the air, the distortion caused by the lens of the camera, but these are all way beyond the capability of the author.

## 4 POST-PROCESSING

### 4.1 Introduction

This chapter presents the methods used to convert raw data (flame images and pressure signals) into useful data for comparing the different flames tested. High-speed imaging was effective in capturing the flame propagation, but an estimated total of 200,000 frames needed to be analysed. Manual analysis was time consuming and labour intensive so some sort of workflow automation was required in order to process the images.

Three, main, software programs were used in the analysis, these were: Phantom Camera Control [103], VirtualDub [104] and MATLAB [84]. Phantom Camera Control was used to prepare the raw video files for processing in MATLAB. The recorded flames were processed by automated tracking via MATLAB to obtain the flame positions as a function of time. The flame positions tracked were the flame front and flame tail, which enabled the calculation of the flame length and flame mean position. An additional parameter, the flame pixel size was also tracked in an effort to represent the flame area projection.

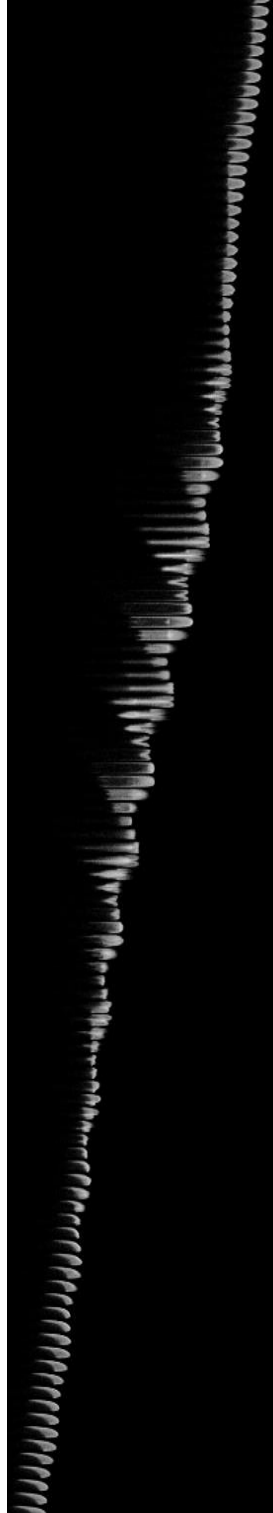
Once tracking was performed, MATLAB was once again used to process the raw data to obtain the flame distance amplitude and velocity. The distance amplitude and velocity were calculated to quantify the effect of thermoacoustic oscillations on the flame propagation. Some important parts of the distance amplitude and velocity were tabulated for comparison, which will be discussed in detail in this chapter. For simplicity, only the flame front was analysed.

In order to further analyse the thermoacoustic oscillations, the distance amplitude and velocity were put through frequency analysis to determine the temporal frequency responsible in causing the oscillations. In relating the thermoacoustic oscillations observed on the flame to the pressure signals, frequency and phase analysis was also performed on the pressure signals collected from the tube end.

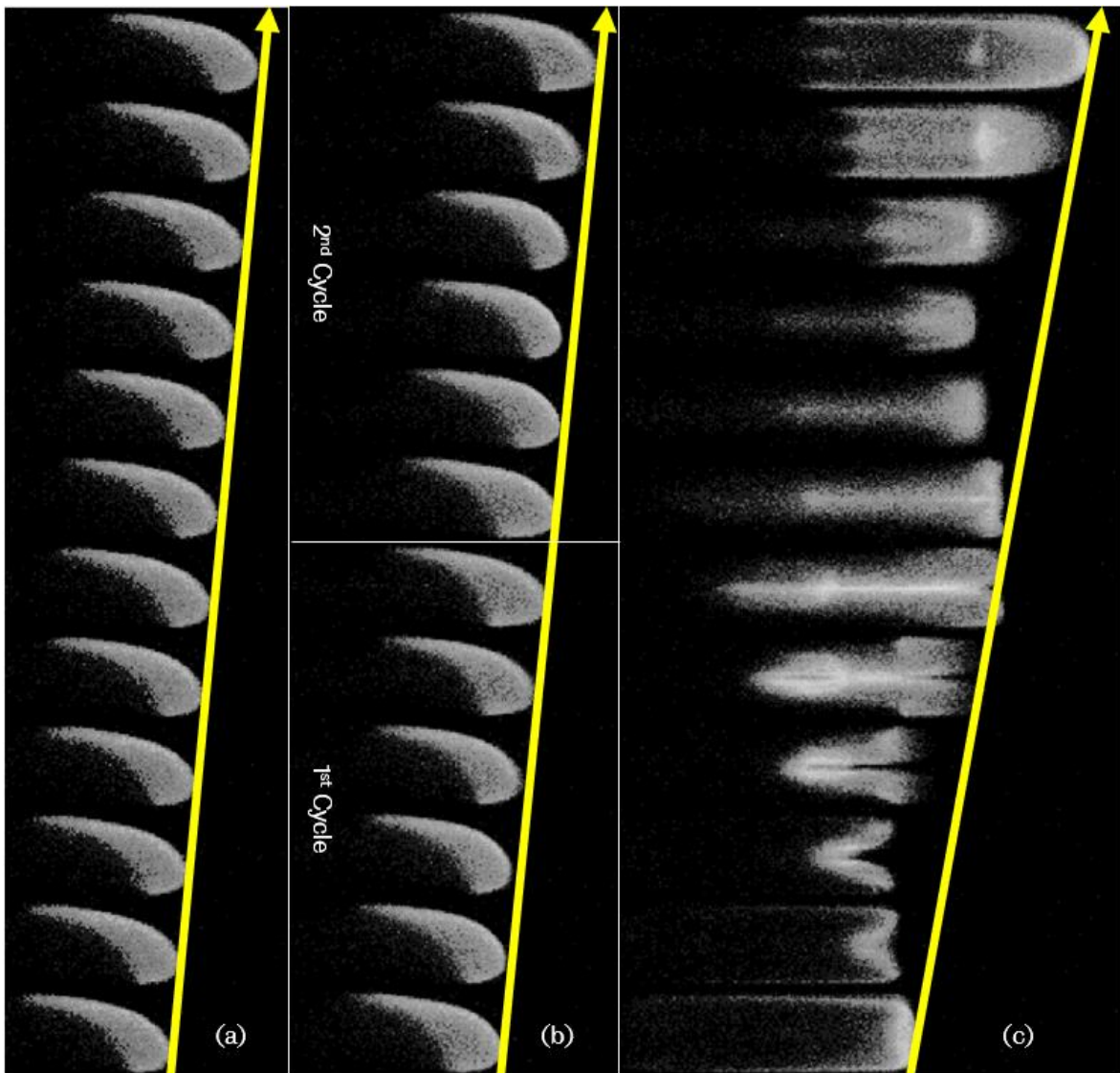
### 4.2 Flame Classifications

The flames imaged in this work is similar to those shown previously by Coward and Hartwell [3], Guenoche [4] and Searby [8]. The flame initially propagated steadily down the tube and then at some point after the flame had travelled halfway the flame was observed to oscillate for a period where the flame shape was observed to dramatically transform and then returned back to steady propagation. An example of a flame passing through all the stages is shown in Figure 4.1. The sequence of the

flame increases upwards with an interval of 0.00067s between them. The post processing, therefore, had a number of different objectives: to track the flame process down the tube and also to provide detailed measurements of how the flame shape changed.



**Figure 4.1 Typical flame propagation sequence with time increment of 0.00067 seconds for each frame upwards.**



**Figure 4.2** Sequential flame images for three types of flame behaviour: a) steady flame, b) pulsating flame and c) oscillating flame. The images are from a  $\phi = 1.2$  methane flame with  $R_H = 0.2$  hydrogen addition. Yellow lines were used to show the flame sequence, with a  $1/1500$  s increment between them upwards the column.

Shown in Figure 4.2 are examples of the different flame shapes encountered. In Figure 4.2(a) a steady flame can be seen. The flame had an almost uniform speed and shape. The diagonal yellow lines ending in an arrow shows how the flame would progress if it had constant mean flame speed. The front edge of the flame and the yellow line can be seen to match up. In the case of Figure 4.2(b) the flame encounters 2 cycles of low amplitude pressure oscillation. The overall flame shape does not change but the flame slightly slows down and speeds up as changes in the pressure within the unburned gas ahead of the flame.

In Figure 4.2(c), the flame encounters one high pressure oscillation resulting in dramatic changes in both the flame shape and its movement, taking twice the time to complete a cycle compared to the flame in Figure 4.2(b). Both behaviours are associated with pulsating and oscillating flames respectively, observed by Markstein [5] and Jost [29] in Figure 2.7. In order to characterise these oscillating flames measurements of both the flame 'size' and its dimensions were performed.

## **4.3 Raw Video Preparation**

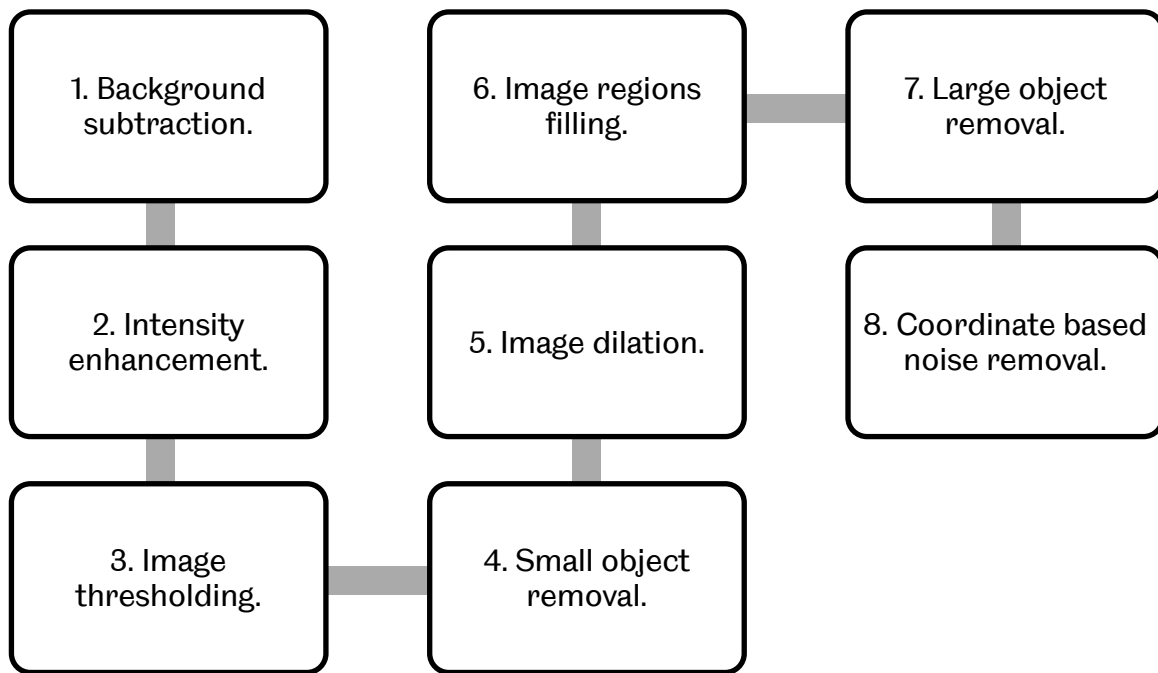
### **4.3.1 Video Cropping and Conversion**

In each high-speed film, the flame propagation typically only consisted of about 20% of the total frames captured. This came about due to the triggering system, which relied on the operator recognising a flame had propagated down the tube and triggering the system. As a result, much more data than the actual event was captured due to the variability in the 'human' response. The video length was cut using the Phantom Camera Control (PCC) [103] software by manually searching for the images where a flame could be seen. The cut file was then saved to as a .avi file format which could be read by MATLAB [84]. A cut raw version was also saved in the proprietary camera format, .cin, which retained useful information such as exposure times and times from the trigger point.

VirtualDub [104] was used in the present work for cropping the video image size before further processing in MATLAB. Videos were cropped in width and height to areas where the flame was visible, in order to reduce subsequent computation time. Most of the videos were cropped from 1028x128 pixels to 904x90 pixels. Edited videos were imported as image sequence in Bitmap format for post-processing in MATLAB, which VirtualDub conveniently numbered sequentially.

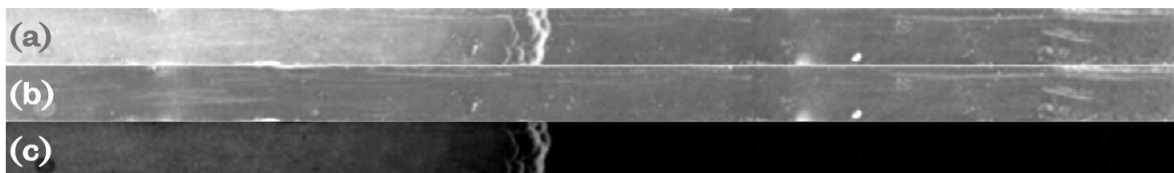
### **4.3.2 Image Denoising**

Image denoising was a challenging part of the present work. If this was not performed it was not possible to track the flame position and the flame dimension measurements became unrepresentative. A total of eight steps were taken to produce a denoised binary image, a flowchart of the process is shown in Figure 4.3, which were 1) background subtraction, 2) intensity enhancement, 3) image thresholding, 4) small object removal, 5) image dilation, 6) image regions filling, 7) large objects removal, and finally 8) coordinate based noise removal.



**Figure 4.3 Image denoising flowchart.**

The first step in denoising an image was to subtract a background from the image. There were 2 background choices, the first or final images of the sequence. The first image was chosen for background subtraction in the present work. The final image was not used due to water vapour formation on the inside walls of the tube in some cases, causing flame signal loss on the subtracted image. Figure 4.4 shows the current, starting and subtracted image, where significant removal of optical related noise can be observed.

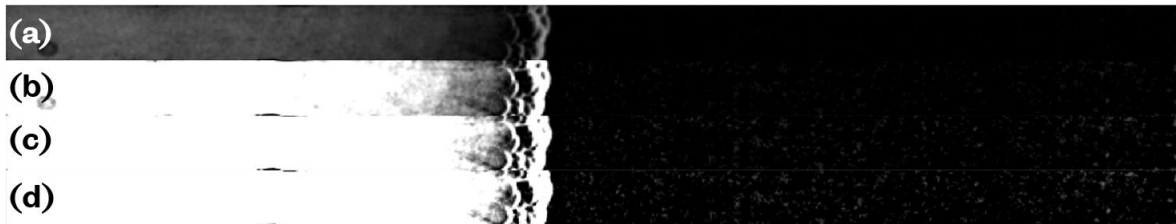


**Figure 4.4 Background subtraction. (a) Current image, (b)First image of the sequence, (c)Subtracted image.**

Following background subtraction, the image intensity was increased by enhancing the subtracted image. This step was performed to reduce flame signal loss during thresholding characterised by faint and thin flames. Figure 4.5 shows the image output for different levels of enhancement. The level used varied depending on the type of flame analysed. The bright portion behind the flame front is water vapour formation, which was the main contributor of unwanted noise behind the burned gases. For this particular flame, 5 times enhancement was used. Enhancing beyond

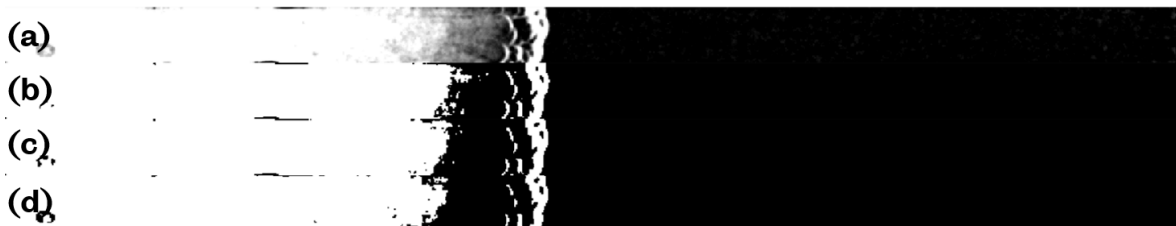


5 times resulted in unwanted noise in unburned gases and the water vapour formation pixels combining with the flame pixels.



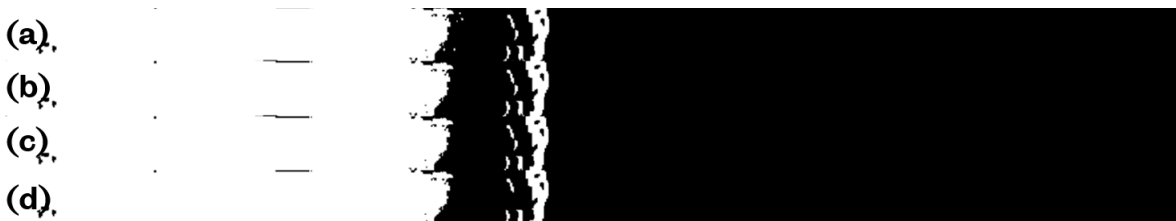
**Figure 4.5 Intensity enhancement. (a) 5x intensity. (b) 10x intensity. (c) 15x intensity and (d) 20x intensity.**

Thresholding was the next step, where a level between 0 – 1 will be defined to convert the image into a binary picture, consisting of only black and white pixels, removing all the grey pixels. Shown in Figure 4.6 are the impact of different levels of thresholding, a threshold of 0.7 was the best among the three. 0.6 and 0.8 threshold levels show unwanted noise and flame signal loss respectively, although the resulting image is relatively insensitive to the level used.



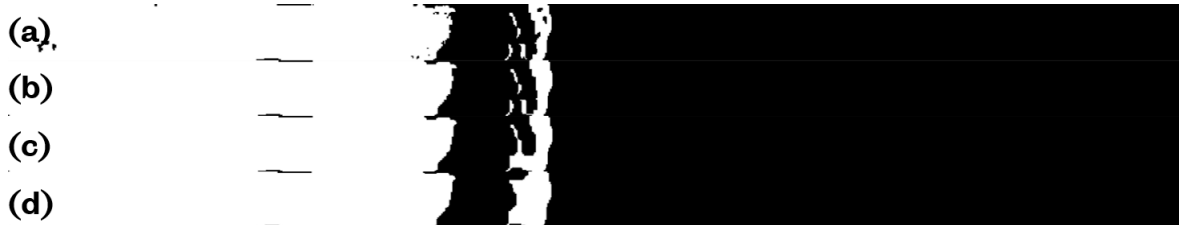
**Figure 4.6 Image thresholding. (a) Grayscale image. (b) 0.6 threshold. (c) 0.7 threshold. (d) 0.8 threshold.**

Small objects removal was then performed to remove small unwanted noise. Object removal worked by removing objects equal to or below the chosen pixel size. Shown in Figure 4.7 are the outputs for different sizes of object removal. In most cases, 5 pixels object removal displayed minimal flame signal loss, while removing the unwanted noise.



**Figure 4.7 Small objects removal. (a) Original image. (b) 5 pixels object removal. (c) 10 pixels object removal. (d) 15 pixels object removal.**

Image dilation was performed next to connect separated components of the flame which were lost due to signal loss. Dilation was performed by selecting a structuring element of a certain size, and in the present work, a disk-shaped element of pixel size 3 was used. Figure 4.8 shows the effect of different pixel sizes on the output image. It was observed that increasing the pixel size too much caused the flame to lose its original outline.



**Figure 4.8 Image dilation. (a) Original image. (b) 3 pixels disk dilation. (c) 6 pixels disk dilation. (d) 9 pixels disk dilation.**

Following image dilation, region filling was performed to fill any holes that were not filled after image dilation. This step was particularly important for propane and methane flames which had significantly larger flame area projection compared to hydrogen flames. Figure 4.9 shows the difference before and after region filling although there was no significant difference in this case.



**Figure 4.9 Region filling. (a) Original image. (b) Filled image.**

Once the main components of the flame were connected, a second object removal was performed. Unlike the first object removal, the second removal took out large areas of noise which were not connected to the main body of the flame. In the present work, the pixel size for the second removal was 50 pixels. Figure 4.10 shows the removal of some parts of the flame which were not connected to the main flame.



**Figure 4.10 Large objects removal. (a) Original image. (b) 50 pixels object removal.**

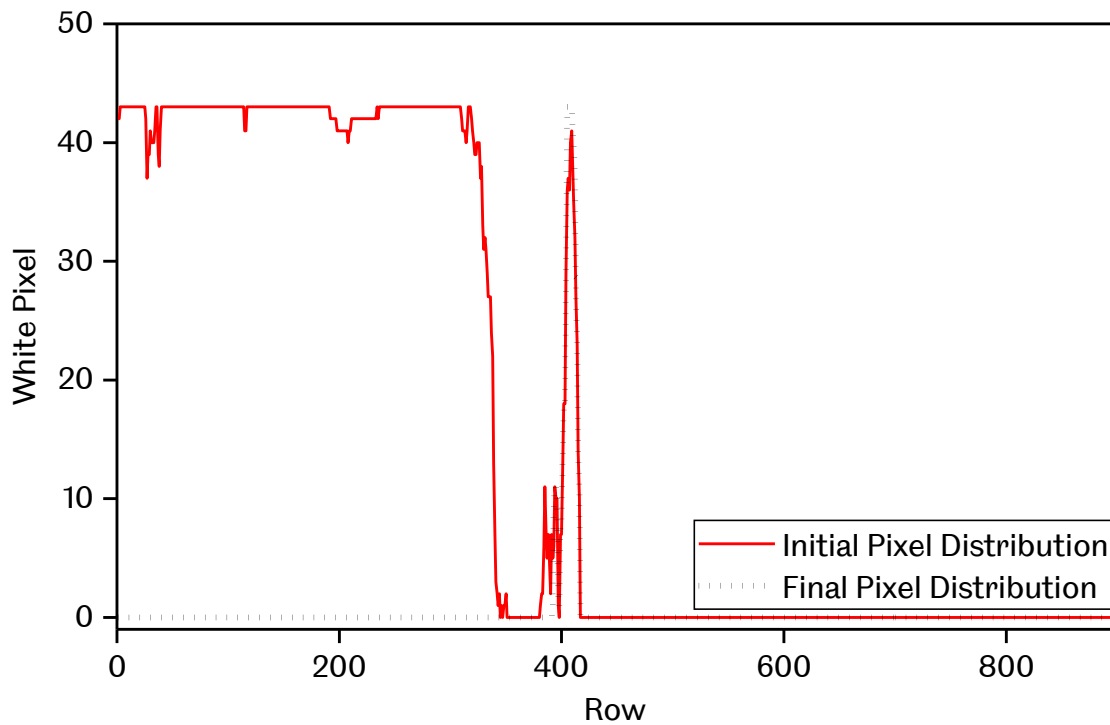
The final step for image denoising was coordinate based noise removal. MATLAB only performs this step on images with more than 2 objects. In order for this to work, no noise can be present in front of the flame, since it utilizes the coordinate of the rightmost pixel of the flame, hence the reason for the second object removal.

MATLAB then calculates centroid coordinates of all remaining bodies in the image, and keeps bodies within 30% range of the rightmost pixel. Figure 4.11(b) shows the removal of the water vapour formation behind the flame observed in Figure 4.11(a) and keeping the flame body.



**Figure 4.11 Coordinate based noise removal. (a) Original image (b) Noise removed beyond 30% of the rightmost pixel.**

Figure 4.12 shows the white pixel count before and after denoising. The denoised white pixel profile was used for further analysis.



**Figure 4.12 Initial and final white pixel count per row.**

#### **4.4 Flame Front, Tail, Mean, Thickness and Size Tracking**

Flame progression was mostly recorded by identifying the leading edge of the flame, and this reference point was used to determine the flame velocity and also for frequency analysis. The leading edge has the advantage that it is easily defined for both the natural light and schlieren images. However, the flame is a three-dimensional shape and other reference points could be defined.

If the flame shape remains the same as it travels down the tube then the velocity obtained at any reference point will be the same. However, when the flame begins to oscillate under the influence of the acoustic field its shape changes and as a result the calculated velocity of a particular reference point will be different.

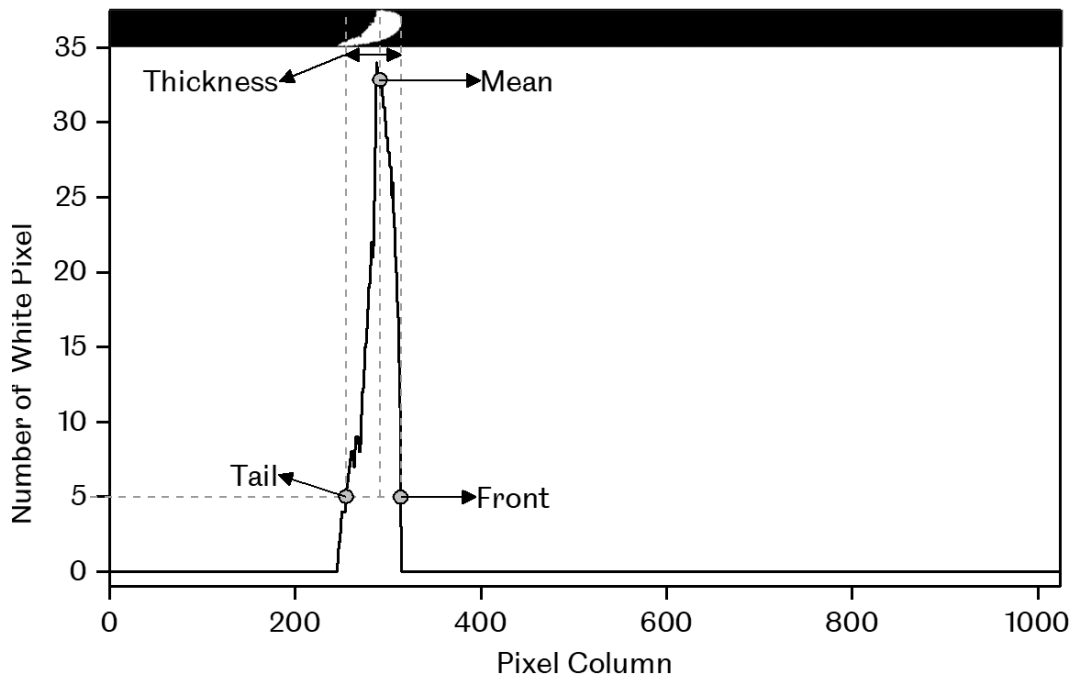
This has been shown to be an issue in the determination of turbulent premixed velocities where a variety of reference positions have been adopted depending on the experimental method used. It can be shown that the reference position found using schlieren imaging is different to that obtained if monitoring pressure resulting in different values of the turbulent burning velocity [105].

Here 3 different flame reference positions were tried on the images these are explained below and shown in Figure 4.13 at different points in the flame progress along a tube.

1. The leading edge of the flame. This was easily determined as the first point light was observed in the unburned gas for natural light images. The flame edge was generally sharp so there was little uncertainty in its value. This is the reference position adopted by previous workers [48], [95].
2. The mean flame position which was found from the binary flame images. The mean was obtained from the coordinates of the flame pixels.
3. The flame tail, which is the rear edge of the flame. This is the farthest point of visible flame within the burned gas. This could be difficult to identify as the light levels from the flame were often low as the flame is surrounded by burned gas and the edge was diffuse. This reference position is most sensitive to the threshold value selected during image processing.

In order to remove noise uncertainty from the flame front and tail, the flame front was defined as the column number with 5 white pixels closest to the unburned gas and the flame tail was the column number with 5 white pixels closest to the burned gas. The flame front and tail column number in Figure 4.13 is 313 and 256 respectively.

The mean flame position was calculated from the white pixel distribution Figure 4.13. The columns with zero value were removed, and the mean was calculated in MATLAB. The output of this process was column number 268. The flame thickness, was obtained by direct subtraction of the flame tail column number from the flame front column number. In the current case, the flame thickness was calculated to be 61 pixels.



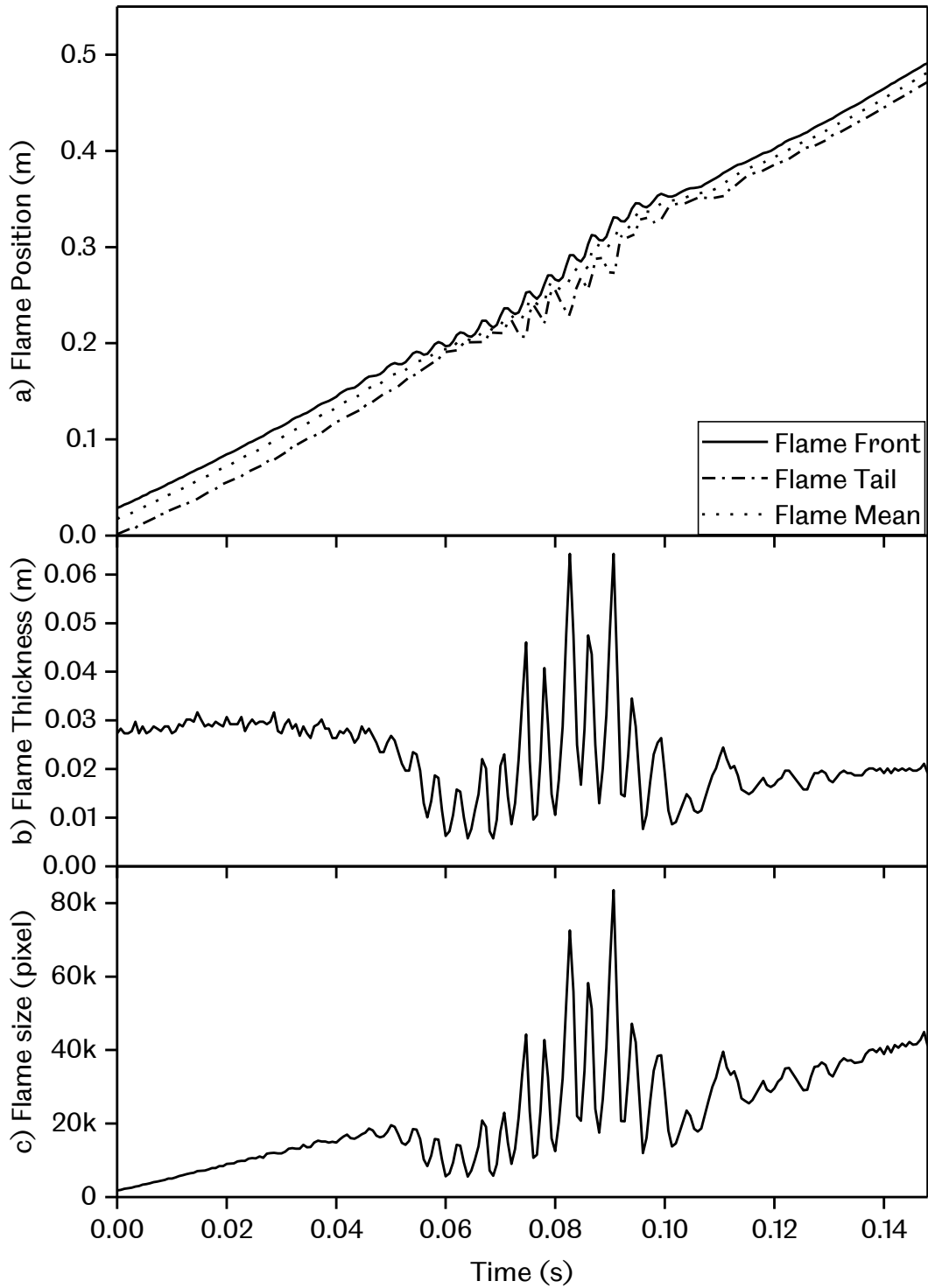
**Figure 4.13 Flame front, tail, mean and thickness definition based on white pixel count per column.**

Flame size was defined as the sum of white pixels present in each frame representing the projected flame area. Although the sum of white pixels does not provide an accurate representation of the true flame area, it is a relative measure of flame size and was easily found. The flame size was not converted into metric units to prevent confusion with the true flame area. The tracked values were multiplied with the pixel-distance conversion rate. For the case presented, the conversion rate was a constant value of  $4.8 \times 10^{-4}$  m/pixel, found by performing a calibration. This value may change if the imaging equipments were moved, which requires a calibration to be performed again.

Tracking of each part was repeated for all the frames present in a flame recording. Tracking was only performed once the flame tail was visible, preventing flame thickness and size error. Tracking was stopped once the flame front reached the final pixel of the recorded frame.

Tracked parts of the flame were plotted in Figure 4.14. It was found that the mean flame position oscillates less compared to the flame front and tail in Figure 4.14(a). Comparing the flame thickness and flame size in Figure 4.14(b) and (c), the oscillated part appeared similar, but with a different underlying value. The underlying value of the flame thickness appeared to maintain between  $\sim 0.02$ - $0.03$ m, as for the flame size, it was constantly increasing from  $\sim 0$ - $40,000$  pixels.

Upon inspection of the recorded film, the flame appeared to be slanted during the beginning of the propagation and became more finger like as it progresses down the tube, effectively increasing the flame size. The thickness however remained relatively constant. These will be further processed in the next section. The full flame tracking code is available in Appendix F.



**Figure 4.14 a) Flame positions, b) Flame thickness and c) Flame size plotted against time.**

#### 4.4.1 Flame Front Analysis

The tracked flame front was used to quantifying the magnitude of the flame oscillations. However, it was difficult to quantify these oscillations based on the flame front position alone. From Figure 4.14(a), the flame front seems to consist of a low frequency (steadily increasing component) and a high frequency component (oscillating component), thus separating the flame into oscillating and non-oscillating components seemed to be the sensible step. For this analysis, a  $\phi = 1.2$  flame with  $R_H = 0.2$  hydrogen addition will be used as an example.

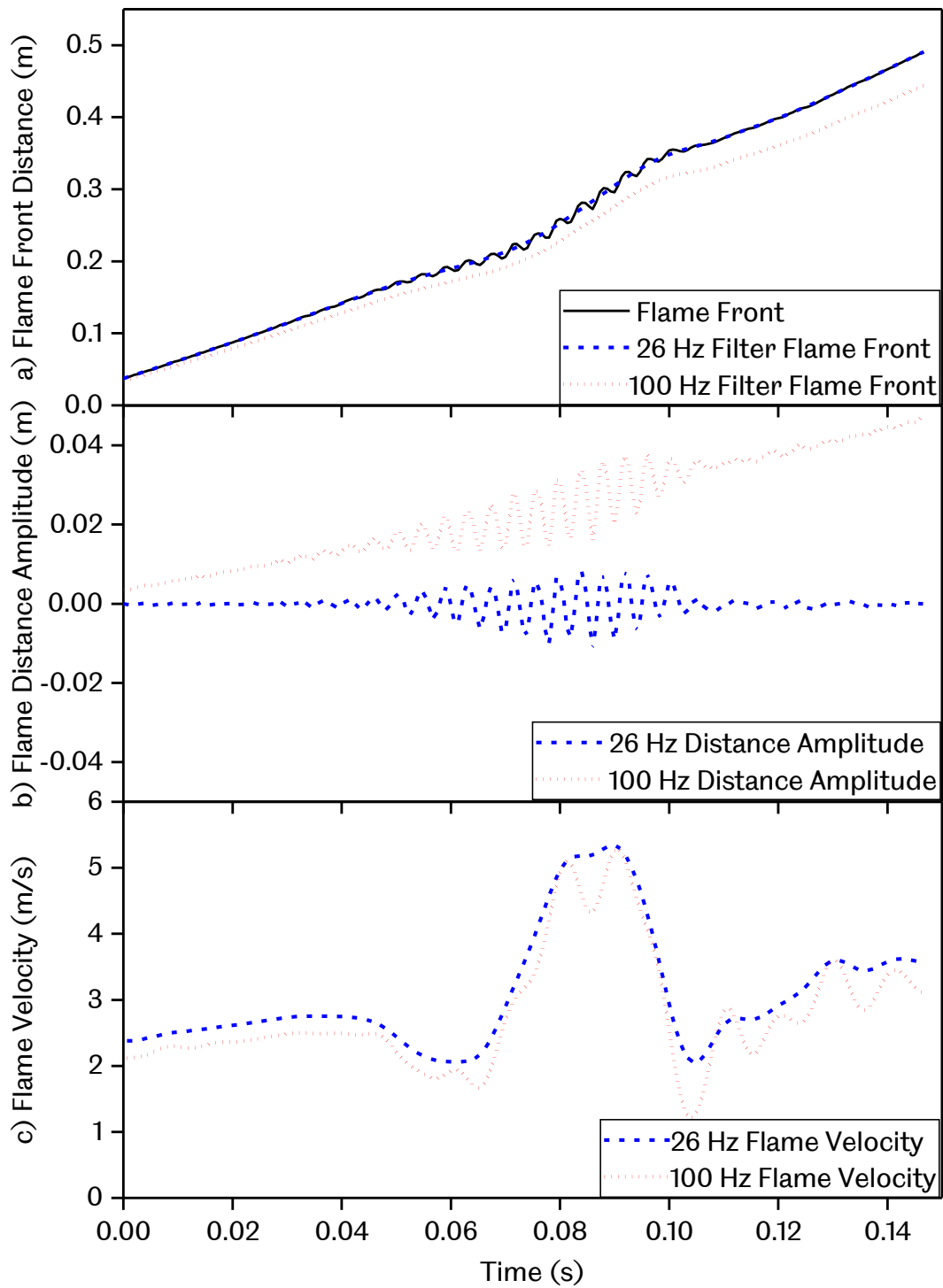
Flame positions were filtered using a low pass Finite Impulse Response (FIR) filter to remove high frequency components. A FIR filter is a commonly used filter which has a finite duration of impulse response. The stability of FIR filters was the reason it was used unlike an Infinite Impulse Response (IIR) filter [106].

Figure 4.15 shows the difference between a 26 Hz and 100 Hz low pass filter. It was observed in Figure 4.15(a) that the 100 Hz filter produced a filtered flame position which deviated significantly from the original flame position. This resulted in a distance amplitude containing low frequency components shown in Figure 4.15(b), indicated by a steadily increasing underlying value of the red dotted line compared to the 26 Hz filter, which fluctuated around the zero-axis.

Once filtered, the underlying flame front was then differentiated to obtain the underlying flame velocity (low pass velocity). The underlying velocity can be imagined as the velocity of the flame without the high frequency oscillations, in short, the overall flame speed. Interpreting the velocity change of the flame without the presence of the high frequency oscillations makes the analysis easier. The following equation was used to calculate the velocity, where  $ds$  represents the difference in displacement, and  $dt$  represents the time interval, which in this case is 1/1500 seconds, calculated based on the frame rate of the camera:

$$v = \frac{ds}{dt} \quad (4.1)$$

Figure 4.15(c) shows the underlying velocity obtained based on 2 different filters, the 100 Hz filter (31<sup>st</sup> order filter) and the 26 Hz filter (16<sup>th</sup> order filter). It was observed that the 100 Hz filter retained unwanted higher frequency components, resulting in sudden changes of velocity at -0.09 and 0.11 seconds. These sudden changes in speed are useful for a later analysis, which performs differentiation on the flame distance amplitude, to calculate the high pass velocity.



**Figure 4.15 Effects of different passband frequency on a) flame position and b) flame distance amplitude and c) underlying flame velocity.**

The filter's properties are listed in Table 4.1. The passband frequency was set at 26 Hz, with a passband ripple of 1 dB, while the stopband frequency was set to 204 Hz with an attenuation of 55 dB, to keep the frequency components below 80 Hz and remove the higher frequencies. The stopband frequency was set to 204 Hz to create



a short filter in order to accommodate data with short length. Reducing the stopband frequency created a long filter, which caused filtering errors in some cases.

**Table 4.1 Low pass Finite Impulse Response filter properties.**

<b>Filter Property</b>	<b>Value</b>
<b>Filter Order</b>	16 <sup>th</sup> Order
<b>Passband Frequency</b>	26 Hz
<b>Stopband Frequency</b>	204 Hz
<b>Passband Ripple</b>	1 dB
<b>Stopband Attenuation</b>	55 dB
<b>Sampling Rate</b>	1,500-10,000 Hz

Once filtered, the low pass flame front (Figure 4.16(c)) was then subtracted from the original flame front position (Figure 4.16(a)) to obtain the flame distance amplitude (Figure 4.16(e)), which is technically the high pass component of the flame front. Figure 4.16(b), (d) and (f) are derivatives of (a), (c) and (e) respectively, computed using equation (4.1).

Once the flame front and raw velocity were broken down into 2 parts, key parameters were tabulated for comparison with other flames: (i) underlying start velocity, (ii) maximum underlying velocity due to oscillations, (iii) maximum high pass flame front amplitude, and (iv) maximum high pass velocity. The maximum values were tabulated for the high pass flame front amplitude and velocity instead of the growth rate since the current research was leaned more towards finding the most reactive fuel mixture, which was believed to be represented better by the maximum values rather than the growth rate.

The example shown in Figure 4.16 is an oscillating flame with a clear underlying velocity peak (refer to Figure 4.16(d)). However, in some cases, the flame did not accelerate, and a value of 0 m/s was assigned for parameter (ii) if the flame did not have an underlying velocity peak. The collection of the parameters (i), (ii), (iii) and (iv) were done using the data extractor code in Appendix G.

Here, the reason for separating the flame front position into low pass and high pass components become clear. Interpreting the raw flame velocity in Figure 4.16(b) is difficult with the presence of the overshadowing high frequency oscillations. Based on the low pass velocity in Figure 4.16(d), it can be seen clearly that the flame

undergoes deceleration and acceleration due to the high pass velocity components observed in Figure 4.16(f),

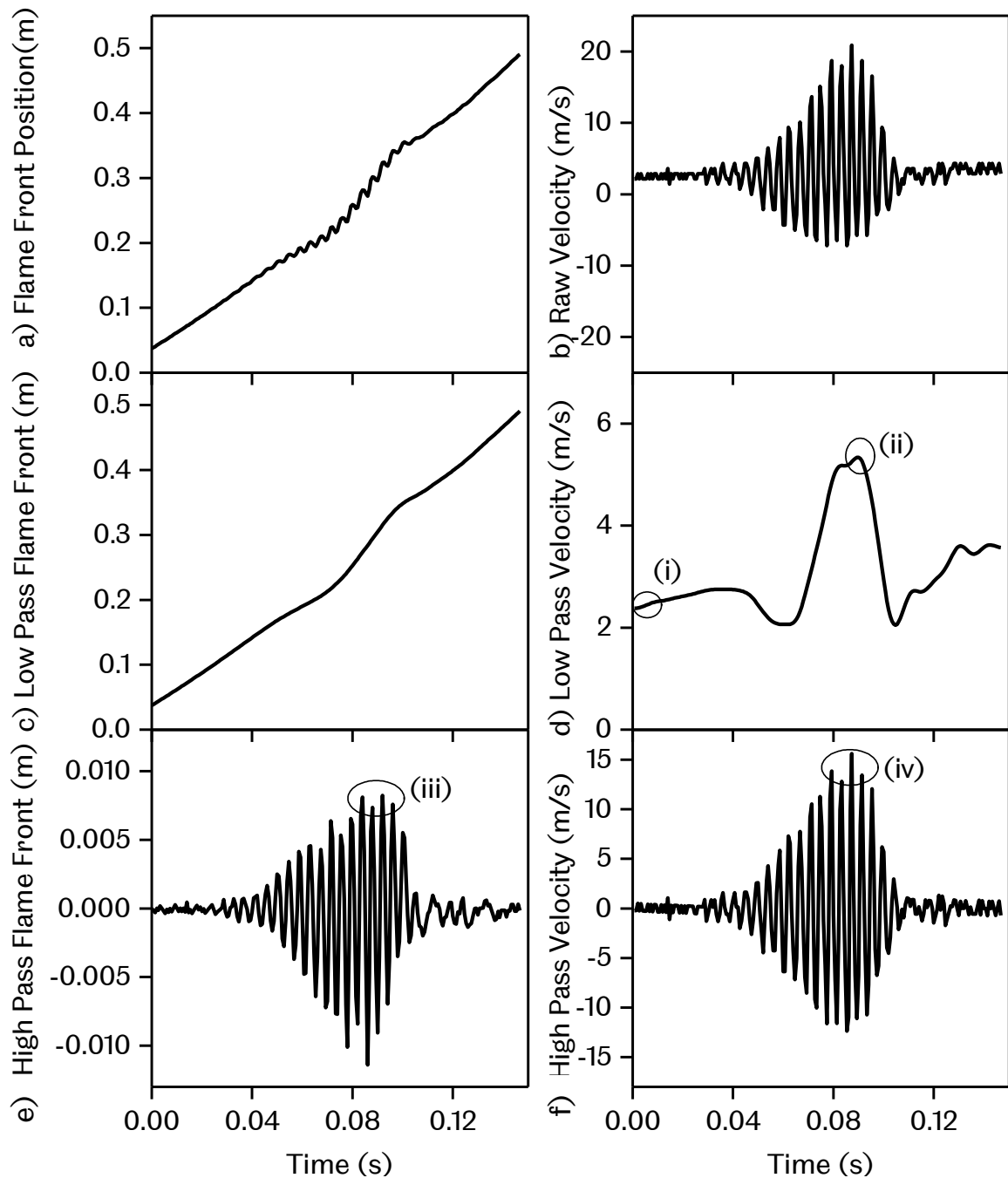


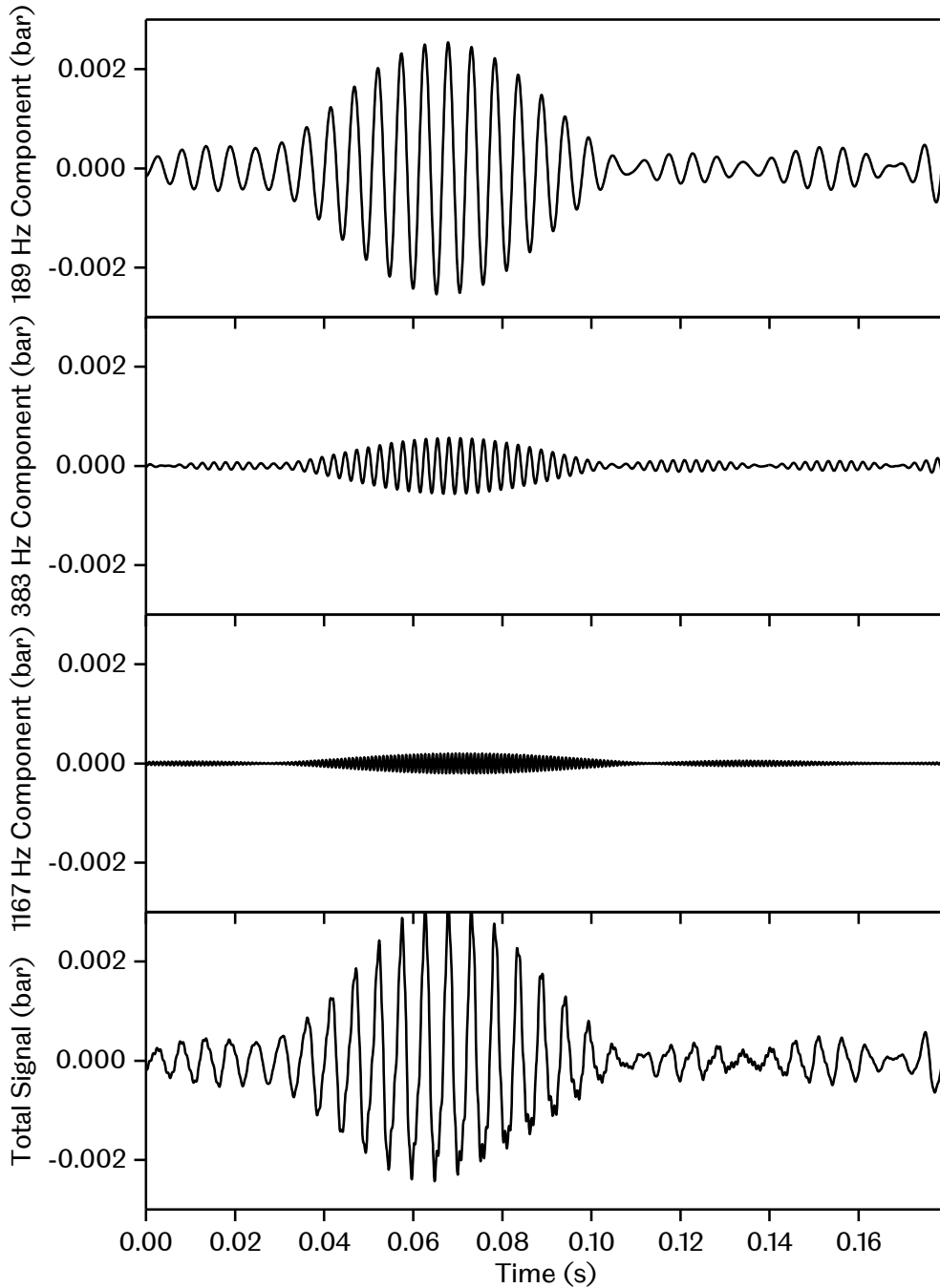
Figure 4.16 Flame front positions and their respective derivatives.

## 4.5 MATLAB Frequency Analysis

Frequency analysis played a major role in the present work. In order to understand the thermoacoustic reaction within the tube, two algorithms were used to analyse the spectral contents of pressure signal and distance amplitude of a flame, Fast Fourier Transform (FFT) and Synchro-Squeezed Wavelet Transform (SST).

### 4.5.1 Fast Fourier Transform (FFT)

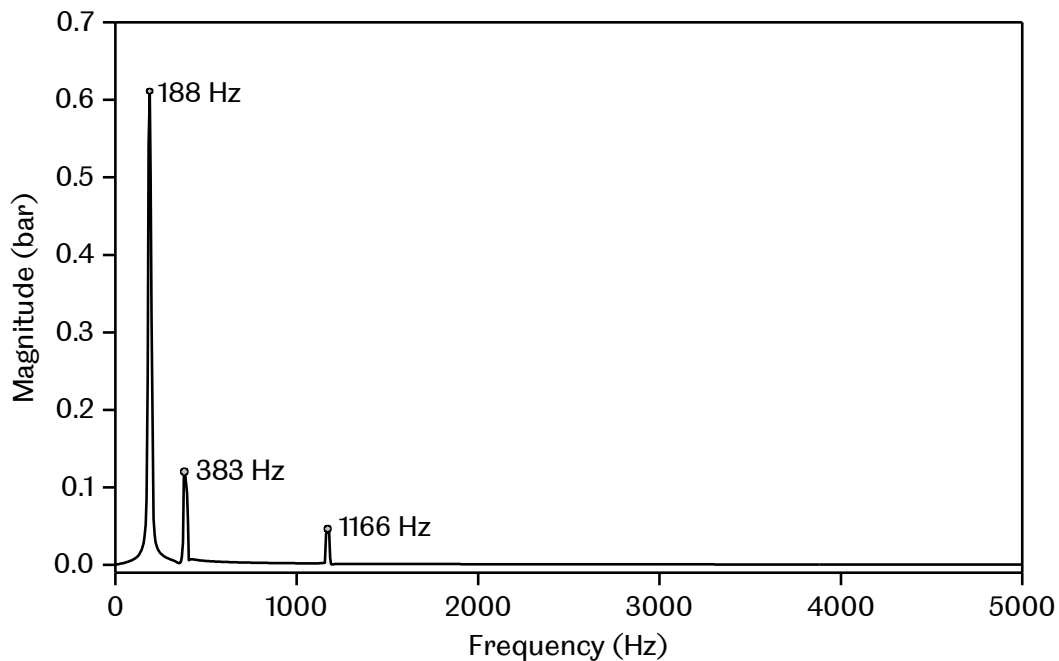
Fast Fourier Transform converts time domain signals into the frequency domain [107]. It assists in detecting the spectral contents of an analysed signal which exhibits oscillation, and is useful in detecting the dominating frequency. In order to exhibit the effectiveness of the algorithm, an artificial pressure signal composed of 3 oscillating components of different frequencies was created, shown in Figure 4.17. The artificial signal had been made up of 3 frequencies 189, 383 and 1167 Hz.



**Figure 4.17 Artificial signal original composition.**

Performing an FFT on the artificial signal produced a typical magnitude-frequency plot shown in Figure 4.18. The 3 distinct peaks observed in the plot signifies the 3 oscillating components shown in Figure 4.17. The frequency location was within 1 Hz of the frequency of the original components.

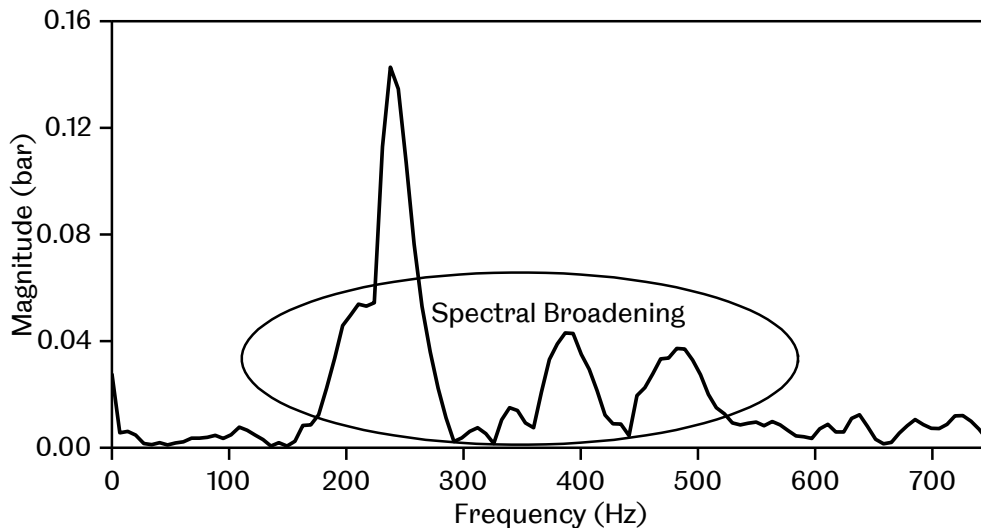
Inverse Fourier Transform (IFFT) was used to convert the signal back from the frequency domain into the time domain [107]. An inversion is necessary to separate the 3 components of the artificial signal by using a bandpass method. A bandpass method can be performed by isolating the 3 peaks in the frequency domain, and converting the 3 separated signals back into the time domain. The reconstructed time-domain signals will then be used to identify important events such as the start of the pressure growth and decay at each frequency. While effective, this method is labour intensive and time consuming.



**Figure 4.18 Fast Fourier Transform on artificial signal.**

#### **4.5.2 Synchrosqueezed Wavelet Transform (SST)**

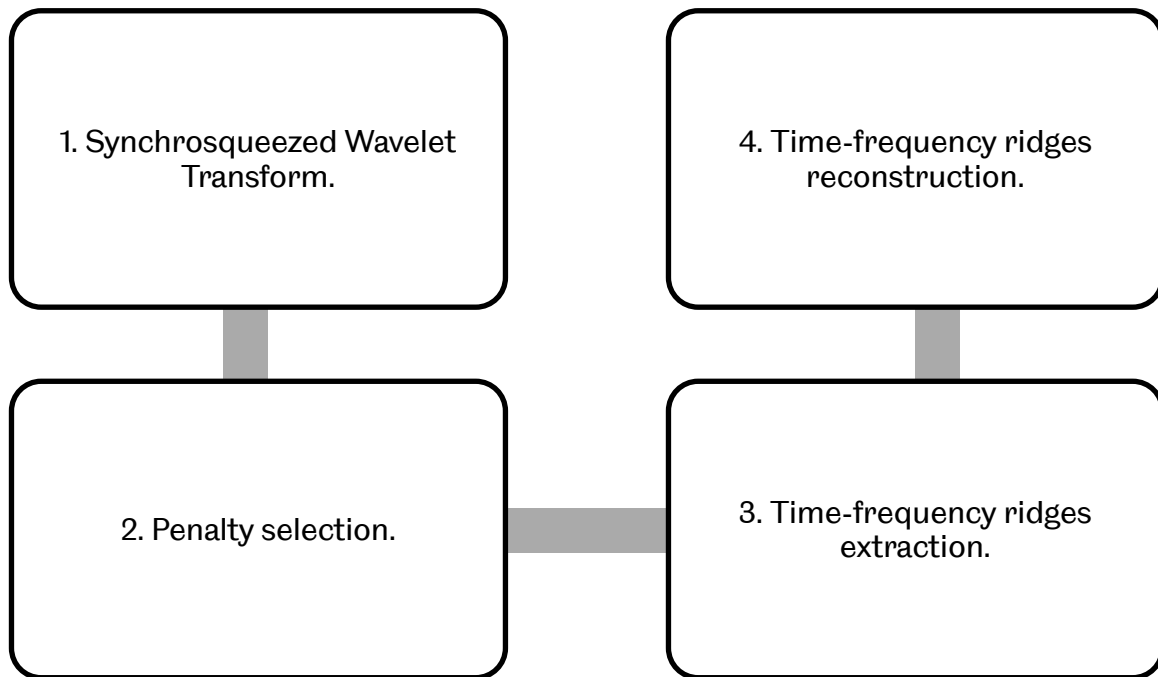
A major weakness of FFT analysis is spectral broadening of the components. The FFT plot shown in Figure 4.18 has very distinct and separated peaks since the components of the artificial signals were of a single frequency. In a typical experimental pressure signal, the oscillatory components shift around their respective harmonics with respect to time, causing spectral broadening as observed in Figure 4.19, and in certain cases, a flat frequency plateau was observed.



**Figure 4.19 Fast Fourier Transform of a  $\phi = 1.2$  methane flame with  $R_H = 0.2$  hydrogen addition, exhibiting spectral broadening.**

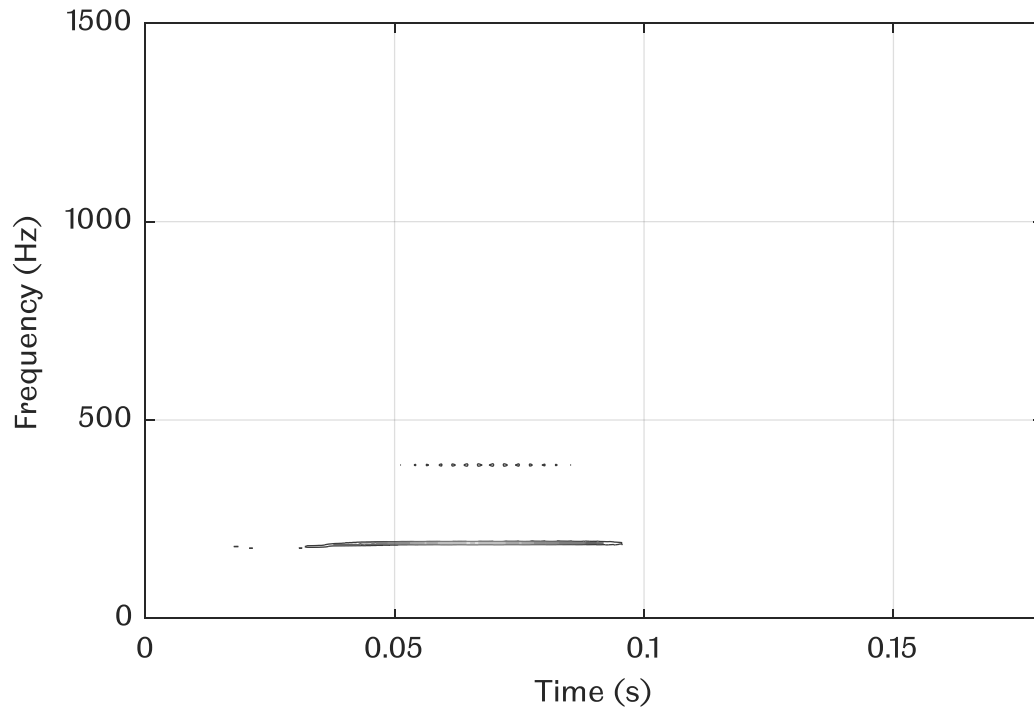
From observation of the raw data, it became evident that the flame propagation excited different resonance modes at different places along the tube, thus at a particular flame position the flame may be subjected to zero, one or two acoustically driven oscillations of different frequency and amplitude. Furthermore, as the flame propagated down the tube the temperature distribution changed resulting in changes to the excitation frequencies. As the proportion of burned gas increases it has been demonstrated that the frequency of each mode should increase [5]. A solution would have been to cut the signal into separate sections and perform an FFT on each one separately.

However the synchrosqueezed wavelet transform (SST) was found, which is a form of empirical mode decomposition tool [75]. SST provides insight into spectral contents of a signal in the time-frequency domain, by utilizing a combination of wavelet analysis and reallocation method [75]. MATLAB offers a synchrosqueezed wavelet transform workflow, which was designed to extract oscillatory modes within a signal. The extraction process consists of four important steps shown in Figure 4.20.



**Figure 4.20 Four main steps of oscillatory modes extraction via synchrosqueezed wavelet transform.**

First step of the whole process is to run the SST algorithm (equation (2.20)), on the artificial signal shown in Figure 4.17, transferring the time-domain information into the time-frequency domain information, producing a contour plot shown in Figure 4.21. Based on the contour plot, two modes of  $\sim 200$  Hz and  $\sim 400$  Hz frequency can be observed, appearing and decaying at different times. The third  $\sim 1200$  Hz component was overshadowed by the magnitude of the first 2 components. The two contours observed did not fluctuate in frequency with time, due to the fact that a constant frequency was used to generate the artificial signal. It is worth noting that the visible contours represent the region with the highest energy within the time-frequency plane, the appearance between  $\sim 0.03$ - $0.05$  seconds indicate that the oscillations were the strongest during this period.

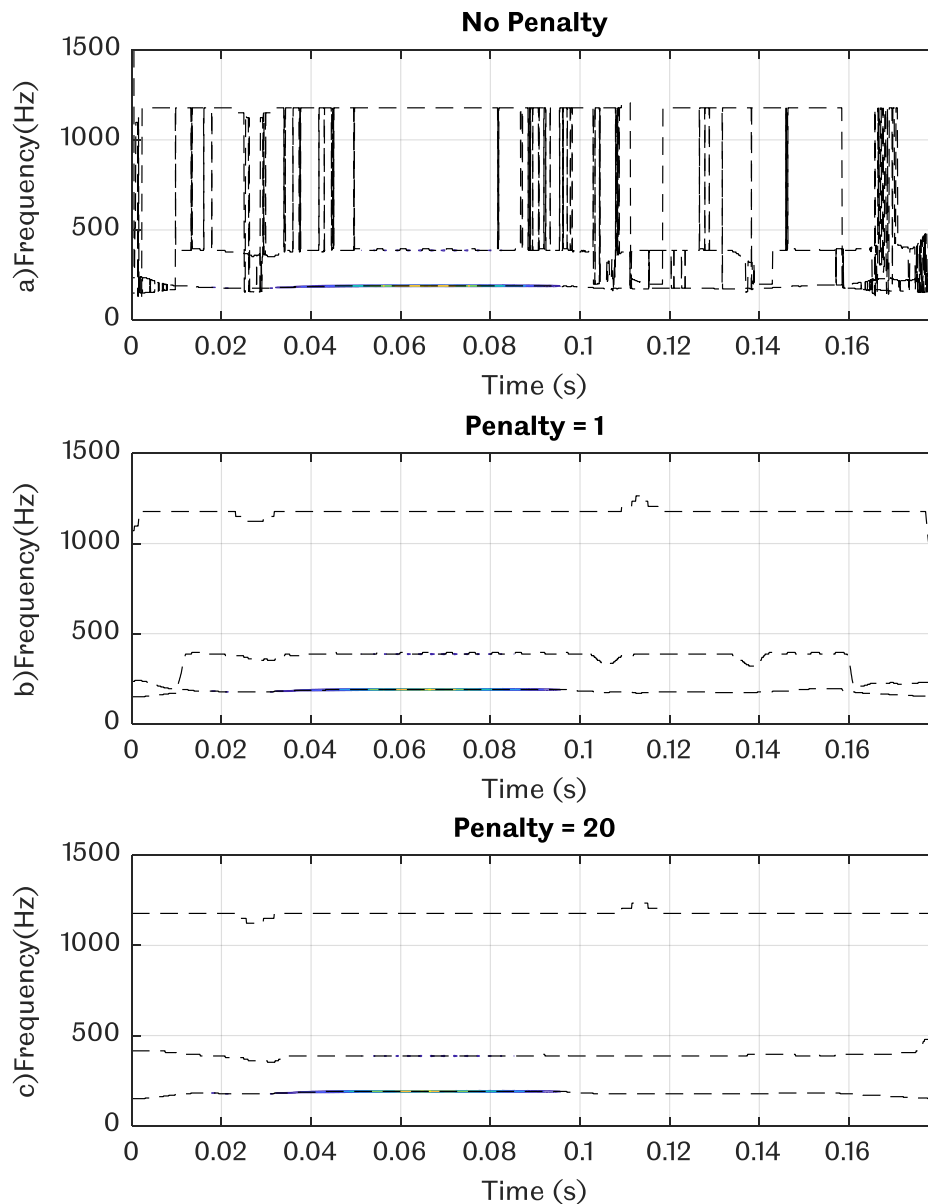


**Figure 4.21 Synchrosqueezed transform contour plot of artificial signal.**

The second step of the process is applying the correct penalty term before the third step, extracting the time-frequency ridges, which are the regions of highest energy within the time-frequency plane, indicated by the contours in Figure 4.21. A penalty term must be used to perform a ridge extraction when there are more than 1 oscillating component within a time-domain signal.

The penalty term used in this context was defined as ‘frequency bins scaling penalty’, a nonnegative scalar value, where ‘frequency bins’ are the interval between the samples in the frequency domain. The frequency interval is usually obtained from the In short, the term penalizes the shift in frequency during the detection of the region of highest energy (contours), by multiplying the penalty value with the squared distance (interval) between frequency bins [80]. For example, for a frequency bin with an interval of 3 Hz, and a penalty value of 10, the resulting penalty would be equal to 90 Hz, preventing the time-frequency ridge from jumping to another ridge within 90 Hz of its range. Further detail is available in [108].

The application of the penalty term on the contours in Figure 4.21 will be demonstrated in Figure 4.22. Three plots with different penalties applied to them are shown in Figure 4.22. The three dashed lines in each plot are known as ‘time-frequency ridges’, which are the instantaneous frequency of the 3 oscillatory components with respect to time.



**Figure 4.22 Effect of penalty levels on the formation of frequency ridges formed from a) no penalty, b) penalty = 1, and c) penalty =20.**

Assuming an interval of 4 Hz between the frequency bins, the resulting frequency penalty from the three penalties applied to the SST plot were tabulated in Table 4.2. It is worth noting that the frequency bins for SST plots are unequally spaced unlike FFT, which relies on the sampling frequency and the number of samples. For the artificial signal shown in Figure 4.21, a total of 288 frequency bins were used, ranging from ~5 – 5000 Hz, with frequency intervals ranging between ~0.13 – 117 Hz.



**Table 4.2 Resulting frequency penalty for different penalty levels.**

<b>Penalty</b>	<b>Frequency Interval, Hz</b>	<b>Frequency Penalty, Hz</b>
0	12	0
1	12	144
20	12	2880

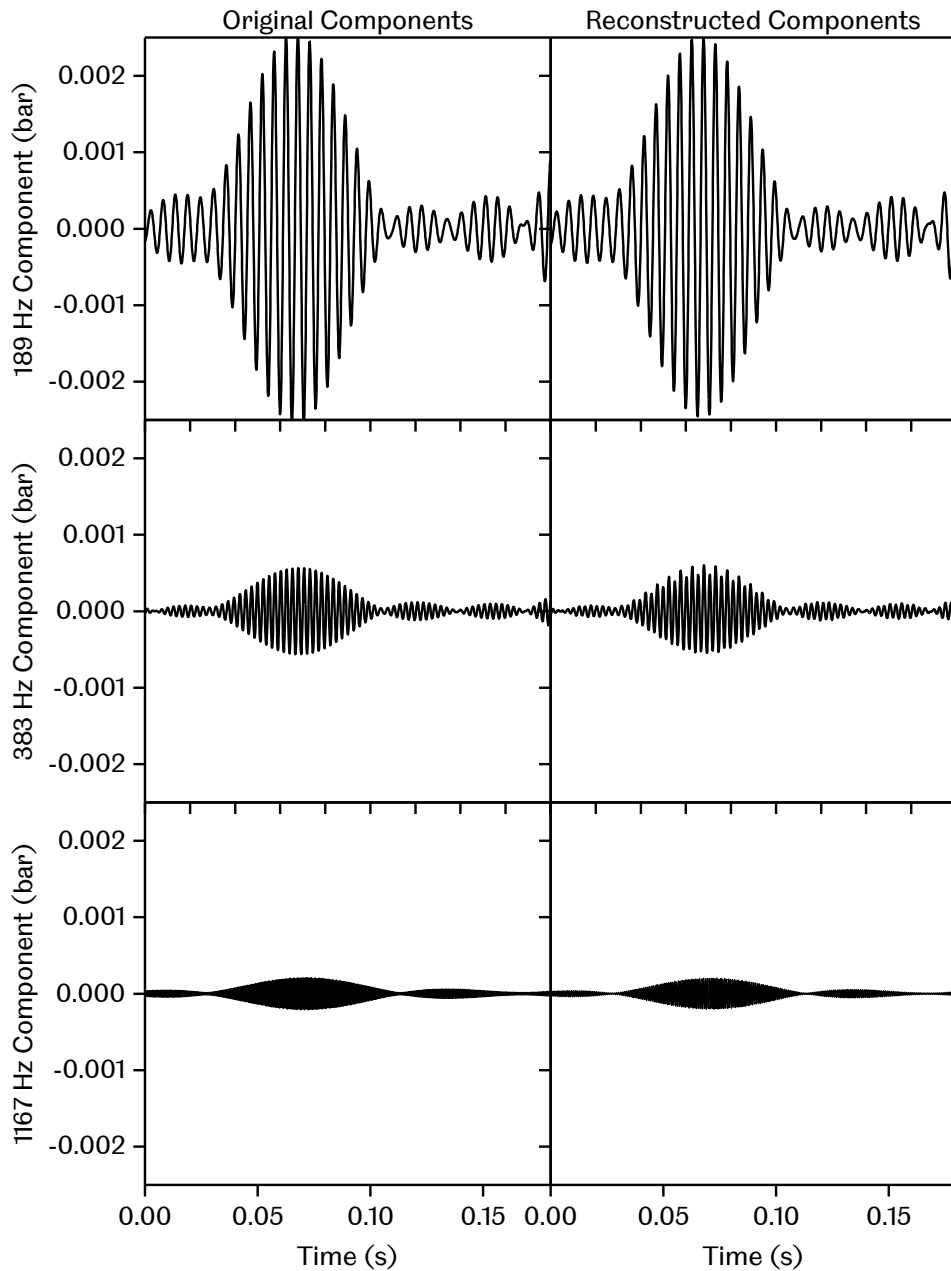
The time-frequency ridges were detected by the time-frequency ridge detection algorithm in MATLAB, which represented the 3 oscillatory components of the artificial signal. The detection algorithm was used to find the region which contains the highest energy in the time-frequency plane [108] formed by the SST in Figure 4.21.

If no penalty was used, the time-frequency ridges to jump from one mode to another, causing an incorrect reconstruction of the modes, as observed in Figure 4.22(a). Based on Table 4.2, the algorithm allows frequency jumping causing the ridges formed to intersect frequently, which will produce signals containing a wideband frequency if reconstructed, which automatically rendered the whole process useless.

Figure 4.22(b) shows the effect of using a penalty of 1, which formed significantly different time-frequency ridges compared to the non-penalized ridges. The ~1200 Hz mode was well separated from the other modes, but the ~200 and ~400 Hz modes were in close proximity at the beginning and the end. Based on Table 4.2, the algorithm penalizes frequency jumps within the 144 Hz range from the ridge, making but allowed beyond the 144 Hz range, thus the jump at the beginning and at the end. A penalty of 20 penalizes frequency jumps within the 2880 Hz range from the ridge, forming well separated time-frequency ridges, shown in Figure 4.22(c). The current work implemented a penalty of 20 in most cases.

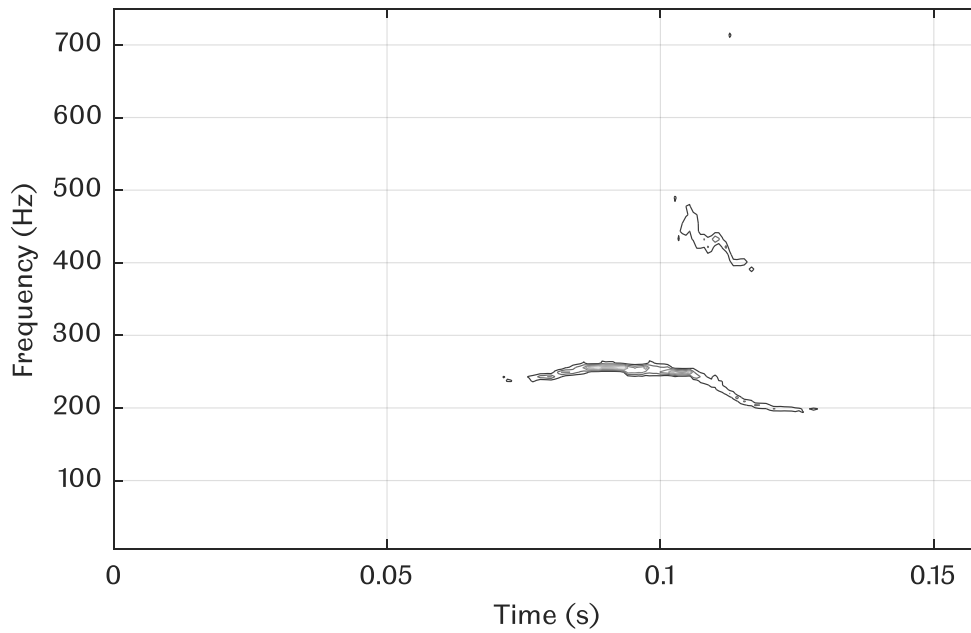
Once the suitable penalty was found, the time-frequency ridges were then extracted in step three. These extracted ridges were then reconstructed in the final step, producing three reconstructed oscillatory modes which made up the artificial signal. Figure 4.23 shows the comparison between the original components of the artificial signal and the reconstructed components. It was observed that the reconstructed signals were similar to each other. It was found that edge effects were significant with SST processing, thus symmetrical extensions on both side of the signal was performed prior to processing. The extended parts were then

cropped accordingly. The reconstructed components were tested with FFT, and the resulting peak frequency was identical to their original counterparts.



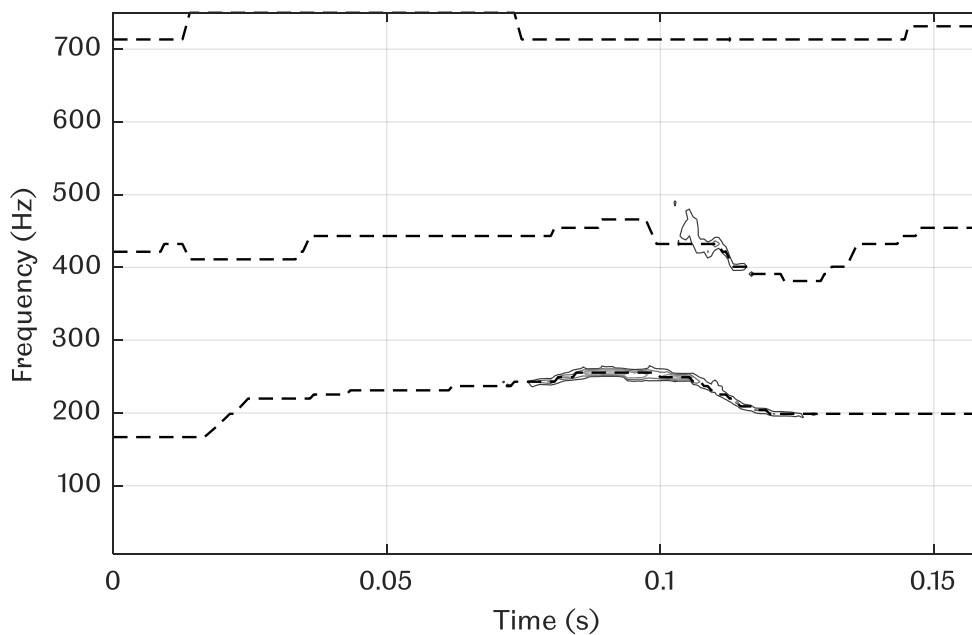
**Figure 4.23 Comparison between original and reconstructed components.**

The SST workflow was implemented on an  $R_H$  0.2,  $\phi = 1.2$  methane hydrogen flame pressure signal. Figure 4.24 shows the SST contour plot for the pressure signal. 2 distinct modes were detected based on the contour plot alone, one in the 200-300 Hz region and the other in the 400-500 Hz region.



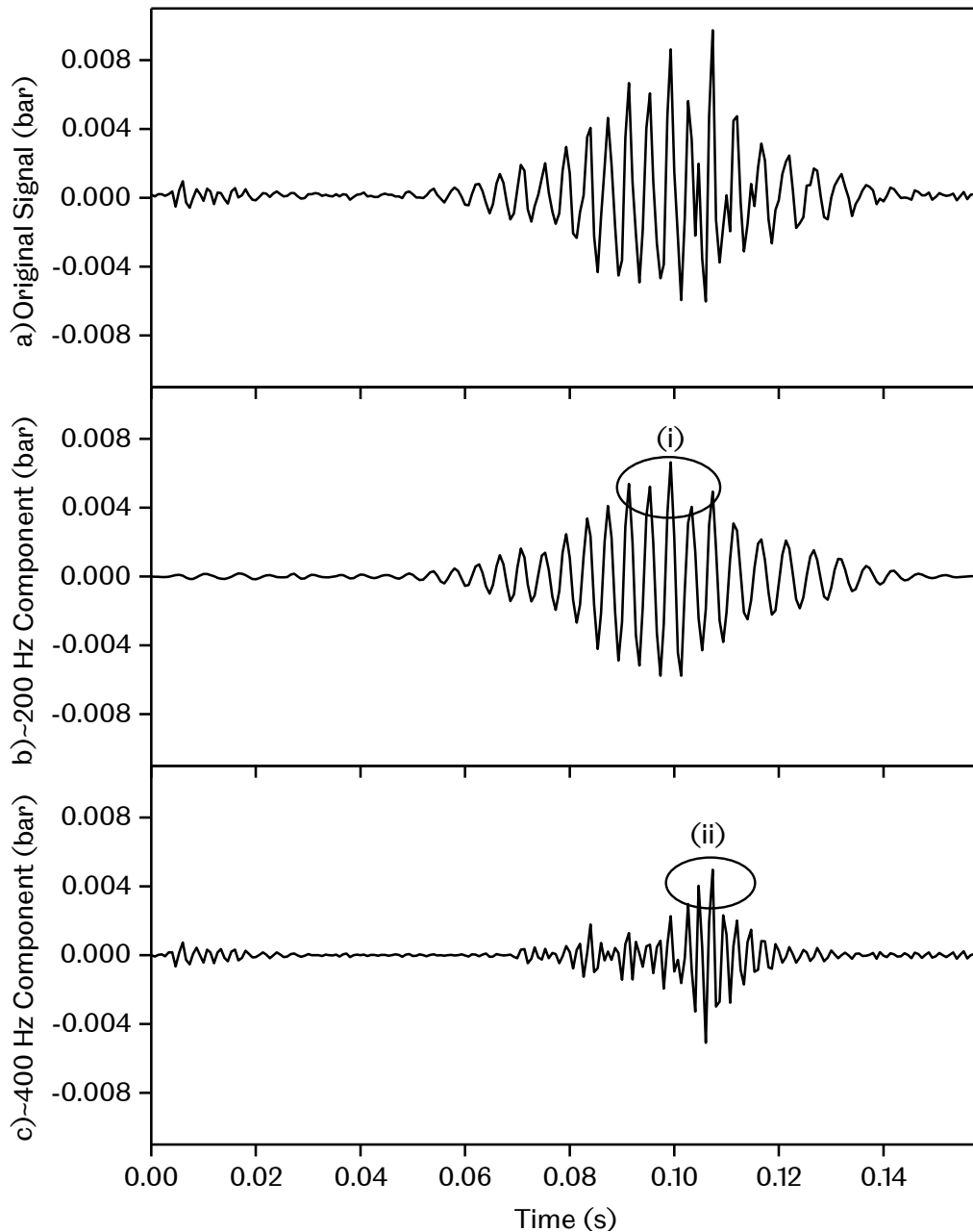
**Figure 4.24 SST contour plot of a  $\phi = 1.2$  methane flame with  $R_H = 0.2$  hydrogen addition pressure signal.**

The signal was analysed further by producing time-frequency ridges shown in Figure 4.25. A third mode was detected by the algorithm, but was clipped at the Nyquist frequency, which is half of the sampling rate of the pressure signal. The clipped mode was not analysed as it does not represent the third mode correctly. The time-frequency ridges suggest that the frequency of each mode increases and decreases at different points in time, as stated by Markstein [5].



**Figure 4.25 Frequency ridges formed from an SST penalty of 20 on a  $\phi = 1.2$  methane flame with  $R_H = 0.2$  hydrogen addition pressure signal.**

The time-frequency ridges were then converted back into their former domain via Inverse Synchrosqueezed Wavelet Transform (ISST) as shown in Figure 4.26, each having a mode frequency of  $\sim 200$  Hz and  $\sim 400$  Hz respectively. 2 parameters were collected from the reconstructed components in Figure 4.26, (i) the maximum 200 Hz pressure component and (ii) the maximum 400 Hz pressure component. The reconstructed components were then used as a thresholding criterion for further post-processing.



**Figure 4.26 Reconstruction of a) the original pressure signal into b)  $\sim 200$  Hz pressure component, and c)  $\sim 400$  Hz pressure component of a  $\phi = 1.2$  methane flame with  $R_H = 0.2$  hydrogen addition. Two parameters collected, i) maximum  $\sim 200$  Hz pressure and ii) maximum  $\sim 400$  Hz pressure component.**

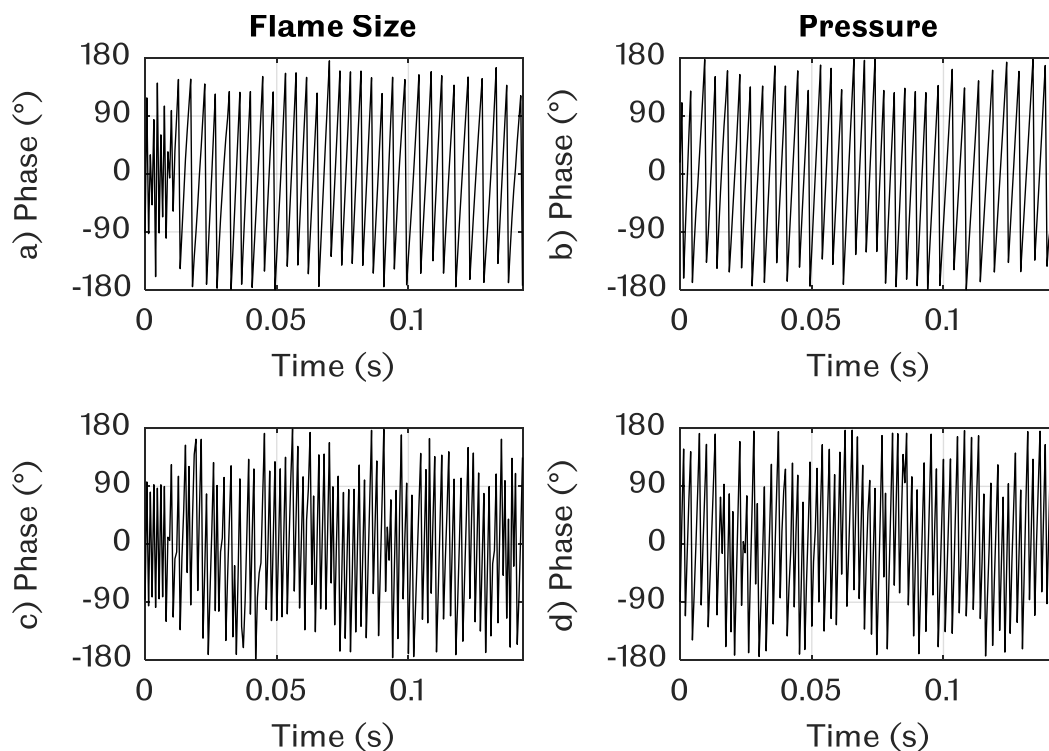
### 4.5.3 Phase Study

The sudden acceleration of confined premixed flames were often associated with thermoacoustic interactions [109]. In order to study the relationship between the pressure signal and the heat release, a phase study was conducted between the pressure signal and the flame size. It was discussed earlier that the flame size is a 2-dimensional projection of the flame, used to represent the flame's heat release, which is usually defined by the amount of heat released by the flame. A Hilbert Transform on the time domain pressure and flame size signals was used to obtain their instantaneous phase. Once the instantaneous phase was obtained, the phase difference between the signals was calculated and plotted against the pressure signal to determine the relationship.

The phase of a signal comes from the imaginary part of the signal. This proved to be a problem with the experimental data as both the pressure and flame front position only contain real parts. The Hilbert Transform generates the imaginary parts by performing a quarter-cycle time shift on the signal, see Smith [92].

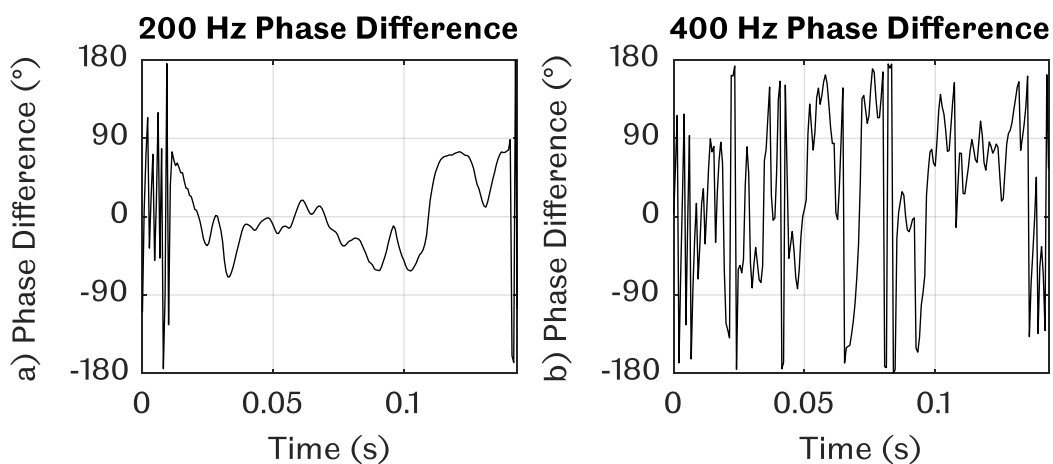
Prior to performing a Hilbert Transform, it was essential to filter the signal with a bandpass filter to remove the unwanted frequency bands, see Cohen [72]. Based on the FFT plot in Figure 4.19, a wideband of frequency exists in the pressure signal, and each frequency has their individual phase. In order to analyse the phase of a particular band, the other frequencies need to be filtered out to remove the unwanted phase information.

In the current study, because of the existence of the ~200 Hz and ~400 Hz components, the signal needed to be bandpass filtered into 2 different components. Here the ISST was used to reconstruct the two oscillatory modes, shown in Figure 4.26. Four phase plots were produced: ~200 Hz and ~400 Hz flame size phase plot, ~200 Hz and ~400 Hz pressure phase plot, shown in Figure 4.27, each displaying the expected sawtooth wave shape, which signifies the phase angle of a sinusoid with respect to time.



**Figure 4.27 Instantaneous phase plots for a) 200 Hz flame size component, b) 200 Hz pressure component, c) 400 Hz flame size component, and d) 400 Hz pressure component.**

The phase difference between the oscillatory components were calculated by direct subtraction between the oscillatory modes, 200 Hz flame size phase subtracted with the 200 Hz pressure phase, and repeated for the 400 Hz component. Figure 4.28 shows the phase difference between the pressure signal and the flame size signal for both the 200 Hz and 400 Hz components.

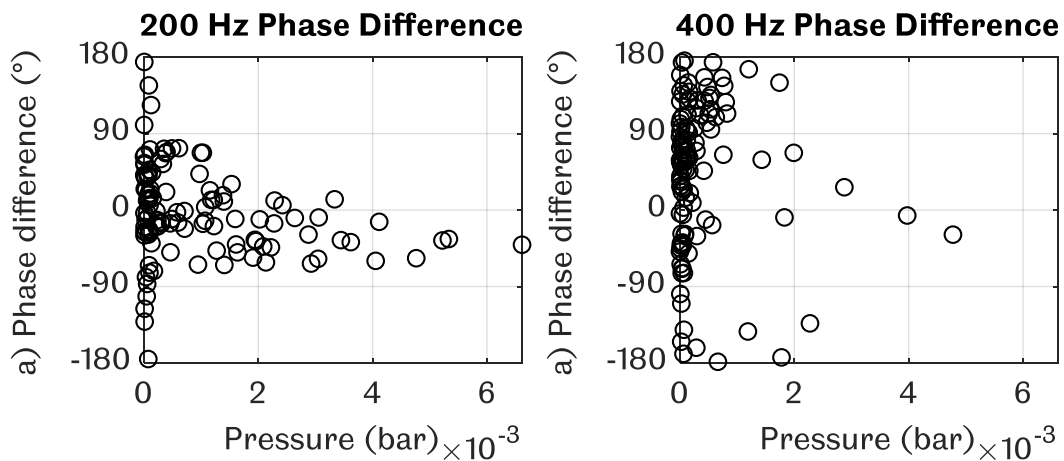


**Figure 4.28 Phase difference of a) 200 Hz components and b) 400 Hz components.**

The 200 Hz components were observed to have a period of phase locking where the phase difference maintained at  $\sim 0^\circ$ , indicating that the signals were oscillating at the same phase. From Figure 4.28(b), the 400 Hz components displayed no phase locking as the phase difference plot was fluctuating throughout the whole duration.

Phase locking phenomenon between two signals usually indicates the formation of a feedback loop that increases the vibration of a system [109] and Rayleigh [12] described that whenever heat is added to a compressed air, or when heat is taken away from a rarefied air, vibration will be encouraged, and if the opposite happens, vibration will decay. In order to test this theory, it would be sensible to plot the phase difference against the pressure of oscillation.

Figure 4.29(a) shows the relationship between the phase difference and the 200 Hz pressure component. It was observed that the pressure was amplified the most at a phase difference of  $0^\circ$  which confirms the statement made by Rayleigh [12] regarding phase locking. Figure 4.29(b) displayed the expected behaviour for a non-phase locking interaction as observed in Figure 4.28(b).



**Figure 4.29 Phase difference vs pressure of oscillation for a) 200 Hz components and b) 400 Hz components.**

## 5 EXPERIMENTAL RESULTS

### 5.1 Introduction

Results for natural light experiments will be presented here. Methane and hydrogen were mixed systematically using the  $R_H$  method and burned in an open-ended horizontal tube. The main objective was to study the change in flame propagation behaviour as hydrogen content was increased systematically. Majority of the results are presented in graphical form to summarize the findings. Numerical values of the figures can be found in the Appendices.

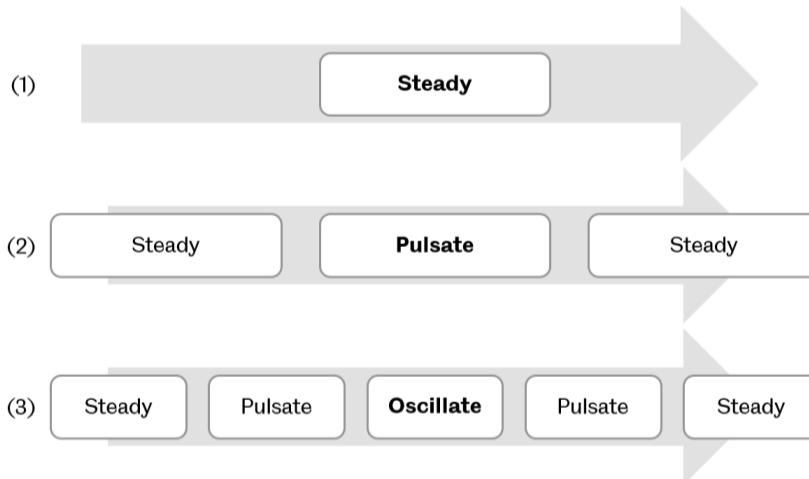
The discussion of results will start with the effect of equivalence ratio and hydrogen addition. The former will discuss the effect of increasing the equivalence ratio while keeping the  $R_H$  constant, whereas the latter discusses the effect of increasing the RH while keeping the equivalence ratio constant. Another additional section will compare three flames with approximately equal laminar burning velocities. All sections will cover the analysis of both tracked flame parts and pressure data. The analysis includes postprocessing and a breakdown of the raw data, which enabled a phase study to be conducted.

The three initial sections cannot summarize the entire experimental data of the present work. Contour plots were used to aid in summarizing the entire data set, starting with tracked flame parts analysis, followed by the pressure analysis. Both sections will then be analysed together to find the relationship between the primary data.

Flame propagation in tubes had been studied in the past, and categorized into 3 different categories by Markstein [5]. The 3 different categories were: (1) steady flames, (2) pulsating flames, and (3) oscillating flames. Similar behaviours were observed in the current study, where all flames fall into either one of the categories.

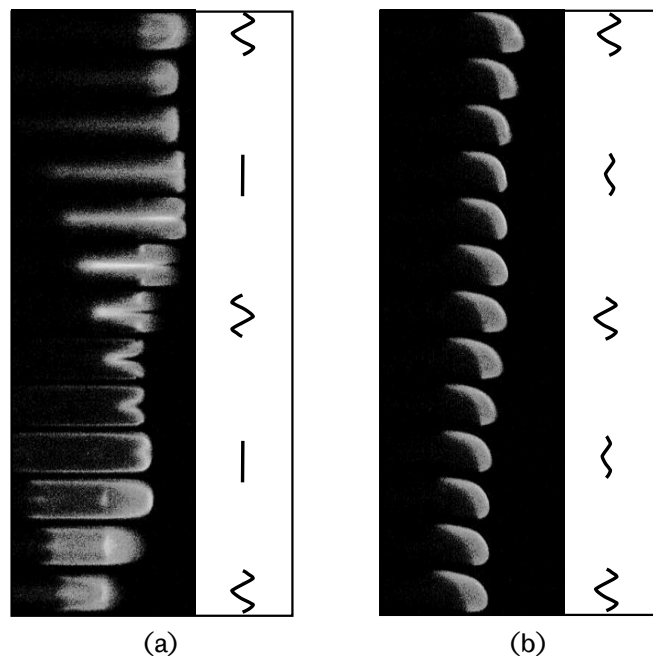
Figure 5.1 describes the normal sequence of flame behaviour. The steady flame is a subset of the pulsating flame, and the pulsating flame is a subset of the oscillating flame. However, this sequence of behaviour should not be used to generalize other flame tube experiments as they are highly sensitive to boundary conditions. Taking work by Searby [8] as an example, his observed flame behaviour vary from the current study since his flame tube was configured to propagate downwards towards a closed end, causing the flames to end as a non-steady flame.





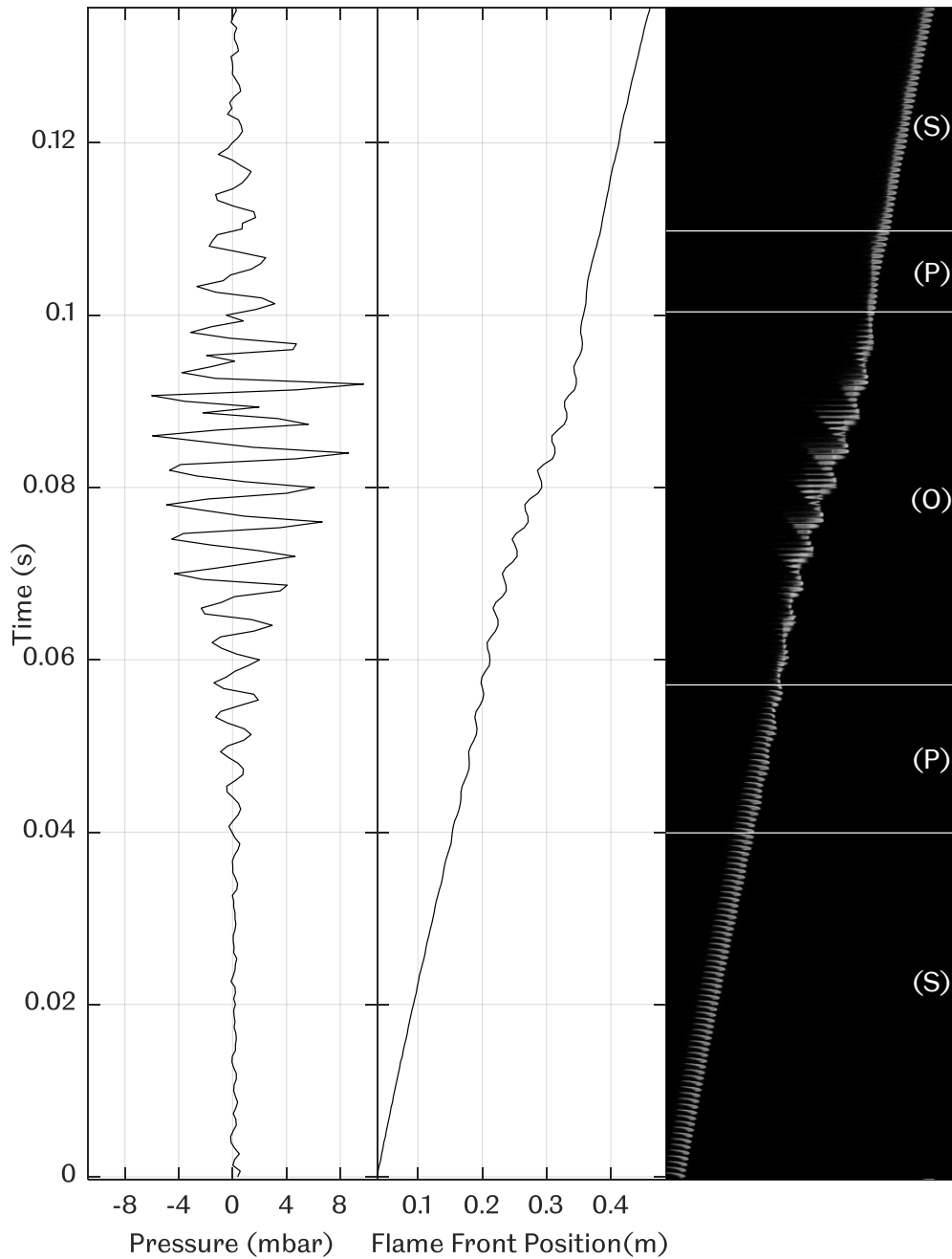
**Figure 5.1 Sequence of flame behaviours, 1) steady flames, 2) pulsating flames, and 3) oscillating flames.**

A comparison between the flame structure described by Markstein [5] in Figure 2.7, with real flame images were shown in Figure 5.2. In Figure 5.2(a), the oscillating flame was observed to flatten from its initially convex shape, which proceeded to become inverted structurally, before flattening and becoming convex again. As for the pulsating flame in Figure 5.2(b), the flame did not flatten from its initially convex shape, but instead maintained its convex shape with a slight reduction in length. Based on the pictures, the oscillating flame took twice the time to return to its convex shape compared to the pulsating flame. These were consistent with the observations made by Markstein[5].



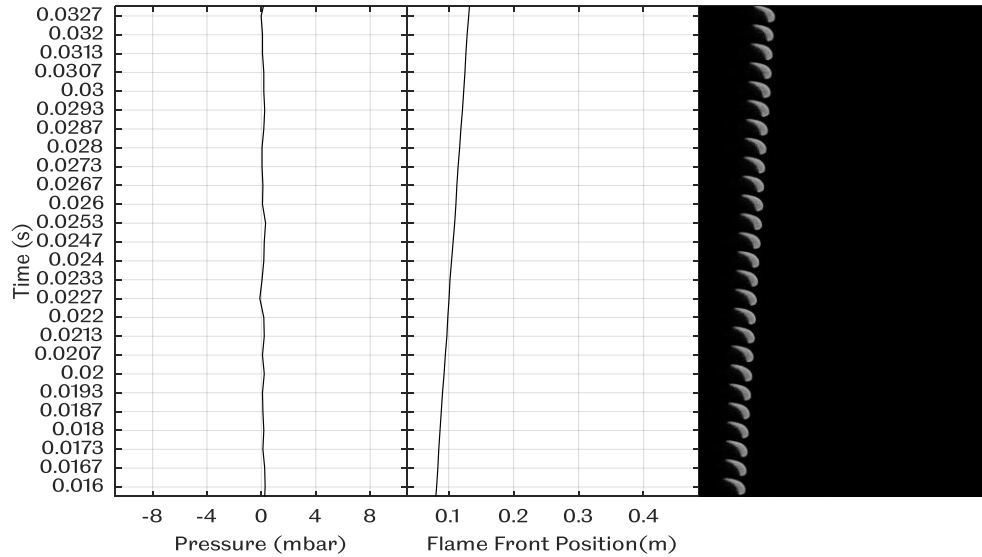
**Figure 5.2 Comparison between real flame images with flame structures described by Markstein[5] in Figure 2.7, for a) oscillating flames and b) pulsating flames.**

Figure 5.3 shows an example of an oscillating flame. The flame initially propagated as a steady flame until  $\sim 0.04$  seconds, before it starts to pulsate between  $\sim 0.04$  seconds to  $\sim 0.058$  seconds. Pulsation was accompanied with a slight increase in pressure fluctuation, reaching  $\sim \pm 3$  mbar. The flame then starts to oscillate until  $\sim 0.1$  seconds. During this period, the tube end pressure tripled to  $\sim \pm 9$  mbar at  $\sim 0.09$  seconds, and reduced back to  $\sim \pm 3$  mbar. The decrease in pressure made the flame return to its pulsating state. The pressure further decays and the flame changed back to a steady flame.



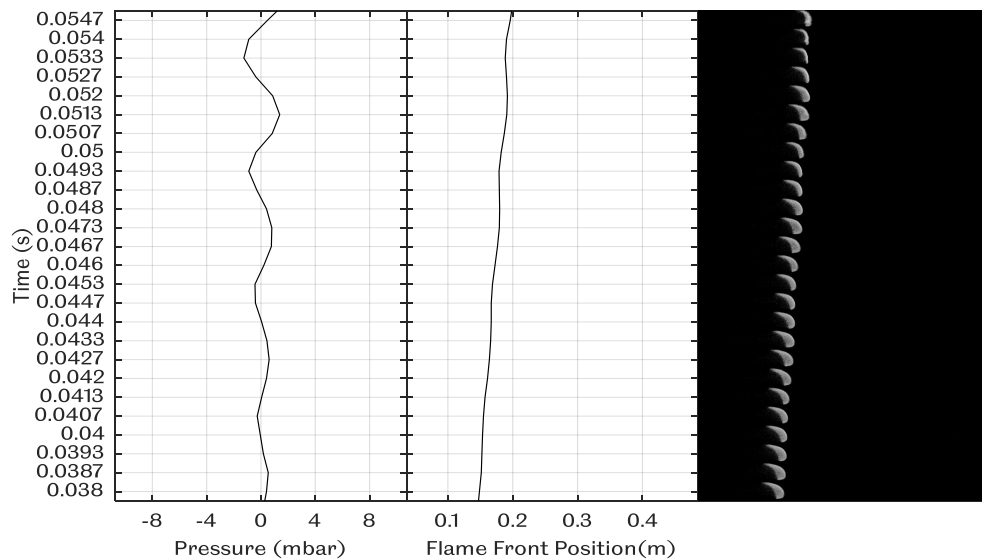
**Figure 5.3 Image sequence of the propagation of an oscillating  $R_H 0.2$ , 1.2 equivalence ratio flame along with pressure and flame front position.**

Figure 5.4 shows the image sequence of a steady flame. The tube end pressure stayed almost constant with minimal oscillations while the flame front position increases steadily during this period. Minimal changes were observed in the flame shape and length.



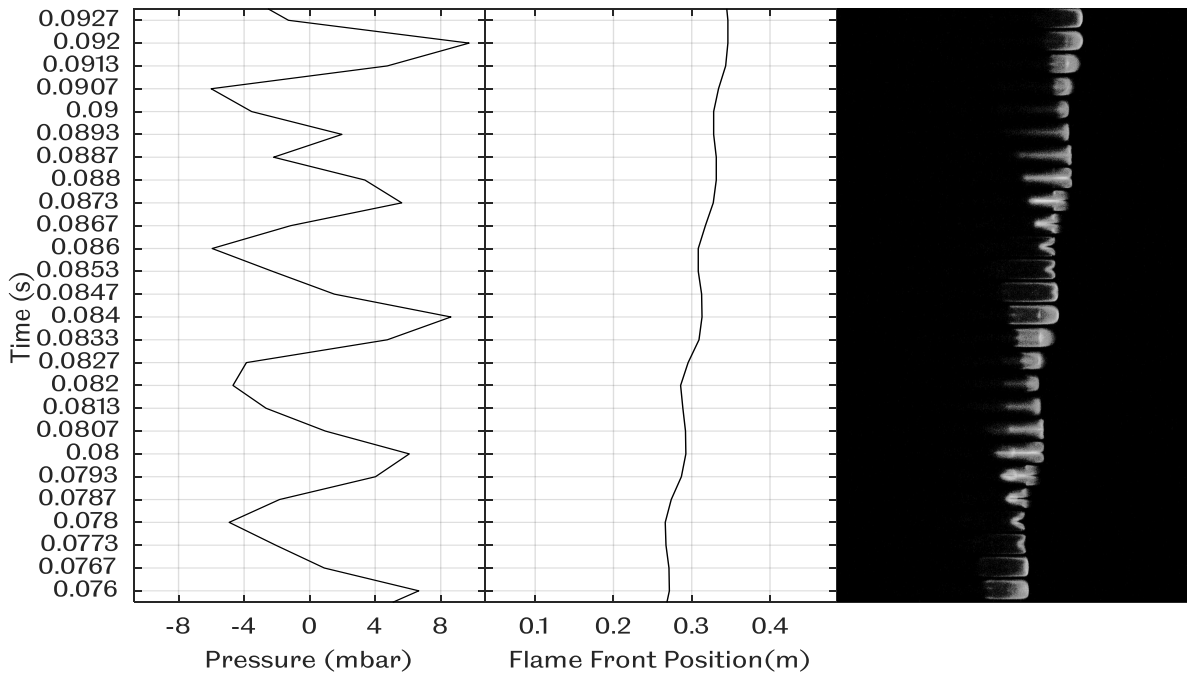
**Figure 5.4 Image sequence, pressure signal and flame front position of a steady flame.**

Figure 5.5 describes the pressure, flame front position and the image sequence of a pulsating flame. The pulsating behaviour was initiated by a slight increase in pressure fluctuation, which gradually builds up. Increase in pressure fluctuation led to the gradual reduction of the flame length, which changes the flame shape from an asymmetrical shape to a fairly symmetrical shape at 0.0547 seconds. The flame front position was observed to fluctuate more as the pressure builds up.



**Figure 5.5 Image sequence, pressure signal and flame front position of a pulsating flame.**

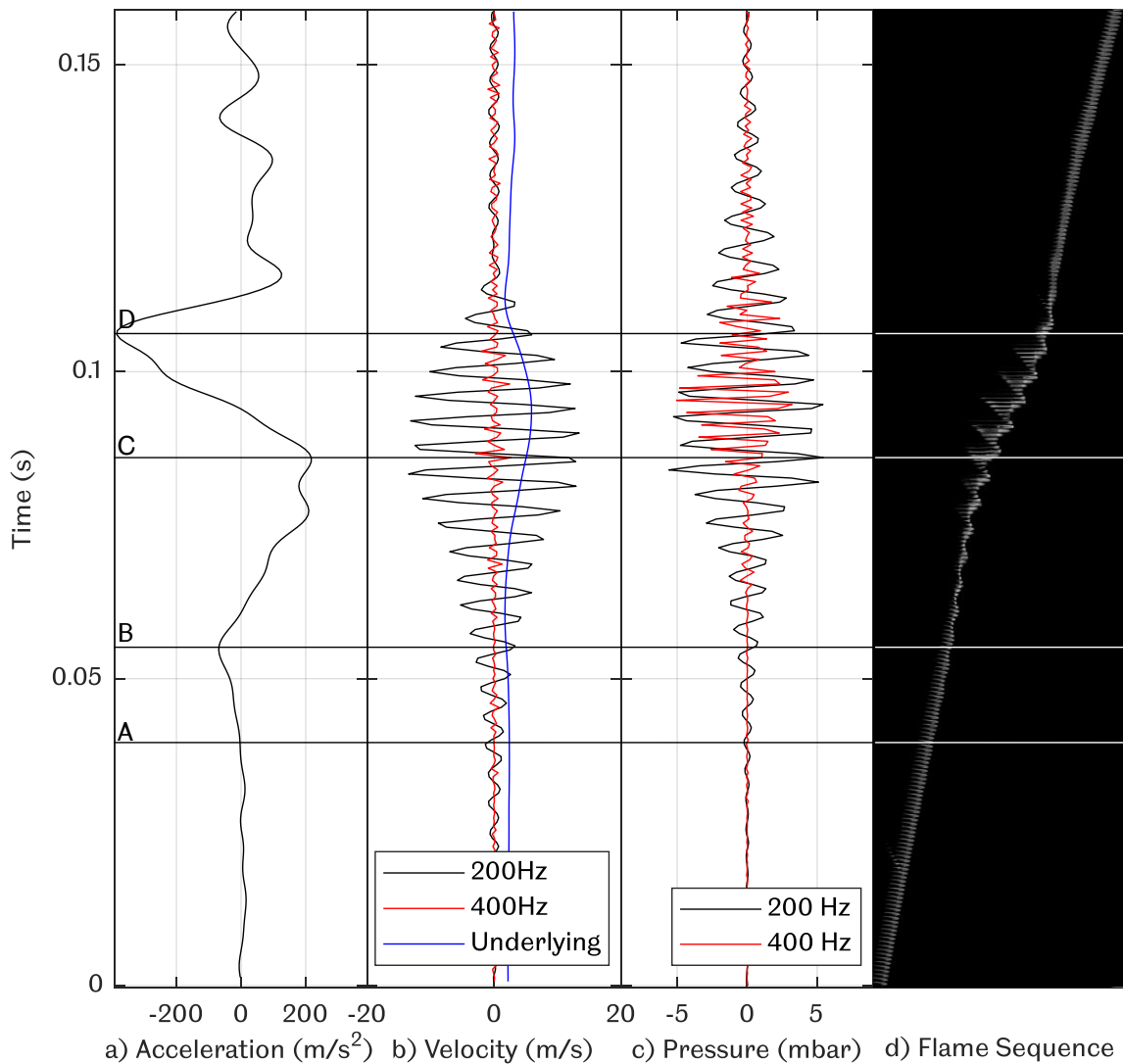
Figure 5.6 shows the propagation of an oscillating flame caused by the pressure build up during the pulsating period. An oscillating flame should not be confused with a pulsating flame. The main difference between the two lies in the flame shape. A pulsating flame elongates and shortens as the pressure fluctuates while an oscillating flame elongates, shortens and accompanied by an alternating flame structure, as described by Markstein [5]. The flame structure alternates between a convex shape (0.076, 0.084, and 0.092 seconds) and a tulip shape (0.0787 and 0.086 seconds).



**Figure 5.6 Image sequence, pressure signal and flame front position of an oscillating flame.**

It was observed that the convex shape usually occurs during a pressure peak (positive pressure) whereas the tulip shape occurs during a pressure trough (negative pressure). Positive and negative pressure in this context refers to the compression and rarefaction of air. A direct correlation between the flame shape and pressure reading cannot be made in the current study since the pressure transducer was located at the end of the tube. This problem was discovered by Ebieto [48], who stated that a pressure transducer placed in the middle of the quartz tube led to a significantly higher pressure reading compared to the pressure reading when the transducer was located at the end of the tube. Despite this disadvantage, the tube end pressure still provides valuable pressure information during the propagation.

The flame length fluctuation throughout the propagation was also observed to have an interesting pattern. The flame length fluctuation appears to be in phase with the pressure despite the alternating flame structure. Referring to the oscillating image sequence in Figure 5.6, it was observed that higher pressure formed longer flames. Utilizing the underlying acceleration derived from the underlying velocity of the flame, the flame shapes were able to be categorized based on the different pressure components acting on the flame. Figure 5.7 shows the flame sequence of a  $R_H = 0.1$ ,  $\phi = 1.2$  methane flame along with the underlying acceleration, decomposed velocity, and decomposed pressure.

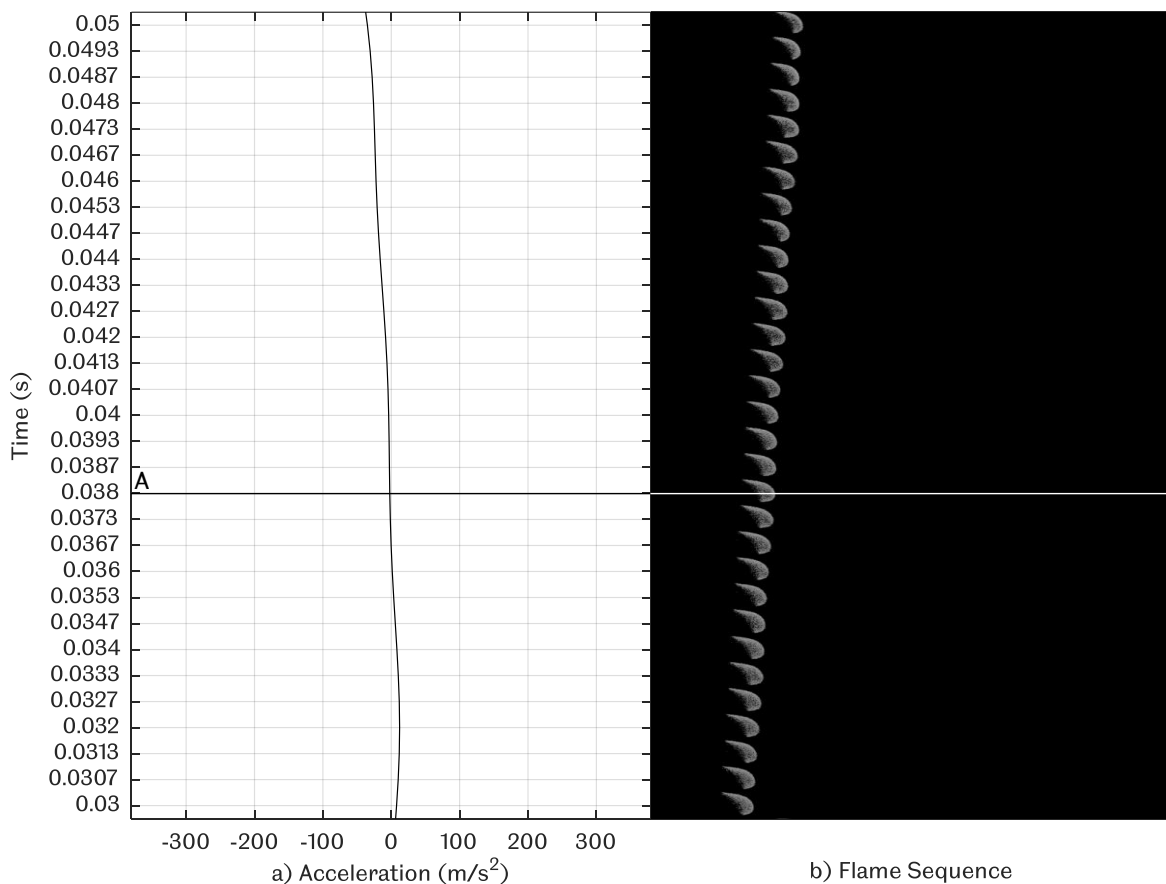


**Figure 5.7 Propagation of a  $R_H = 0.1$ ,  $\phi = 1.2$  methane flame with a) underlying acceleration, b) decomposed velocity, c) decomposed pressure and d) flame sequence.**

Based on Figure 5.7, 4 new points were proposed based on the underlying acceleration of the flame, which are A) decrease of underlying acceleration, B)

increase of underlying acceleration, C) 2<sup>nd</sup> decrease of underlying acceleration, and finally D) 2<sup>nd</sup> increase of underlying acceleration. If the four points were categorized based on the flame behaviour, period A-B would be the pulsating period, period B-D would be the oscillating period.

The flame started pulsating at point A as shown in Figure 5.8. The flame shape appeared to be convex towards the unburnt gas, propagating at a steady velocity while the underlying velocity starts to decrease. Beyond point A, the flame appears steady, but based on Figure 5.7(b), the 200 Hz flame velocity was fluctuating at  $\sim\pm 2.7$  m/s, indicating a pulsating flame. The  $\sim 400$  Hz velocity component remained constant at a low amplitude. No inversions were present in the flame surface, which rules out the possibility of an oscillation beyond point A. The  $\sim 200$  Hz pressure component appeared to grow slowly up to  $\sim\pm 0.4$  mbar beyond point A, whereas the  $\sim 400$  Hz pressure component was constant at a low amplitude, with no significant signs of growth.

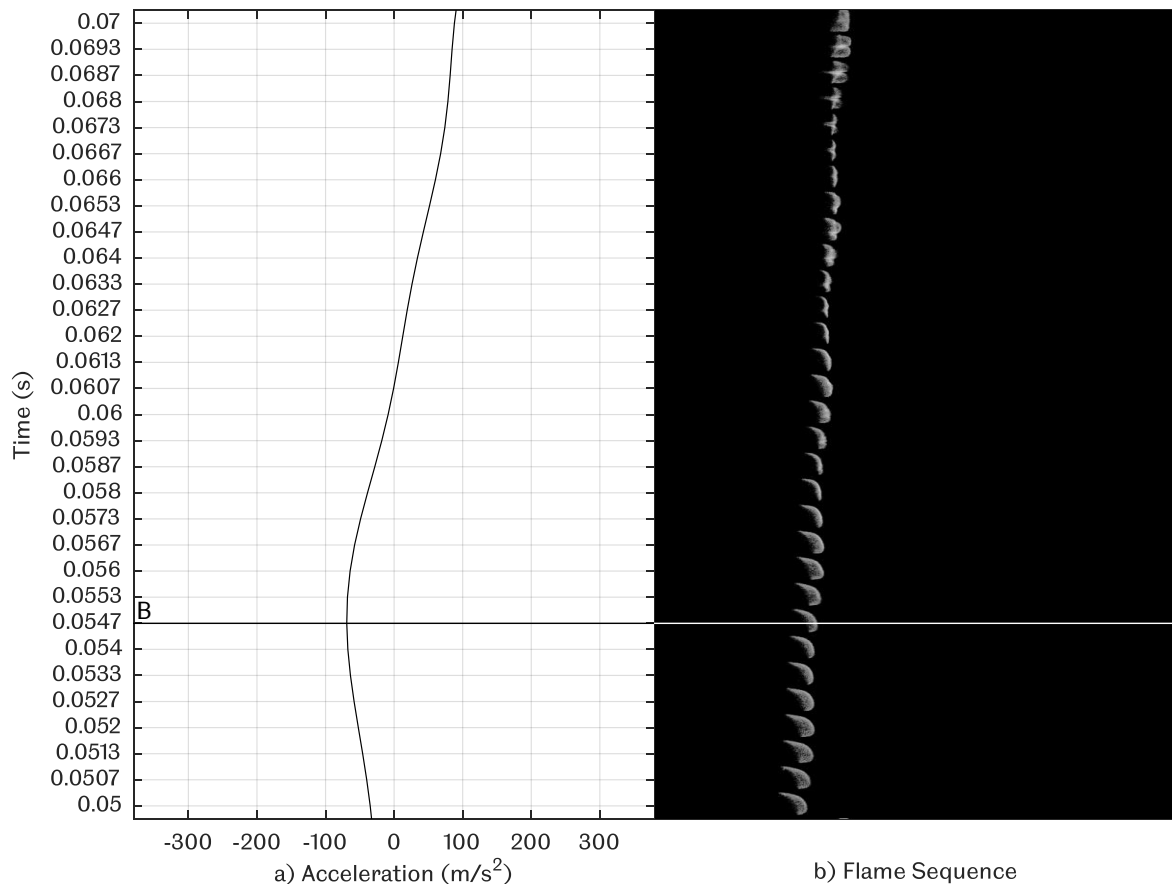


**Figure 5.8 Flame propagation at point A, where a) flame underlying acceleration, b) flame sequence.**

The flame propagation at point B was plotted in Figure 5.9. Point B was defined as the point of the first increase in acceleration. The main reason for the increase in

acceleration was found to be the start of the flame surface inversion towards the burnt gas, which is the characteristic behaviour of an oscillating flame. It was mentioned in the literature that inversion of the flame surface refers to period doubling, which basically means it takes twice the time for an oscillating flame to return back to its original convex shape compared to a pulsating flame.

The flame inversion was not obvious until 0.0593 seconds, where a small inversion was present on the flame surface. The flame inversion heats up the unburnt gas pushed into the burnt gas, and at the same time increasing the surface area of the flame. The size of the inversion eventually grew larger with every cycle, a good example of the flame surface inversion can be seen at 0.0673 seconds. Figure 5.7(c) shows that the  $\sim 200$  Hz pressure components at this point continued growing up to  $\sim \pm 2$  mbar, while the  $\sim 400$  Hz component appeared to remain constant at low amplitude. It was observed in Figure 5.7(b) that the  $\sim 200$  Hz velocity oscillation increased to  $\sim \pm 5$  m/s, while the  $\sim 400$  Hz velocity remained at a low amplitude.

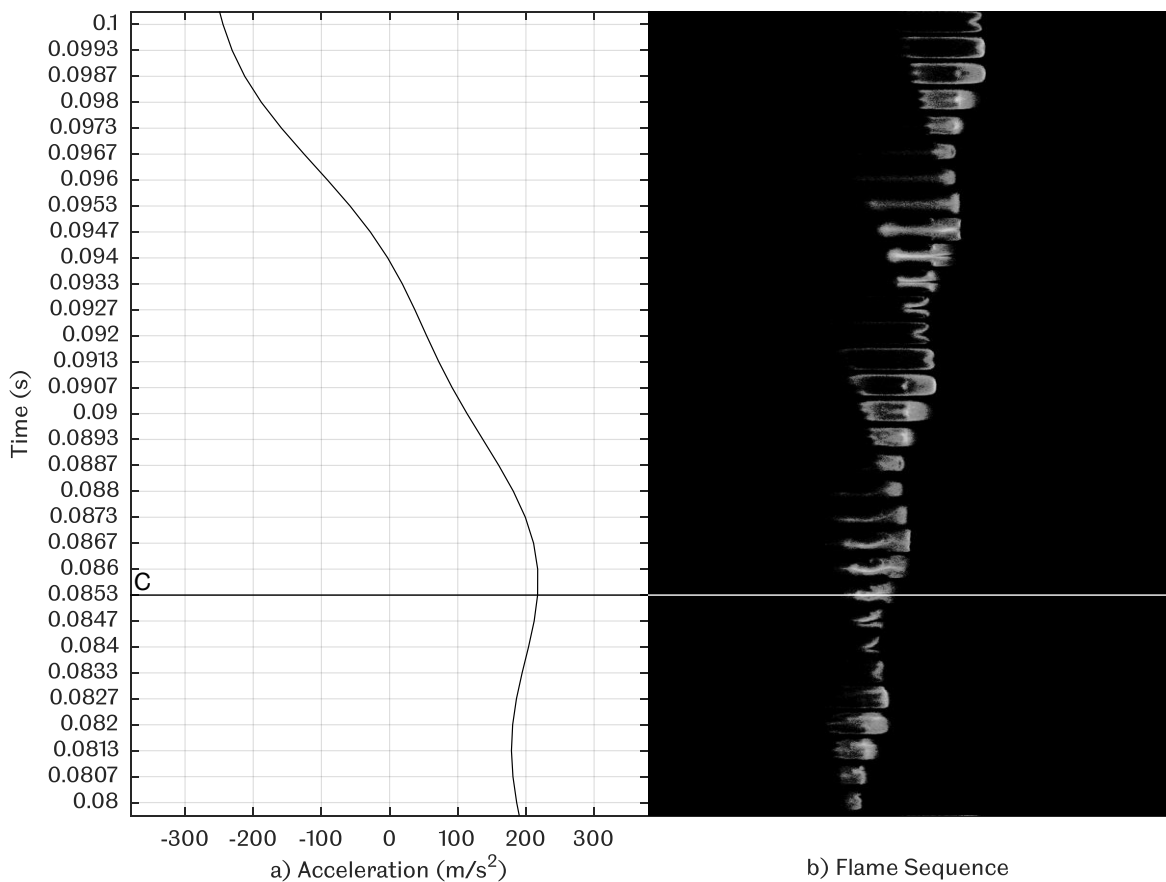


**Figure 5.9 Flame propagation at point B, where a) flame underlying acceleration, b) flame sequence.**

Figure 5.10 shows the flame propagation sequence at point C. A significant decrease in the acceleration was observed beyond point C despite the fact that it was

oscillating with a steadily increasing flame size. Referring to Figure 5.7(c), it was observed that the  $\sim 200$  Hz pressure component was oscillating at an approximately constant amplitude of  $\sim \pm 5$  mbar accompanied with a sudden growth to  $\sim \pm 3$  mbar for the  $\sim 400$  Hz pressure component.

The flame surface inversion was very clear beyond point C, with pockets of unburnt gas being pushed into hot burnt gas at 0.094 seconds. Here the period doubling was clearly seen, starting at 0.09 seconds, and ending at 0.0987 seconds. The violent oscillation of the flame was reflected in the  $\sim 200$  Hz velocity component in Figure 5.7(b), where it reached a maximum oscillating amplitude of  $\sim 13.4$  m/s, while the  $\sim 400$  Hz velocity component remains relatively low, despite the sudden growth of  $\sim 400$  Hz pressure oscillations.

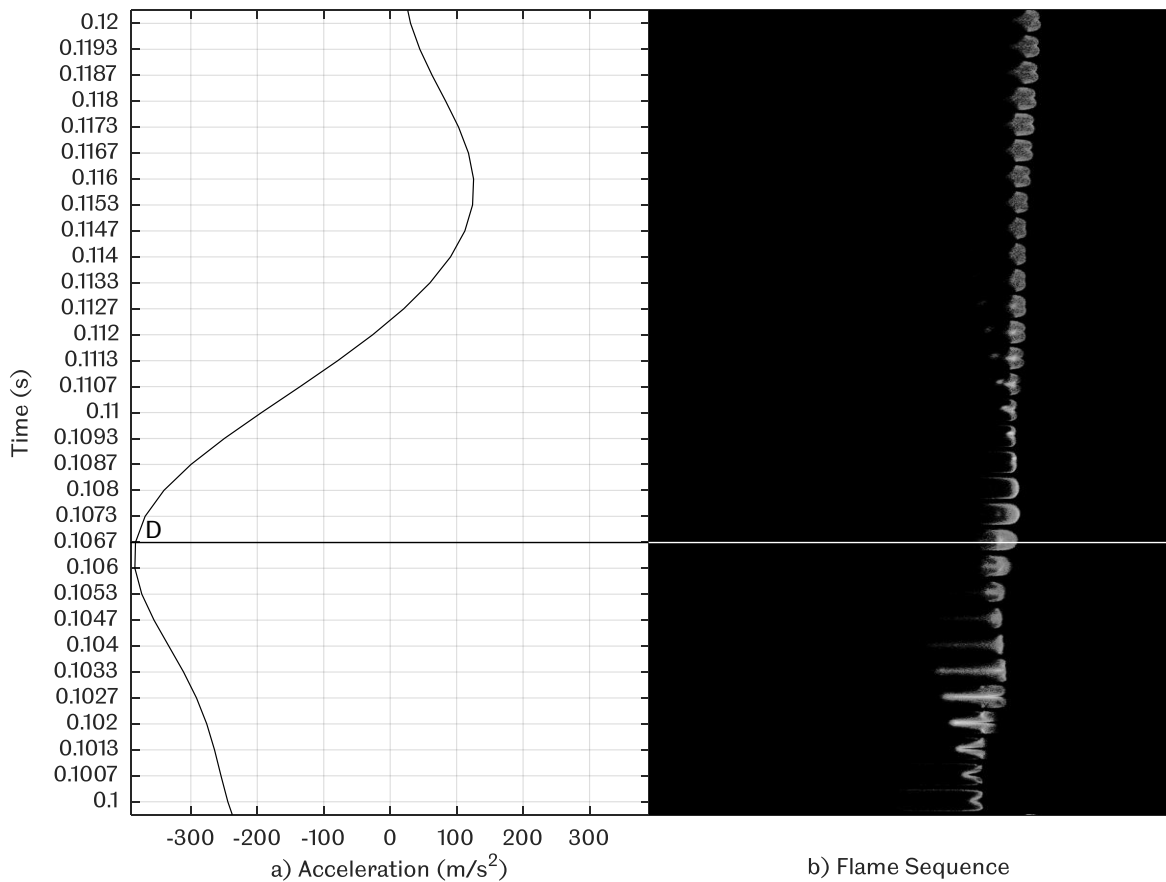


**Figure 5.10 Flame propagation at point C, where a) flame underlying acceleration, b) flame sequence.**

The propagation at the final point, point D was shown in Figure 5.11. it was observed that the oscillation returned back to pulsation beyond point D. A significant reduction in flame size was observed, which was reflected in the sudden reduction in both flame pressure components and the  $\sim 200$  Hz velocity components, shown in



Figure 5.7. The underlying acceleration of the flame increased steadily with the decay of pressure.



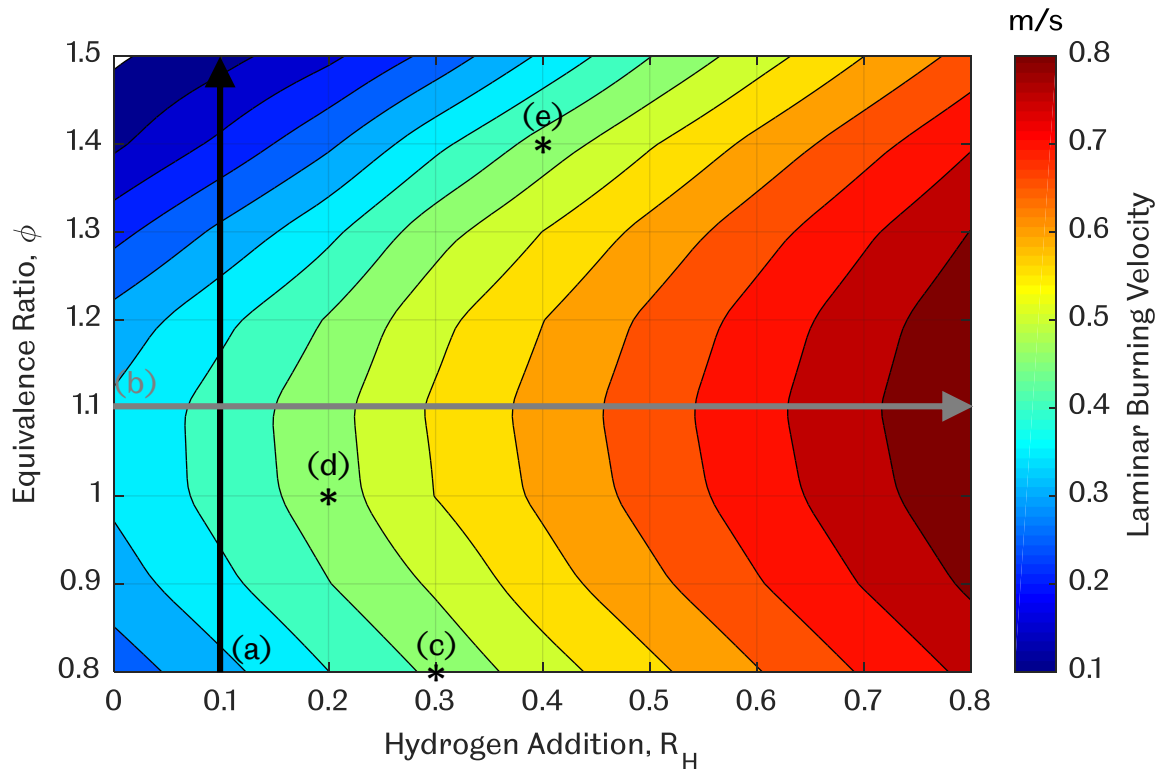
**Figure 5.11 Flame propagation at point D, where a) flame underlying acceleration, b) flame sequence.**

These 4 points were observed in all oscillating flames in the present work. For pulsating flames, only point A and B were present and finally no points were present in steady flames. The 4 new proposed points highlights the impact of different pressure components on different flame behaviours based on the underlying acceleration of the flame, tabulated in Table 5.1.

**Table 5.1 Impact of pressure components on the underlying acceleration of a flame.**

Point	Behaviour	Pressure Components		Velocity Components		Underlying Acceleration
		~200 Hz	~400 Hz	~200 Hz	~400 Hz	
<b>A</b>	Pulsating	Increase	Constant	Increase	Constant	Decrease
<b>B</b>	Oscillating	Increase	Constant	Increase	Constant	Increase
<b>C</b>	Oscillating	Constant	Increase	Decrease	Constant	Decrease
<b>D</b>	Pulsating	Decrease	Decrease	Decrease	Constant	Increase

In order to analyse the experiments systematically, effect of the two main variables will be analysed first, starting with equivalence ratio, followed by hydrogen addition. Figure 5.12 shows a contour plot of theoretical laminar burning velocity obtained from CHEMKIN [101] for equivalence ratio,  $\phi = 0.8 - 1.5$  and hydrogen addition,  $R_H 0 - 0.8$ . For the equivalence ratio effect, only flames from  $R_H 0.1$  hydrogen addition will be analysed, represented by line (a) in Figure 5.12, while for the hydrogen effect, only equivalence ratio,  $\phi = 1.1$  will be analysed, represented by line (b) in Figure 5.12.



**Figure 5.12 Range of flames analysed based on the theoretical laminar burning velocity contour plot, where a) flames with increasing equivalence ratio,  $\phi$  at constant hydrogen addition  $R_H = 0.1$ , b) flames with increasing hydrogen addition,  $R_H$  at constant equivalence ratio,  $\phi = 1.1$ , and finally 3 flames of approximately similar laminar burning velocity at points (c), (d), and (e).**

The study will be followed by a comparison between 3 flames of approximately similar laminar burning velocity,  $\phi = 0.8, R_H 0.3$  (0.4604 m/s),  $\phi = 1.0, R_H 0.2$  (0.4771 m/s), and  $\phi = 1.4, R_H 0.4$  (0.4709 m/s), represented by points (c), (d) and (e) respectively in Figure 5.12. The whole set of experiments will then be concluded in a later section with the aid of contour plots, similar to Figure 5.12, covering all the hydrogen addition levels and equivalence ratios.

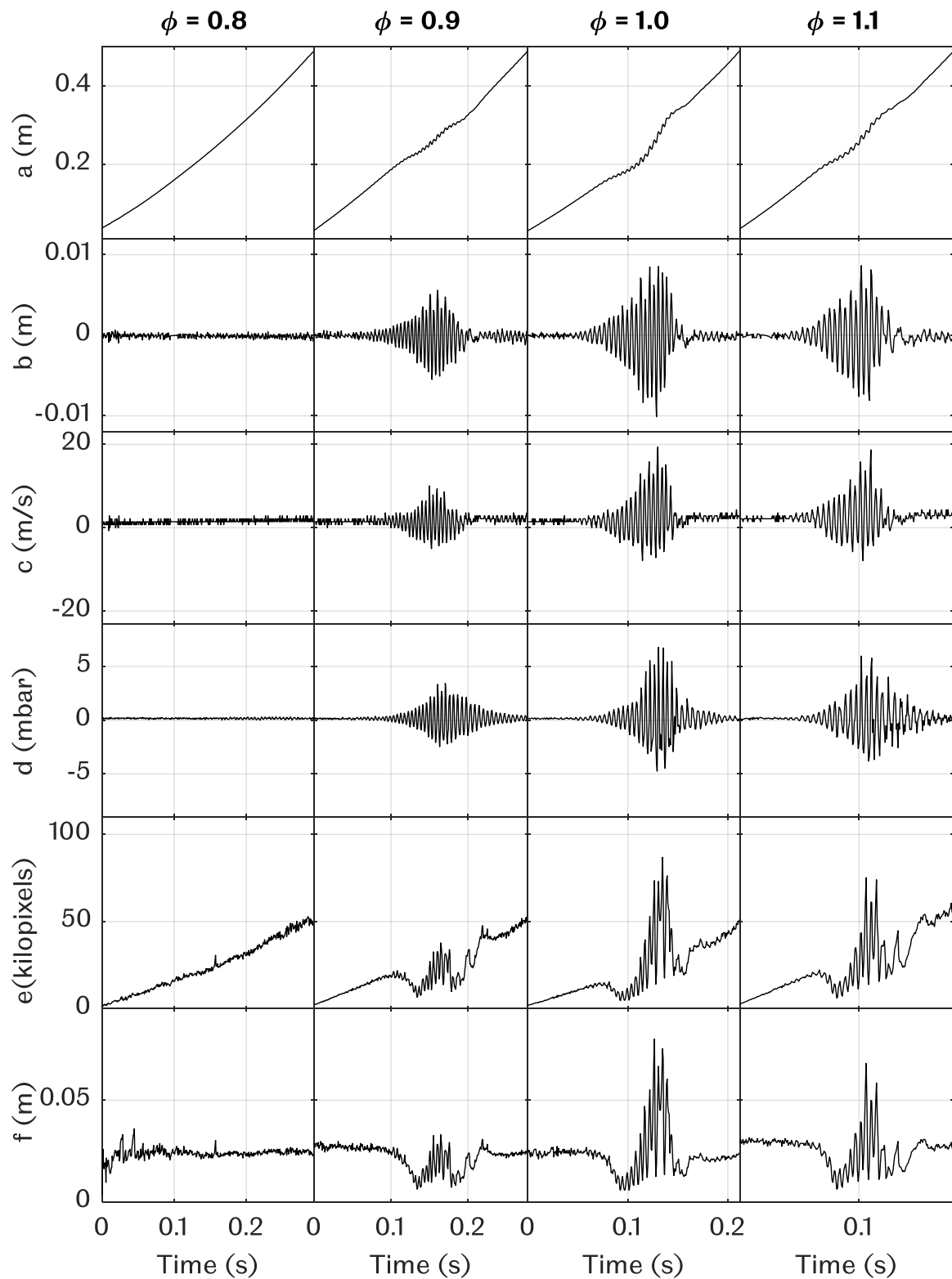
## 5.2 Equivalence Ratio Effect

### 5.2.1 Initial Study

Figure 5.13 shows the analysis performed on the flame images and pressure recordings for flames with hydrogen addition,  $R_H = 0.1$ , and equivalence ratio,  $\phi = 0.8 - 1.1$ . The flame front positions were plotted against time in Figure 5.13(a) and it was observed that the  $\phi = 0.8$  flame propagated steadily whereas the other flames were subjected to oscillations. The oscillations started to affect the  $\phi = 0.9$  and 1.1 flames at  $\sim 0.2$  m distance, while the  $\phi = 1.0$  flame started at  $\sim 0.15$  m. All the oscillations stopped at roughly the same distance of  $\sim 0.35$  m distance. It was observed that the  $\phi = 1.0$  and 1.1 flames oscillated more compared to the  $\phi = 0.9$  flame.

Figure 5.13(b) shows the flame front position amplitudes against time, which were obtained by high-pass filtering the flame front positions. All three flames were observed to have a similar growth in distance amplitude initially. The fluctuations eventually increased dramatically for  $\phi = 1.0$  and 1.1 flames compared to the  $\phi = 0.9$  flame. The increase in flame front position amplitude was expected due to the increase in laminar burning velocity as the equivalence ratio was increased from 0.8 - 1.1. The fluctuations in the flame front amplitude reduced abruptly at a certain point instead of decaying slowly.

The flame front position in Figure 5.13(a) was differentiated to obtain the raw flame front speed in Figure 5.13(c). All flames started with a velocity of  $\sim 1.4$  m/s and ended with a velocity of  $\sim 2.8$  m/s. Raw flame front speed oscillations were more obvious in  $\phi = 0.9 - 1.1$  flames compared to the steady  $\phi = 0.8$  flame. The maximum raw speed was dependent on the magnitude of flame front displacement, where both  $\phi = 1.0$  and 1.1 flames reached a raw speed of  $\sim 20$  m/s while  $\phi = 0.9$  flame only reached  $\sim 10$  m/s.



**Figure 5.13 Effect of equivalence ratio on  $R_H 0.1$  flames on a) flame front position, b) flame front position amplitude, c) flame front speed, d) tube end pressure, e) flame size, and finally f) flame length for equivalence ratios,  $\phi = 0.8 - 1.1$ .**

The tube end pressure signals were plotted against time in Figure 5.13(d). The  $\phi = 0.8$  flame pressure signal was expected to remain constant throughout the propagation, while the other 3 showed large amplitude pressure fluctuations during their oscillatory periods. The maximum pressure reached by the oscillating flames were  $\sim 3$  mbar,  $\sim 7$  mbar and  $\sim 6$  mbar for  $\phi = 0.9, 1.0$  and  $1.1$  respectively.

Unlike the flame front position amplitude, the pressure signals kept fluctuating with decreasing amplitude towards the end. This observed phenomenon was thought to be the decay of the built-up pressure in the tube. It was also noticed that the fluctuating pressure signals of  $\phi = 1.0$  and  $1.1$  flames were disrupted in the negative region, which appeared to be of a higher order frequency from the main oscillatory component. This will be analysed further in the frequency analysis section.

Plots of flame size against time is shown in Figure 5.13(e). All flames increased from an initial flame size of  $\sim 2$  kilopixels to  $\sim 50$  kilopixels at the end. This increase in flame size was reflected in the raw flame front speed which initially started from  $\sim 1.4$  m/s and ended with  $\sim 2.8$  m/s in Figure 5.13(c). A steady increase was observed for the  $\phi = 0.8$  flame, while the other 3 flames fluctuated in flame size during their oscillatory period.

The flame size response to the increase in pressure was different from the previously tracked parameters, where the flame size was reduced before increasing back with larger amplitude oscillations. The other parameters were found to increase proportionally with the pressure build-up. All oscillated flames decreased in flame size before increasing during the oscillation, each reaching different magnitudes, which was thought to be dependent on the tube end pressure.

Figure 5.13(f) shows the plot of flame length against time. Unlike the flame size, the flames initial and ending length remained fairly constant except for the  $\phi = 0.8$  flame, which started with a lower thickness compared to its ending thickness. The fluctuations in the flame length appeared to be similar to the flame size during their oscillatory periods. This was expected since a thicker flame would have a larger flame size and vice versa.

One interesting observation was that the flame thickness did not increase towards the end despite the increase in flame size. A comparison was made between the starting and ending flame images, and it was found that the starting flame shape was slightly slanted compared to the ending flame shape. The symmetrical flame shape at the end contributed to the larger flame size as shown in Figure H.1.

Figure 5.14 is the continuation of Figure 5.13, describing  $\phi = 1.2 - 1.5$  flames. Figure 5.14(a) shows the flame front position plotted against time. The oscillations started

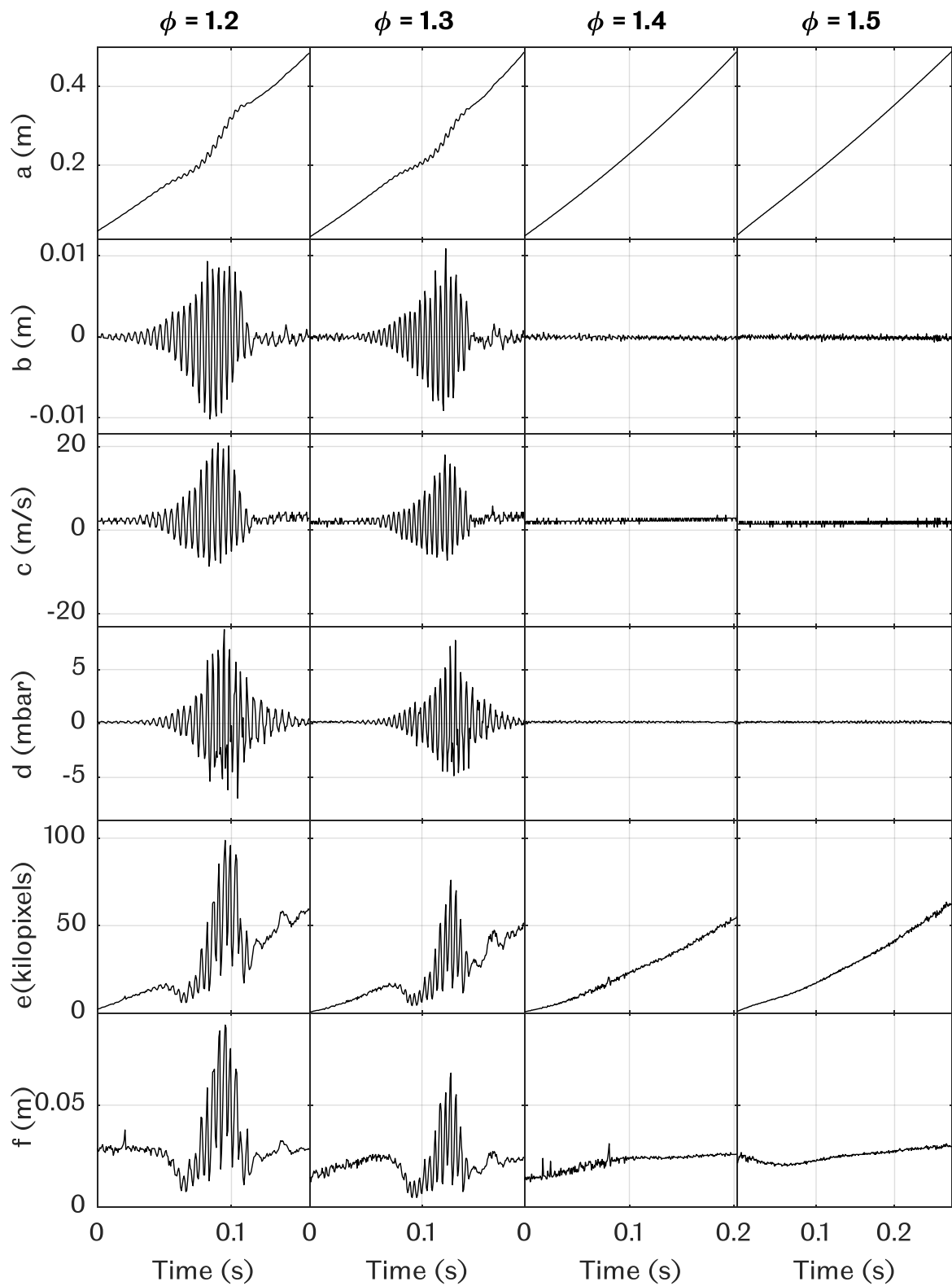
to affect the  $\phi = 1.2$  flame at  $-0.15$  m, similar to the  $\phi = 1.1$  flame, while the  $\phi = 1.3$  flame was affected at  $-0.19$  m. Both  $\phi = 1.2$  and  $1.3$  flames stopped oscillating at  $-0.35$  m, similar to the leaner oscillated flames. Reduction in the disturbance was expected as the laminar burning velocity drops beyond  $\phi = 1.1$ , as shown by line (a) in Figure 5.12. However, the drop in laminar burning velocity did not affect the oscillations directly. The  $\phi = 1.2$  and  $1.3$  flames continued to oscillate with roughly the same magnitude as the  $\phi = 1.0$  and  $1.1$  flames. Unlike the gradual increase in oscillations observed from  $\phi = 0.8 - 1.1$  flames, the oscillations did not decrease gradually from  $\phi = 1.1 - 1.5$ , but instead the oscillations disappeared suddenly at  $\phi = 1.4$ .

The flame distance amplitude against time was plotted in Figure 5.14(b). Based on the figure, the  $\phi = 1.3$  flame appears to fluctuate unpredictably while the  $\phi = 1.2$  flame fluctuations increased steadily before reaching a plateau, where the displacement amplitude fluctuations stayed fairly constant for a few cycles before decaying. The final two flames,  $\phi = 1.4$  and  $1.5$  showed almost no sign of distance amplitude fluctuations, similar to  $\phi = 0.8$  flame.

Raw speeds of the flames were plotted against time in Figure 5.14(c). It was observed that the starting and ending velocity of the flames became lower with increasing equivalence ratio as expected. Raw speed fluctuations during their oscillatory period were higher than expected. The  $\phi = 1.2$  and  $1.3$  flames fluctuated in a similar manner to those observed in  $\phi = 0.9 - 1.1$  flames. Out of all the oscillated flames,  $\phi = 1.2$  reached the highest raw speed of  $\sim 20$  m/s. One interesting point worth pointing out is that the raw speed of all oscillated flames did not fall below  $-10$  m/s, which was thought to be the characteristic of the tube.

Figure 5.14(d) shows the plot of tube end pressure signal against time. The  $\phi = 1.2$  flame reached the highest maximum pressure of  $\sim 9$  mbar, making it the most oscillated flame among all the  $R_H = 0.1$  flames. Despite having a lower laminar burning velocity, the  $\phi = 1.3$  reached a higher maximum pressure of  $\sim 8$  mbar compared to leaner oscillated flames.

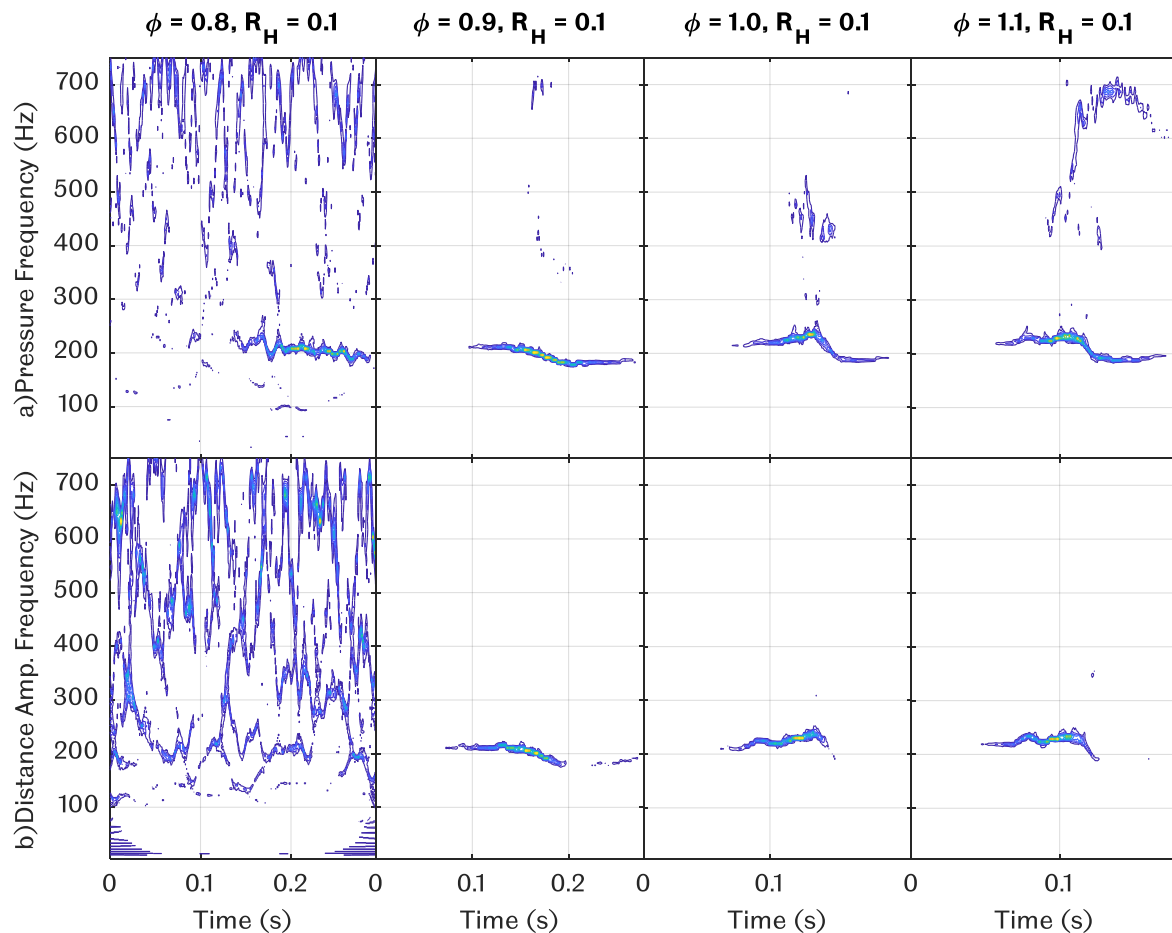
Flame size and thickness were plotted against time in Figure 5.14(e) and Figure 5.14(f). The flame size and thickness of the  $\phi = 1.2$  flame was again the highest, reaching  $\sim 100$  kilopixels in size and  $\sim 0.09$  m thickness. The flame size for the steady flames,  $\phi = 1.4$  and  $1.5$ , did not behave as expected. Despite their low laminar burning velocity, their flame size managed to grow up to  $\sim 60$  kilopixels and maintained a flame length of  $\sim 0.03$  m. This was thought to be an effect of richer flames having an overall brighter appearance compared to leaner flames.



**Figure 5.14 Effect of equivalence ratio on RH 0.1 flames on a) flame front position, b) flame front position amplitude, c) flame front speed, d) tube end pressure, e) flame size, and finally f) flame length for equivalence ratios,  $\phi = 1.2 - 1.5$ .**

## 5.2.2 Frequency Analysis

The raw speed and pressure signals were separated into different components using Synchrosqueezed Wavelet Transform (SST) to analyse the spectral components within the signals in order to understand their relationship. Figure 5.15 shows the SST plots for a) pressure signal and b) distance amplitude signal of methane flames with constant hydrogen addition,  $R_H = 0.1$  and increasing equivalence ratio,  $\phi = 0.8 - 1.1$ . The  $\phi = 0.8$  flame did not oscillate, producing a noisy plot with unclear traces of oscillation apart from the  $\sim 200$  Hz pressure oscillation between  $\sim 0.1 - 0.3$  seconds of propagation.



**Figure 5.15 SST plots for a) pressure signal and b) distance amplitude signal of methane flames with constant hydrogen addition,  $R_H = 0.1$ , and increasing equivalence ratio,  $\phi = 0.8 - 1.1$ .**

The other 3 flames showed clear signs of oscillation with fluctuating frequency within  $\sim 190 - 250$  Hz frequency range in both their pressure and distance amplitude signals, whereas higher order frequencies only appear in the pressure signals. To prevent confusion, the appearance of the contours at a certain frequency and time



indicates regions with high energy content. The absence of contours in other parts does not indicate the absence of other oscillating frequencies, but instead indicates low energy content. In short, the absence of the higher order frequencies in the distance amplitude plots simply indicates low amplitude, high frequency oscillations

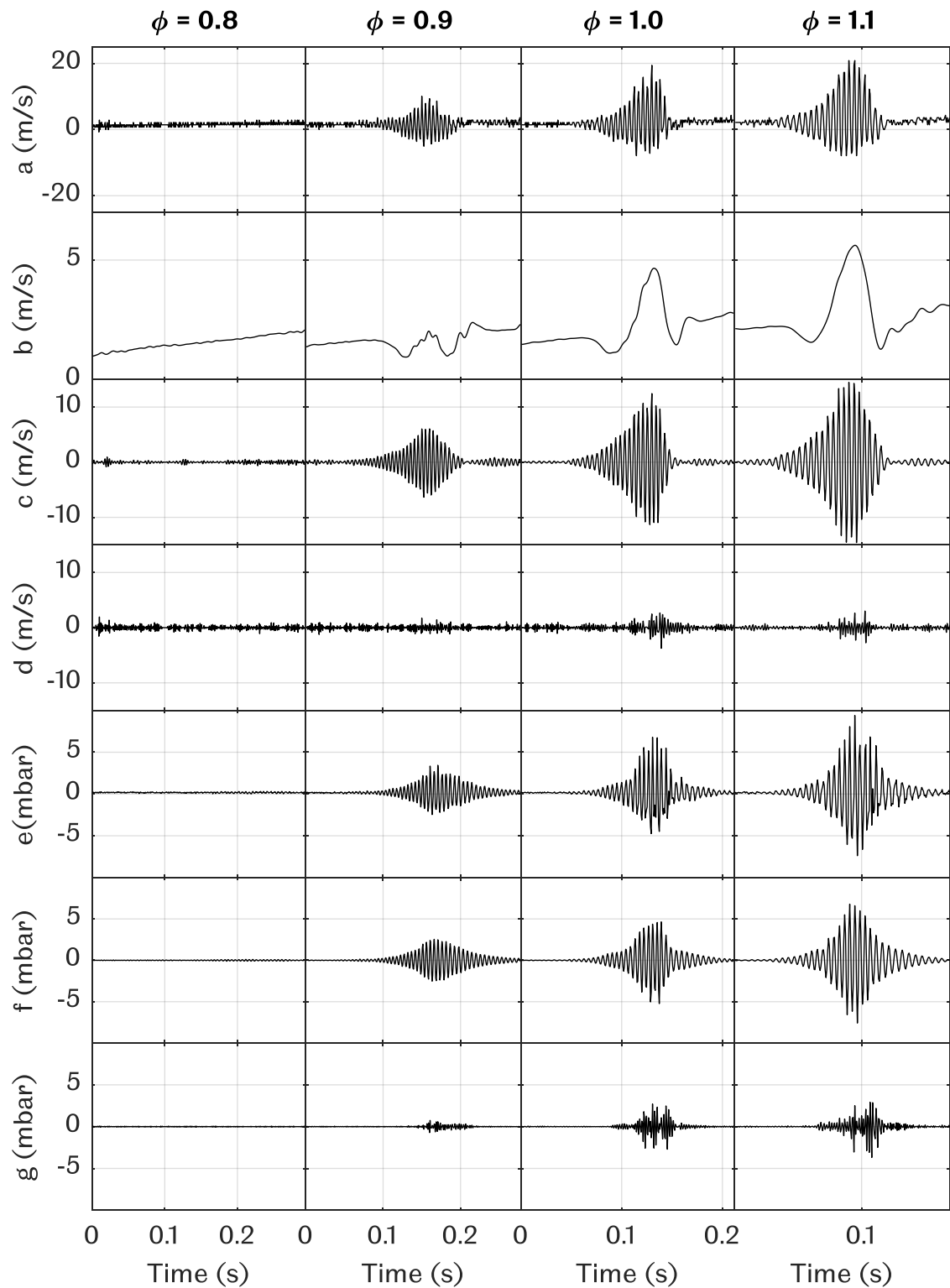
The distance amplitude oscillations appeared earlier compared to the pressure oscillations in all oscillating flames, which might indicate that the flame propagation was responsible for exciting the pressure oscillations. It is worth noting that the excitation of the higher order frequencies coincides with the decay of the ~200 Hz oscillating components in the pressure signal, which lasted almost to the end of the propagation.

Upon further inspection, the excitation of the higher order frequencies appears to depend on the fluctuation of the ~200 Hz component. Comparing the  $\phi = 0.9$  pressure SST plot to the  $\phi = 1.0$  and 1.1, the fluctuation of the former mixture appeared to stay constant before decaying, whereas the latter mixtures had a sudden frequency increase before decaying.

Figure 5.16 shows the breakdown of the raw speed and the pressure signal of  $\phi = 0.8$  – 1.1 flames. The raw speed signals (Figure 5.16(a)) were separated into 3 components, the underlying flame speed (Figure 5.16(b)), 200 Hz component (Figure 5.16(c)) and the 400 Hz component (Figure 5.16(d)), while the raw pressure signals (Figure 5.16(e)) were broken down into 200 Hz (Figure 5.16(f)) and 400 Hz (Figure 5.16(g)) components.

Figure 5.16(a) shows the raw flame speed plot against time, which was quite difficult to interpret as it is. The raw speed fluctuations were not symmetrical over the x-axis due to the different spectral components. The underlying flame speeds were plotted against time in Figure 5.16(b). It was observed that the  $\phi = 0.8$  flame speed increased steadily with time, while the other 3 showed a similar pattern of deceleration, acceleration and another deceleration before their underlying speed normalizes.

In general, the first deceleration was thought to be the result of the pulsating flame behaviour discussed in Figure 5.5, while the acceleration was caused by the oscillating flame behaviour discussed in Figure 5.6. The acceleration continues until the flame reaches its peak speed, and starts to decelerate. At this point, the flame continues oscillating, but with reduction in flame length with every cycle of oscillation. The reduction in flame length causes the flame speed to reduce, which returns the oscillating flame back to its pulsating state. Once the pulsating stops, the flame speed increases slightly and continues to propagate as a steady flame.



**Figure 5.16** Frequency analysis of a) raw flame speed, broken down into b) underlying flame speed, c) 200 Hz flame speed component, and d) 400 Hz speed component for ,  $\phi = 0.8 - 1.1$ . Analysis continued with e) raw pressure signal, broken down into f) 200 Hz pressure signal component and g) 400 Hz pressure signal component.

Back to Figure 5.16(b), it was observed that the initial underlying speed of the flames increased with their laminar burning velocity as expected. The increase in laminar burning velocity also contributed to the peak underlying speed achieved by the flames. The  $\phi = 1.1$  flame achieved the highest peak speed of  $\sim 6$  m/s while the  $\phi = 1.0$  and 0.9 flames achieved a speed of  $\sim 5$  m/s and  $\sim 2$  m/s respectively.

Figure 5.16(c) shows the plot of 200 Hz component speed against time. The 200 Hz components appear to be fairly symmetrical along the x-axis. It was observed that the 200 Hz speed component was responsible for the underlying speed fluctuations seen in Figure 5.16(b). The steady  $\phi = 0.8$  flame did not have large amplitude fluctuations in its 200 Hz speed component compared to the other oscillating flames. This led to the assumption that the underlying speed fluctuations are dependent on the 200 Hz speed component. It was also noticed that a higher magnitude fluctuation in the 200 Hz speed component led to a higher peak speed in the underlying flame speed. The  $\phi = 0.9, 1.0$  and 1.1 flames reached a maximum peak amplitude of  $\sim \pm 6$  m/s,  $\sim \pm 11$  m/s and  $\sim \pm 15$  m/s respectively.

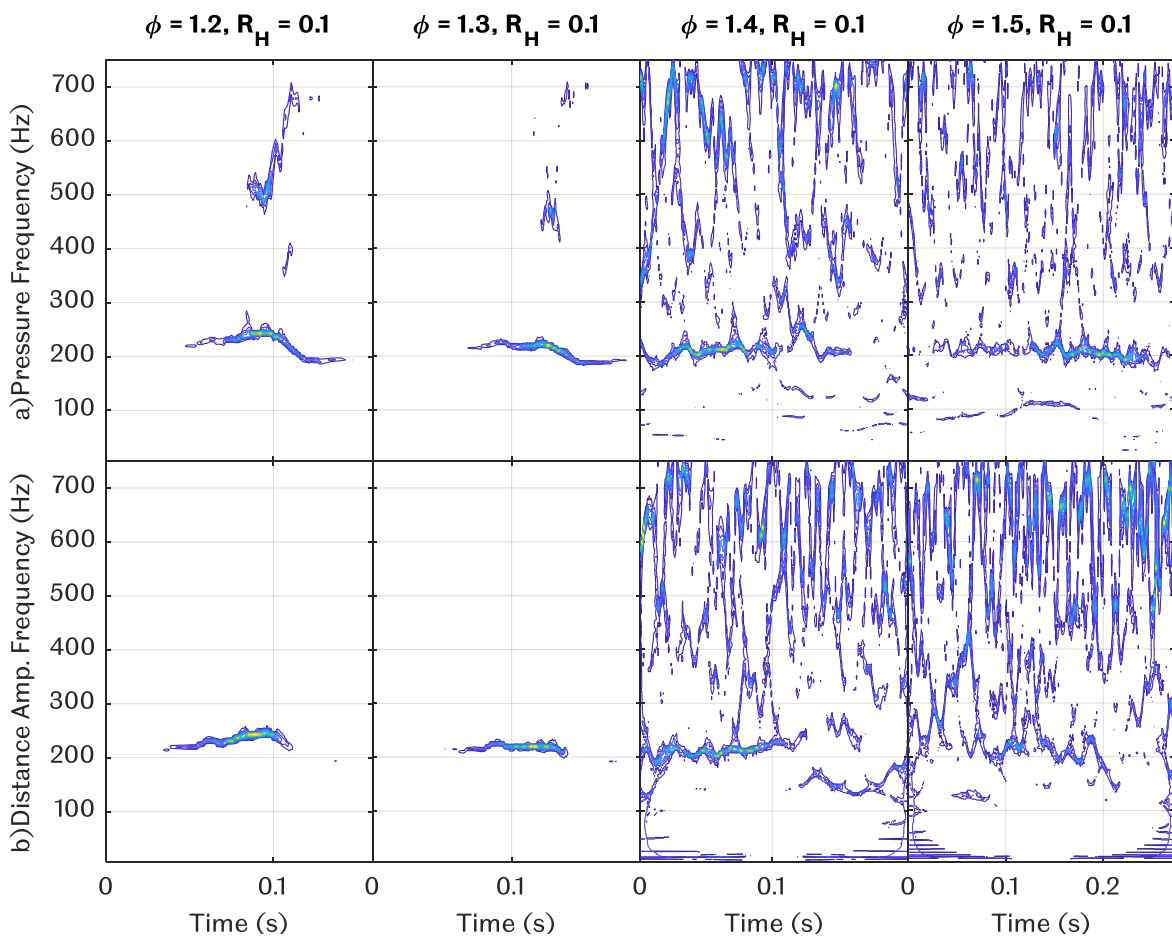
The third speed component, 400 Hz speed component, were plotted against time in Figure 5.16(d). The  $\phi = 0.8$  and 0.9 flames did not show significant speed fluctuations in their 400 Hz speed component, compared to  $\phi = 1.0$  and 1.1 flames, which reached a maximum speed fluctuation of  $\sim \pm 3$  m/s for both flames. The 400 Hz speed component fluctuation appears to be dependent on the 200 Hz speed component fluctuation. The decay of the 200 Hz component led to the decay of the 400 Hz speed component.

The raw tube-end pressure signals in Figure 5.16(e) were broken down into 200 Hz and 400 Hz components, plotted in Figure 5.16(f) and Figure 5.16(g) respectively. It was observed that the 400 Hz pressure component was similar to the 400 Hz speed component, appearing only in the presence of a 200 Hz component fluctuation. The 200 Hz pressure component of the  $\phi = 0.9$  flame reached a maximum magnitude of  $\sim \pm 3$  mbar, which led to the excitement of its 400 Hz component, which reached a magnitude of  $\sim \pm 1$  mbar. The excitement of the 200 Hz pressure component in  $\phi = 1.0$  and 1.1 flames reached a maximum magnitude of  $\sim \pm 5$  mbar and  $\sim \pm 7$  mbar respectively. The higher fluctuation magnitude observed in the 200 Hz component of the  $\phi = 1.1$  flame led to a higher 400 Hz pressure fluctuation magnitude of  $\sim \pm 4$  mbar, compared to  $\sim \pm 3$  mbar of the  $\phi = 1.0$  flame.

Figure 5.17 shows the SST plot for a) pressure signals and b) distance amplitude signals for methane flames with  $R_H = 0.1$  and equivalence ratio ranging from  $\phi = 1.2 - 1.5$ . The  $\phi = 1.2$  and 1.3 flames were oscillated, thus producing  $\sim 200$  Hz contours on

both signals, similar to the  $\phi = 1.1$  flame, accompanied by higher order frequencies for the pressure signal. Similar to the findings in Figure 5.15, the sudden increase in the  $\sim 200$  Hz pressure signal frequency of  $\phi = 1.2$  flame appears to excite the higher order frequencies more compared to the  $\phi = 1.3$  flame.

Appearance of the distance-amplitude contour was earlier compared to the pressure contour, consistent with the findings in the previous SST plots in Figure 5.15. The flame stopped oscillating at  $\phi = 1.4$ , causing a wideband of frequency to appear as high-energy regions on the SST plot. However, a faint trace of continuous contour in the  $\sim 200$  Hz region was visible in the pressure and distance amplitude plot for both  $\phi = 1.4$  and 1.5 flames, which was thought to be an oscillatory behaviour where the damping exceeds the gain of the interaction, causing no pressure build up in the system.



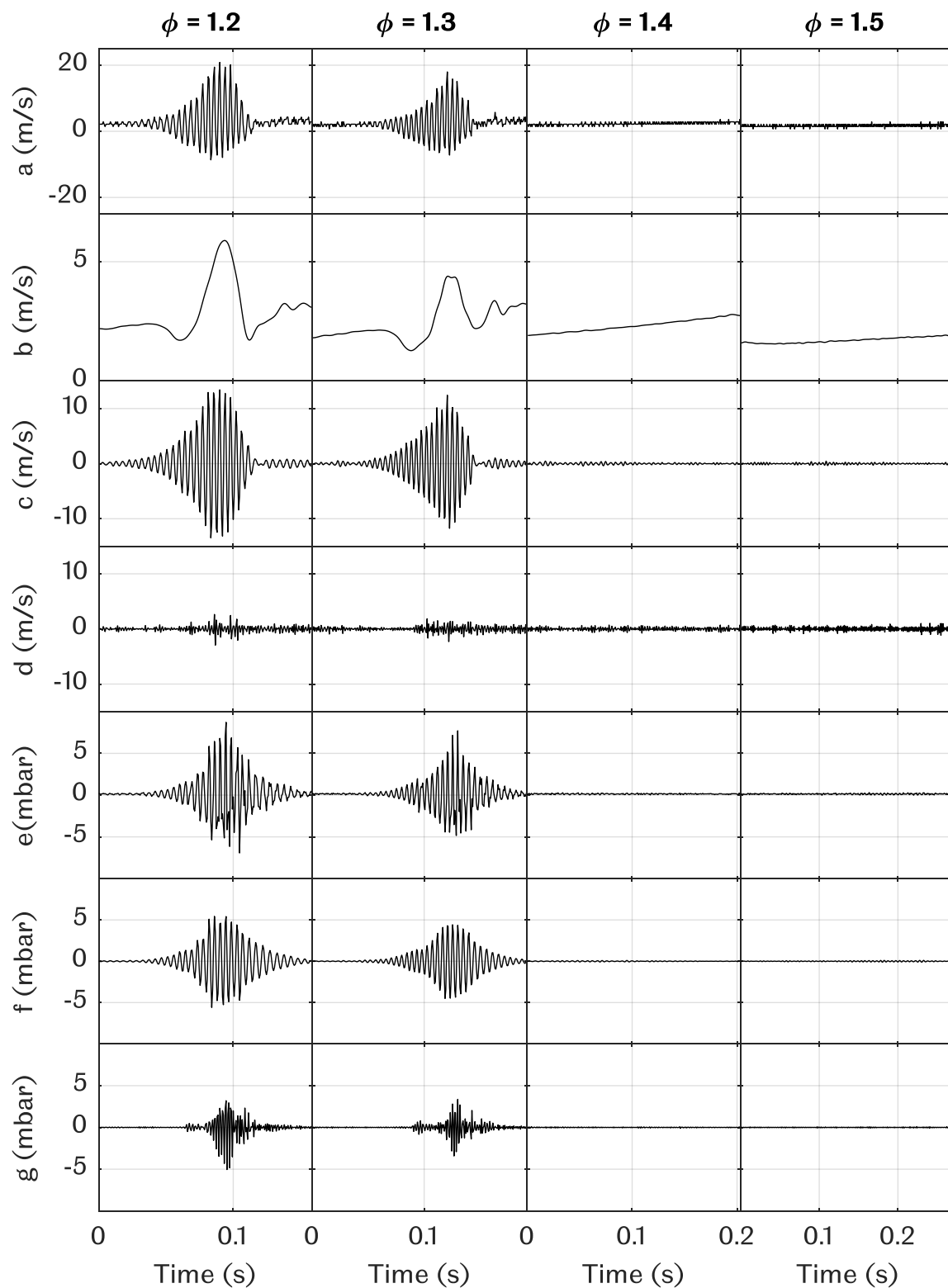
**Figure 5.17 SST plots for a) pressure signal and b) distance amplitude signal of methane flames with constant hydrogen addition,  $R_H = 0.1$ , and increasing equivalence ratio  $\phi = 1.2 - 1.5$ .**

Figure 5.18 is the continuation of Figure 5.16, covering  $\phi = 1.2 - 1.5$ . The final two flames,  $\phi = 1.4$  and  $1.5$  were both steady, showing minimal fluctuations in their 200 Hz and 400 Hz components for both flame speed and tube-end pressure signal. Their underlying flame speed showed a gradual increase with time. It was observed that the  $\phi = 1.5$  flame propagated slower and with lower acceleration compared to the  $\phi = 1.4$  flame. This reduction in speed was expected since the laminar burning velocity reduces as the mixture became richer.

However, the sudden disappearance of the oscillations between  $\phi = 1.3$  and  $\phi = 1.4$  was not expected. The reduction of the laminar burning velocity as the equivalence ratio increases beyond 1.1 is gradual as indicated by line (a) in Figure 5.12, and the oscillations were expected to reduce accordingly. It was also observed that the  $\phi = 1.2$  flame had a similar flame speed magnitude with the  $\phi = 1.1$  flame, reaching a maximum underlying velocity of  $\sim 6$  m/s, a 200 Hz speed component of  $\sim \pm 15$  m/s and a 400 Hz speed component of  $\sim \pm 3$  m/s.

Comparing the raw pressure signal of  $\phi = 1.1$  and  $1.2$  flame, they appear to be similar, but after broken down to their 200 Hz and 400 Hz components, it was discovered that the  $\phi = 1.2$  flame had a lower magnitude of 200 Hz pressure oscillation of  $\sim \pm 5$  mbar compared to the  $\phi = 1.1$  flame which reached  $\sim \pm 7$  mbar. It was also found that the  $\phi = 1.2$  flame had a higher 400 Hz pressure component, reaching a maximum of  $\sim \pm 5$  mbar, compared to the  $\phi = 1.1$  flame which only reached  $\sim \pm 4$  mbar. This difference was not noticed in the flame speed breakdown. It is worth noting that the maximum magnitude of the  $\phi = 1.2$  flame for both 200 Hz and 400 Hz pressure components were similar.

The  $\phi = 1.3$  flame showed a gradual decrease in its flame speed magnitude, reaching a maximum underlying speed of  $\sim 4$  m/s, a 200 Hz speed component of  $\sim \pm 12$  m/s, and a 400 Hz speed component of  $\sim \pm 2$  m/s. The breakdown of the raw pressure signal showed a similar behaviour observed in the  $\phi = 1.2$  flame, where both the 200 Hz and 400 Hz pressure component reached a similar magnitude of oscillation,  $\sim \pm 4$  mbar.



**Figure 5.18** Frequency analysis of a) raw flame speed, broken down into b) underlying flame speed, c) 200 Hz flame speed component, and d) 400 Hz speed component for ,  $\phi = 1.2 - 1.5$ . Analysis continued with e) raw pressure signal, broken down into f) 200 Hz pressure signal component and g) 400 Hz pressure signal component.

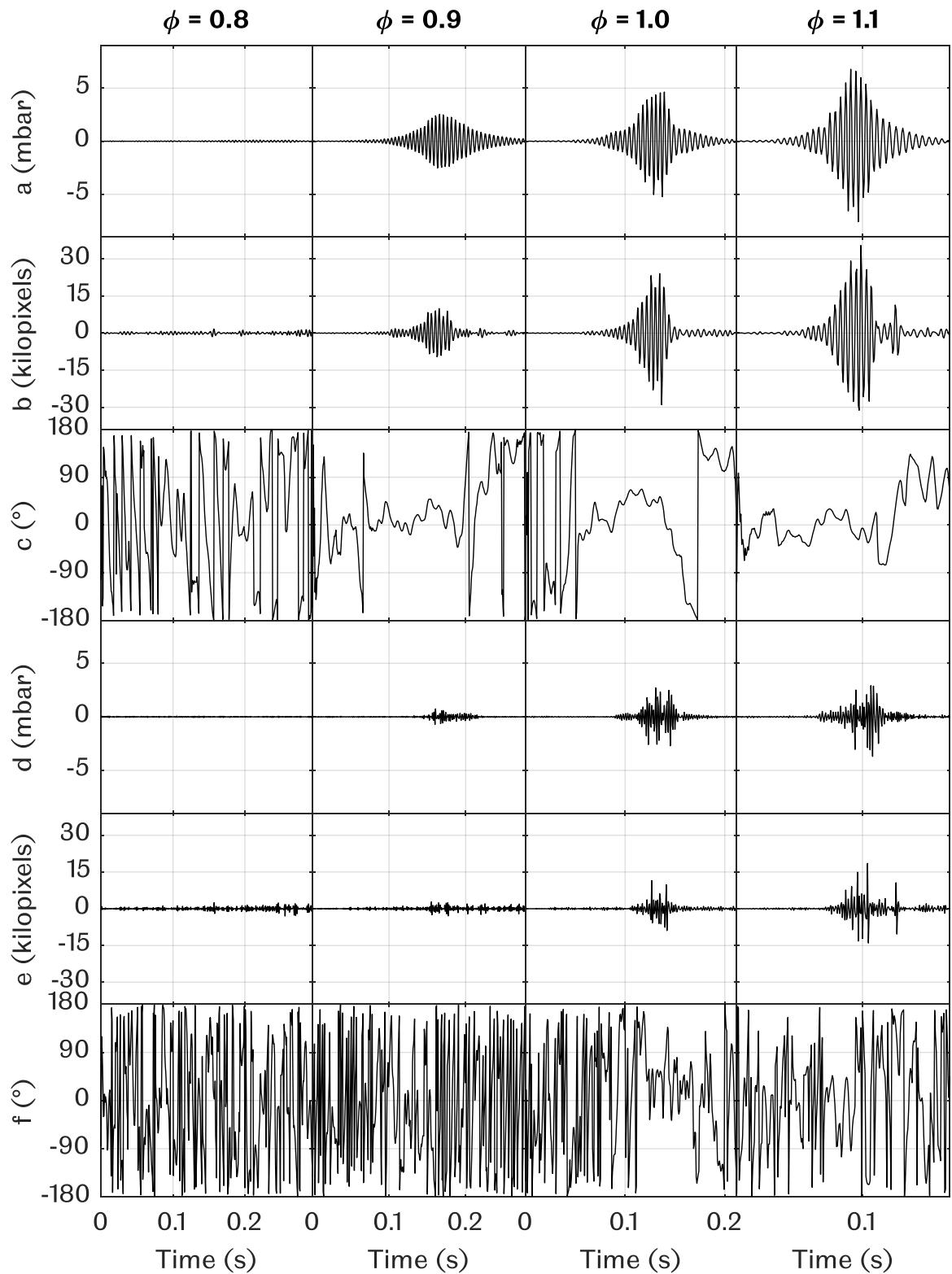
### 5.2.3 Phase Analysis

Figure 5.19 shows the phase study conducted between the flame pressure and size. The raw signals were broken down into their 200 Hz and 400 Hz component and phase difference was calculated for both frequency range. Phase difference between pressure and flame size was of interest to find the relationship between them. Phase difference of  $0^\circ$  signifies phase matching between the flame pressure signal and the flame size which causes the pressure to amplify.

Referring to Figure 5.19(c), phase matching was not evident in the  $\phi = 0.8$  flame based on the erratic fluctuation of its phase difference. The other 3 flames were observed to be in phase during their oscillating period indicated by a reduction in their phase difference within the range of  $0^\circ - \pm 90^\circ$ . This phenomenon proves the dependency between the 200 Hz component of the flame pressure and the flame size. In general, the phase difference fluctuation starts to reduce to  $0^\circ$  even before the amplification of both signals, and increases back once the flame size reduces abruptly. It is worth noting that the abrupt reduction in flame size did not happen to the flame pressure, which instead decays gradually. This behaviour was unexpected, since the growth in flame size and pressure was observed to be gradual for most cases.

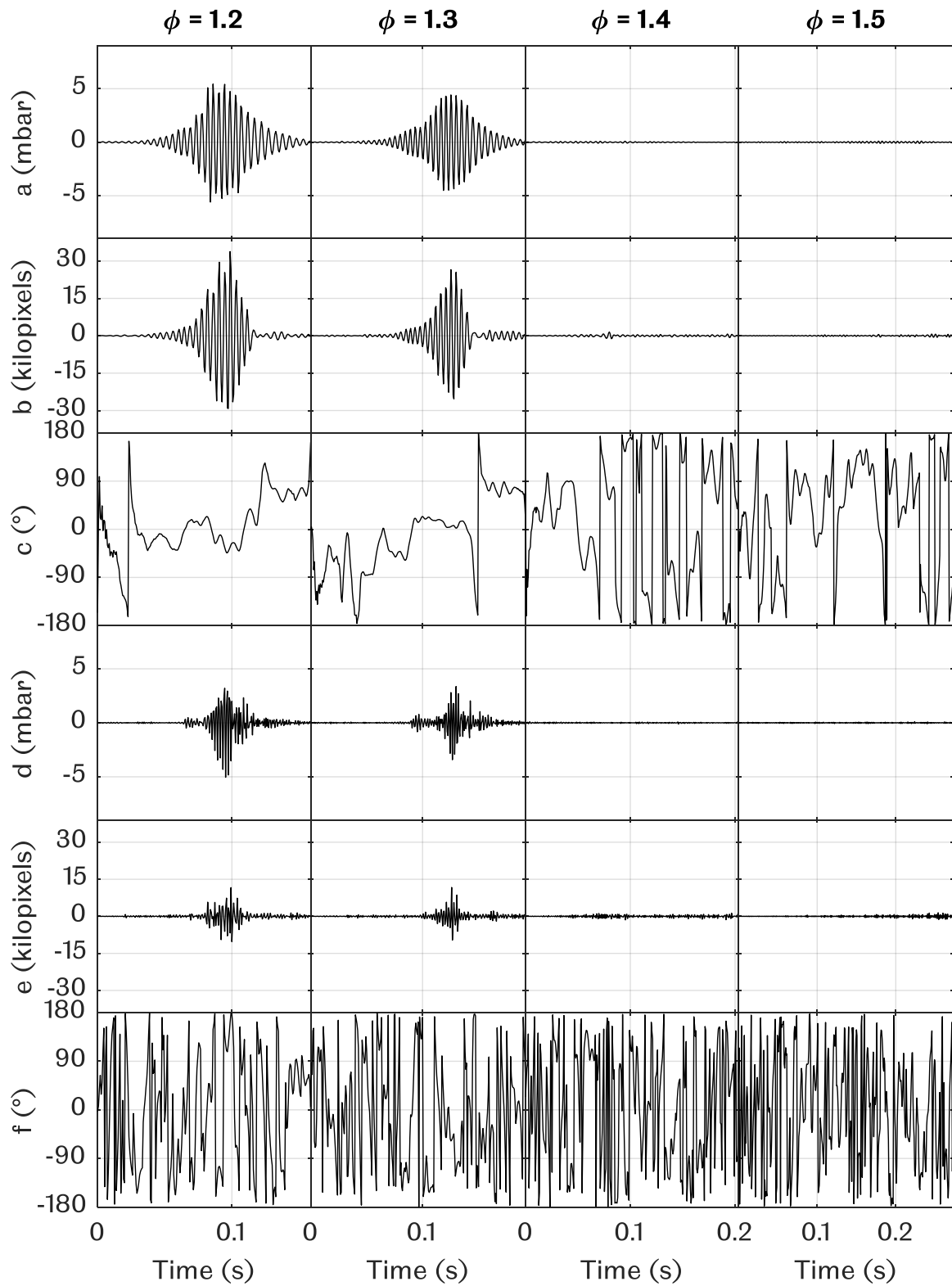
Figure 5.19(f) shows the phase difference between the 400 Hz component of the flame pressure and flame size. For the  $\phi = 0.8$  and  $0.9$  flames, no phase matching was observed while the  $\phi = 1.0$  and  $1.1$  flames showed very short period of phase matching despite the observed growth in their flame pressure and flame size. This was enough to show the independency between the 400 Hz component of the flame pressure and flame size.

Figure 5.20 continues the study for  $\phi = 1.2 - 1.5$  flames. Similar behaviours were observed for both the 200 Hz and 400 Hz component phase difference in Figure 5.20(c) and Figure 5.20(f) respectively. Despite the larger growth in amplitude observed in the 400 Hz component of the  $\phi = 1.2$  flame, its growth still cannot be attributed to phase matching as indicated by the unpredictable fluctuations observed in its phase difference. It is worth noting that the  $\phi = 1.4$  flame showed some signs of phase matching in earlier parts of its propagation, but it did not sustain long enough to cause an increase in the magnitude of both the flame pressure and flame size.



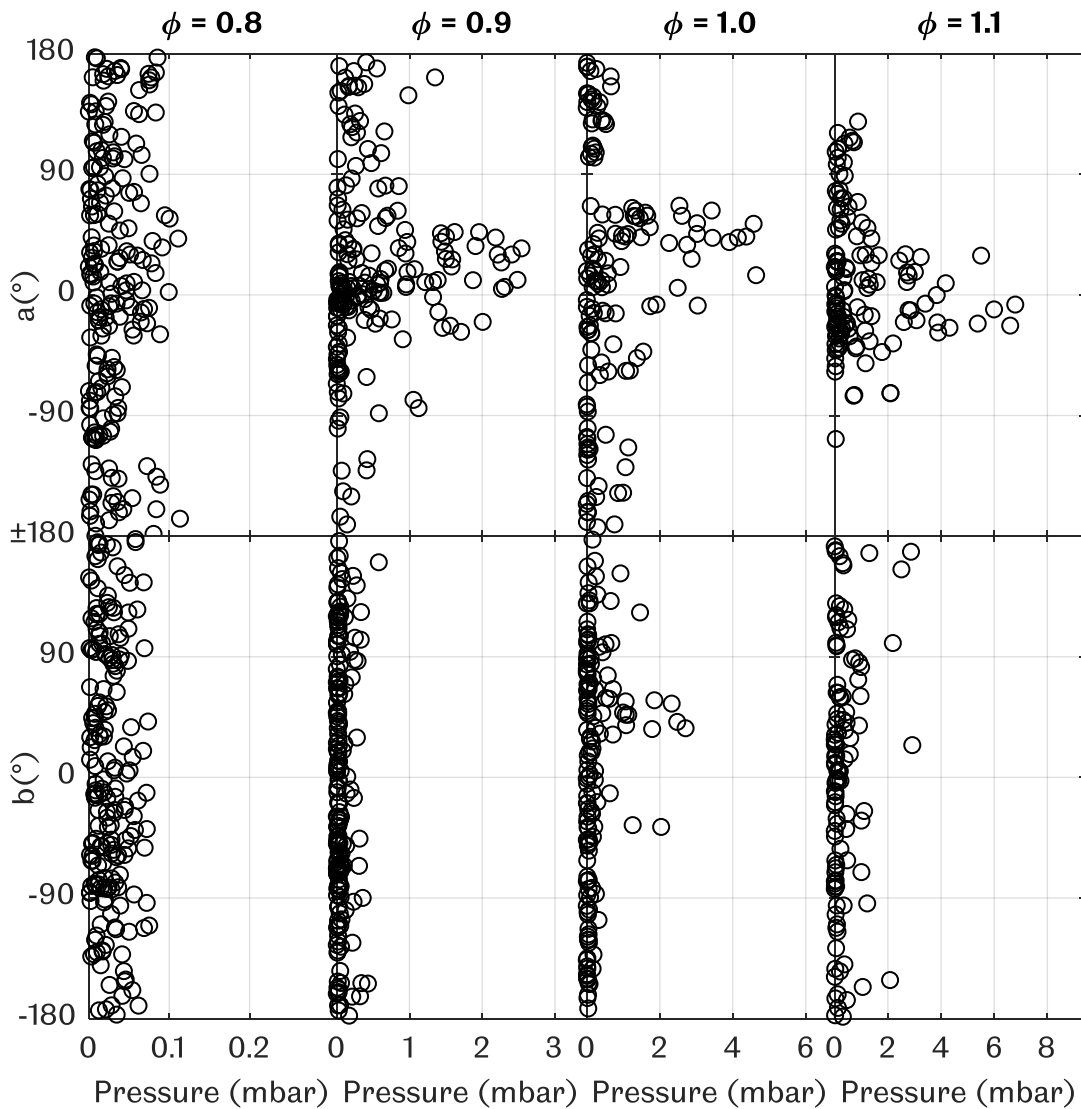
**Figure 5.19 Phase study between tube end pressure and flame size for  $\phi = 0.8 - 1.1$ . Raw signals broken down into 200 Hz component of a) flame pressure, b) flame size, c) phase difference between a) and b). 400 Hz component of d) flame pressure, e) flame size and f) phase difference between d) and e).**





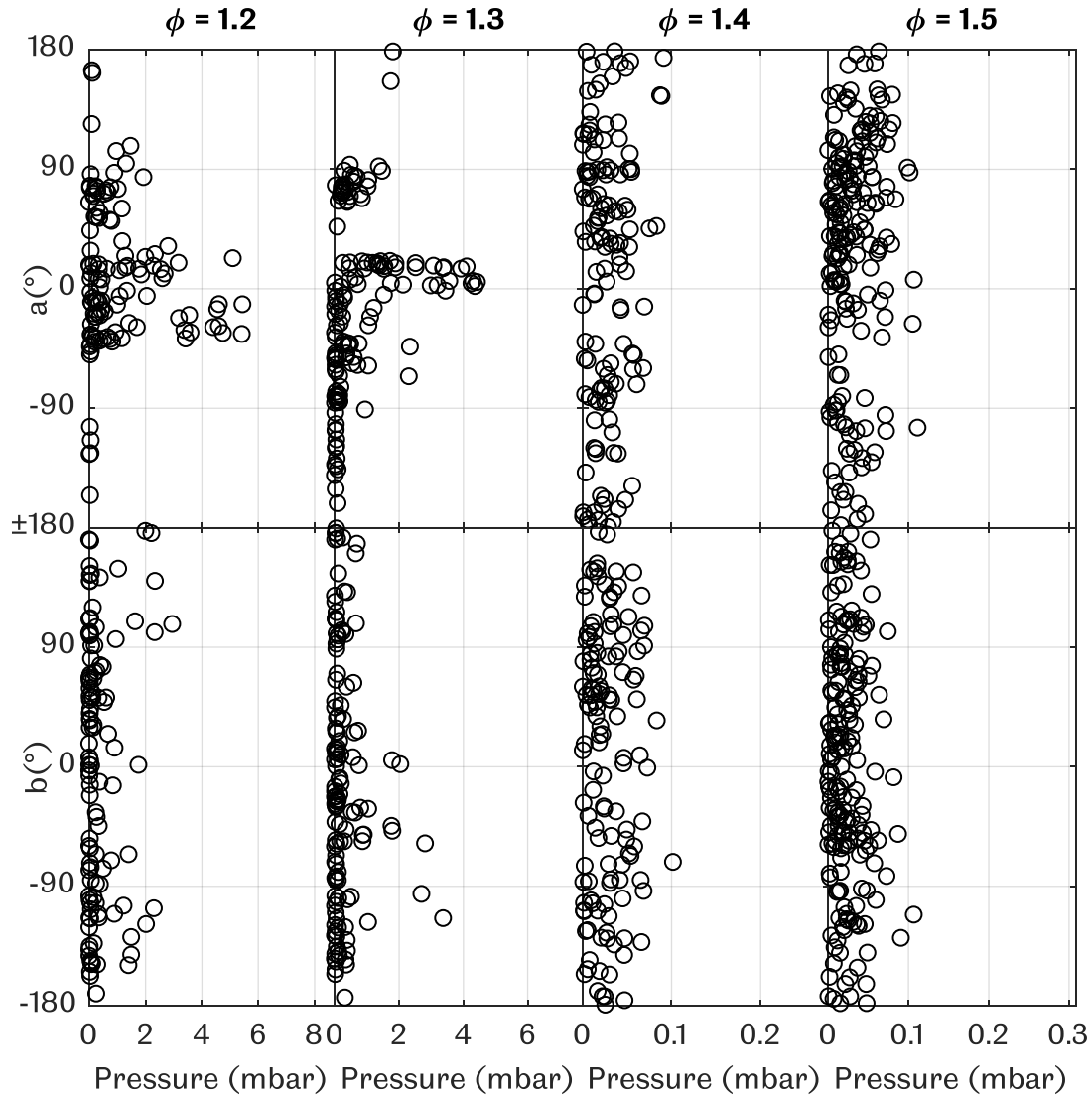
**Figure 5.20 Phase study between tube end pressure and flame size for  $\phi = 1.2 - 1.5$ . Raw signals broken down into 200 Hz component of a) flame pressure, b) flame size, c) phase difference between a) and b). 400 Hz component of d) flame pressure, e) flame size and f) phase difference between d) and e).**

A different approach was taken to analyse the effect of phase matching on the tube end pressure. Phase difference against pressure were plotted for both 200 Hz and 400 Hz components  $\phi = 0.8 - 1.1$  flames in Figure 5.21(a) and Figure 5.21(b) respectively. In general, it was observed that pressure amplifications were more obvious in the 200 Hz components, specifically within the phase difference range of  $0^\circ - \pm 90^\circ$ . Similar to the observations made in Figure 5.19, the maximum pressure increases with equivalence ratio until  $\phi = 1.1$ . No specific trend was observed in the pressure amplifications of the 400 Hz components in Figure 5.21(b), confirming the theories suggested previously based on the time domain graphs in Figure 5.19.



**Figure 5.21 Phase difference for a) 200 Hz component and b) 400 Hz component plotted against tube end pressure signal for flames  $\phi = 0.8 - 1.1$ .**

Figure 5.22 continues the study for  $\phi = 1.2 - 1.5$  flames. The pressure amplification within  $0^\circ - \pm 90^\circ$  phase difference range was also observed in  $\phi = 1.2$  and  $1.3$  flames. The  $\phi = 1.4$  and  $1.5$  flames did not show any pressure amplification, indicating that phase matching occurs only in flames with pulsations and oscillations.



**Figure 5.22 Phase difference for a) 200 Hz component and b) 400 Hz component plotted against tube end pressure signal for flames  $\phi = 1.2 - 1.5$ .**

#### 5.2.4 Non-steady Flame Shape Analysis

The flame shapes were analysed and compared between different mixtures to find any key differences between them during their oscillatory period, thus only points B and C of oscillating flames will be covered for this section. Table 5.2 shows the flame sequence at point B, represented by the white line in each sequence for oscillating flames, which were  $\phi = 0.9 - 1.3$  with constant hydrogen addition,  $R_H = 0.1$ . The  $\phi =$

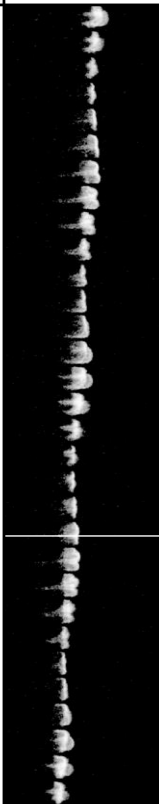
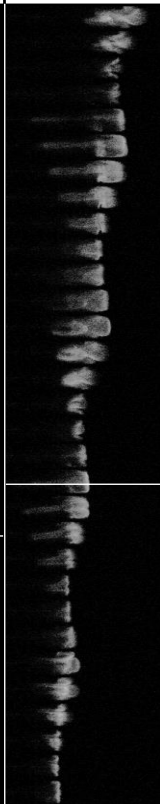
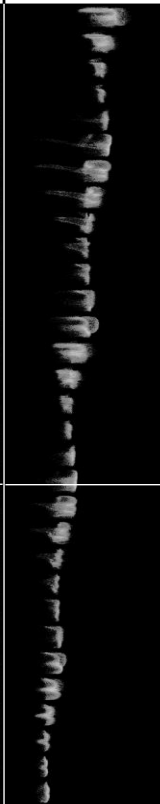
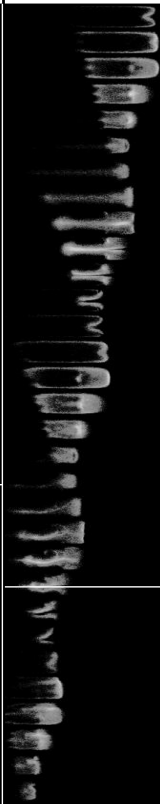
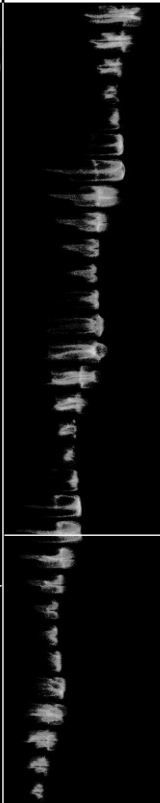
0.9 flame appeared to be brighter than the other flames because the images were brightened since the original images were faint.

**Table 5.2 Flame sequence at point B (white line) for methane flames at constant hydrogen addition,  $R_H = 0.1$ , with increasing equivalence ratio,  $\phi = 0.9 - 1.3$ . Interval of 1/1500 seconds increment for every frame upwards.**

Equivalence Ratio, $\phi$	0.9	1.0	1.1	1.2	1.3
Hydrogen Addition, $R_H$	0.1	0.1	0.1	0.1	0.1
Flame Sequence					

Point B was defined as the point of acceleration increase, where the flame transitions from a pulsatory behaviour to an oscillatory behaviour, thus increasing the flame size due to flame surface inversion. The flames before point B appeared similar in nature, and started oscillating after point B. During the early phases of oscillation, flame  $\phi = 1.1$  and  $1.2$  appeared to be thinner compared to the other flames. The analysis was continued with flame sequence at point C, defined as the point where the flame's underlying acceleration reduces, tabulated in Table 5.3.

**Table 5.3 Flame sequence at point C (white line) for methane flames at constant hydrogen addition,  $R_H = 0.1$ , with increasing equivalence ratio,  $\phi = 0.9 - 1.3$ . Interval of 1/1500 seconds increment for every frame upwards.**

Equivalence Ratio, $\phi$	0.9	1.0	1.1	1.2	1.3
Hydrogen Addition, $R_H$	0.1	0.1	0.1	0.1	0.1
Flame Sequence					

Just before point C, the flames had a more defined oscillating flame shape compared to the oscillating flames observed in Table 5.2, with tails of unburnt gas pushed into the hot burnt gas. The oscillating flame shapes appear to be random and asymmetrical before point C. Beyond point C, the oscillating flame shapes became longer and more symmetrical, except for the lean flame,  $\phi = 0.9$ .

The  $\phi = 0.9$  flame appeared to be consistently oscillating with an approximately constant flame length, which explains the mild increase in underlying flame speed in Figure 5.16(b), while the other flames had a significant increase in their underlying flame speed. The oscillating flames appeared to alternate between a convex flame (normal propagation) and a tulip flame (reversed propagation). The whole flame propagation sequence and flame shape analysis for the equivalence ratio effect study are available in Appendix H and Appendix K respectively.

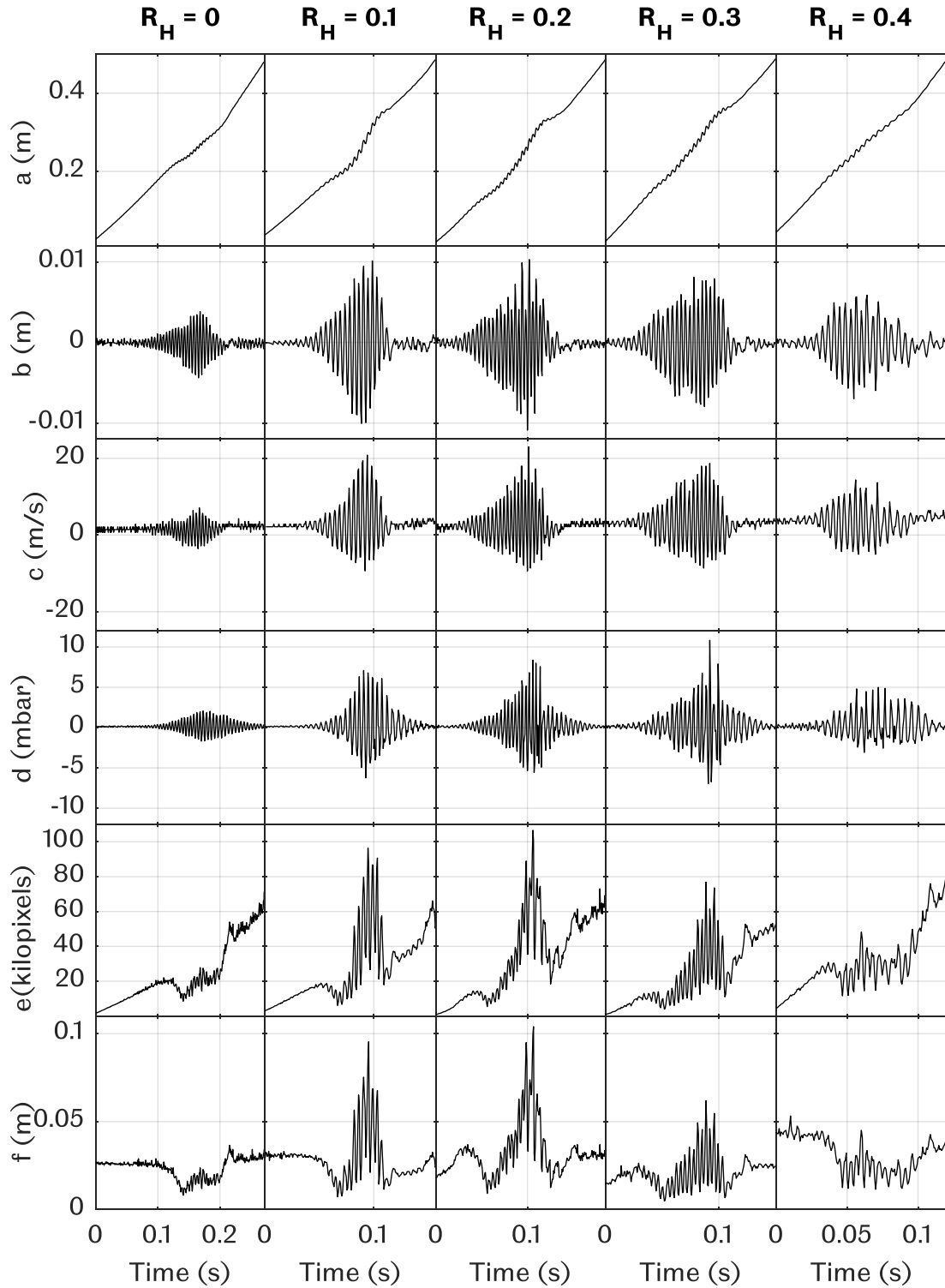
## 5.3 Hydrogen Addition Effect

### 5.3.1 Initial Study

This section analyses the effect of hydrogen addition on flame propagation, while maintaining the same equivalence ratio,  $\phi = 1.1$ . Referring to line (b) in Figure 5.12, this section covers levels of hydrogen addition from  $R_H = 0 - 0.8$ . The increasing laminar burning velocity with each level of hydrogen addition was of interest in order to relate the magnitude of oscillations to the laminar burning velocity of the flames. The flame front position was plotted against time in Figure 5.23(a) and it was observed that all the flames were oscillating.

Based on Figure 5.23(b), the pure methane flame,  $R_H = 0$  oscillated the least compared to the other flames, reaching only  $\sim \pm 0.004$  m of flame front amplitude. Adding hydrogen causes the oscillations to increase almost twice in magnitude, as observed in  $R_H = 0.1$  and  $0.2$  flames. A further increase beyond  $R_H = 0.2$  causes the oscillations to reduce to  $\sim \pm 0.008$  m and  $\sim \pm 0.006$  m for  $R_H = 0.3$  and  $0.4$  respectively. The increase in flame front amplitude in the  $R_H = 0.1$  and  $0.2$  flames were expected with increasing laminar burning velocity. However, the gradual reduction observed as the hydrogen addition was increased beyond  $R_H = 0.2$  was unexpected since the steady increase in laminar burning velocity was expected to cause a monotonic increase in the flame front amplitude.

The raw flame speed was plotted against time in Figure 5.23(c). In general, the initial raw flame speeds appear to increase steadily with increasing hydrogen addition. Similar to the raw flame speed in the previous section, the fluctuations were asymmetrical along the x-axis and did not fall below  $-10$  m/s. On the positive side of the raw speed plots, the highest peak speed was attained by the  $R_H = 0.2$  flame, reaching  $\sim 23$  m/s, followed by the  $R_H = 0.1$  flame with a maximum raw speed of  $\sim 21$  m/s. A gradual decrease in the maximum raw speed was observed as hydrogen was increased beyond  $R_H = 0.2$ .



**Figure 5.23** Effect of hydrogen addition on  $\phi = 1.1$ ,  $R_H = 0 - 0.4$  flames, on a) flame front position, b) flame front position amplitude, c) flame front speed, d) tube end pressure, e) flame size, and f) flame length.

Figure 5.23(d) shows the tube end pressure plot against time. The pure methane flame shows the lowest pressure oscillation magnitude of  $\pm 2$  mbar followed by  $R_H = 0.4$  flame with  $\pm 5$  mbar. Despite having a lower raw speed compared to  $R_H = 0.1$  and  $0.2$  flames, the  $R_H = 0.3$  flame achieved the highest oscillation in pressure of  $\pm 10$  mbar compared to the other two flames.

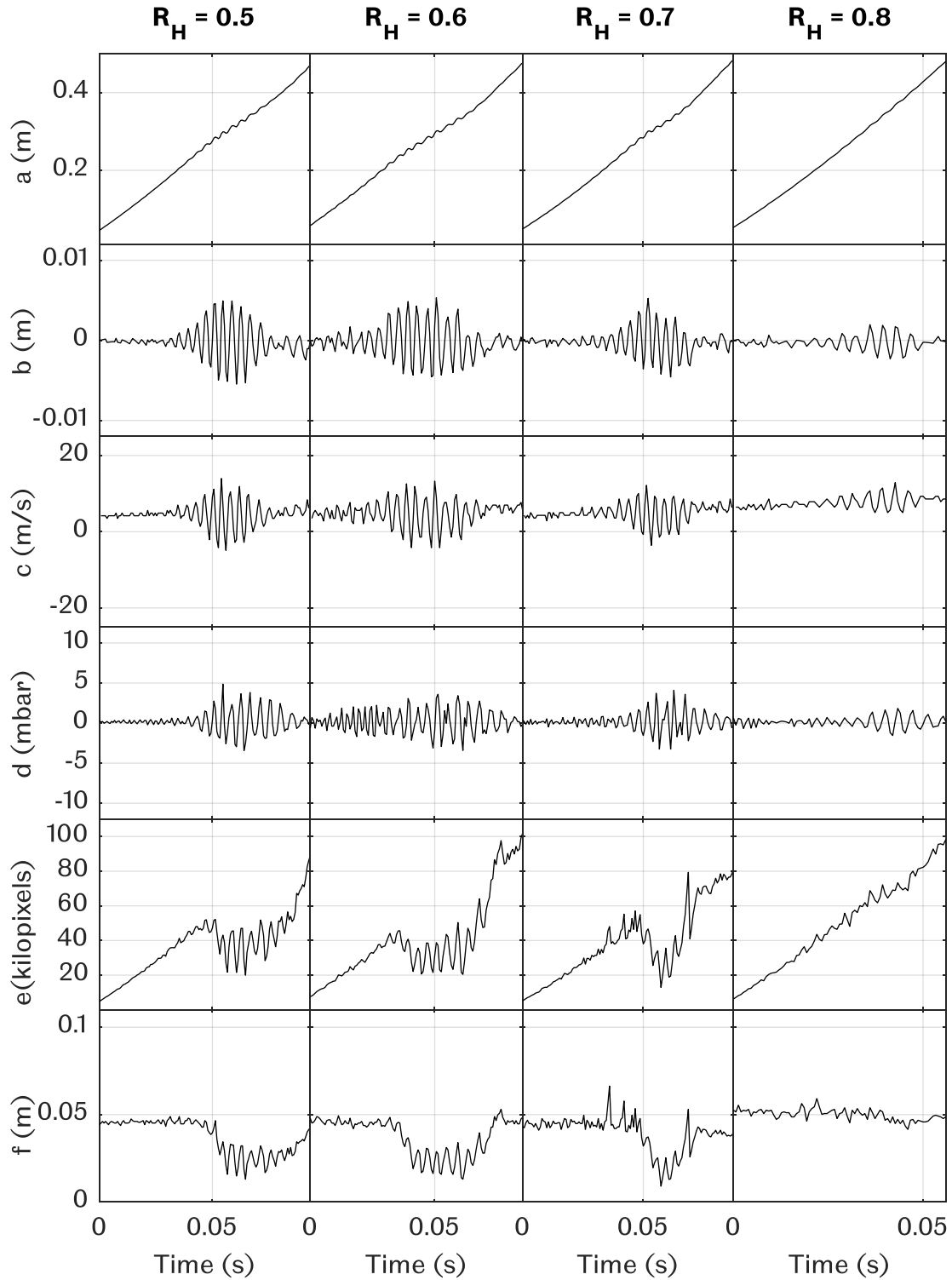
Flame size against time was plotted in Figure 5.23(e). A steady increase in flame size was observed on all flames, starting with an initial size of  $\sim 2$  kilopixels and ending within the range of  $\sim 50$ - $80$  kilopixels. During their oscillatory period, the flames decreased in size before increasing. The  $R_H = 0.1, 0.2$  and  $0.3$  flames increased in size dramatically, reaching  $\sim 110$  kilopixels, while the  $R_H = 0$  and  $0.4$  flames increase in size was insignificant. This behaviour was reflected in their raw speed, where  $R_H = 0.1, 0.2$  and  $0.3$  flames increased in speed by a significant amount whereas the other two flames did not.

Figure 5.23(f) are plots of flame length against time. All flames increased slightly in length as they propagate towards the end of the tube, except for the  $R_H = 0.4$  flame, which decreased in length towards the end of propagation. Similar to the flame size, the flame length oscillation increased significantly during their oscillatory period for  $R_H = 0.1, 0.2$  and  $0.3$  flames, while the other two flames increased by a slight amount.

Proceeding with the remaining flames, Figure 5.24 covers the  $R_H = 0.5 - 0.8$  flames. It was observed that oscillations in the flame starts to reduce as the hydrogen addition was increased further in Figure 5.24(a). With the increase in hydrogen, the propagation time became less, resulting in less cycles of oscillation impacting on the flame as observed in Figure 5.24(b). The reduction in number of cycles was the most obvious in the  $R_H = 0.8$  flame, which only achieved a flame front amplitude of  $\sim \pm 0.002$  m, while the other three flames reached an amplitude of  $\sim \pm 0.005$  m.

The increase in laminar burning velocity obviously increased the raw flame speed, which caused the raw flame speed to barely reach a negative value compared to flames with lower hydrogen addition. The  $R_H = 0.8$  flame in particular did not reach a negative raw flame speed, which might explain why it was the least oscillated flame compared to other flames.





**Figure 5.24 Effect of hydrogen addition on constant equivalence ratio,  $\phi = 1.1$ , and increasing hydrogen addition,  $R_H = 0.5 - 0.8$  flames on a) flame front position, b) flame front position amplitude, c) flame front speed, d) tube end pressure, e) flame size, and f) flame length.**

Plots of tube end pressure signal was plotted against time in Figure 5.24(d). Similar behaviour was observed in the pressure signals, where an increase in pressure amplitude oscillation was observed during the oscillatory period of the flame. The  $R_H = 0.6$  flame appears to be a little different compared to the other flames, where a higher order frequency was clearly visible during its initial stage of propagation. This higher order frequency oscillation was not obvious in the other parameters measured in the experiment, and will be discussed further during frequency analysis.

Figure 5.24(e) are plots of flame size against time. The  $R_H = 0.5, 0.6$  and  $0.7$  flames decreased in size during their oscillatory period, before increasing back once they stop oscillating. The  $R_H = 0.8$  flame size was the least oscillated, which appears similar to a steady flame propagation. The steadiness of the  $R_H = 0.8$  flame size might be explained by its raw flame speed, which did not fall into the negative region.

Figure 5.24(f) shows the plot of flame length against time. Similar to the flame size, the  $R_H = 0.8$  flame remained fairly constant in length, while the other three flames reduced in length during their oscillatory period. This reduction in length is usually associated with pulsating flame behaviour discussed in the earlier parts of this chapter.

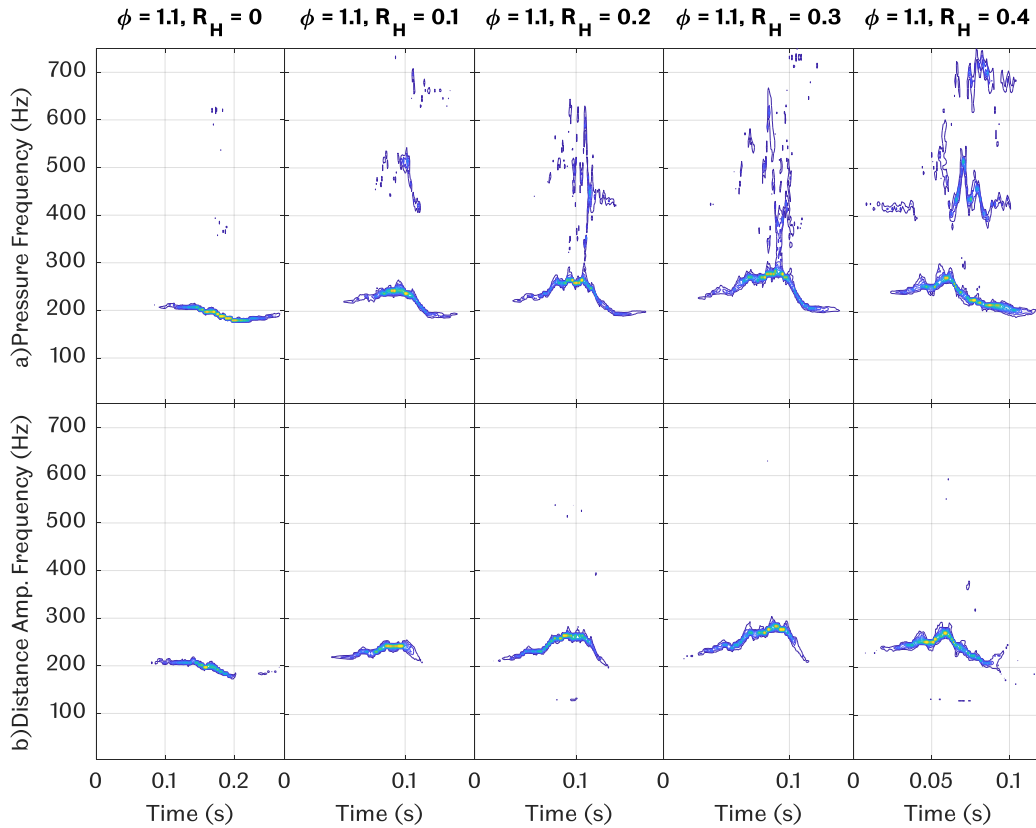
### 5.3.2 Frequency Analysis

The SST plots of pressure and distance amplitude for methane flames with constant equivalence ratio,  $\phi = 1.1$  and increasing hydrogen addition,  $R_H = 0 - 0.4$  were plotted in Figure 5.25. All flames were oscillated at the  $\sim 200$  Hz frequency region, ranging between  $\sim 190 - 300$  Hz for both pressure and distance amplitude signals. The maximum frequency in the  $\sim 200$  Hz region appears to change proportionally with the hydrogen addition,  $R_H$ , increasing from  $\sim 210$  Hz in the  $R_H = 0$  flame up to  $\sim 290$  Hz in the  $R_H = 0.3$  flame, which eventually went down to  $\sim 270$  Hz for the  $R_H = 0.4$  flame.

The excitation of the  $\sim 200$  Hz pressure component appears to excite the higher order pressure frequency for all the flames, indicating that the higher order frequency would not appear without the presence of a  $\sim 200$  Hz oscillation. However, at  $R_H = 0.4$ , higher order frequencies appeared without the presence of a  $\sim 200$  Hz oscillation, between  $\sim 0.01- 0.04$  seconds, attributed to the hydrogen addition.

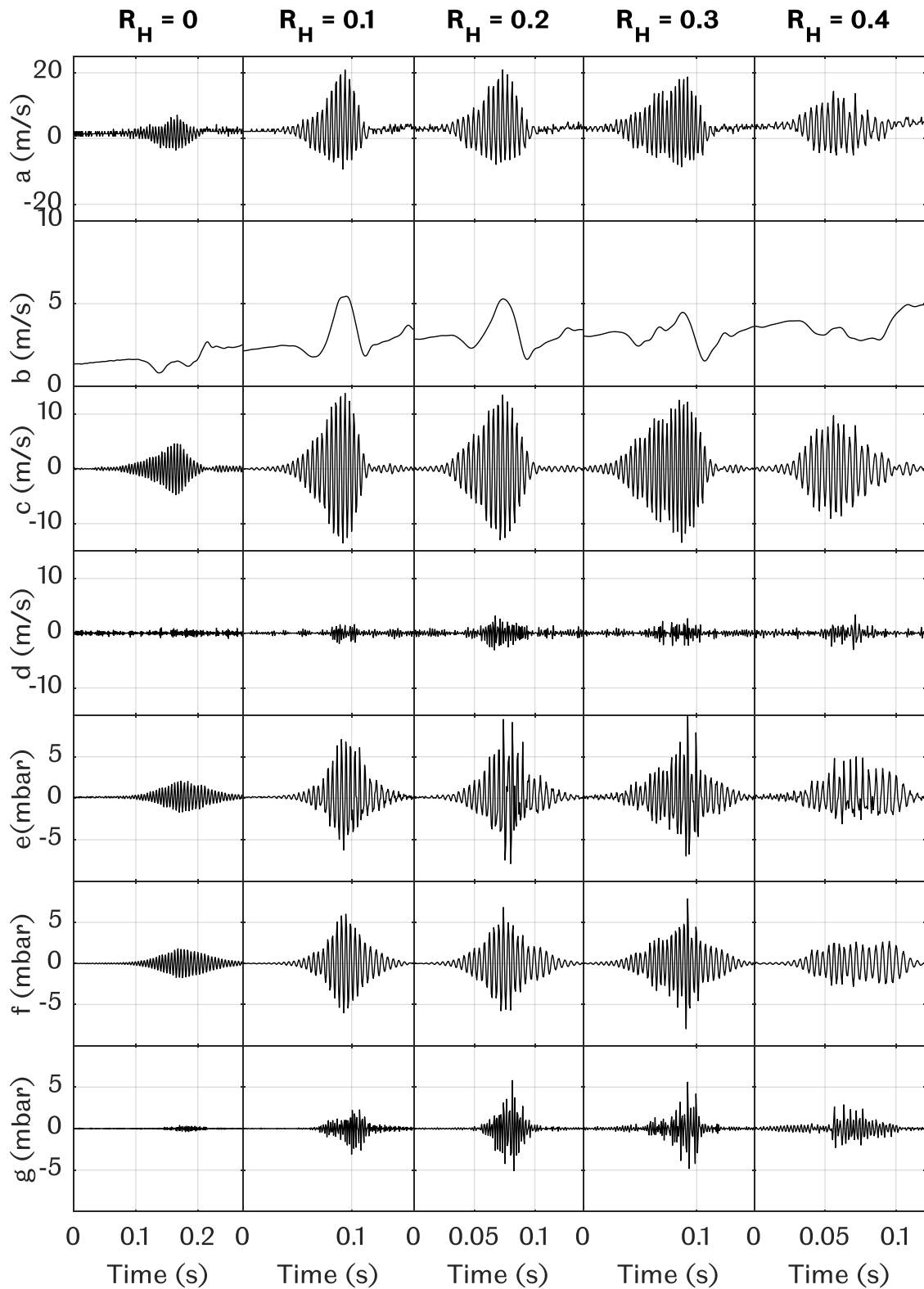
The distance amplitude contours in Figure 5.25 were observed to appear first before the pressure contours, indicating that the flame oscillation excites the pressure oscillations. However, the distance amplitude contours appeared to decay first before the pressure contours. The shift in frequency was similar, which was thought

to be attributed to phase locking between the pressure and distance amplitude signal. In general, the duration of oscillations was getting shorter with increasing amount of hydrogen content. These findings were consistent with the SST plots in the previous section.



**Figure 5.25 SST plots for a) pressure signal and b) distance amplitude signal of methane flames with constant equivalence ratio,  $\phi = 1.1$  and increasing hydrogen addition,  $R_H = 0 - 0.4$ .**

The frequency analysis of the raw flame speed and tube end pressure were plotted in Figure 5.26. Raw flame speed of  $R_H = 0.1 - 0.3$  flames plotted in Figure 5.26(a) appear to be similar in magnitude, while the  $R_H = 0$  and  $0.4$  flames were lower in magnitude. The underlying flame speed was plotted against time in Figure 5.26(b), revealing a different story compared to their raw counterparts. Generally, a steady increase in their initial underlying speed was observed, which was expected with an increase of hydrogen content. It was observed that the  $R_H = 0.1 - 0.3$  flames were accelerated to a higher speed compared to their initial and ending underlying speed, while  $R_H = 0$  and  $0.4$  flames did not show any significant acceleration. Based on this observation, it was concluded that hydrogen addition does not necessarily lead to a sudden acceleration, consistent with the previous findings.



**Figure 5.26** Frequency analysis of a) raw flame speed, broken down into b) underlying flame speed, c) 200 Hz flame speed component, and d) 400 Hz speed component for  $\phi = 1.1$  flames,  $R_H = 0 - 0.4$ . Analysis continued with e) raw pressure signal, broken down into f) 200 Hz pressure signal component and g) 400 Hz pressure signal component.

Proceeding with the 200 Hz speed component in Figure 5.26(c), it was observed that the oscillations increased from  $\sim\pm 5$  m/s at  $R_H = 0$ , to  $\sim\pm 12$  m/s for  $R_H = 0.1, 0.2$  and  $0.3$ . The oscillation speed decreased to  $\sim\pm 10$  m/s when hydrogen was added further at  $R_H = 0.4$ . It was thought that the 200 Hz speed component is responsible for the acceleration/deceleration observed in the underlying flame speed since the increase in the 200 Hz speed was usually accompanied by an increase/decrease in the underlying flame speed. The magnitude of the 200 Hz speed oscillation seems to be the deciding factor whether the flame undergoes a sudden acceleration or continues decelerating after the initial deceleration.

The 400 Hz speed component was plotted against time in Figure 5.26(d). Small fluctuations of equal amplitude were observed in the  $R_H = 0$  flame. Similar to the 200 Hz speed component, an increase was observed with hydrogen addition, but of a smaller magnitude. The increase in the 400 Hz speed component coincides with the peak magnitude of the 200 Hz speed component, suggesting that the increase in the 400 Hz component is a result from an increase in the 200 Hz speed component.

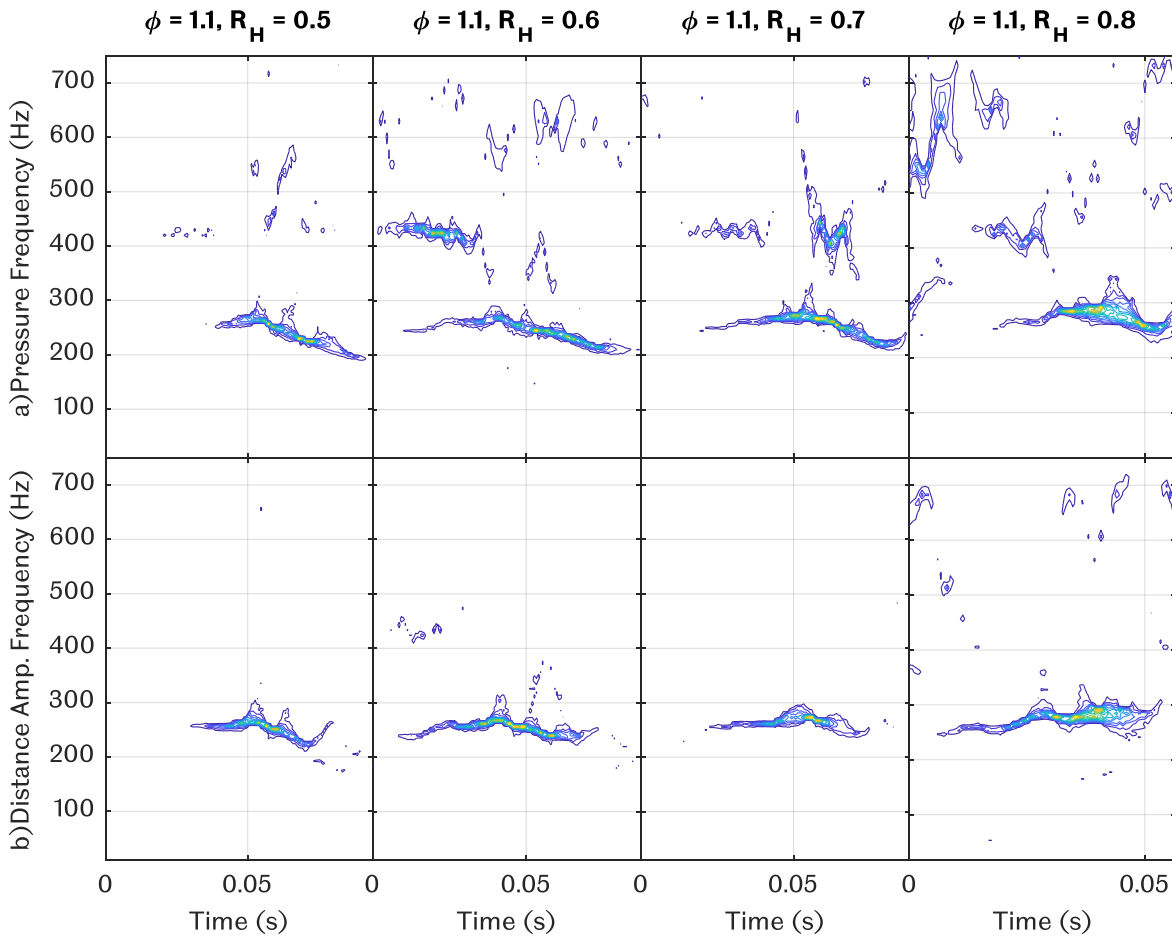
Figure 5.26(f) are plots of the 200 Hz pressure component against time, broken down from the raw pressure signal in Figure 5.26(e). The 200 Hz pressure component appeared to be the main oscillating component and displayed similar fluctuation in magnitude as the 200 Hz speed component. The main difference was the gradual decay of the oscillatory pressure component compared to the sudden reduction in the 200 Hz speed component. It is also worth noting that the growth of the 200 Hz pressure component started after the growth of the 200 Hz speed component, suggesting that the pressure was driven by the change in flame speed. This hypothesis was further supported by the gradual decay observed in the 200 Hz pressure component after the sudden decrease in the 200 Hz speed component.

Figure 5.26(g) shows the plot of 400 Hz pressure component against time. In general, the 400 Hz pressure components appear to be more prominent compared to the 400 Hz speed components, some reaching similar magnitude to their 200 Hz pressure components of  $\sim\pm 5$  mbar. This behaviour was not observed in the 400 Hz speed component, which were significantly lower compared to their 200 Hz speed component.

It was also observed that the 400 Hz pressure component fluctuations were very low in the  $R_H = 0$  flame compared to other flames, which suggests the relationship between hydrogen addition and the 400 Hz pressure component. For low hydrogen content flames, the 400 Hz pressure component only increases when an increase in the 200 Hz pressure component was observed. A different behaviour was observed

for the  $R_H = 0.4$  flame, where a slight increase in the 400 Hz component was recorded before there was a significant increase in the 200 Hz component.

Frequency analysis was continued for the  $R_H = 0.5 - 0.8$  flames with SST plots of pressure and distance amplitude signals in Figure 5.27. The excitation of higher order frequencies without the presence of a  $\sim 200$  Hz oscillation was more evident in higher hydrogen cases, previously observed in the  $R_H = 0.4$  flame in Figure 5.25. The duration of  $\sim 200$  Hz oscillations were observed to be shorter, which was expected with an increase in laminar burning velocity with hydrogen addition.



**Figure 5.27 SST plots for a) pressure signal and b) distance amplitude signal of methane flames with constant equivalence ratio,  $\phi = 1.1$  and increasing hydrogen addition,  $R_H = 0.5 - 0.8$ .**

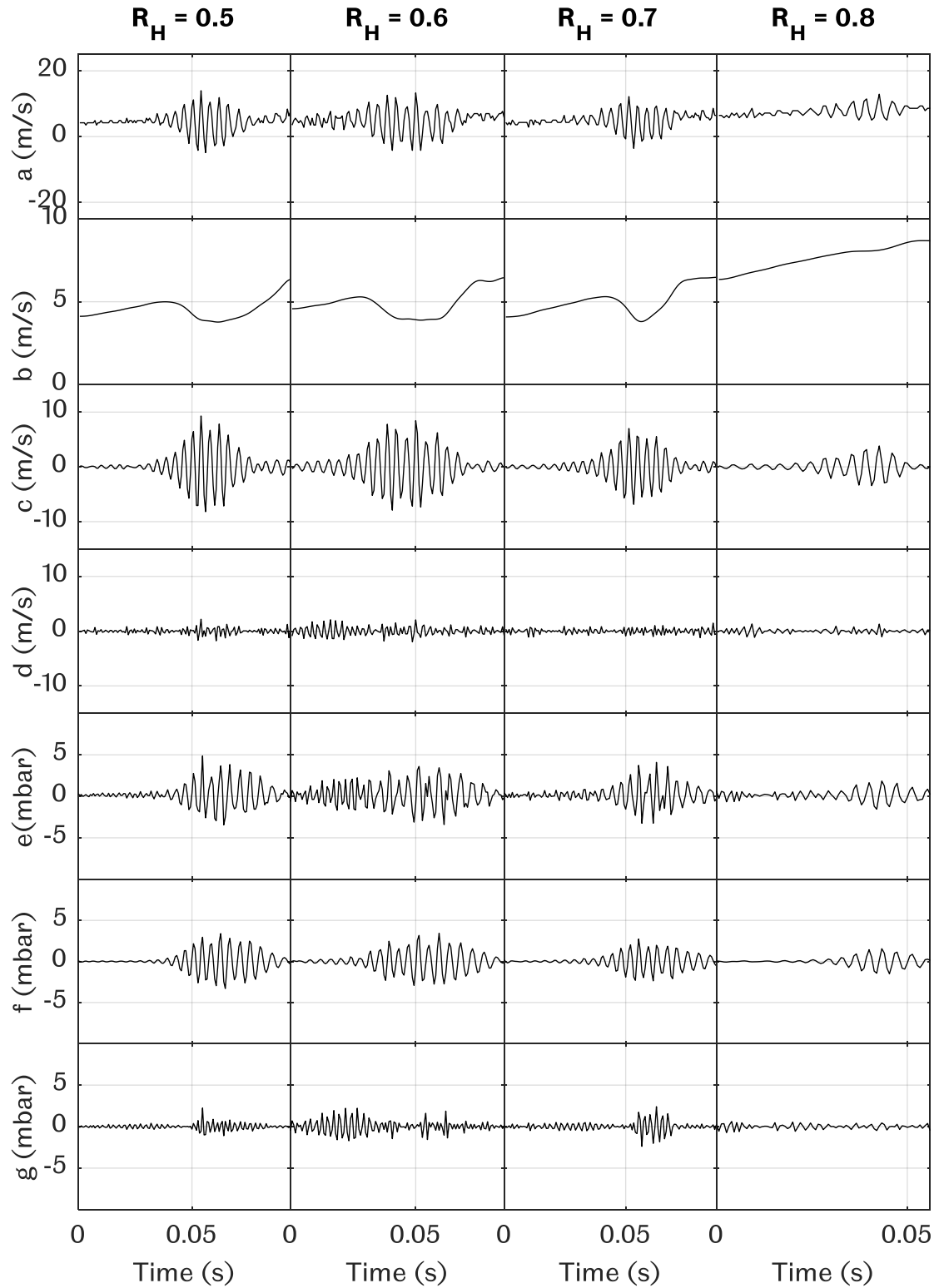
The shift in frequency of the  $\sim 200$  Hz oscillations were observed to be less dramatic compared to lower hydrogen content flames. However, the frequency of oscillations was higher compared to lower hydrogen content flames, most starting with a frequency of  $\sim 250$  Hz. This was thought to be the effect of hydrogen addition, which effectively reduces the density of the resultant mixture, thus increasing the resonance frequencies in the tube.

The raw speed was plotted against time in Figure 5.28(a), showing a similar looking raw speed profile for the  $R_H$  0.5 and 0.6 flames. The raw speed looks slightly different for the  $R_H$  0.7 and 0.8 flames as the duration and magnitude of the oscillation appears to be gradually decreasing with hydrogen addition.

Figure 5.28(b) shows the plot of the underlying flame speed against time. It was observed that the initial underlying speed for  $R_H = 0.5 - 0.7$  flames were approximately similar at  $\sim 4.5$  m/s, while the  $R_H = 0.8$  flame started with an underlying speed of  $\sim 6$  m/s. The first three flames experienced a slight deceleration as they propagate through the tube, signified by the dip in their underlying speed, whereas the  $R_H = 0.8$  flame did not show any significant deceleration.

The observed deceleration in the underlying speed for the  $R_H$  0.5 - 0.7 flames were thought to be a direct cause of the 200 Hz speed component oscillation plotted in Figure 5.28 (c). The 200 Hz speed component in the decelerated flames reached a magnitude of  $\sim \pm 9$  m/s, while the  $R_H = 0.8$  flame only reached a magnitude of  $\sim \pm 5$  m/s. The observed deceleration may look like a new behaviour, but it is not. The deceleration is instead the same as the initial deceleration observed in the lower hydrogen content flames of  $R_H = 0 - 0.4$ . The gradual increase in laminar burning velocity with increasing hydrogen content causes the flame to propagate faster, giving less time for the oscillations to build up.

Figure 5.28(d) shows the 400 Hz speed component plotted against time. In lower hydrogen content flames, the 400 Hz speed component only increases when an increase in the 200 Hz speed component was observed. This behaviour changed as the hydrogen content was increased, where the 400 Hz speed component increased even before there was any significant increase in the 200 Hz speed component, as observed in the  $R_H$  0.6 flame. The 400 Hz speed oscillation however, was not able to cause any significant changes in the underlying flame speed. The observed reduction in the 200 Hz speed oscillation caused minimal oscillations in the 400 Hz speed component.



**Figure 5.28** Frequency analysis of a) raw flame speed, broken down into b) underlying flame speed, c) 200 Hz flame speed component, and d) 400 Hz speed component for  $\phi = 1.1$  flames,  $R_H = 0.5 - 0.8$ . Analysis continued with e) raw pressure signal, broken down into f) 200 Hz pressure signal component and g) 400 Hz pressure signal component.



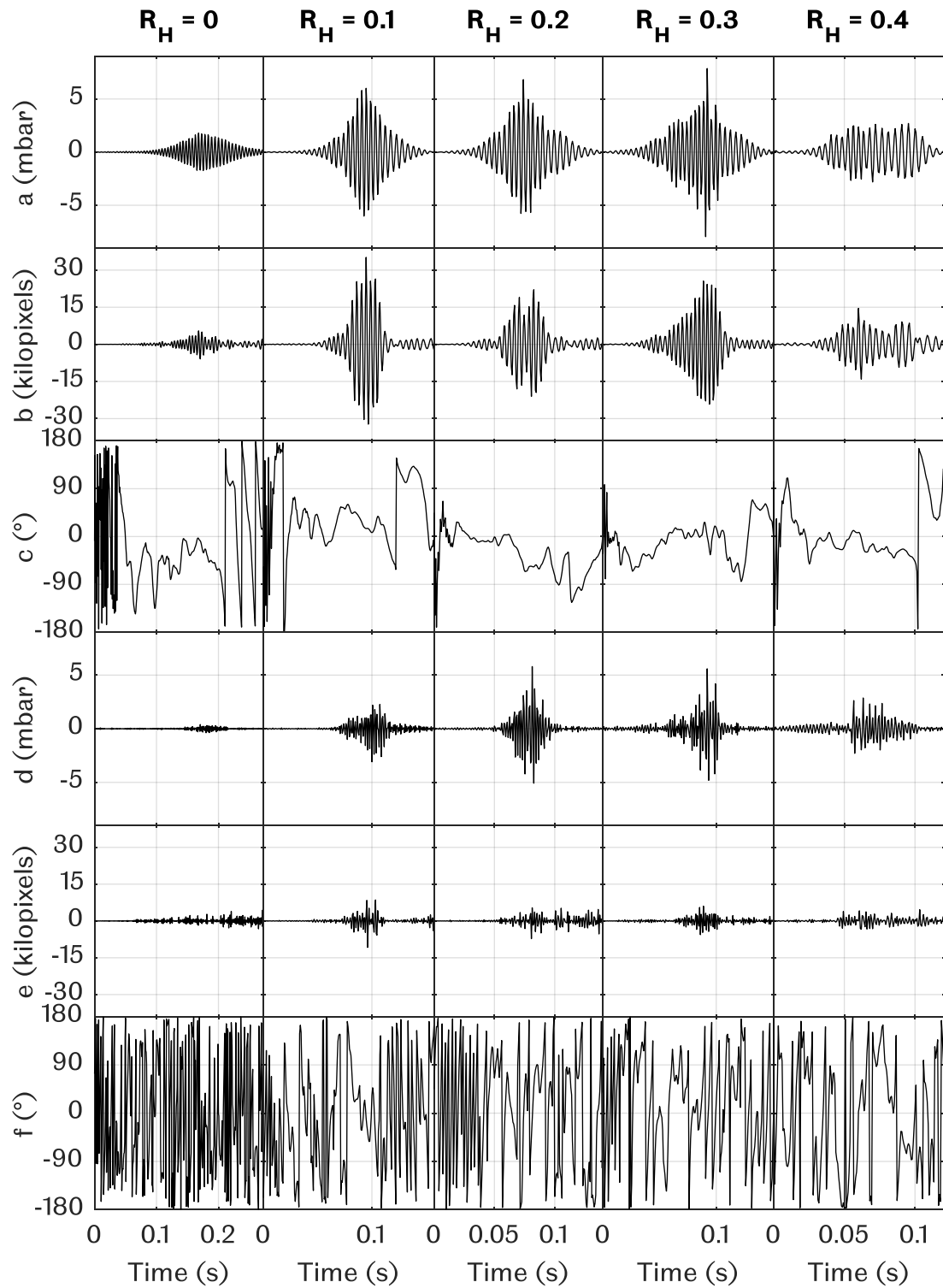
The raw pressure signals in Figure 5.28(e) was broken down into their 200 Hz and 400 Hz components in Figure 5.28(f) and Figure 5.28(g) respectively. The oscillatory component of the raw pressure signals for  $R_H$  0.5 - 0.7 flames were of a similar magnitude, while the  $R_H = 0.8$  flame was smaller. The decomposed pressure signals appear to be similar to the broken-down signals of previous flames, except for the  $R_H = 0.6$  flame. The 400 Hz pressure component of the  $R_H = 0.6$  flame built up to a significant level before there was an increase in the 200 Hz pressure component. The increase in the 400 Hz pressure component was reflected in its speed component, which was discussed in the previous paragraph. This behaviour reveals that the 400 Hz pressure component could build up even without an increase in the 200 Hz pressure component.

### 5.3.3 Phase Analysis

Phase study between the tube end pressure and flame size was conducted for  $R_H = 0 - 0.4$  flames in Figure 5.29. The 200 Hz component of the tube end pressure and flame size were plotted against time in Figure 5.29(a) and Figure 5.29(b) respectively. It was previously mentioned that the 200 Hz pressure component of  $R_H = 0.1 - 0.3$  flames were of a similar peak amplitude, but it was not reflected in their flame size, with  $R_H = 0.2$  flame having a noticeably lower peak amplitude at  $\sim \pm 23$  kilopixels compared to the  $R_H = 0.1$  and  $0.3$  flames at  $\sim \pm 30$  kilopixels.

Despite the lower peak amplitude, pressure amplification still occurred in the  $R_H = 0.2$  flame. This was also observed in the  $R_H = 0$  and  $0.4$  flames which had considerably lower flame size compared to the other flames. It was also noticed that the pressure oscillations built up first before the flame size, suggesting that the flame size oscillations were driven by the pressure. However, the influence of pressure on the flame size stopped once the pressure started to decay, similar to the behaviour observed in the 200 Hz speed component.

The phase difference between the 200 Hz components were plotted against time in Figure 5.29(c). In general, all the flames had a period of phase matching which led to a build-up in both pressure and flame size oscillations, followed by an increase in the phase difference once the flame size was reduced abruptly. It was noticed that the  $R_H = 0.4$  flame did not reach similar peak pressure to the  $R_H = 0.1-0.3$  flames despite having an approximately similar period of phase matching, indicating that phase matching does not necessarily lead to high peak pressures.



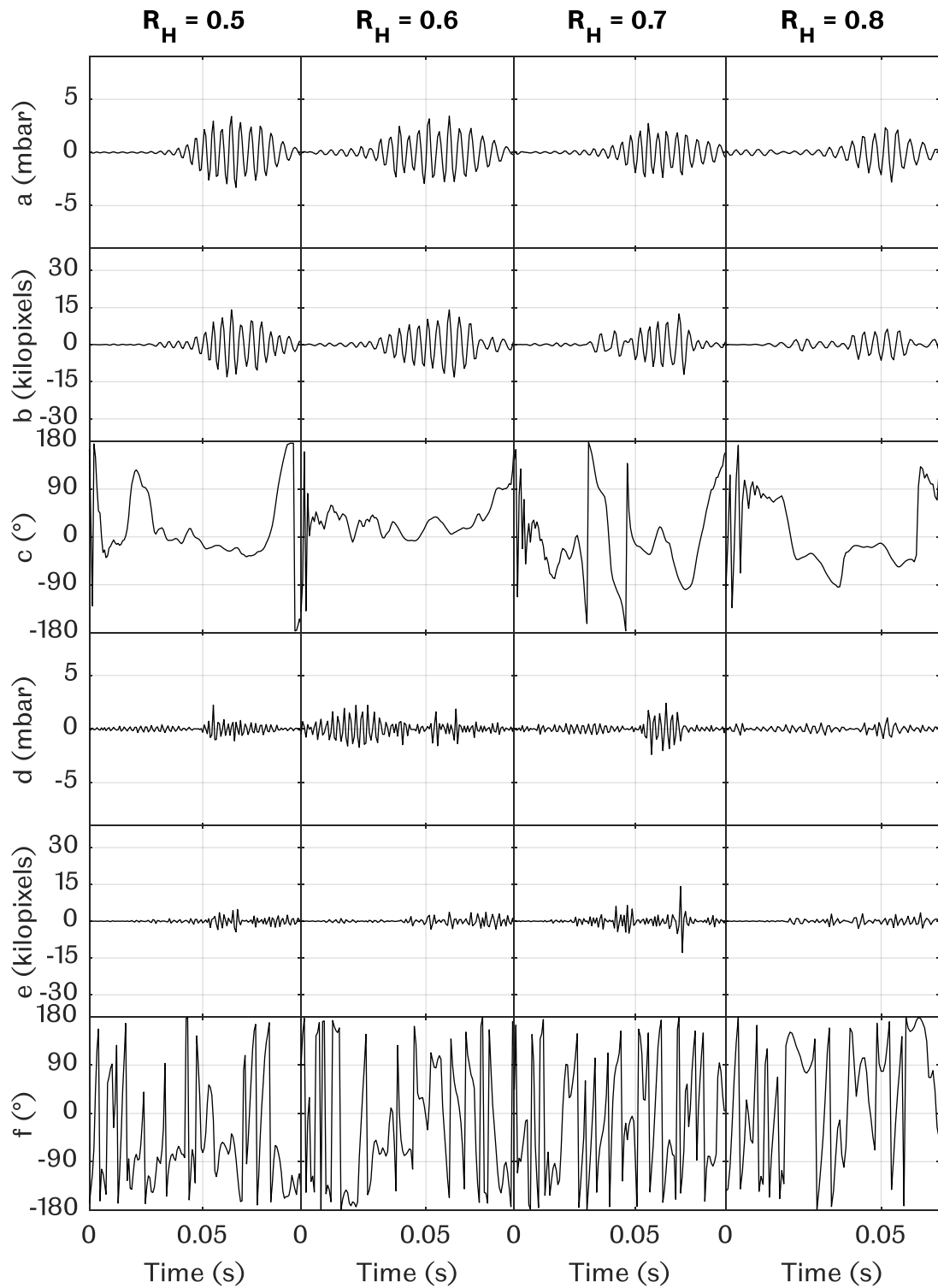
**Figure 5.29 Phase study between tube end pressure and flame size for  $\phi = 1.1$  flames,  $R_H = 0 - 0.4$ . Raw signals broken down into 200 Hz component of a) flame pressure, b) flame size, c) phase difference between a) and b). 400 Hz component of d) flame pressure, e) flame size and f) phase difference between d) and e).**

Proceeding with the 400 Hz component phase difference, despite the significant growth in the 400 Hz pressure component in Figure 5.29(d), its flame size counterpart in Figure 5.29(e) were not affected significantly. This was further supported by the phase difference between the 400 Hz components in Figure 5.29(f), which shows very little evidence of phase matching. It cannot be denied that there were cases where the flame size amplification occurred during pressure amplification, suggesting phase matching, for example at  $R_H = 0.1$  and  $0.3$ , but other cases suggested otherwise. The  $R_H = 0$  and  $0.2$  flames exhibited flame size amplification even without pressure amplification.

Figure 5.30 continues the phase study for  $R_H = 0.5 - 0.8$  flames. Despite the lower oscillatory magnitude in the 200 Hz pressure and flame size component in Figure 5.30(a) and Figure 5.30(b), phase matching was still evident as suggested by the phase difference in Figure 5.30(c). While phase matching was thought to be an uninterrupted phenomenon, the  $R_H = 0.7$  flame had proven that the components can be out of phase in the middle of an oscillation. The initial reduction in phase difference was interrupted midway between  $-0.025 - 0.05$  seconds, suggesting that the pressure and flame size were out of phase, before becoming in phase again, causing a steady growth of both flame size and pressure.

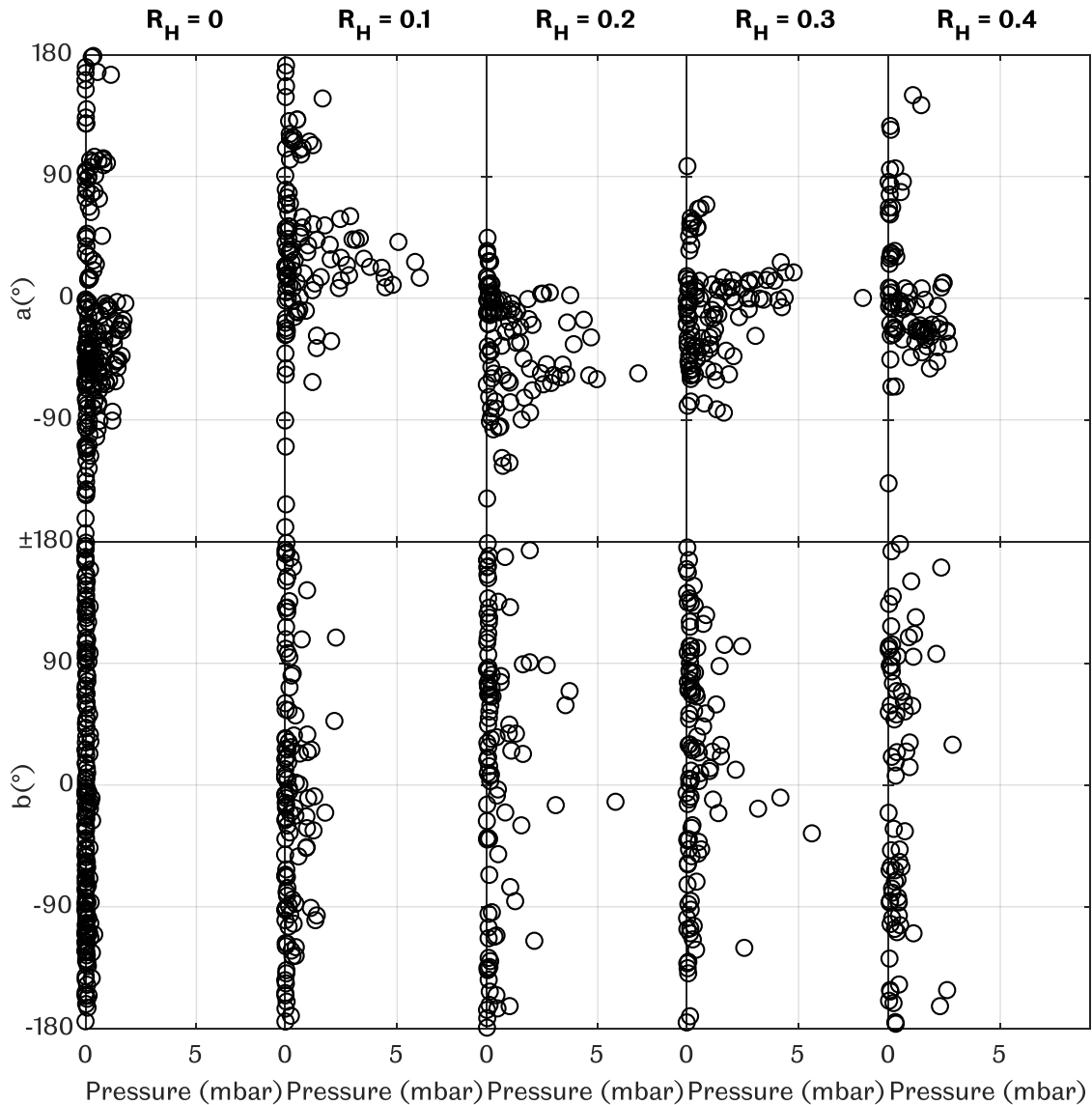
Unlike the  $R_H = 0.4$  flame,  $R_H = 0.5$  and  $0.6$  flames were observed to have a shorter period of phase matching, but reached higher peak pressure of  $\sim \pm 3.4$  mbar, compared to  $\sim \pm 2.6$  mbar for  $R_H = 0.4$  flame. An increase in the hydrogen content makes the flame propagate faster, giving less time for the flame to interact with the pressure fluctuations, which can be seen in the  $R_H = 0.8$  flame, reaching only  $\sim \pm 2.3$  mbar. In general, these observations indicate that a shorter period of phase matching does not necessarily lead to a lower pressure build-up.

The 400 Hz components of pressure and flame size were plotted against time in Figure 5.30(d) and Figure 5.30(e) respectively. Similar to the lower hydrogen flames in Figure 5.29, no significant phase matching was observed in the phase difference plots in Figure 5.30(f), suggesting that significant amplification in the 400 Hz pressure component did not necessarily affect the 400 Hz flame size component.



**Figure 5.30 Phase study between tube end pressure and flame size for  $\phi = 1.1$  flames,  $R_H = 0.5 - 0.8$ . Raw signals broken down into 200 Hz component of a) flame pressure, b) flame size, c) phase difference between a) and b). 400 Hz component of d) flame pressure, e) flame size and f) phase difference between d) and e).**

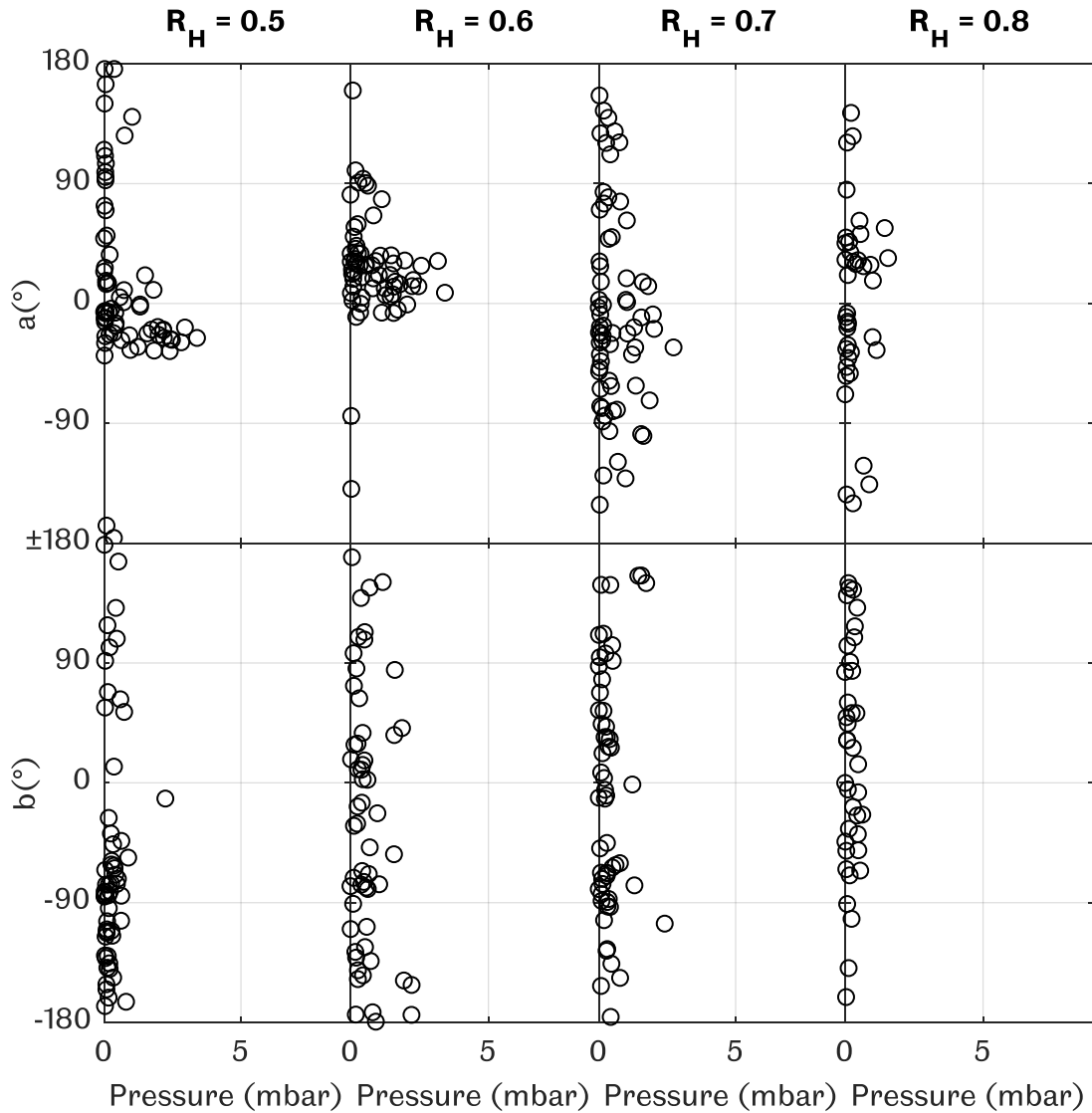
Phase difference of  $\phi = 1.1$ ,  $R_H = 0 - 0.4$  flames were plotted against their tube end pressure in Figure 5.31, for both the 200 Hz and 400 Hz components. Phase difference for the 200 Hz components in Figure 5.31(a) shows that the pressure amplification occurred within the phase difference range of  $0 \pm 90^\circ$  despite the difference in pressure magnitude, while a scattered pressure amplification was observed for the 400 Hz components in Figure 5.31(b).



**Figure 5.31 Phase difference for a) 200 Hz component and b) 400 Hz component plotted against tube end pressure signal for  $\phi = 1.1$  flames,  $R_H = 0 - 0.4$ .**

The observed phase matching in the 200 Hz component suggests that the pressure and flame size formed a feedback loop in the 200 Hz frequency range only, while the absence of phase matching in the 400 Hz component suggests that another mechanism was responsible for the amplifications observed in both pressure and

flame size. It is worth noting that with a steady increase in hydrogen, the scattered 400 Hz pressure amplification reached a magnitude similar to the 200 Hz pressure. The study was continued for the  $R_H = 0.5 - 0.8$  flames in Figure 5.32. Even with a gradual reduction in the pressure with increasing hydrogen, phase matching was still observed in the 200 Hz components, shown in Figure 5.32(a), while the 400 Hz phase difference in Figure 5.32(b) still shows no evidence of phase difference.




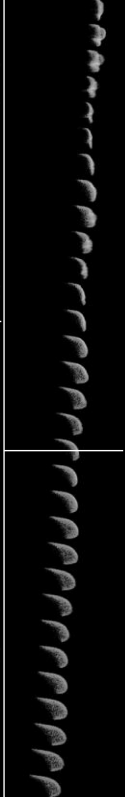
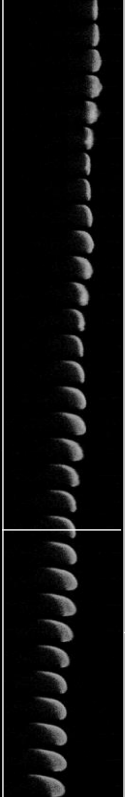

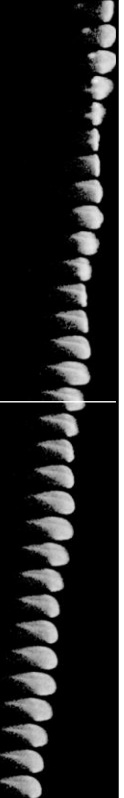
**Figure 5.32 Phase difference for a) 200 Hz component and b) 400 Hz component plotted against tube end pressure signal for  $\phi = 1.1$  flames,  $R_H = 0.5 - 0.8$ .**

### 5.3.4 Non-steady Flame Shape Analysis

Points B and C were analysed in this section to find key differences between unsteady flame propagations in this batch of studied flames. Table 5.4 shows the sequence of flames at point B for flames at a constant equivalence ratio,  $\phi = 1.1$ , and

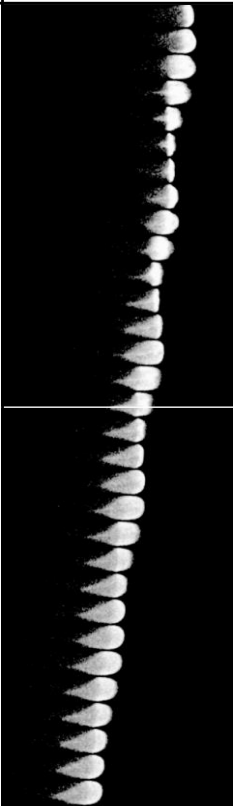
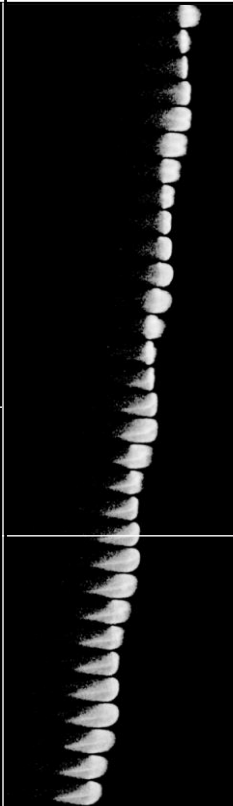
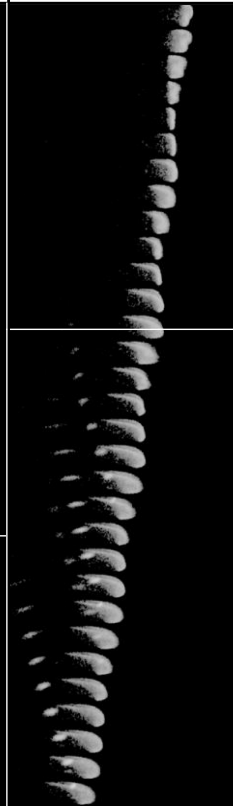
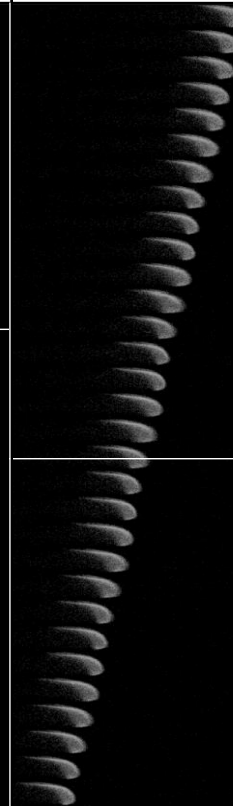
increasing hydrogen addition,  $R_H = 0 - 0.4$ . The  $R_H = 0.4$  flame was brightened because of the faintness of the original images.

**Table 5.4 Flame sequence at point B (white line) for methane flames at constant equivalence ratio,  $\phi = 1.1$ , with increasing hydrogen addition,  $R_H = 0 - 0.4$ . Interval of 1/1500 seconds increment for every frame upwards.**

Equivalence Ratio, $\phi$	1.1	1.1	1.1	1.1	1.1
Hydrogen Addition, $R_H$	0	0.1	0.2	0.3	0.4
Flame Sequence					

Visual comparison between the flames shows a reduction in the flame brightness with increasing hydrogen addition, which was believed to be the result of reduction in the carbon content in the mixtures. It was also noticed that the increase in hydrogen contributed to the increase in flame area, due to increased reactivity from the addition of hydrogen. The appearance of flame surface inversions (Rayleigh-Taylor tail) was more apparent with higher hydrogen content. Apart from the difference in terms of tail appearance, the flames did not exhibit any significant difference between each other in terms of flame shape, as observed previously in the equivalence ratio effect study. Study was continued with the flame sequence at point B for flames with further addition of hydrogen,  $R_H = 0.5 - 0.8$ , shown in Table 5.5.

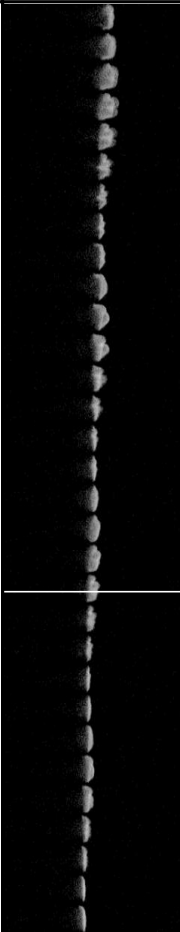

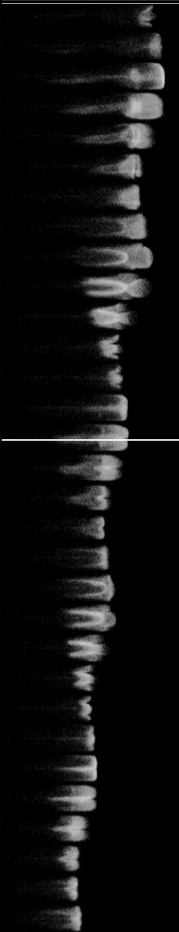


**Table 5.5 Flame sequence at point B (white line) for methane flames at constant equivalence ratio,  $\phi = 1.1$ , with increasing hydrogen addition,  $R_H = 0.5 - 0.8$ . Interval of 1/1500 seconds increment for every frame upwards.**

Equivalence Ratio, $\phi$	1.1	1.1	1.1	1.1
Hydrogen Addition, $R_H$	0.5	0.6	0.7	0.8
Flame Sequence				

Based on Table 5.5, flame surface inversions became less obvious with increasing hydrogen. The  $R_H = 0.7$  and  $0.8$  flames appeared to continue pulsating instead of oscillating. The drastic increase in laminar burning velocity made the flames respond less to the pressure perturbations, which ultimately made the flame only pulsate. All the flames in Table 5.5 did not continue with significant oscillatory behaviour, but instead returned pulsating. The flames in Table 5.4 continued oscillating to a significant magnitude, and were analysed in Table 5.6.



**Table 5.6 Flame sequence at point C (white line) for methane flames at constant equivalence ratio,  $\phi = 1.1$ , with increasing hydrogen addition,  $R_H = 0 - 0.4$ . Interval of 1/1500 seconds increment for every frame upwards.**

Equivalence Ratio, $\phi$	1.1	1.1	1.1	1.1	1.1
Hydrogen Addition, $R_H$	0	0.1	0.2	0.3	0.4
Flame Sequence					

Significantly oscillated flames at constant equivalence ratio,  $\phi = 1.1$ , and increasing hydrogen addition,  $R_H = 0 - 0.4$  at point C were tabulated and analysed in Table 5.6. Obvious difference between the flame oscillations were observed in the flame sequence. The  $R_H = 0$  flame appears to be oscillating with minimal elongation. An increment to  $R_H = 0.1$  shows a significant difference both in shape and speed of the flame, which appears to be of similar magnitude to the  $R_H = 0.2$  and  $0.3$  flames.

Comparing their underlying velocity in Figure 5.26, all  $R_H = 0.1 - 0.3$  flames achieved an underlying velocity of  $\sim 5$  m/s, 200 Hz velocity component of  $\sim \pm 12$  m/s, but a difference in their  $\sim 400$  Hz velocity component, which was low for the  $R_H = 0.1$  flame.

It was observed that the  $R_H = 0.1$  flame was asymmetrical compared to the  $R_H = 0.2$  and  $0.3$  flames. The higher  $\sim 400$  Hz amplitude was thought to be the effect of the symmetrical flame shape. The whole flame propagation sequence and flame shape analysis for the hydrogen addition effect study are available in Appendix I and Appendix L respectively

## 5.4 Constant Laminar Burning Velocity Comparison

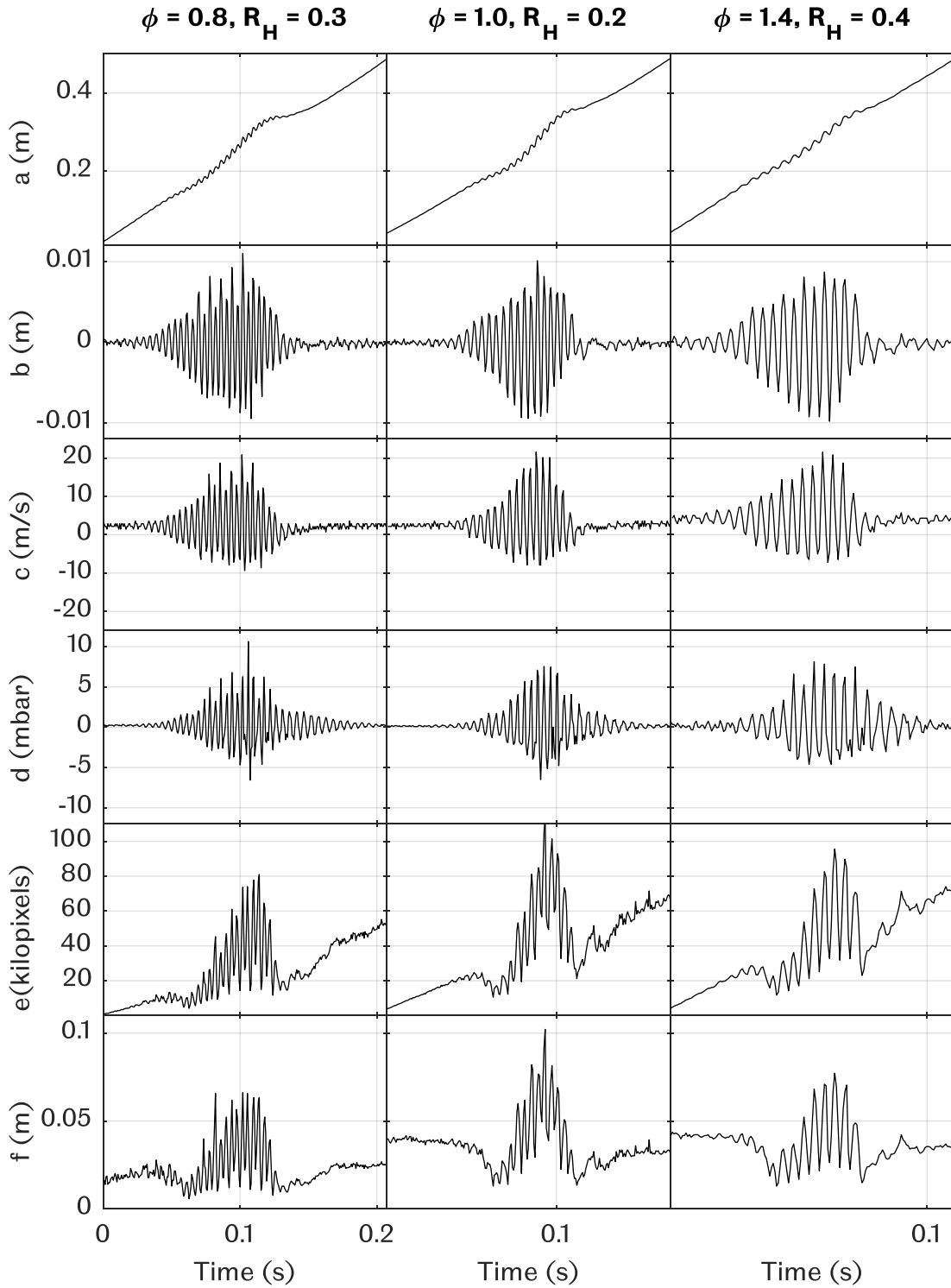
### 5.4.1 Initial Study

The effect of equivalence ratio and hydrogen addition had both been covered in the previous sections, almost always showing an increase in the flame oscillations with increasing laminar burning velocity. A different approach was taken in this section, where flames with approximately similar laminar burning velocity will be compared side by side to find any differences.

Three flames with approximately similar laminar burning velocity were selected for comparison. The first flame was  $\phi = 0.8$ ,  $R_H = 0.3$  flame (0.4604 m/s), second one was  $\phi = 1.0$ ,  $R_H = 0.2$  (0.4771 m/s) and finally  $\phi = 1.4$ ,  $R_H = 0.4$  flame (0.4709 m/s) as shown in Figure 5.12. This approach was used to find differences between a lean, stoichiometric and rich flame with approximately similar laminar burning velocity.

Flame front position was plotted against time in Figure 5.33(a). The stoichiometric flame appears to be the most affected by the oscillations, followed by the lean flame, and finally the rich flame. It was observed that the time taken to complete their propagation were different. The lean flame took the longest to complete at  $\sim 0.2$  seconds, followed by the stoichiometric flame at  $\sim 0.16$  seconds and finally the rich flame at  $\sim 0.11$  seconds.

The difference was reflected in their flame front position amplitude in Figure 5.33(b). Although they share the same peak amplitude of  $\sim \pm 0.01$ m, the amount of oscillations was less for richer flames, suggesting that slower flames will propagate through more oscillations compared to faster flames. The raw flame speed against time was plotted in Figure 5.33(c). The peak amplitude was similar for all three, reaching  $\sim \pm 20$  m/s. Despite the similarity, the rich flame appears to have a higher initial and ending speed compared to the other two, explaining the difference between their propagation time.



**Figure 5.33 Comparison between  $\phi = 0.8, R_H = 0.3$ ,  $\phi = 1.0, R_H = 0.2$  and  $\phi = 1.4, R_H = 0.4$  flames, where a) flame front position, b) flame front position amplitude, c) flame front speed, d) tube end pressure, e) flame size, and f) flame length.**

Comparing their tube end pressure in Figure 5.33(d), it was observed that their peak pressure was approximately similar, reaching an average magnitude of  $\sim \pm 8$  mbar.

All three flames appear to contain a higher order frequency, which will be confirmed in the frequency analysis section.

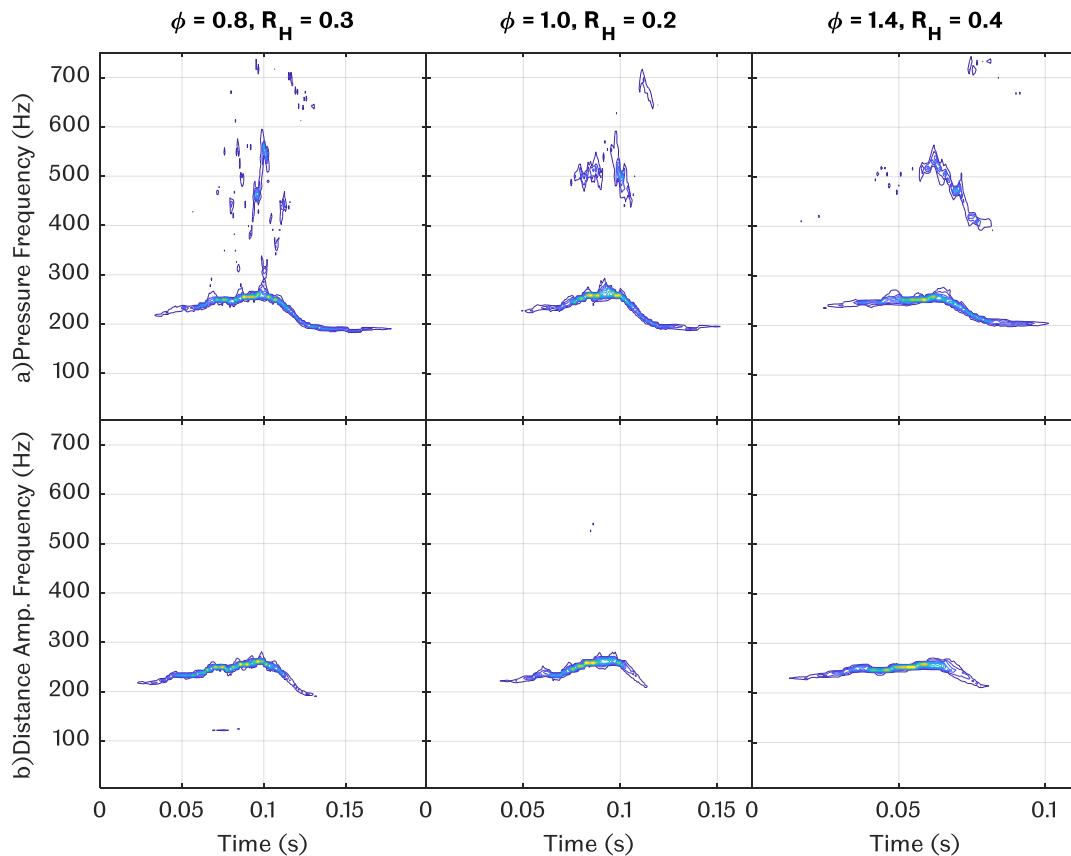
Figure 5.33(e) shows the plot of flame size against time. Similar to the flame front position, the stoichiometric flame appears to be the most oscillated flame amongst the three, reaching a size of ~105 kilopixels, followed by the rich flame at ~ 100 kilopixels, and finally the lean flame at ~ 80 kilopixels. This trend was not expected since the rich flame should have the highest flame size since it is the fastest flame. However, this difference in flame size was thought to be the effect of hydrogen addition, since a higher hydrogen content causes the flame to get less bright.

Finally, the flame length was compared between the three flames in Figure 5.33(f). Comparing their initial and ending length, the lean flame was the shortest, followed by the stoichiometric flame and the rich flame was the longest. During the oscillation, the stoichiometric flame was the longest, reaching a magnitude of ~ 0.1m, followed by the rich flame with a magnitude of ~ 0.075m, and finally the lean flame with a magnitude of ~ 0.06m.

#### **5.4.2 Frequency Analysis**

The SST plots for the pressure and distance amplitude signals were plotted in Figure 5.34. It appeared that similar laminar burning velocities excites the ~200 Hz oscillations in a similar manner, despite the difference in duration of propagation, indicating that the frequency shift of the ~200 Hz oscillations was independent of the duration of propagation, but instead dependent on the laminar burning velocity. Starting at ~210 Hz, the frequency shifted to ~290 Hz before decaying to ~200 Hz.

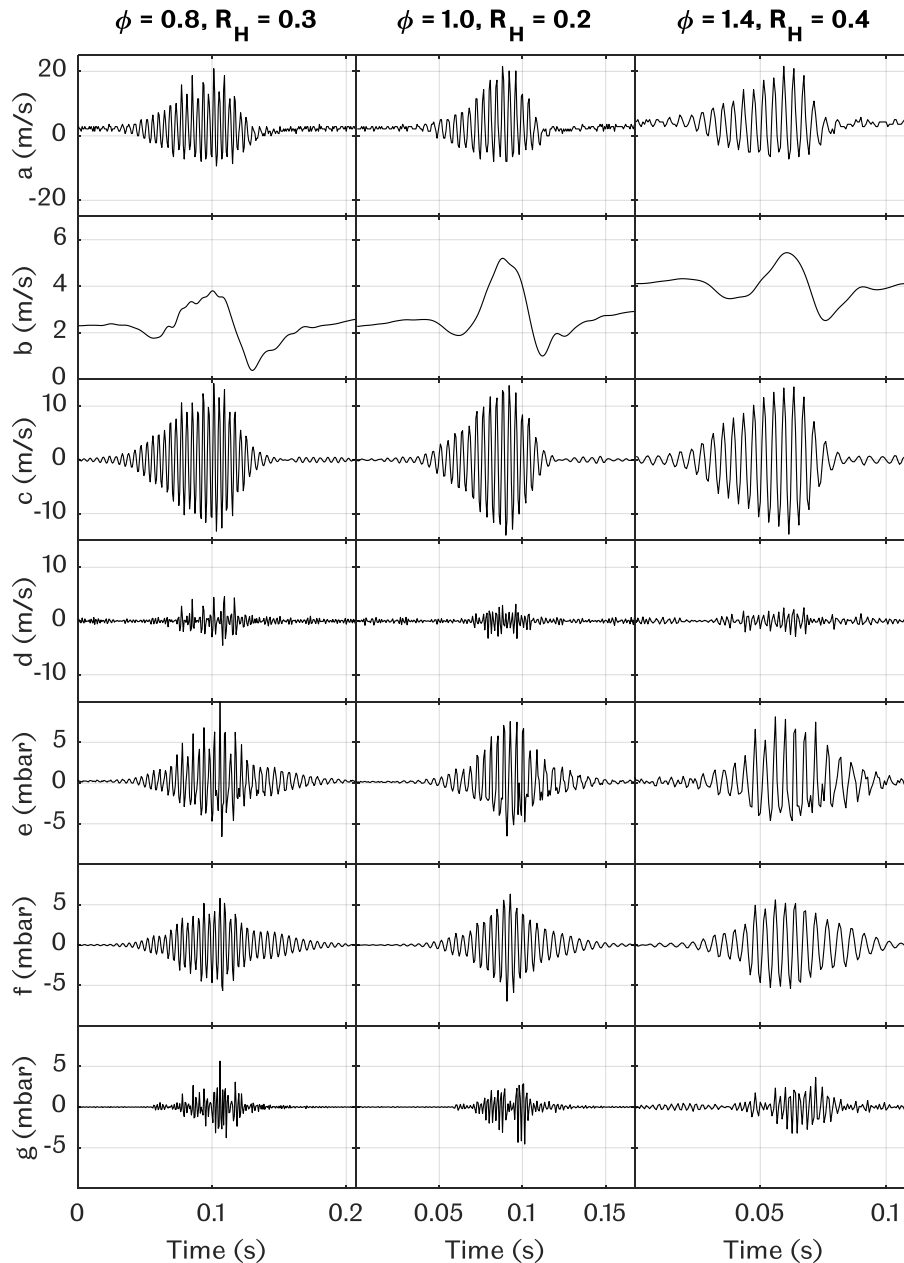
Significant excitation of higher order frequencies in the pressure signal only occurred in the presence of the ~200 Hz pressure component, despite the high hydrogen content. This was contrary to the findings in Figure 5.25 and Figure 5.27, where high hydrogen content flames were observed to induce significant excitation of higher order frequencies without excitation from the ~200 Hz pressure oscillations. Similar to other SST plots, the distance amplitude signals appeared and decayed before the pressure signals, indicating that the pressure oscillations were driven by the flame oscillations.



**Figure 5.34 SST plots for a) pressure signal and b) distance amplitude signal of methane flames with approximately similar laminar burning velocity,  $\phi = 0.8$ ,  $R_H = 0.3$ ,  $\phi = 1.0$ ,  $R_H = 0.2$  and  $\phi = 1.4$ ,  $R_H = 0.4$ .**

The analysis was continued with the frequency analysis in Figure 5.35. The raw speed of the three flames in Figure 5.35(a) were broken down into 3 parts, the underlying flame speed in Figure 5.35(b), the 200 Hz flame speed component in Figure 5.35(c) and finally the 400 Hz speed component in Figure 5.35(d). The raw flame speed in Figure 5.35(a) shows minor differences between the flames. It was noticed that the number of cycles were proportional to the duration of propagation. Despite the different number of cycles, all flames reached a maximum raw flame speed of  $\sim \pm 20$  m/s.

The underlying flame speed was plotted against time in Figure 5.35(b). The lean and stoichiometric flame had an initial underlying speed of  $\sim 2$  m/s and ended with a speed of 3 m/s, whereas the rich flame was  $\sim 4$  m/s at the beginning and ended with the same speed. During their oscillatory period, the lean flame reached a maximum underlying speed of  $\sim 4$  m/s, while the stoichiometric and rich flame reached a maximum speed of  $\sim 5$  m/s. Even though the lean flame had the greatest number of oscillations, the maximum underlying speed achieved was the lowest among the three flames.



**Figure 5.35** Frequency analysis of a) raw flame speed, broken down into b) underlying flame speed, c) 200 Hz flame speed component, and d) 400 Hz speed component for  $\phi = 0.8$ ,  $R_H = 0.3$ ,  $\phi = 1.0$ ,  $R_H = 0.2$  and  $\phi = 1.4$ ,  $R_H = 0.4$  flames. Analysis continued with e) raw pressure signal, broken down into f) 200 Hz pressure signal component and g) 400 Hz pressure signal component.

The analysis was continued with the 200 Hz flame speed component in Figure 5.35(c). In general, all the 200 Hz flame speed components reached a maximum speed of  $\sim \pm 12$  m/s. It was observed that the 200 Hz speed growth and decay of both the stoichiometric and rich flame were quite smooth compared to the lean flame, which had a few unusual spikes.

Proceeding with the 400 Hz speed component in Figure 5.35(d), the lean flame reached the highest magnitude of  $\sim\pm 4$  m/s, compared to  $\sim\pm 2$  m/s for the other two flames. The observed spikes in the 200 Hz speed component of the lean flame coincides with the spikes observed in its 400 Hz component, which were less obvious in the stoichiometric and rich flames. It was thought that the unusual spikes observed in the 400 Hz component was responsible for the irregularity in the 200 Hz speed component growth and decay.

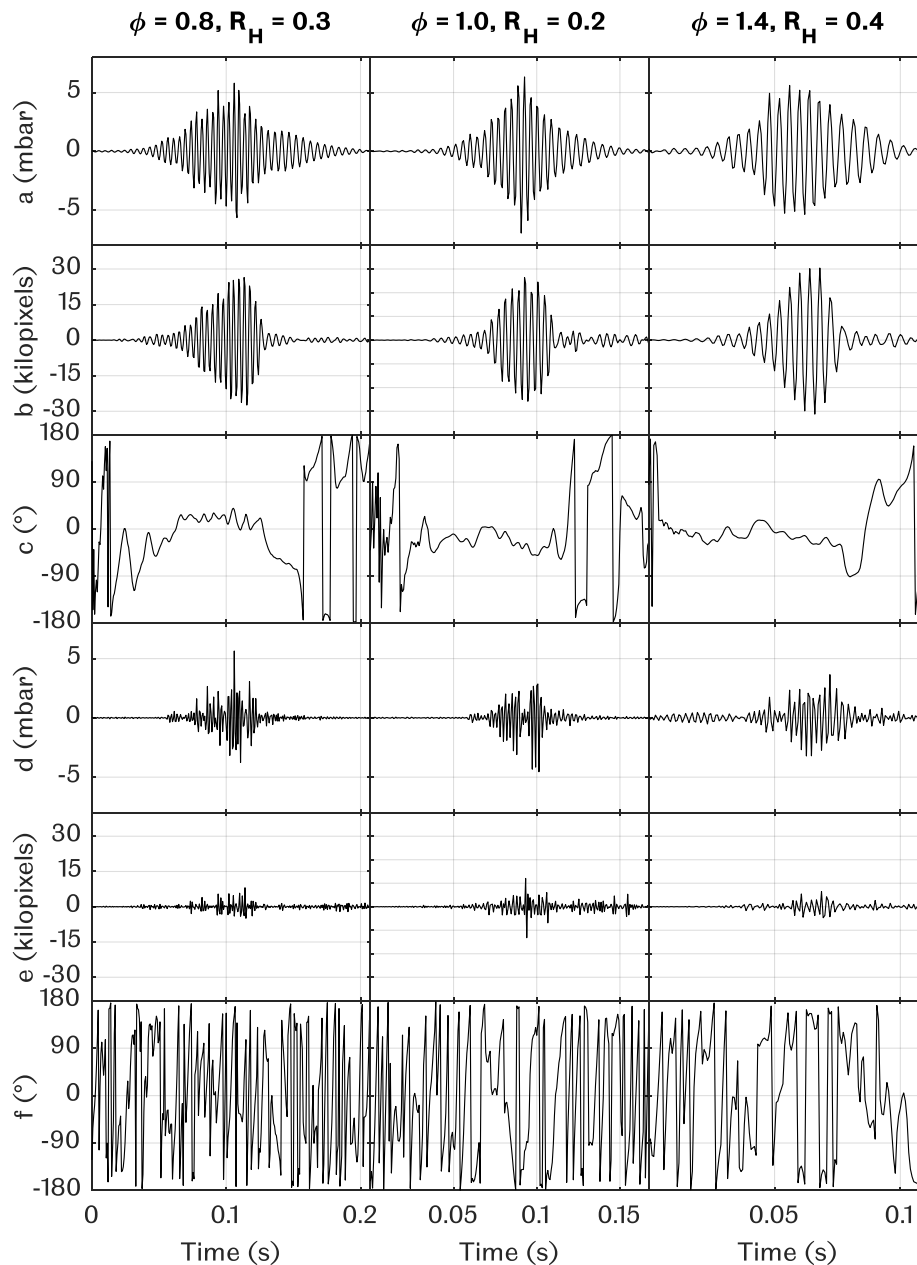
The raw pressure was plotted against time in Figure 5.35(e). Similar to the raw flame speed, no obvious difference was spotted in the raw pressure profiles other than the different number of cycles, which were proportional to the duration of propagation. The maximum raw pressure achieved by the lean flame was  $\sim\pm 9$  mbar, while the stoichiometric and rich flame only reached a maximum raw pressure of  $\sim\pm 7$  mbar.

The 200 Hz pressure component was plotted against time in Figure 5.35(f). The stoichiometric and rich flames 200 Hz pressure component growth and decay were smooth while the lean flame contains the same unusual spikes observed in its flame speed counterpart. The observed difference however did not influence the maximum 200 Hz pressure magnitude achieved by the flames which were equal at  $\sim\pm 5$  mbar.

The final 400 Hz pressure component was plotted against time in Figure 5.35(g). The lean flame reached a maximum pressure of  $\sim\pm 5$  mbar, while the stoichiometric and rich flames reached a pressure of  $\sim\pm 4$  mbar. All the 400 Hz pressure component increased when there was an increase in the 200 Hz pressure component. The rich flame was a little different, where small oscillations were observed even before the growth of the 200 Hz pressure component. The oscillations decayed once the 200 Hz pressure started to grow.

### 5.4.3 Phase Analysis

A phase study was conducted between the tube end pressure and flame size for the three approximately similar laminar burning velocity flames. Figure 5.36(a) shows the 200 Hz pressure component plotted against time, while the 200 Hz flame size component was plotted in Figure 5.36(b). All flames were oscillated to a maximum 200 Hz pressure of  $\sim\pm 6$  mbar and a maximum 200 Hz flame size component of  $\sim\pm 30$  kilopixels.



13.

**Figure 5.36 Phase study between tube end pressure and flame size for  $\phi = 0.8, R_H = 0.3$ ,  $\phi = 1.0, R_H = 0.2$  and  $\phi = 1.4, R_H = 0.4$  flames. Raw signals broken down into 200 Hz component of a) flame pressure, b) flame size, c) phase difference between a) and b). 400 Hz component of d) flame pressure, e) flame size and f) phase difference between d) and e).**

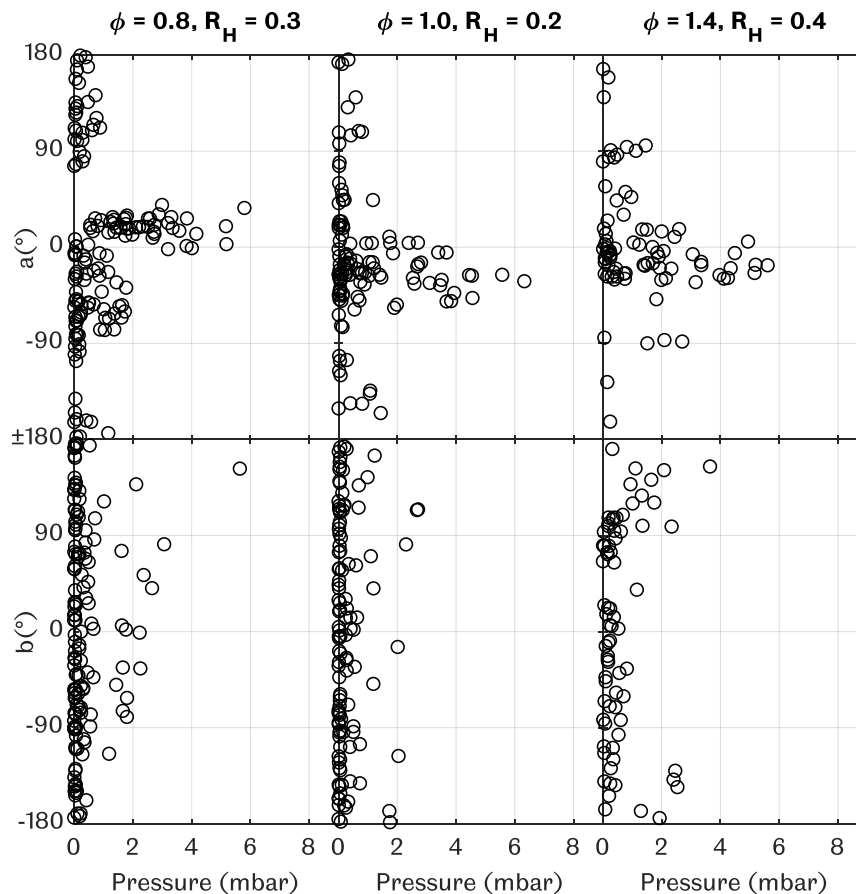
The phase difference between the 200 Hz components were plotted against time in Figure 5.36(c). Phase matching was observed in all the flames as expected. Similar to previous cases, the phase difference was initially fluctuating. As the pressure builds up, the phase difference became steady and stayed within  $0^{\circ} - \pm 90^{\circ}$ , and starts to fluctuate again once the flame size was reduced abruptly. Even with the



sudden reduction in flame size, the pressure component decayed gradually, suggesting that the pressure was the driving component in this interaction.

The phase study was continued with the 400 Hz components, plotted in Figure 5.36(d) and Figure 5.36(e) for the pressure and flame size respectively. The 400 Hz components were observed to be more obvious in the pressure signal compared to the flame size signal. The phase difference between them were plotted in Figure 5.36(f), which showed very little sign of phase matching.

The phase study was concluded by plotting the phase difference for the 200 Hz and 400 Hz components against their respective pressure. The 200 Hz phase difference was plotted against pressure in Figure 5.37(a) which showed clear signs of pressure amplification in all flames within the  $-90^\circ - 90^\circ$  phase difference range, reaching a maximum pressure of  $\sim \pm 6$  mbar. The 400 Hz component phase difference was plotted against pressure in Figure 5.37(b). Scattered pressure amplifications were observed suggesting that the amplifications were not due to phase matching between the 400 Hz components.

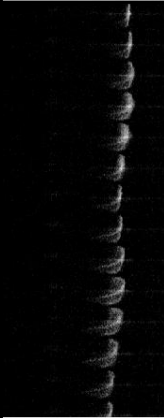
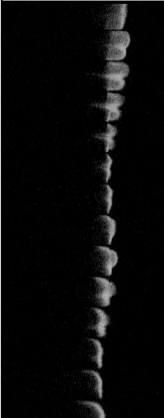

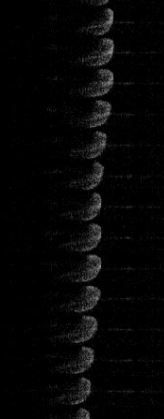
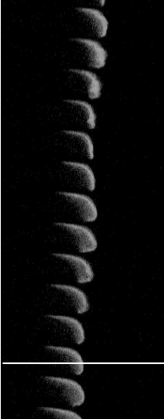






**Figure 5.37 Phase difference for a) 200 Hz component and b) 400 Hz component plotted against tube end pressure signal for  $\phi = 0.8, R_H = 0.3, \phi = 1.0, R_H = 0.2$  and  $\phi = 1.4, R_H = 0.4$  flames.**

#### 5.4.4 Non-steady Flame Shape Analysis

The flame shapes of three approximately equal laminar burning velocity flames were studied in this section. The flame shape at point B for lean ( $\phi = 0.8$ ,  $R_H = 0.3$ ), stoichiometric ( $\phi = 1.0$ ,  $R_H = 0.2$ ), and rich ( $\phi = 1.4$ ,  $R_H = 0.4$ ) flame of the same laminar burning velocity were compared in Table 5.7. None of the flame images were increased in brightness, and an increasing brightness was observed as the equivalence ratio was increased from lean to rich despite the difference in hydrogen content. This was reflected in their underlying velocity in Figure 5.35(b), where an increase in overall speed was observed with increasing brightness of the flames.

**Table 5.7 Flame sequence at point B (white line) for methane flames with constant burning velocity,  $\phi = 0.8$ ,  $R_H = 0.3$ ,  $\phi = 1.0$ ,  $R_H = 0.2$ , and  $\phi = 1.4$ ,  $R_H = 0.4$ . Interval of 1/1500 seconds increment for every frame upwards.**

Equivalence Ratio, $\phi$	0.8	1.0	1.4
Hydrogen Addition, $R_H$	0.3	0.2	0.4
Flame Sequence			
			
			

It was observed that the  $\phi = 0.8$  was smaller in size, which became symmetrical quicker than the stoichiometric and rich flame. However, the smaller flame size did not stop the lean flame from oscillating, similar to oscillating flames in previous sections, leading to formation of flame surface inversion beyond point B in all three flames. Apart from the symmetry of the flame beyond point B, the flames were also observed to be larger with increasing equivalence ratio. The analysis was continued with flame shape sequence at point C in Table 5.8.

**Table 5.8 Flame sequence at point C (white line) for methane flames with constant burning velocity,  $\phi = 0.8$ ,  $R_H = 0.3$ ,  $\phi = 1.0$ ,  $R_H = 0.2$ , and  $\phi = 1.4$ ,  $R_H = 0.4$ . Interval of 1/1500 seconds increment for every frame upwards.**


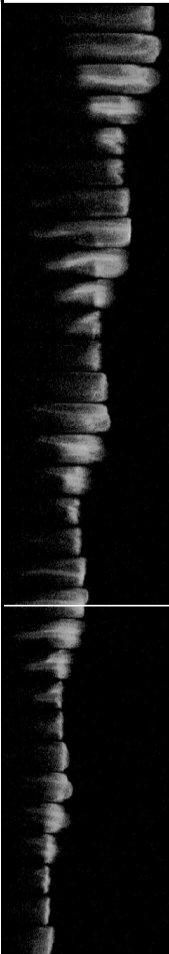
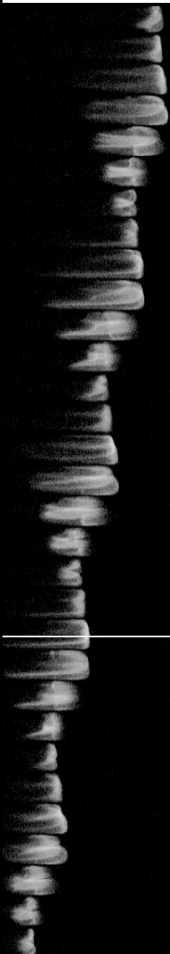
Equivalence Ratio, $\phi$	0.8	1.0	1.4
Hydrogen Addition, $R_H$	0.3	0.2	0.4
Flame Sequence			

Table 5.8 shows the flame shape sequence at point C. All three flames oscillated similarly with increasing flame length. It was observed that the lean flame became

symmetrical even before point C, whereas the other two were still asymmetrical. Relating the symmetry of the flames to their ~400 Hz velocity component in Figure 5.35(d), it was observed that the lean flame had a higher ~400 Hz velocity component compared to the other two asymmetrical flames, consistent with the findings in the previous section.

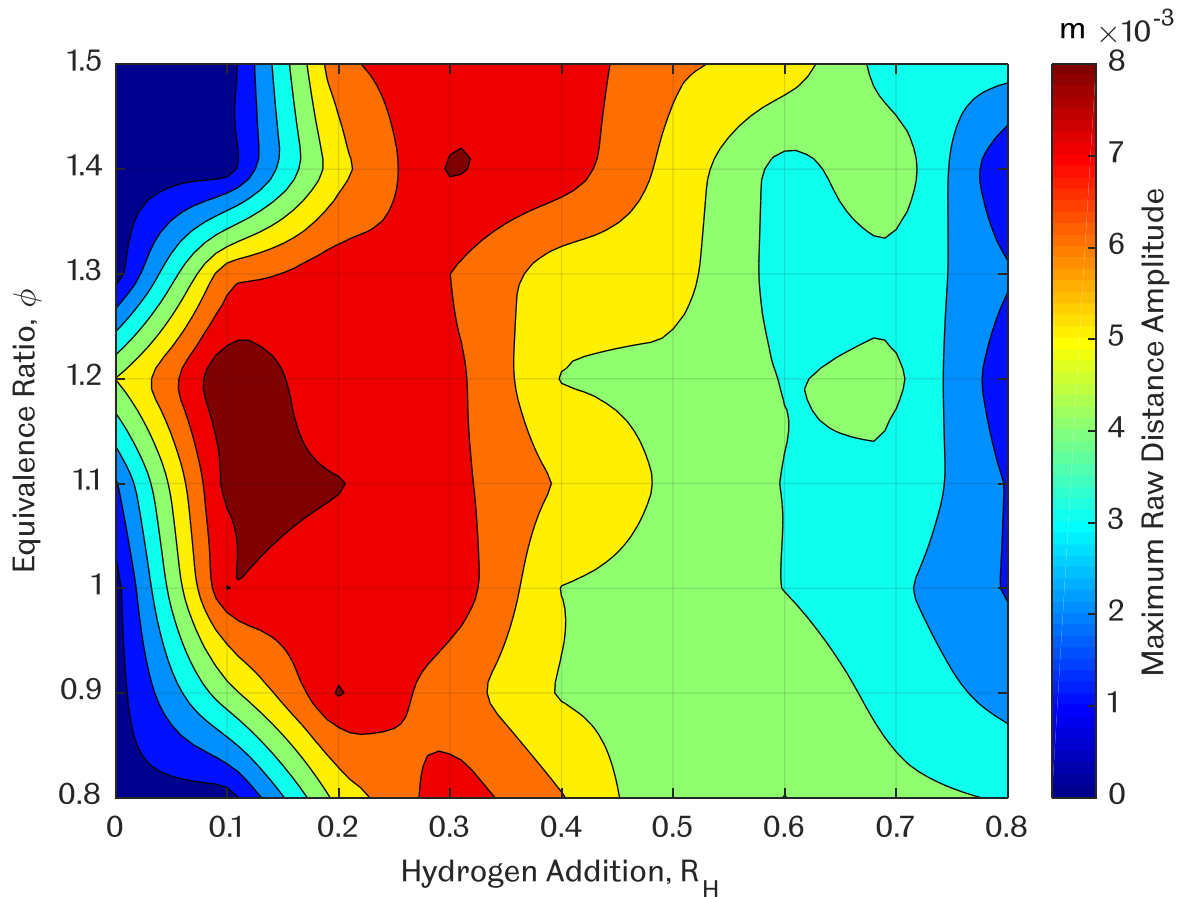
One obvious difference was observed, which was the flame size during the formation of flame surface inversion (RT tail) and convex flame. During the formation of the RT tail, the leaner flames were observed to be smaller in size, but equal in length, whereas during the formation of convex flame, the leaner flames ( $\phi = 0.8$  and  $1.0$ ) were both shorter and smaller in size compared to the  $\phi = 1.4$  flame. The whole flame propagation sequence and flame shape analysis for the constant laminar burning velocity study are available in Appendix J and Appendix M respectively

## 5.5 Overall Flame Analysis

### 5.5.1 Overall Flame Propagation Analysis

An extensive amount of contour plots will be used in this section to represent the whole range of data extracted from the experiments. The “linear” interpolation method implemented in MATLAB by default on the data made the contour plots difficult to interpret with the existence of illogical interpolated data (i.e. negative maximum tube pressure), thus a “natural” method was implemented, which was described as a triangulation-based natural neighbour interpolation by MATLAB [84]. A mesh size of 0.01 was chosen to smooth out the contour plots.

The contour plot in Figure 5.38 shows the maximum raw distance amplitude of all the experiments conducted. Referring to the colour bar on the left, blue colours represent steady regions whereas yellowish-red colours represent oscillated regions. Starting from the left side of the graph, the hydrogen addition,  $R_H$ , was increased by 0.1 to the right from 0 - 0.8. Equivalence ratio,  $\phi$ , was increased by 0.1 from the bottom of the graph to the top from 0.8 - 1.5. This method of plotting was used for all the other contour plots used in the present work.



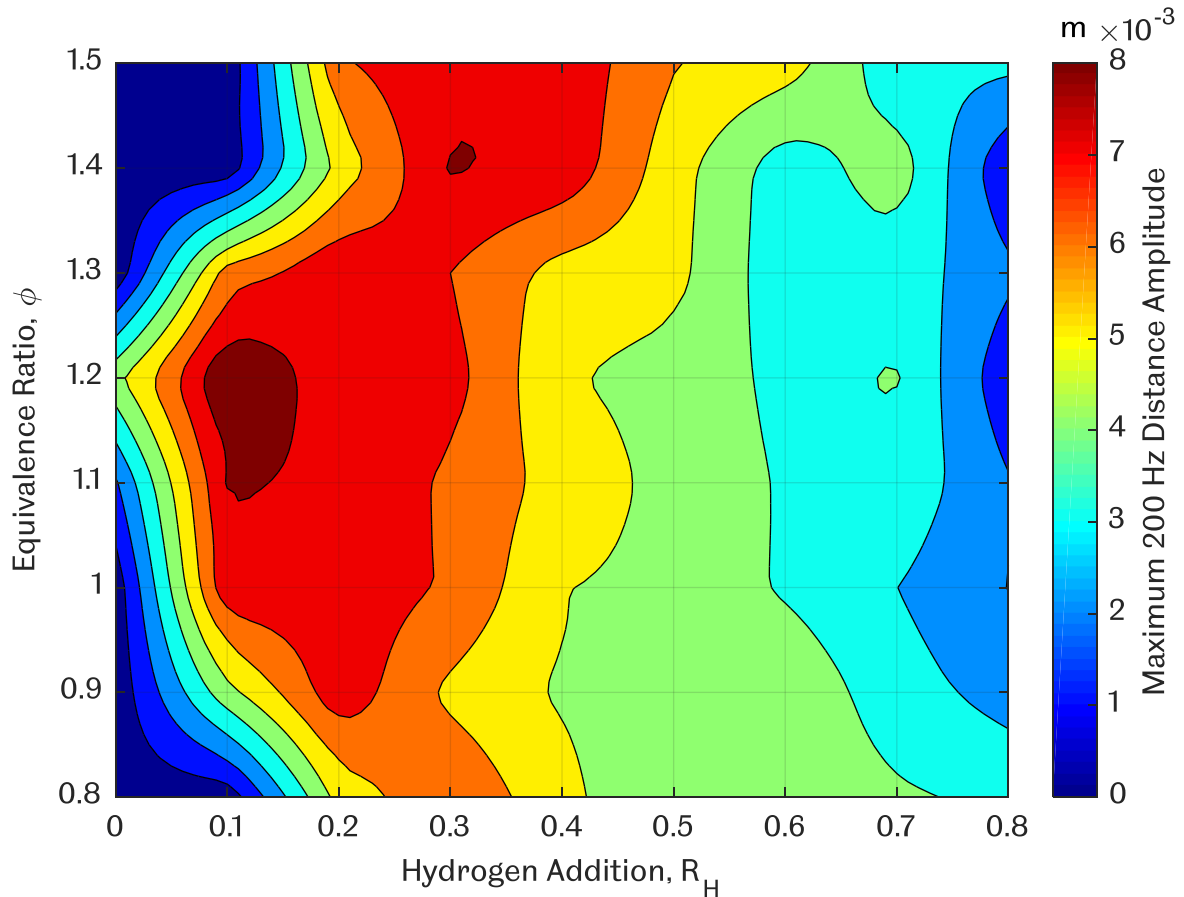
**Figure 5.38 Contour plot of maximum raw flame front distance amplitude.**

Small distance between the contour lines between  $R_H = 0 - 0.2$  indicates the existence of a steep slope. These steep slopes represent the sudden increment in the maximum raw distance amplitude from one mixture to another. For example, the steep slope between the  $\phi = 1.4, R_H = 0.1$  flame to the  $\phi = 1.4, R_H = 0.2$  flame indicates the sudden increase in its maximum raw distance amplitude. This sudden increment represents the transition from a steady flame to an oscillated flame.

The oscillations started to reduce gradually beyond  $R_H = 0.4$ , indicated by the widely spaced contour lines, which continued reducing until  $R_H = 0.8$ . A slight increase was observed at  $\phi = 1.2, R_H = 0.7$  and  $\phi = 1.4, R_H = 0.7$ , which both had lower amplitude at  $R_H = 0.6$ . Initially, a steady increase in distance amplitude was expected as hydrogen addition was increased for each equivalence ratio. This was proven to be incorrect since each equivalence ratio had a sudden increase in their maximum raw distance amplitude, followed by a gradual decrease. A region of instability was discovered instead of a monotonic increase in instability.

The raw distance amplitude was decomposed using SST and revealed that the oscillations were a superposition of a few components, but the analysis was

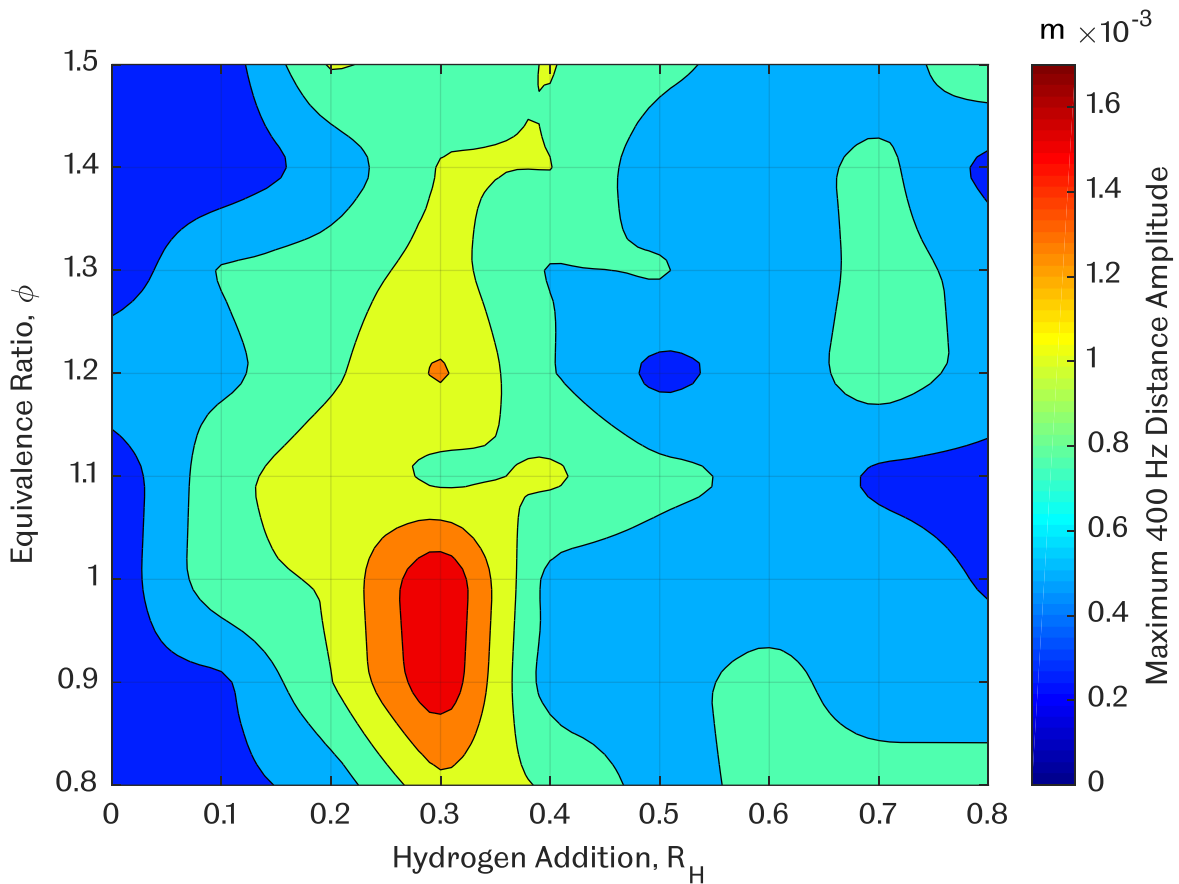
focused on 2 main components, the ~200 Hz and ~400 Hz components. Figure 5.39 shows the contour plot of the 200 Hz maximum distance amplitude, ranging between 0 – 0.008 m. In general, the contour plot had a similar shape to the maximum raw distance amplitude contour plot in Figure 5.38, indicating that the oscillations were dominated by the 200 Hz component. The main difference between the two plots was the region between  $\phi = 0.8 - 1.2$ , and between  $R_H = 0.1 - 0.4$ , suggesting that the region was affected by 400 Hz oscillations.



**Figure 5.39 Contour plot of maximum 200 Hz flame front distance amplitude.**

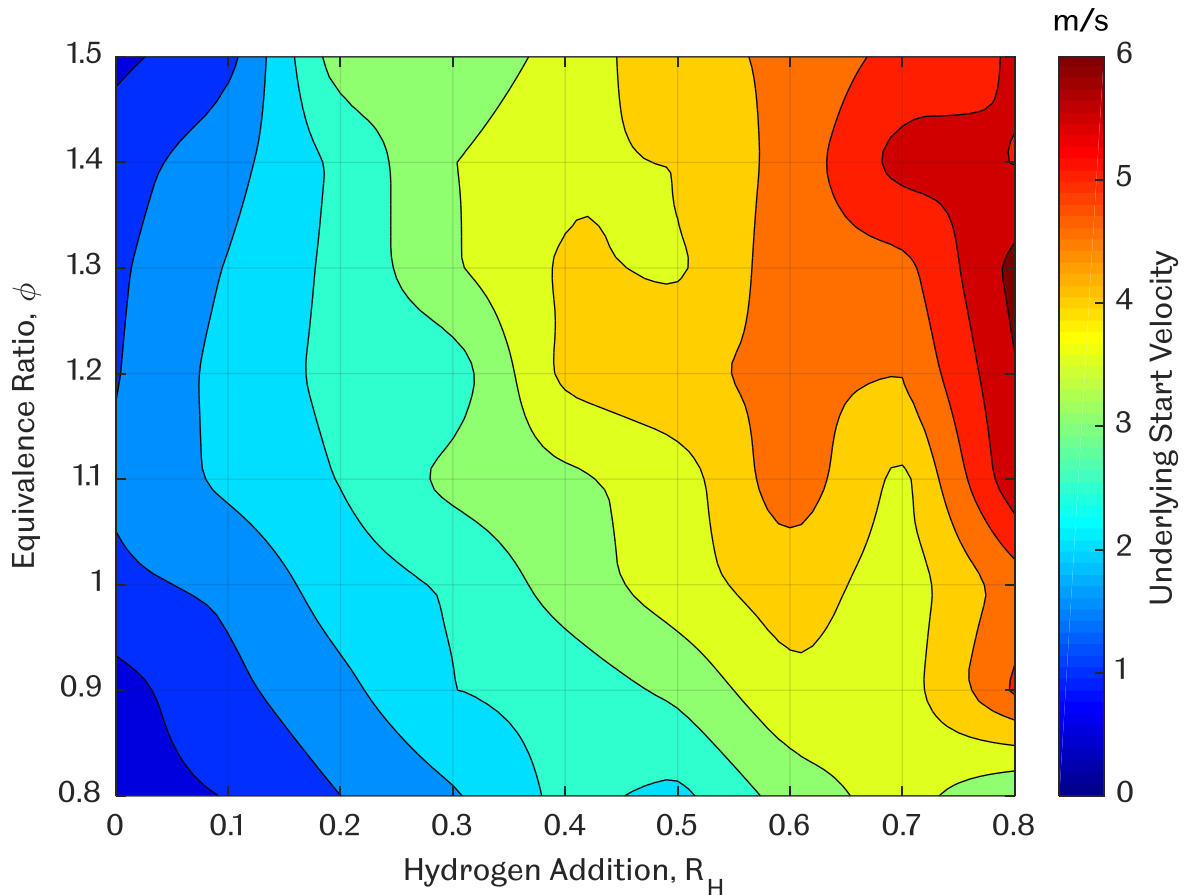
Figure 5.40 which shows the contour plot of maximum 400 Hz flame front distance amplitude, confirms the deduction made from Figure 5.39. The 400 Hz oscillations in the flame distance amplitude ranged from 0.0002 - 0.0017 m, with the strongest oscillations occurring in the region mentioned previously, between  $\phi = 0.8 - 1.2$  and  $R_H = 0.1-0.4$ . The excitation of the 400 Hz component by the 200 Hz component suggests that Figure 5.40 should appear similar to Figure 5.39, which was true as an elevated contour can be observed between  $R_H = 0.1-0.4$ . However, this hypothesis was true only to a certain degree since the maximum contour lines did not coincide with each other. Maximum excitation in the 400 Hz component was observed to occur between  $\phi = 0.9-1.0$  at  $R_H = 0.3$ , instead of  $\phi = 1.1-1.2$  at  $R_H = 0.1$  in Figure 5.39.

This non-linear behaviour implies that the excitation of the 400 Hz component was not solely dependent on the 200 Hz component, and might be related with the flame shape.



**Figure 5.40 Contour plot of maximum 400 Hz flame front distance amplitude.**

Analysis on the flame front amplitude was continued with the flame velocity. The contour plot of initial underlying velocity of all the flames were shown in Figure 5.41. The initial underlying velocity of the flames ranged between 0.05 - 6 m/s. The contour was expected to follow the contours of the laminar burning velocity in Figure 5.12, but it was proven to be very different. In Figure 5.12, the peak laminar burning velocity at different hydrogen addition levels stayed at  $\phi = 1.1$ , while the initial underlying velocity plot showed the peak velocity shifting from  $\phi = 1.1$  towards the richer region as hydrogen content was increased. The peak initial underlying velocity was at  $\phi = 1.3$  at  $R_H = 0.8$ , reaching  $\sim 6$  m/s.

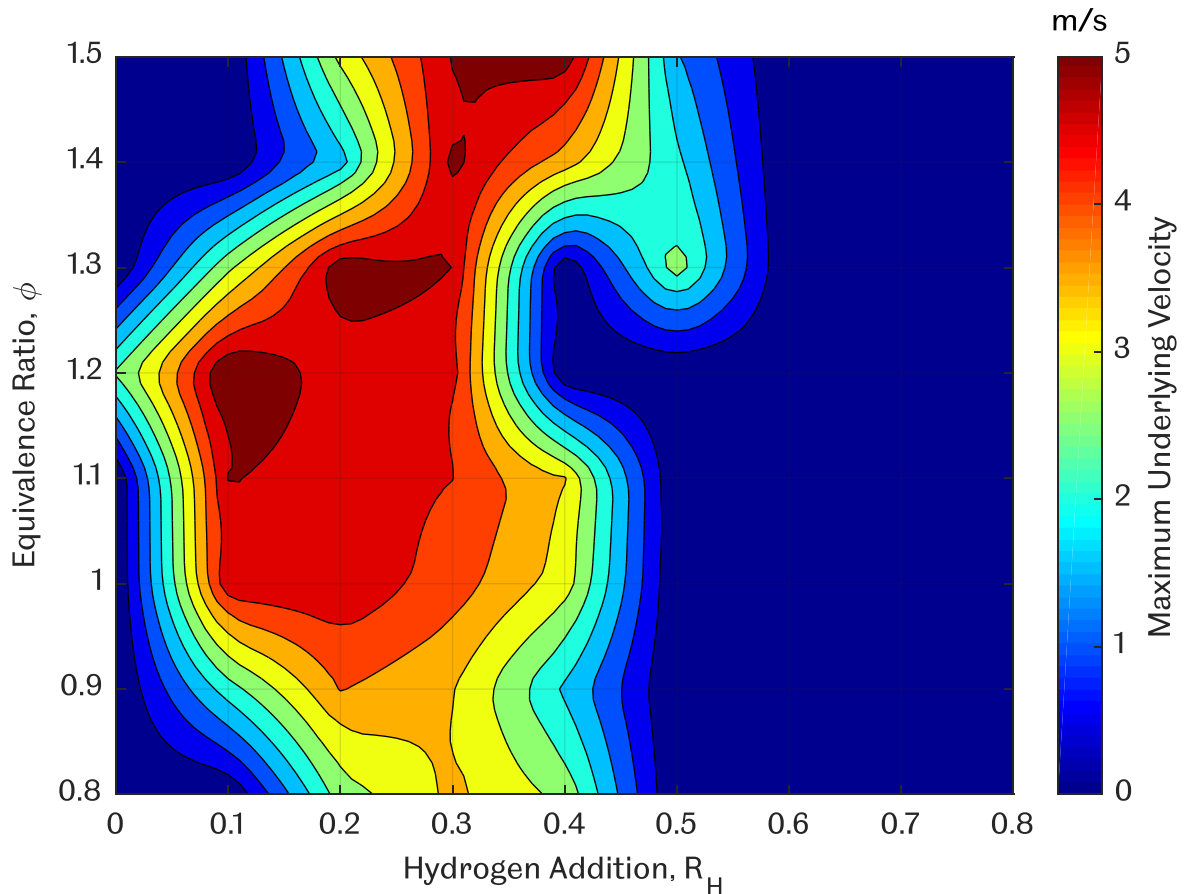


**Figure 5.41 Contour plot of initial underlying flame velocity.**

The maximum underlying flame velocity due to oscillations were plotted in a contour plot in Figure 5.42, ranging from 0 - 5 m/s. Referring back to Figure 4.16(d), the parameter refers to the peak velocity due to oscillations at point (ii). If the disturbance led to a deceleration in the flame speed, it was denoted as 0 m/s, represented by the dark blue regions in Figure 5.42.

Based on Figure 5.42, it was discovered that oscillations which led to flame accelerations started at  $R_H = 0$ , and ended at  $R_H = 0.5$ . For pure methane flames at  $R_H = 0$ , only the  $\phi = 1.2$  flame had an accelerating oscillation, reaching speeds of  $\sim 2.5$  m/s. Despite the lower laminar burning velocity of the  $\phi = 1.2$  flame compared to the  $\phi = 1.1$  flame, the latter did not experience an accelerating oscillation.





**Figure 5.42 Contour plot of maximum underlying flame velocity.**

The first hydrogen addition at  $R_H = 0.1$  led to an accelerating oscillation for flames between  $\phi = 1.0 - 1.3$ . Out of the four flames, the  $\phi = 1.1$  and  $1.2$  flames reached a maximum underlying velocity of  $\sim 5$  m/s, while the  $\phi = 1.0$  and  $\phi = 1.3$  flames only reached 4.5 m/s and  $\sim 2.5$  m/s respectively. The  $\phi = 0.9$  flame was found to be oscillating, but it did not lead to accelerations, while the  $\phi = 0.8, 1.4$  and  $1.5$  flames were steady.

Further increment of hydrogen at  $R_H = 0.2$  caused an even wider range of equivalence ratios to experience an accelerating oscillation, starting from  $\phi = 0.8 - 1.3$ . Lean flames at  $\phi = 0.8-0.9$  flame only reached a maximum underlying velocity of  $\sim 2.5$  m/s and  $\sim 4$  m/s respectively, while flames between  $\phi = 1.0 - 1.2$  reached a velocity of  $\sim 4.5$  m/s. It was noticed that the maximum underlying velocity shifted from the  $\phi = 1.2$  at  $R_H = 0.1$  to  $\phi = 1.3$  at  $R_H = 0.2$ , reaching a speed of  $\sim 5$  m/s. The  $\phi = 1.4$  and  $1.5$  flames were found to have oscillations which did not cause them to accelerate.

All flames at  $R_H = 0.3$  were accelerated by their self-induced oscillations. Starting from the lean flames,  $\phi = 0.8$  and  $0.9$ , their maximum underlying speed was  $\sim 3.5$  m/s,

followed by the  $\phi = 1.0$  flame, which reached an underlying speed of  $\sim 4$  m/s. The  $\phi = 1.1 - 1.3$  were on the same underlying velocity contour of  $\sim 4.5$  m/s, while the remaining two flames,  $\phi = 1.4$  and  $1.5$  were on the highest contour of  $\sim 5$  m/s. The shift in peak underlying speed was observed once again, with a similar trend of moving towards richer flames.

Disappearance of accelerating oscillations were observed at  $R_H = 0.4$  hydrogen addition, specifically at  $\phi = 1.2$  and  $1.3$ . The  $\phi = 0.8$  reached a maximum underlying velocity of  $\sim 2.5$  m/s, while the  $\phi = 0.9$  flame only reached a velocity of  $\sim 1.5$  m/s. A  $\sim 1$  m/s drop was observed for the  $\phi = 1.0$  and  $1.1$  flame maximum underlying speed compared to their  $R_H = 0.3$  counterpart. This gradual reduction was not observed in the  $\phi = 1.2$  and  $1.3$  flames as their oscillations did not lead to an acceleration. The  $\phi = 1.4$  flame dropped from  $\sim 5$  m/s to  $\sim 3.5$  m/s as hydrogen content was increased, while the  $\phi = 1.5$  flame maintained its maximum underlying speed at  $\sim 5$  m/s.

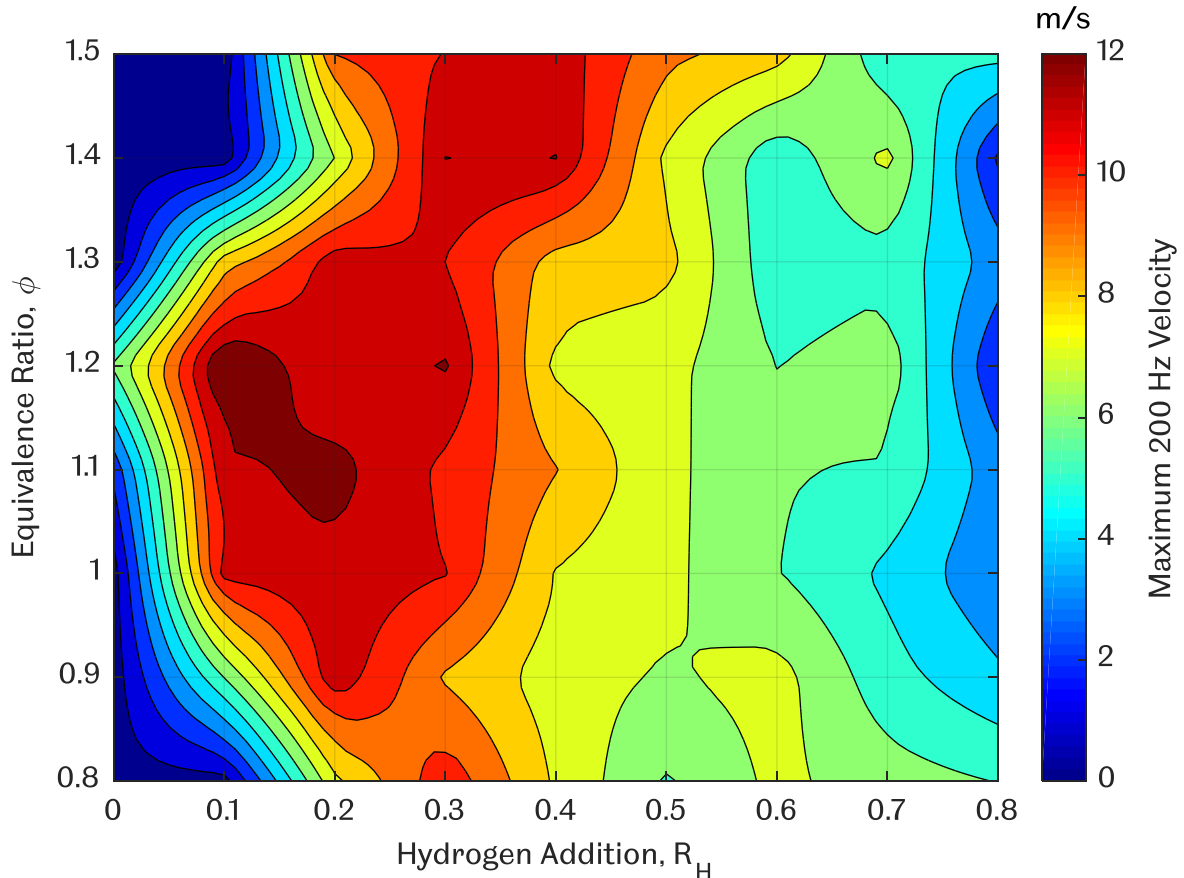
Flames at  $R_H = 0.5$  were observed to have oscillations, but most of them reduced the underlying speed of the flame, except for the rich flames at  $\phi = 1.3 - 1.5$ . The reduction in flame speed were associated with the pulsating flame behaviour discussed in the flame behaviour section. The  $\phi = 1.3 - 1.5$  flames reached a maximum underlying speed of  $\sim 2.5$  m/s,  $\sim 2$  m/s, and  $\sim 1.5$  m/s respectively. The remaining hydrogen addition at  $R_H = 0.6 - 0.8$  were observed to cause a reduction in the flame underlying velocity via pulsation.

The maximum 200 Hz flame velocity for all flames were plotted in Figure 5.43. In order to avoid confusion, the 200 Hz flame velocity can be imagined as a component in the flow acting on the flame at a frequency of 200 Hz, sweeping the flame left and right, at different velocities, causing the underlying flame velocity to increase or decrease. The overall shape of the contour plot was observed to be quite similar to the maximum underlying velocity plot in Figure 5.42, indicating the dependence of the maximum underlying velocity on the maximum 200 Hz velocity. The 200 Hz velocity component was observed to range between 0 - 12 m/s, depending on the fuel composition.

Five peaks were observed in the contour plot at  $\phi = 1.1$  at  $R_H = 0.2$ ,  $\phi = 1.2$  at  $R_H = 0.1$  and  $0.3$ , and finally at  $\phi = 1.4$  at  $R_H = 0.3$  and  $0.4$ , which corresponds to a maximum 200 Hz velocity of 12 m/s. It was found that the 200 Hz velocity had a maximum value of twice the underlying flame velocity, suggesting that the 200 Hz velocity was the main driving component in the flame oscillations. Comparing Figure 5.42 and Figure 5.43, it was observed that a 200 Hz velocity component ranging between  $\sim 8-12$  m/s

were mostly responsible for causing flame oscillations while 200 Hz velocity components ranging between ~1-8 m/s usually leads to flame pulsations.

Despite the fact that hydrogen addition increases the laminar burning velocity of methane flames, it was observed that the 200 Hz velocity did not follow this trend, indicating that the onset of the 200 Hz velocity component did not depend exclusively on the laminar burning velocity.

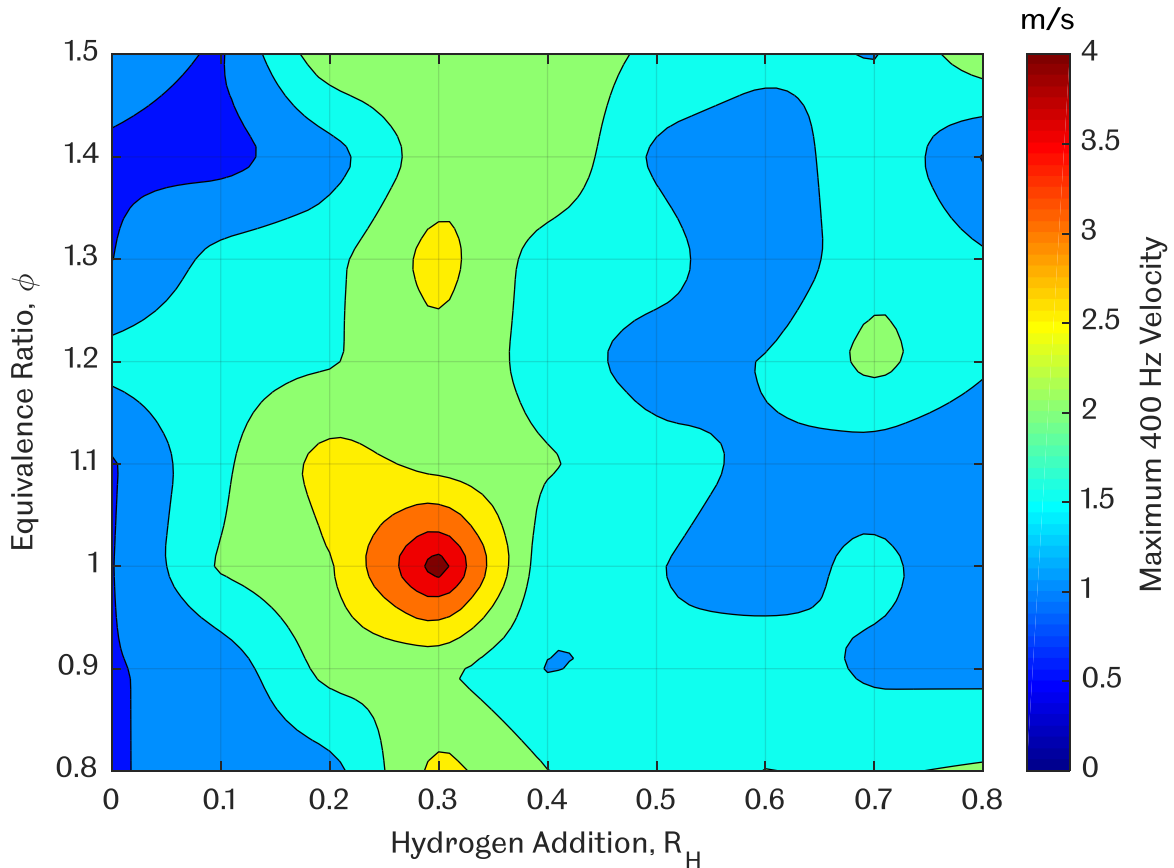


**Figure 5.43 Contour plot of maximum 200 Hz flame velocity.**

The third component of the raw velocity breakdown, the maximum 400 Hz flame velocity was plotted in Figure 5.44, varying between ~0.5 - 4 m/s. It was observed that the flame with the highest 400 Hz flame velocity was the  $\phi = 1.0$  flame at  $R_H = 0.3$ . This peak in velocity lies on top of a flat plateau of ~2 m/s velocity, which ranged between  $R_H = 0.1 - 0.5$ , and between  $\phi = 0.8 - 1.5$ . This flat plateau coincides with the region of strongly oscillated flames in Figure 5.43. This suggests that the 400 Hz velocity oscillations were partly induced by the 200 Hz velocity oscillations.

It was observed that there were no steep contour slopes, indicating that the 400 Hz velocity oscillations existed in most of the flames, unlike the steep contour slopes observed in Figure 5.43, within the range of  $R_H = 0 - 0.2$ . A slight reduction in the 400

Hz maximum velocity to  $\sim 1$  m/s was observed within the  $R_H = 0.5 - 0.8$  range, between  $\phi = 0.9 - 1.4$ , which also coincided with the reduction in velocity observed in the 200 Hz flame velocity in Figure 5.43. The speed reduction was followed by a slight speed increase to  $\sim 2$  m/s for the  $\phi = 1.2$  flame at  $R_H = 0.7$ . This slight increase towards the  $R_H = 0.8$  hydrogen addition was believed to be associated with high hydrogen content.

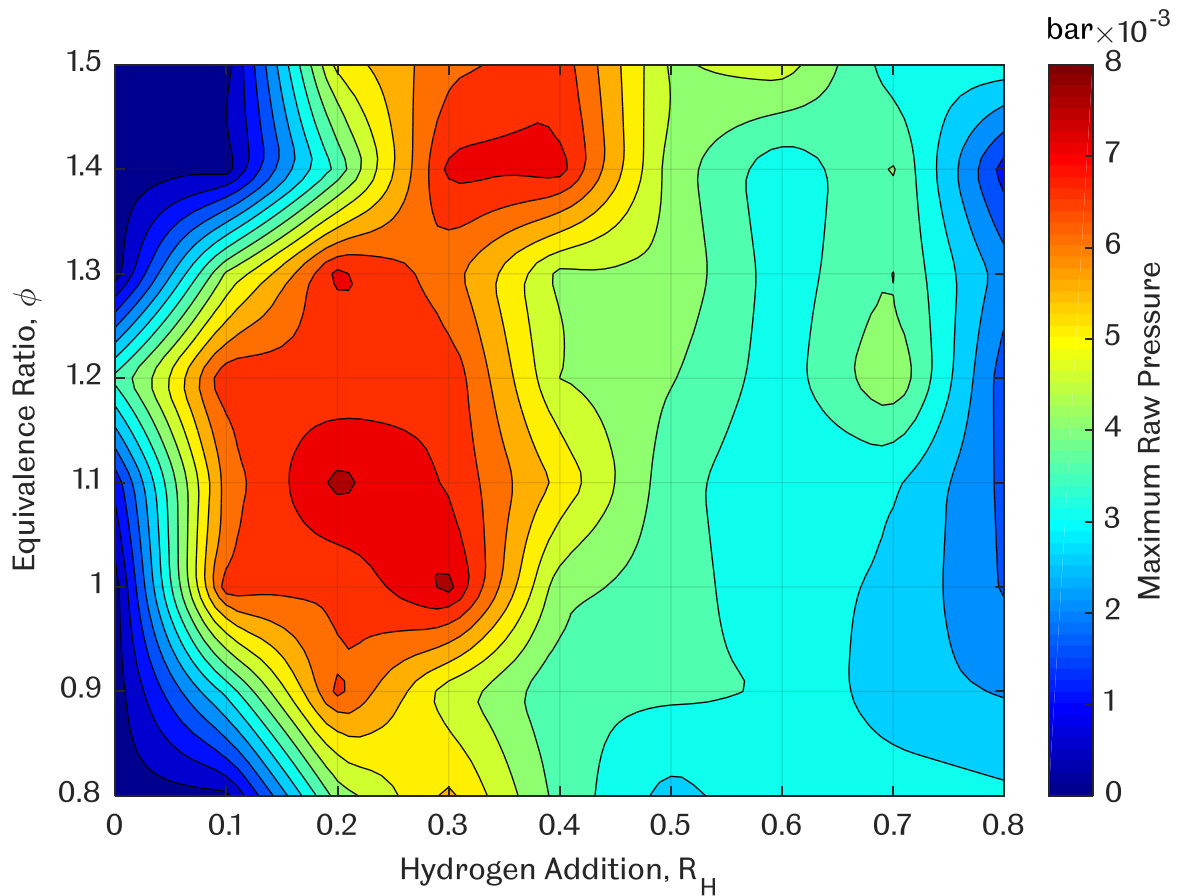


**Figure 5.44 Contour plot of maximum 400 Hz flame velocity.**

### 5.5.2 Overall Tube End Pressure Analysis

The maximum raw tube end pressure was plotted in Figure 5.45. The overall shape of the contour plot was found to be similar to the contour plot of raw flame distance amplitude in Figure 5.38, indicating the relationship between the flame distance amplitude and the tube end pressure. The contour plot values range from 0 - 8 mbar. The maximum raw pressure was located at  $\phi = 1.1$ ,  $R_H = 0.2$  and  $\phi = 1.0$ ,  $R_H = 0.3$ , indicated by the 8 mbar peaks at each location. The same range of flames mentioned in Figure 5.38 experienced the oscillations, indicated by the step increase in raw pressure on the left side of the plot, followed by a gradual reduction in raw pressure on the right. The gradual reduction towards the high hydrogen

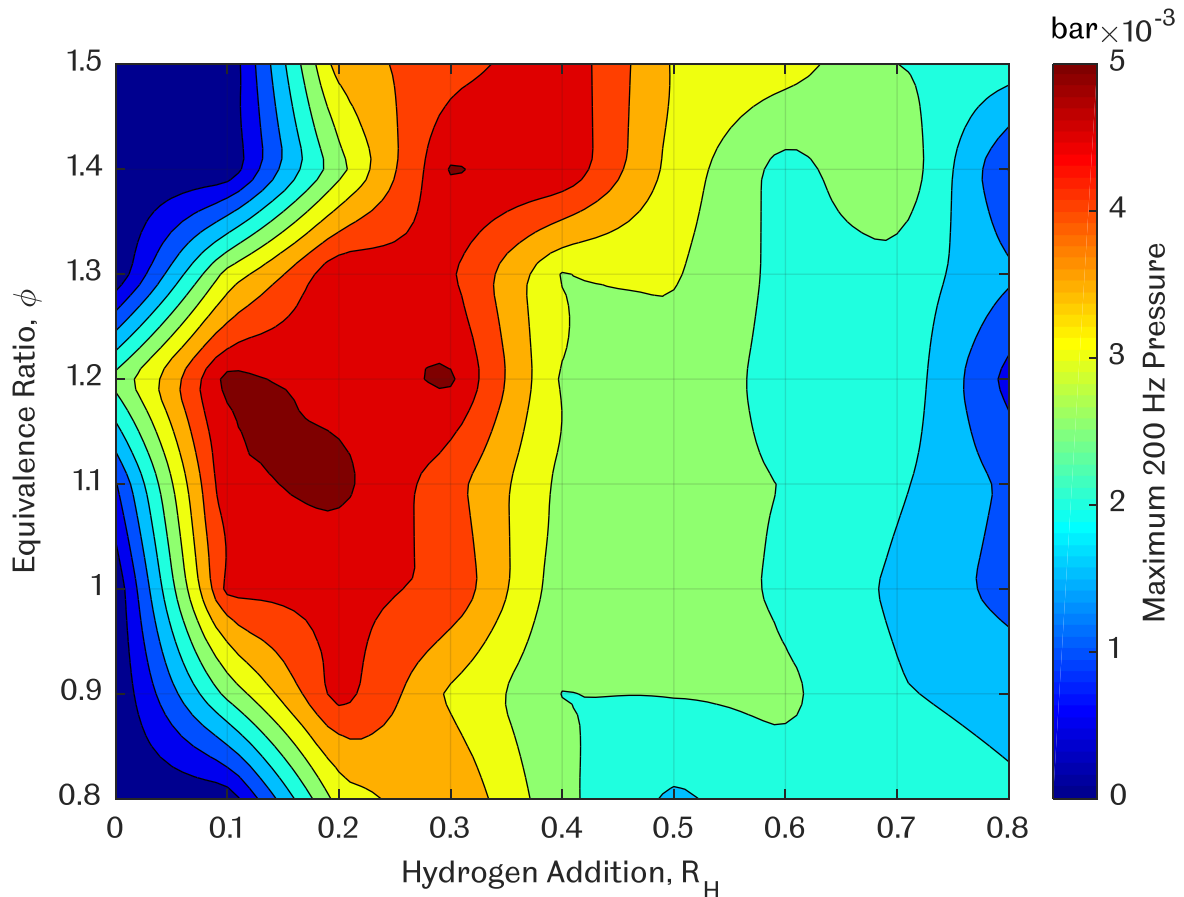
content flames were accompanied by a slight increase in raw pressure at  $R_H = 0.7$ , between  $\phi = 1.2 - 1.4$ .



**Figure 5.45 Contour plot of maximum raw tube end pressure signal.**

The raw tube end pressure was broken down into 2 components, the 200 Hz and 400 Hz pressure component. The maximum 200 Hz pressure components were plotted in Figure 5.46, with pressure values ranging between 0 - 6 mbar. The small difference between the pressure range of Figure 5.45 and Figure 5.46 suggests that the 200 Hz pressure component is the dominant component. It was found that the contour plot peaks at 4 different locations,  $\phi = 1.1$  at  $R_H = 0.2$ ,  $\phi = 1.2$  at  $R_H = 0.1$  and  $0.3$ , and finally  $\phi = 1.4$  at  $R_H = 0.3$ . The maximum pressure reached by these flames was  $\sim 6$  mbar.

The main difference between the raw pressure plot and the 200 Hz pressure plot was the flames surrounding the  $\phi = 1.0$  flame at  $R_H = 0.3$  and  $\phi = 1.2$  at  $R_H = 0.7$ . The peaks at these flames did not exist in the 200 Hz pressure plot, which suggests that strong 400 Hz pressure component exists in those flames. A gradual reduction in 200 Hz pressure component was observed as the hydrogen addition was increased steadily.



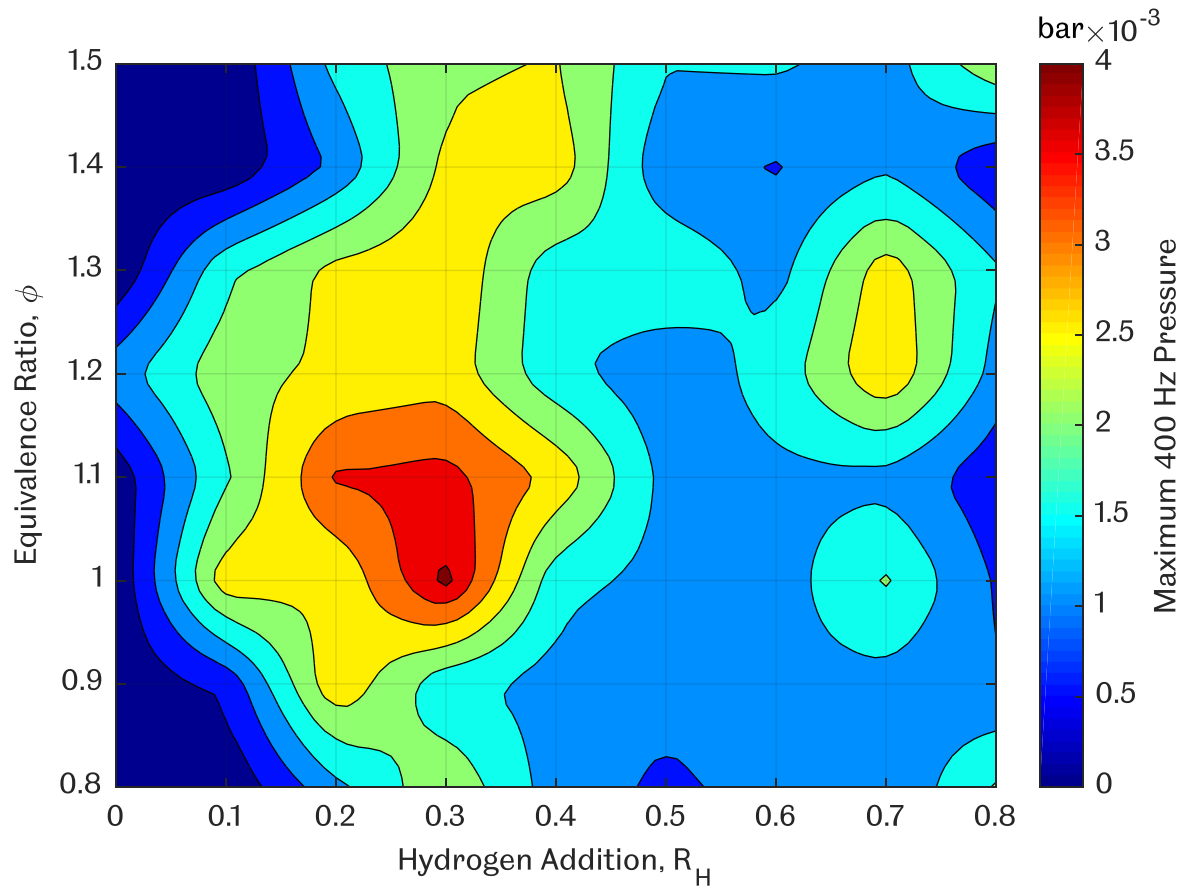
**Figure 5.46 Contour plot of maximum 200 Hz tube end pressure signal.**

The maximum 400 Hz pressure component was plotted in Figure 5.47, with a contour plot range between 0 - 5 mbar. In general, the plot suggests that most of the flame had a 400 Hz pressure component of ~2 mbar and below, except for flames within the  $\phi = 0.9 - 1.5$  range between  $R_H = 0.1 - 0.4$ . The mentioned range of flames coincided with the oscillated range of flames in the 200 Hz pressure component.

However, there were 3 flames which had higher 400 Hz pressure component compared to others, which were the  $\phi = 1.0$  flame at  $R_H = 0.3$  and  $\phi = 1.1$  flame at  $R_H = 0.2$  and  $0.3$ . When the 200 Hz and 400 Hz pressure components of the mentioned flames were compared between Figure 5.46 and Figure 5.47, they were either higher or approximately equal to each other in terms of magnitude, suggesting that the 400 Hz pressure component was dominant in these specific flames. This behaviour was also reflected in the 400 Hz flame velocity contour plot in Figure 5.44, indicating the existence of an interaction between the 400 Hz pressure and flame velocity.

A slight increase in the 400 Hz pressure component was observed in the  $\phi = 1.2$  and  $1.3$  flames at  $R_H = 0.7$ , which reached ~2.5 mbar, higher compared to their 200 Hz counterpart. The increase in the 400 Hz pressure component at this particular area

suggest that rich flames with high hydrogen content are prone to developing 400 Hz oscillations without the 200 Hz oscillations.



**Figure 5.47 Contour plot of maximum 400 Hz tube end pressure signal.**

## 6 DISCUSSIONS

### 6.1 Discussions on Equivalence Ratio Effect

Propagation of premixed methane flames in a horizontal tube with increasing equivalence ratio,  $\phi = 0.8 - 1.5$  and constant hydrogen addition,  $R_H = 0.1$  was studied. Important mixture characteristics were tabulated in Table 6.1. Out of the 8 mixtures, 5 of them were observed to have oscillations during propagation, which were  $\phi = 0.9 - 1.3$ , with laminar burning velocities ranging between  $0.312 - 0.421$  m/s. It was observed that the faster flames were prone to having oscillations compared to slower ones.

The oscillatory behaviour of the  $\phi = 1.3$  flame was not expected, since it has a significantly lower laminar burning velocity compared to the  $\phi = 0.9$  flame, but yet achieved a higher underlying flame speed and maximum pressure compared to the faster  $\phi = 0.9$  flame. This had been observed previously by Markstein and Somers [28], who concluded that slower burning flames may develop larger oscillations since they remain longer in regions prone to vibratory movements.

**Table 6.1 Mixtures tested for studying the effect of equivalence ratio.**

<b>Equivalence Ratio, <math>\phi</math></b>	<b>Hydrogen Addition, <math>R_H</math></b>	<b>Laminar Burning Velocity, <math>S_u</math> (m/s)</b>	<b>Expansion Ratio, <math>\alpha</math></b>	<b>Propagation Type</b>
0.8	0.1	0.335	6.695	Steady
0.9	0.1	0.388	7.113	Oscillating
1.0	0.1	0.418	7.417	Oscillating
1.1	0.1	0.421	7.474	Oscillating
1.2	0.1	0.389	7.371	Oscillating
1.3	0.1	0.312	7.239	Oscillating
1.4	0.1	0.211	7.101	Steady
1.5	0.1	0.133	6.960	Steady

This however presented another question to why the slightly faster flame,  $\phi = 0.8$ , did not oscillate compared to the  $\phi = 1.3$  flame. It was believed to be the effect of the hydrodynamic instability, which has a growth rate proportional to the laminar burning velocity, expansion ratio and the wave number  $k$ , based on equation (2.5)



[56]. The low expansion ratio of the  $\phi = 0.8$  flame might not be enough to initiate an oscillation, whereas the  $\phi = 1.4$  and 15 flame was simply not fast enough.

The SST plot presented in Figure 5.15 and Figure 5.17 shows a slight increase and decrease in the  $\sim 200$  Hz frequency component of the oscillating flames, and in some cases, exciting the higher order frequencies. This was also observed by Markstein and Somers [28], where they detected a complex sequence of frequency, amplitude, wave shape and flame speed during vibratory movements during their experiments. The shift and increase in the  $\sim 200$  Hz frequency component was thought to be an effect caused by the different phase of heat supply relative to the phase of pressure stated by Wood [17].

The increase in tube end pressure was also believed to be linked to the phase of heat supply relative to the phase of pressure, where they must be in phase to produce amplification stated by Rayleigh [7] and Wood [17], but with a condition that the pressure amplification overcomes the pressure dissipation. In most oscillating flames, pressure amplifications were observed during the period of amplification, where phase difference of the  $\sim 200$  Hz components were observed to be bounded within the  $\pm 90^\circ$  phase difference range, indicating phase locking, shown in Figure 5.19(c) and Figure 5.20(c). The pressure amplifications were more obvious in the  $\sim 200$  Hz frequency components compared to the  $\sim 400$  Hz components.

In the case of a slowly increasing frequency, it was noticed that the flame was under acceleration, while the decreasing frequency occurred during the deceleration of the flame. Wood stated that a phase of heat supply relative to the phase of pressure a quarter period before ( $-90^\circ$ ) would lead to an increase in frequency of vibration, whereas a quarter period after ( $90^\circ$ ) would lead to a decrease in frequency of the vibration [17]. Based on the phase difference plots of oscillated flames in Figure 5.19(c) and Figure 5.20(c), after a period of in phase oscillations, the phase difference was observed to stay roughly around the  $90^\circ$ , causing a decrease in frequency of the  $\sim 200$  Hz pressure oscillations based on the SST plots in Figure 5.15(a) and Figure 5.17(a).

The flame shapes at point B in Table 5.2 for all flames were pulsating, which reduced the size of the flame with every cycle of pressure oscillation, eventually leading to a flame surface inversion. The start of the flame surface inversion marks the start of the flame oscillation, which increased the flame surface area, thus increasing the heat supplied by the flame to the system. The transition from a pulsating flame to an oscillating flame was observed previously by Markstein [5] as shown in Figure 2.7, and described by Taniyama and Fujita [21] in Figure 2.4.

Flame shapes at point C in Table 5.3 showed the development of the oscillating flames from point B. The oscillating flames were clearly elongated compared to their initial shape, except for the  $\phi = 0.9$  flame. The elongated flames were observed to be similar in shape with the one described by Xiao et al. [23], [26] theoretically. The instabilities were observed to have features of a body-force instability, discussed in Section 2.2.1, where the flame alternates between shape (a), (b) and (c) shown in Figure 2.10. Shape (a) was described as a normal mode perturbation [22], (b) a free-surface bubble [36], [37] and (c) a falling spike in negligible density medium [38].

## 6.2 Discussions on Hydrogen Addition Effect

Propagation of premixed methane flames in a horizontal tube with increasing hydrogen addition,  $R_H = 0 - 0.8$  at a constant equivalence ratio,  $\phi = 1.1$  was studied. The mixtures used along with their important parameters were tabulated in Table 6.2. Out of the 9 mixtures, 5 oscillated with significant amplitude which were  $R_H = 0 - 0.4$  flames, while the remaining flames were found to only pulsate. The laminar burning velocity have minimal response towards the pressure perturbations. Flames which oscillated ranges between 0.360 – 0.618 m/s. Flames with laminar burning velocities beyond 0.618 m/s were found to only pulsate.

**Table 6.2 Mixtures tested for studying the effect of hydrogen addition.**

<b>Equivalence Ratio, <math>\phi</math></b>	<b>Hydrogen Addition, <math>R_H</math></b>	<b>Laminar Burning Velocity, <math>S_u</math> (m/s)</b>	<b>Expansion Ratio, <math>\alpha</math></b>	<b>Propagation Type</b>
1.1	0	0.360	7.521	Oscillating
1.1	0.1	0.421	7.474	Oscillating
1.1	0.2	0.482	7.433	Oscillating
1.1	0.3	0.558	7.396	Oscillating
1.1	0.4	0.618	7.363	Oscillating
1.1	0.5	0.677	7.334	Pulsating
1.1	0.6	0.735	7.307	Pulsating
1.1	0.7	0.792	7.283	Pulsating
1.1	0.8	0.847	7.262	Pulsating

Mandilas et al. [65] observed earlier onset of laminar flame instabilities due to hydrogen addition in their work. Their conclusion was found to be true only for  $R_H = 0 - 0.3$ , where the instabilities were initiated before reaching flame propagation distance of 0.2 m, deduced by comparing Figure 5.23(a) and Figure 5.23(b). Beyond  $R_H = 0.3$ , no clear trend of instability initiation was observed, as shown in Figure 5.24(a) and Figure 5.24(b).

It was expected that an increasing laminar burning velocity would lead to an even more drastic oscillatory behaviour in the flame, but it was found that slower flames had larger pressure and velocity fluctuations. Previously observed by Markstein and Somers [28], the slower burning flames had a longer period in the regions prone to vibratory movements, which gives more chance for the flame to develop a positive thermoacoustic feedback. The faster flames which only pulsated were observed to almost ignore the vibratory movements caused by the pressure fluctuations.

The theoretical expansion ratios of the flames calculated from GASEQ[102], were inversely proportional to the hydrogen addition, which may affect the growth rate of their hydrodynamic instability. Growth rate of hydrodynamic instabilities is proportional to the laminar burning velocity, expansion ratio and wave number based on equation (2.5) [56]. Although the laminar burning velocity increases with hydrogen content, the decreasing expansion ratio may have a countering effect on the growth rate of the hydrodynamic instability of the flame.

SST plots in Figure 5.25 and Figure 5.27 shows a consistent excitation of the ~200 Hz component in all oscillating flames, both in the pressure and distance amplitude signal. The mildly oscillating flame,  $R_H = 0$ , was found to stay fairly constant followed by a gradual decrease in its ~200 Hz components whereas the  $R_H = 0.1 - 0.7$  flames generally started oscillating significantly at a frequency of ~200 Hz, which increased gradually to ~300 Hz as the oscillatory amplitude grew, followed by a sudden drop back to ~200 Hz. Higher hydrogen content led to 'noisy' SST plots, which basically meant a reduction in the magnitude of oscillation of the oscillatory components, thus the appearance of low amplitude noises from other frequencies.

The increase and decrease of the ~200 Hz component was thought to be related with the phase relation between the heat source and pressure explained by Wood [17] in Figure 2.1. Prior to the drop in frequency, excitation of the higher order frequencies was observed, which were mainly in the ~400 Hz range, reconstructed in Figure 5.26(d) and Figure 5.26(g). Excitation of the higher order frequencies was consistent with the findings in the equivalence ratio effect section, and was related

with period doubling observed by Markstein [5]. The excitation of the higher order frequencies was reflected in the ~400 Hz velocity and pressure components,

Relating the SST plots with the flame shapes, it was observed that the heavily oscillated flames ( $R_H = 0.1 - 0.3$ ) exhibit the formation of flame surface inversion shown in Table 5.6, which were referred to as tulip flames by previous researchers [24], [26], [60], leading to a significant increase in the underlying speed of the flames.

It was observed that the formation of the tulip flames only happened in cases with high oscillatory amplitude of the ~200 Hz velocity components, which were not obvious in the  $R_H = 0$  and  $R_H = 0.4-0.8$  flames. This then led to a conclusion that a sufficient oscillatory amplitude of the ~200 Hz component is required in order to produce a tulip flame, which initiates period doubling [5], exciting the ~400 Hz component.

### 6.3 Discussions on Constant Laminar Burning Velocity

Premixed methane flames propagating in a horizontal tube with approximately similar laminar burning velocity were studied. The mixtures tested were tabulated in Table 6.3, along with their laminar burning velocity and expansion ratio. The oscillating laminar burning velocity range discovered in the previous section was found to be between 0.360 – 0.618 m/s, and the flames tested in this section were ~0.47, thus all flames were found to oscillate during their propagation as expected.

**Table 6.3 Mixtures tested for studying the effect of equal laminar burning velocity.**

<b>Equivalence Ratio, <math>\phi</math></b>	<b>Hydrogen Addition, <math>R_H</math></b>	<b>Laminar Burning Velocity, <math>S_u</math> (m/s)</b>	<b>Expansion Ratio, <math>\alpha</math></b>	<b>Propagation Type</b>
0.8	0.3	0.460	6.743	Oscillating
1.0	0.2	0.477	7.368	Oscillating
1.4	0.4	0.471	7.127	Oscillating

Despite their similarity in laminar burning velocity and flame behaviour, subtle differences were found, which may be attributed to their expansion ratio and equivalence ratio. The expansion ratio and laminar burning velocity of the stoichiometric flame was the highest among the three, but according to their underlying flame velocity in Figure 5.35(b), the  $\phi = 1.4$  flame had the highest underlying velocity peak. This was not expected, since the growth of a hydrodynamic instability is directly proportional to its laminar burning velocity and expansion ratio

according to equation (2.5) [56]. It was thought that the increasing reactivity due to the higher hydrogen content led to this effect.

The SST plots in Figure 5.34 displayed similar trends for significantly oscillated flames analysed in the previous sections, where a gradual increase in the ~200 Hz components was observed followed by a sudden decrease following the excitation of higher order frequencies. Comparing the three plots, it was observed that the fastest flame,  $\phi = 1.4$ , had a less significant shift in the ~200 Hz frequency despite the high underlying flame speed shown in Figure 5.35(b).

The difference in SST plots led to a deduction that shifts in the ~200 Hz frequency component may be attributed to the magnitude of underlying velocity change. Both the  $\phi = 0.8$  and 1.0 underlying velocity increased significantly from ~2 m/s to ~4 m/s and ~5 m/s respectively, whereas the  $\phi = 1.4$  flame only increased from ~4 m/s to 5 m/s. The ~200 Hz components of both velocity and pressure appear to be similar in magnitude, reaching a magnitude of  $\sim\pm 12$  m/s and  $\sim\pm 5$  mbar.

The excitation of the ~200 Hz component had been observed by Markstein and Somers [28], who utilized two 0.0915 m internal diameter tube with different length, 0.6 m and 1.2 m tubes, downwards towards a closed end. Despite the difference in boundary conditions compared to the present work, it was discovered that the ~200 Hz pressure components in both tubes they tested responded systematically with the change in equivalence ratio. In short, the peak pressure amplitudes were proportional to the change in laminar burning velocity.

Based on this comparison, it was thought that the growth of ~200 Hz oscillatory components is a function of the laminar burning velocity of a premixed flame propagating within a tube. This was found to be consistent in most SST plots of oscillating flames observed in this section, along with the equivalence ratio and hydrogen addition effect sections. The theory starts to become invalid for premixed flames with higher laminar burning velocity, causing the flame to have insufficient time within the oscillatory region of the tube, thus having no time to build up in pressure.

According to Wood [17], an increase in frequency only happens if the pressure drives the heat release within the oscillating system, which could be related to the current situation. The pressure of the system was building up during the start of the oscillatory period, which drives the oscillation of the flame speed (technically heat supply), leading to an increase in the frequency. During the peak of the oscillation, it was observed that the flame speed was driving the oscillation, leading to a downward shift of frequency in the ~200 Hz frequency component. It eventually

came to a point where the flame speed suddenly stopped oscillating, while the pressure kept oscillating with a gradual reduction which finally stabilized the flame. The flame shapes observed were consistent with the highly oscillated flames from previous sections. Tulip flame formation were similar compared to literature [24], [26], [60] in the  $\phi = 0.8$  flame, unlike the  $\phi = 1.0$  and 1.4 flames, which may appear unclear, but the alternation between the flame surface inversion and convex flame could still be distinguished.

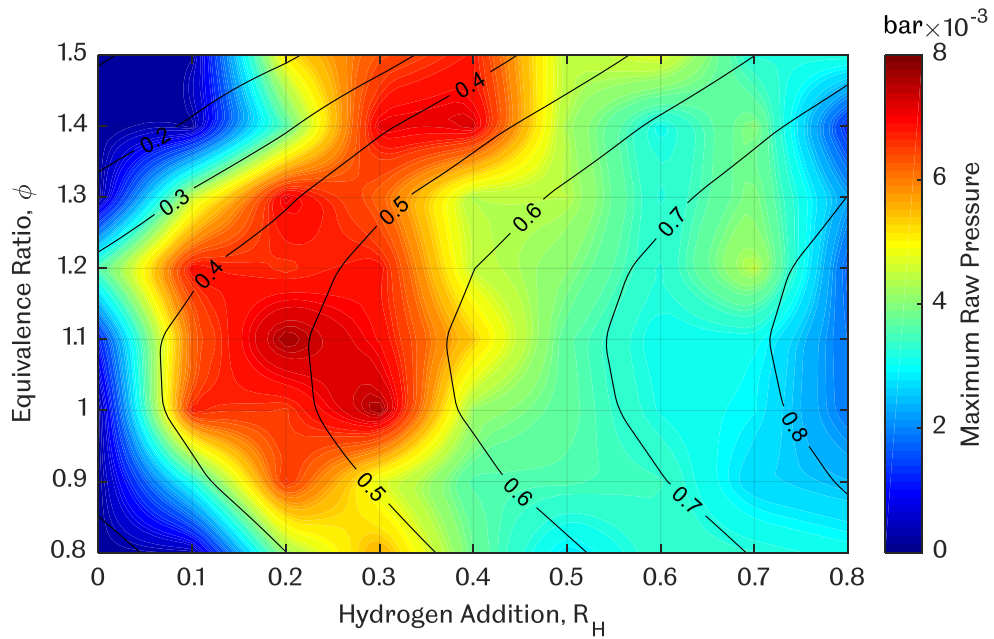
## 6.4 Overall Discussion

Two main type of contour plots were plotted based on the raw data obtained from the experiments, which were contour plot of peak distance amplitude in Figure 5.38, and contour plot of peak tube end pressure amplitude in Figure 5.45. Markstein and Somers [28] were only able to plot the contour plot of peak pressure amplitude for 0.6 m and 1.2 m tubes, shown in Figure 2.19 and Figure 2.20 respectively.

Despite the change in tube length, the frequency of oscillation which responded systematically to the change in equivalence ratio was fairly constant,  $\sim 260$  Hz for both tubes [28], which was the fundamental mode of oscillation for the 0.6 m tube, and the first harmonic for the 1.2 m tube. Their data analysis was only limited to pressure oscillations due to low filming rate (6 frames per second), thus no correlation was made between the tube pressure and flame movements.

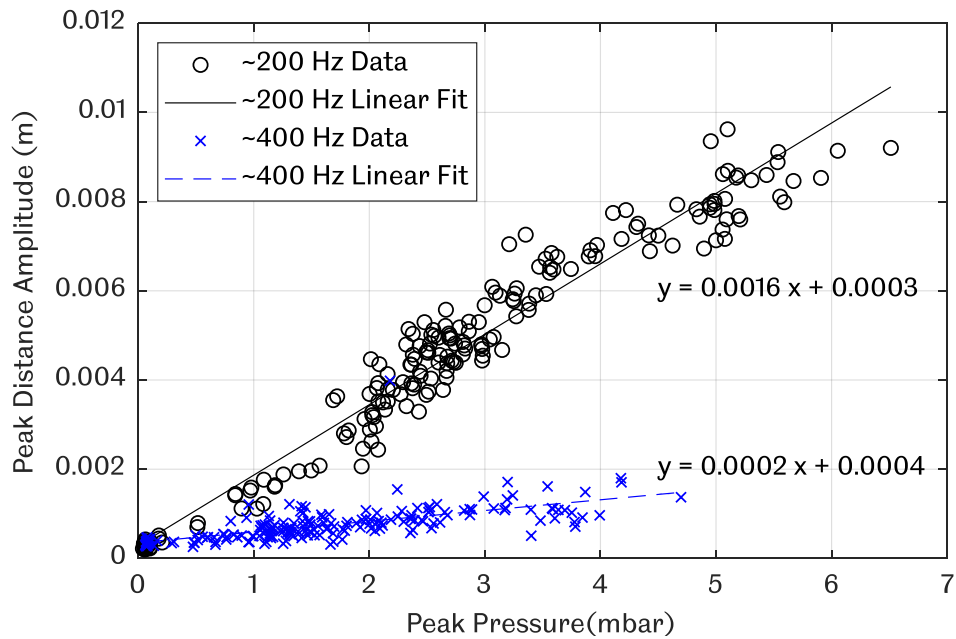
The contour plot of maximum raw pressure amplitude overlapped with theoretical laminar burning velocity contour lines were plotted in Figure 6.1. In general, most of the area with high pressure amplitude was observed to be within the 0.3 – 0.6 m/s laminar burning velocity range. Within the range, it was discovered that the rich mixtures were more prone to oscillations compared to the lean mixtures. Mandilas et al. [65] discovered that fuel rich methane and methane-hydrogen mixtures showed no evidence of cellularity, which suggests that the oscillations observed in the fuel rich regions of the present work were not caused by cellular structures.

The cellularity of the lean methane-hydrogen mixtures was thought to be the reason for the low amplitude oscillation within the 0.3 – 0.6 m/s laminar burning velocity range. Another conclusion made by Mandilas et al. [65] was the earlier onset of laminar flame instabilities due to hydrogen addition. The conclusion was found to be contradicting with the findings of the current work, as shown by the blue contour at  $R_H = 0.8$ , indicating little to none instabilities.



**Figure 6.1 Maximum raw pressure contour plot with theoretical laminar burning velocity contour lines.**

In order to understand the relationship between the magnitude of flame front instabilities with regards to pressure, a scatter plot of the peak distance amplitude against the peak tube end pressure for all experiments were plotted in Figure 6.2. Both the ~200 Hz data and ~400 Hz data were plotted, together with a best fit line defining their relationship. Both best fit lines displayed a linear relationship between the peak distance amplitude and the peak pressure amplitude.



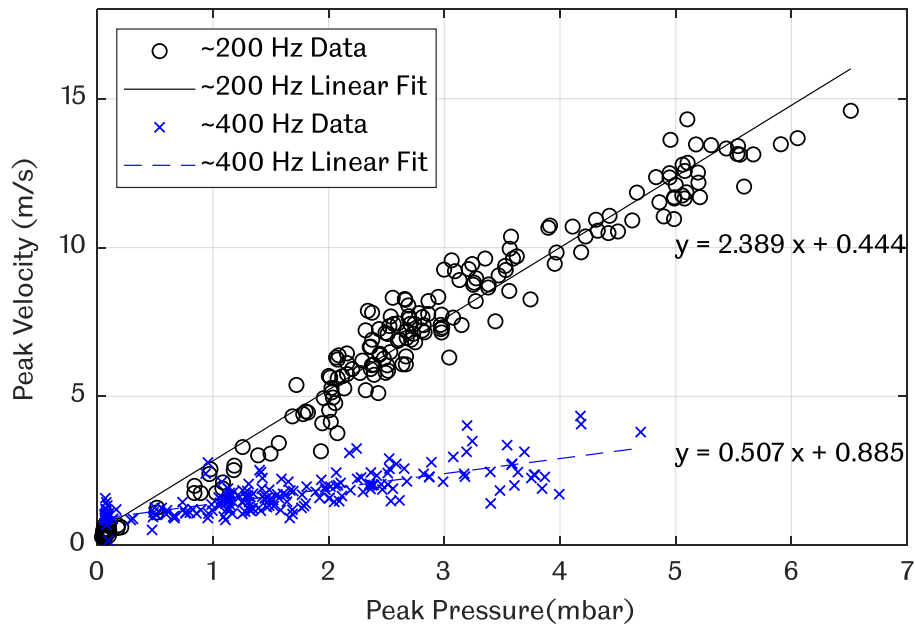
**Figure 6.2 Peak distance amplitude against peak pressure scatter plot for ~200 Hz and ~400 Hz components for all unsteady flames.**

Based on Figure 6.2, the linear relationship between the ~200 Hz data was defined by  $y = 0.0016x + 0.0003$  ( $R^2 = 0.9515$ ), whereas the ~400 Hz data was defined by the equation  $y = 0.0002x + 0.0004$  ( $R^2 = 0.4271$ ). The y-intercept were 0.0003 and 0.0004 for the ~200 Hz and ~400 Hz components respectively, theoretically suggesting that the ~400 Hz peak distance amplitude has a higher value compared to the ~200 Hz peak distance amplitude at ambient pressure. The ~200 Hz data displayed a steeper gradient compared to the ~400 Hz data, indicating a higher increase in the peak distance amplitude for the same amount of pressure compared to the ~400 Hz data, suggesting the dominance of the ~200 Hz oscillations compared to the ~400 Hz oscillations.

Dominance of the ~200 Hz component in the whole flame propagation was also shown when the raw peak distance amplitude plot in Figure 5.38 was compared to the ~200 Hz peak distance amplitude contour plot in Figure 5.39. The similarity between the two contour plots was enough to suggest the dominance of the ~200 Hz oscillations. It was observed that the increase in the ~200 Hz oscillations were associated with elongation of the flames, based on the flame propagation images at point C in Table 5.3, Table 5.6, and Table 5.8.

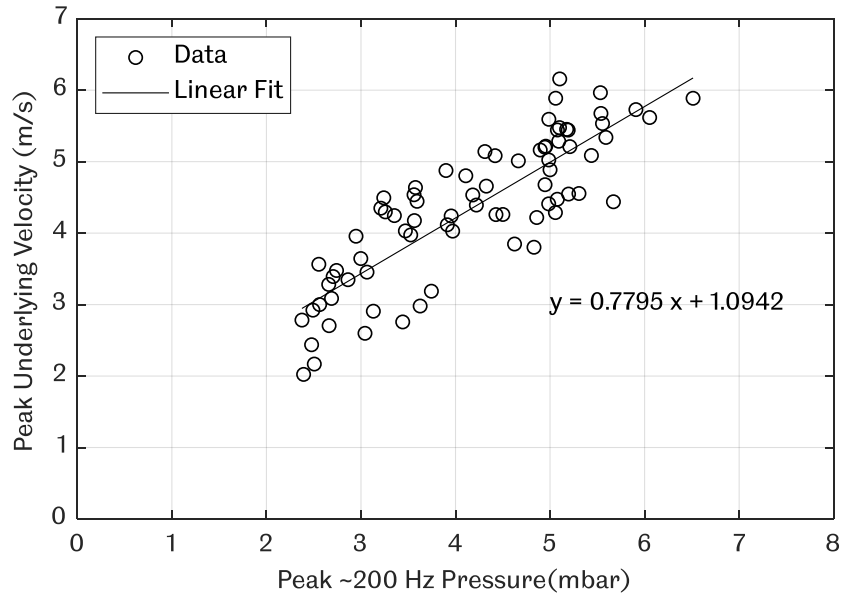
The contour plot of the ~400 Hz peak distance amplitude in Figure 5.40 shows a significant elevation along the  $R_H = 0.3$  line, especially in the lean mixtures, which also coincided with the gradual drop in the ~200 Hz peak distance amplitude contour plot in Figure 5.39. This indicates an oscillating flame which did not lead to a significant elongation of the flame, which appears to be obvious only in lean flames. Oscillating flames, which were related to period doubling, observed by Markstein [5] explains the increase in the ~400 Hz components, which was obvious based on their flame propagation images. Figure 6.3 shows the scatter plot for peak velocity against peak pressure for ~200 Hz and ~400 Hz data for all tested flames.





**Figure 6.3 Peak velocity against peak pressure scatter plot for all unsteady flames.**

Figure 6.3 displayed the expected similar trend in Figure 6.2. A linear trend was observed in both ~200 Hz and ~400 Hz components. The ~200 Hz component was represented by the equation  $y = 2.389x + 0.444$  ( $R^2 = 0.9621$ ), whereas the ~400 Hz component by the equation  $y = 0.507x + 0.885$  ( $R^2 = 0.6133$ ). Similar to the previous findings in Figure 6.2, the y-intercept for the ~400 Hz data was higher at 0.885 m/s compared to the ~200 Hz data at 0.444 m/s, suggesting that ~400 Hz peak velocity is higher than ~200 Hz peak velocity at ambient pressure. The gradients were however steeper for the ~200 Hz data, which indicates a more significant increase in peak velocity at the same peak pressure amplitude compared to the ~400 Hz data. Since the ~200 Hz component appears to be the dominant cause in the flame propagation instability, the peak ~200 Hz pressure was plotted against the peak underlying velocity in Figure 6.4, for heavily oscillated flames only.



**Figure 6.4 Peak underlying velocity against peak pressure scatter plot for ~200 Hz and ~400 Hz components of oscillating flames.**

Out of 216 experimental runs, only 77 experiments were observed to have heavily oscillated flames. The 77 runs were plotted in Figure 6.4, which displayed a linear trend represented by the equation  $y = 0.7795x + 1.0942$  ( $R^2 = 0.713$ ). Extrapolation towards the y-axis was not possible, since any flames with a ~200 Hz peak pressure lower than 2 mbar were not heavily oscillated. Since the peak ~200 Hz pressure was limited to the boundary conditions of the tube, the data was only able to reach ~6.5 mbar. It was thought that given a condition where the peak pressure was increased beyond ~6.5 mbar, the corresponding peak underlying velocity would obey the equation representing the equation  $y = 0.7795x + 1.0942$ .

Despite the vast range of fuels investigated in both portion of the current work, the instabilities observed fell into 3 different behaviours which were previously observed by Markstein [5]. Each behaviour had a certain set of distinct features which were used to categorize them.

The first observed behaviour was the classic steady flame, which had a distinct convex shape, attributed to non-slip walls condition, similar to previous researchers [6], [9], [31]. The steady flame was seen to occur in two distinctly different conditions, a slow steady flame without pressure oscillations, and a fast flame with pressure oscillations. A slow flame was steady since no coupling occurred between the heat release and the tube pressure, whereas the fast flame was too fast and did not respond to its self-generated pressure oscillations. Despite the difference, both flames exhibit a gradual velocity increment as they propagate to the end of the tube.

The second flame behaviour observed was the pulsating flame. Pulsating indicates the existence of pressure and heat release coupling, which usually causes flame speed reduction, observed experimentally and numerically in [5], [15], [24], [26], [73], [74], [110]–[112]. An initially steady flame will start to pulsate if the pressure build-up was enough to cause a reduction in the flame area as the flame responds to the pressure oscillations. The periodic oscillation of the pressure at ~200 Hz caused the flame to pulsate, and returns to a steady flame as the pressure oscillations decay and flame area started to increase slowly.

The third flame behaviour was the oscillating flame, which occurs if the pressure was strong enough to cause an increase in the flame area via flame surface inversion towards the hot burnt gas, causing a sudden acceleration of the flame. An oscillated flame started as a steady flame, which starts to pulsate due to increasing ~200 Hz pressure oscillations to a point where the pressure was strong enough to cause the flame to experience an increase in flame area in the form of a spike, towards the hot burnt gas, which Markstein [5] termed as an oscillating flame. This flame has been the interest of many researchers including [24–26], [60], [113] to name a few.

Following the formation of an oscillating flame, it was observed that the ~400 Hz pressure component was excited to a significant level. This spike was thought to be the result of the Rayleigh-Taylor instability as suggested by McIntosh [46]. The increase in flame area technically increases the surface area of the flame, hence the rate of reaction, causing a sudden increase in flame speed. If the ~200 Hz oscillation was in phase with the ~200 Hz heat release oscillation, a significant amplification in both the flame speed and pressure oscillation was observed. This phenomenon was related to Rayleigh's criterion, proposed by Lord Rayleigh [7].

The flame in its excited state exhibits period doubling (excitation of the ~400 Hz component) compared to a pulsating flame, the extra cycle coming from the period with Rayleigh-Taylor instability. Based on the phase study, both the ~400 Hz component of heat release and pressure were excited, but no phase matching was evident. The flame oscillation eventually stops and returns back to a pulsating flame, followed by a steady flame. It is worth noting that these behaviours occur sequentially.

From the 3 behaviours stated, the current work was able to identify 4 new points, used to describe the flame propagation with further detail, applicable to all unsteady flames. The points were A) pulsating flame with decreasing acceleration, B) oscillating flame with increasing acceleration, C) oscillating flame with decreasing acceleration, and finally D) pulsating flame with increasing acceleration. These 4

points were present in all oscillating flames while pulsating flames were observed to have only points A and D.

The different frequency components acting on the flame were responsible for the fluctuation of the underlying flame velocity. During point A, the pulsating flame was slowed down by the  $\sim 200$  Hz pressure build up, whereas at point B, the oscillating flame was accelerated by the  $\sim 200$  Hz pressure build up. The main difference between the two points were the flame shape, where the former had no flame surface inversion, but present in the latter. This event was expected as it had been observed previously in literature.

Following point B, the oscillating flame at point C was observed to be slowed down, which was not expected based on the literature. It was well established that oscillating flames will accelerate indefinitely due to the increase in flame surface area. The reduction in speed was thought to be the result of the amplitude increase in the  $\sim 400$  Hz oscillation, while the  $\sim 200$  Hz pressure oscillations stayed constant. This behaviour of having 2 different oscillations leading to a reduced pressure amplitude was observed by a recent study by Rao et al. [31], which they categorized as a dual-frequency oscillation mode. The flame then returned to a pulsating behaviour at point D, but with an increasing velocity, which was also never observed in previous literature. The gradual increase in velocity was attributed to the decaying  $\sim 200$  Hz and  $\sim 400$  Hz pressure as the flame approaches the end of the tube.

Exploring the frequency domain further using Synchrosqueezed Wavelet Transform (SST), the approximate start and end position of harmonic excitations were detected. The starting location was between 0.45-0.55m ( $\sim 2/5$  length of tube), reached the maximum velocity  $\sim 0.65$ m ( $\sim 1/2$  length of tube), and abruptly slowing down at  $\sim 0.7$ m ( $\sim 3/5$  length of tube). Slight variation of the starting point was observed, which was dependent on the pressure magnitude, a higher pressure led to an earlier starting point and vice versa. Peak values of the instabilities range from 0.002-0.011 bar for the natural light experiments.

Hydrogen addition to methane-air mixtures of any equivalence ratio shows a monotonic increase in their theoretical laminar burning velocity which were computed from CHEMKIN [101]. It was assumed that a systematic increase in the laminar burning velocity would lead to a systematically increasing maximum pressure and distance amplitude due to the unsteady behaviour of the flame. However, this was only found to be true until a hydrogen addition of  $R_H = 0.4$ . A further increase in hydrogen addition was observed to reduce the maximum pressure and distance amplitude. Markstein and Somers [28] observed a similar

event using methane and n-butane mixtures, and stated that slower flames had more time to interact with their self-generated noise compared to a faster flame.

The breakdown of the raw pressure and raw distance amplitude signal via SST showed that the ~200 Hz contour plots were almost identical to each other across the different mixtures used, unlike the ~400 Hz contour plots, which indicates phase matching only exists in the ~200 Hz region. The coupling of the ~200 Hz pressure and flame distance amplitude was attributed to the tube harmonics, which were calculated for a 1.2 m tube to be 149 Hz for the fundamental mode, 297 Hz for the first harmonic, and 446 Hz for the second harmonic. During the flame oscillations, the instantaneous frequency of the ~200 Hz components, obtained from the SST plots, increased towards 297 Hz during pressure build up, which then reduces once the pressure amplitude decays.

Markstein and Somers [28] obtained a similar pressure excitation despite the different boundary conditions compared to the present work. Two tubes of varying lengths (~0.6 and ~1.2 m and 9.15 cm internal diameter) were utilized to test their methane and n-butane mixtures and they discovered that a ~260 Hz oscillation was responsible for the excitation of the tube pressure. The second tube, which was similar in length with the current work, was found to be oscillating unpredictably at the fundamental frequency, which was not observed in the present work. The first harmonic of their tube was found to respond systematically with the equivalence ratio of the fuels tested similar to the present work. This led to a conclusion that the ~200 Hz oscillations are sensitive to the changes made in the fuel composition, unlike the other harmonics.

## 7 CONCLUSIONS

Premixed hydrocarbon and hydrogen air flames propagation in open ended horizontal tubes were investigated. Interesting unsteady behaviour of the flames were observed as they propagate along the tube, similar to the ones observed by researchers, compiled and compared by Markstein [5]. However, the past literatures were more motivated by the effect of the boundary condition compared to the flame chemistry, in other words, the tube dimensions were altered while using pure fuels with varying equivalence ratios.

There were very few exceptions to this norm, taking Markstein and Somers [28] as an example, where the physical and chemical factors affecting the unsteady propagation in tubes were investigated, but were only limited to rich premixed hydrocarbon mixtures of methane and butane. The scarcity made it desirable to further explore the chemical factors affecting unsteady propagation by keeping the physical factors constant and altering the chemical factors systematically. The difference in research approach was enough to justify a detailed investigation to be conducted.

The current study was conducted by keeping the tube diameter constant at 0.02 m and 1.2 m length in a horizontal orientation with both side open to the atmosphere. Optical access was provided via a quartz tube of 0.65m length of the same diameter, and recorded over a length of approximately 0.5m using a high-speed camera, which was sufficient to record the flame's whole period of instability. A pressure transducer was fitted to the opposite end from the ignition to track the tube pressure. One of the main advantages of the configuration was the relatively small amount of fuel used compared to other premixed flame rig, reducing hazard significantly.

The mixtures tested in the study consisted of methane and hydrogen. Equivalence ratios from 0.8-1.5 with 0.1 increments were investigated at each level of hydrogen addition defined by the term  $R_H$ , starting from  $R_H = 0$ , up to  $R_H = 0.8$  with similar increments of 0.1, ensuring each equivalence ratio to be systematically enriched with hydrogen.

The minor changes in the flame reactant enabled the current study to establish a relationship between the flame properties with the observed instabilities. The main flame properties that were changed are the laminar burning velocity, density ratio, speed of sound and the Lewis number. Theoretical values of the properties were calculated using CHEMKIN [101] and Gaseq [102]. The theoretical calculation of the Lewis number cannot be achieved for methane-hydrogen mixtures since no method

had been established for the  $R_H$  mixing method, but it was assumed to be inversely proportional to the hydrogen addition.

The current work was able to detect four different points of flame propagation as opposed to three based on previous literature. The four points are A (decelerating pulsating flame), B (oscillating accelerating flame), C (oscillating decelerating flame) and finally D (pulsating accelerating flame). This was achieved via time-domain signal decomposition using Synchrosqueezed wavelet transform, which was never used previously on thermoacoustic flame analysis. The impact of the different pressure components on the flame velocity made the correlation possible.

## 7.1 Future Work

Coming to the end of the present work, the author realized there are so many different paths to be taken in the future to further investigate the current data. Among them are exploring the possibilities of studying the growth rate of the instabilities in the decomposed oscillatory data, which would provide valuable information to modellers. Initially, the idea of studying growth rates was dismissed due to the unpredictable nature of the oscillatory components. The implementation of Empirical Mode Decomposition on the oscillatory data has now made the idea feasible, since the decomposed data seems to have distinct peaks and minimal distortion in them, which were the main culprit which halted the growth rate path.

After conducting the study up to  $R_H = 0.8$  hydrogen addition, the author is very curious on how pure hydrogen would behave in a flame tube. But of course, it would not be possible using a round tube due to the fact that pure hydrogen flame does not emit any light. The only option available to record a hydrogen flame is to record it using Schlieren imaging, which needs a flat surface confining the flame to be able to record any density difference in the air. This could be made possible by constructing a square cross-sectional tube made with quartz windows in order for the Schlieren imaging to work.

It would also be interesting to further explore the chemical side of things by adding carbon dioxide to the current mixture. Adding carbon dioxide would reduce the reactivity of the mixtures, thus opening a whole new range of experiments to be explored. However, this would be a difficult task to perform since there are very limited literatures in methane/hydrogen/carbon dioxide blends in existence.

With the huge amount of data available, the author plans to implement machine learning in analysing the existing data. With the amount of data available, it would be sufficient to conduct algorithm training using 2/3 of the data, and perform

verification using the remaining 1/3. The ultimate goal of this work is to obtain a flame classifier based on the pressure data alone, thus eliminating the need of a high-speed camera.



## REFERENCES

- [1] E. Mallard and H. Le Chatelier, "Annales des Mines, 8th Series," *Ann. des Mines*, vol. 17, p. 296, 1883.
- [2] W. Mason and R. Wheeler, "XCII.—The 'uniform movement' during the propagation of flame," *J. Chem. Soc. Trans.*, 1917.
- [3] H. F. Coward, F. J. Hartwell, and E. H. M. Georgeson, "306. Studies in the mechanism of flame movement. Part IV. The vibratory period," *J. Chem. Soc.*, p. 1482, 1937.
- [4] H. Guénoche, "Flame Propagation in Tubes and in Closed Vessels," in *Nonsteady Flame Propagation*, 1964, pp. 107–181.
- [5] G. H. Markstein, "Nonsteady Flame Propagation," 1964.
- [6] C. Clanet, G. Searby, and P. Clavin, "Primary acoustic instability of flames propagating in tubes: Cases of spray and premixed gas combustion," *J. Fluid Mech.*, vol. 385, pp. 157–197, 1999.
- [7] J. W. S. B. Rayleigh, "The Explanation of Certain Acoustical Phenomena," *Nature*, vol. 18, no. 455, pp. 319–321, 1878.
- [8] G. Searby, "Acoustic Instability in Premixed Flames," *Combust. Sci. Technol.*, vol. 81, no. March 2015, pp. 221–231, 1992.
- [9] G. Searby and D. Rochwerger, "A parametric instability in premixed flames," *J. Fluid Mech.*, vol. 231, pp. 529–543, 1991.
- [10] G. Yu, C. K. C. Law, and C. C. K. Wu, "Laminar flame speeds of hydrocarbon + air mixtures with hydrogen addition," *Combust. Flame*, vol. 63, no. 3, pp. 339–347, Mar. 1986.
- [11] B. Higgins, "On the sound produced by a current of hydrogen gas passing through a tube," *J. Nat. Philos. Chem. Arts*, vol. 1, pp. 130–131, 1802.
- [12] J. W. S. B. Rayleigh, *The Theory of Sound (2nd Edition)*, vol. 1. 1945.
- [13] A. A. Putnam and W. R. Dennis, "Survey of Organ-Pipe Oscillations in Combustion Systems," *J. Acoust. Soc. Am.*, vol. 28, no. 2, pp. 246–259, Mar.

1956.

- [14] E. H. W. Schmidt, H. Steinicke, and U. Neubert, "Flame and schlieren photographs of combustion waves in tubes," *Symp. Combust.*, vol. 4, no. 1, pp. 658–666, Jan. 1953.
- [15] W. E. Kaskan, "An investigation of vibrating flames," *Symp. Combust.*, vol. 4, no. 1, pp. 575–591, Jan. 1953.
- [16] M. N. Mikhail and M. R. El-Tantawy, "The acoustic boundary layers: a detailed analysis," *J. Comput. Appl. Math.*, vol. 51, no. 1, pp. 15–36, 1994.
- [17] A. Wood, *Acoustics*. London and Glasgow: Blackie & Son Limited, 1941.
- [18] P. L. Rijke, "Notiz über eine neue Art, die in einer an beiden Enden offenen Röhre enthaltene Luft in Schwingungen zu versetzen," *Ann. Phys.*, vol. 183, no. 6, pp. 339–343, 1859.
- [19] H. Young and R. Freedman, *University Physics*, 12th Editi. San Francisco, CA: Addison Wesley, 2008.
- [20] S. Candel, "Combustion dynamics and control: Progress and challenges," *Proc. Combust. Inst.*, vol. 29, no. 1, pp. 1–28, Jan. 2002.
- [21] Y. Taniyama and O. Fujita, "Initiation and formation of the corrugated structure leading to the self-turbulization of downward propagating flames in a combustion tube with external laser absorption," *Combust. Flame*, vol. 161, no. 6, pp. 1558–1565, Jun. 2014.
- [22] G. Taylor, "The instability of liquid surfaces when accelerated in a direction perpendicular to their planes. I," *Proc. R. Soc. ...*, 1950.
- [23] H. Xiao, W. An, Q. Duan, and J. Sun, "Dynamics of premixed hydrogen/air flame in a closed combustion vessel," *Int. J. Hydrogen Energy*, vol. 38, no. 29, pp. 12856–12864, Sep. 2013.
- [24] B. Ponizy, A. Claverie, and B. Veyssière, "Tulip flame - the mechanism of flame front inversion," *Combust. Flame*, vol. 161, no. 12, pp. 3051–3062, 2014.
- [25] A. Hariharan and I. S. Wichman, "Premixed Flame Propagation and Morphology

- in a Constant Volume Combustion Chamber,” *Combust. Sci. Technol.*, vol. 186, no. 8, pp. 1025–1040, Aug. 2014.
- [26] H. Xiao, R. W. Houim, and E. S. Oran, “Formation and evolution of distorted tulip flames,” *Combust. Flame*, vol. 162, no. 11, pp. 4084–4101, Nov. 2015.
- [27] G. H. Markstein, “Interaction of Flow Pulsations and Flame Propagation,” *J. Aeronaut. Sci.*, vol. 18, no. 6, pp. 428–429, Jun. 1951.
- [28] G. H. Markstein and L. M. Somers, “Cellular flame structure and vibratory flame movement in N-butane-methane mixtures,” *Symp. Combust.*, vol. 4, no. 1, pp. 527–535, Jan. 1953.
- [29] W. Jost, *Explosions- und Verbrennungsvorgänge in Gasen*. Berlin, Heidelberg: Springer Berlin Heidelberg, 1939.
- [30] C. M. Coats, Z. Chang, and P. D. Williams, “Excitation of thermoacoustic oscillations by small premixed flames,” *Combust. Flame*, vol. 157, no. 6, pp. 1037–1051, 2010.
- [31] Z. Rao, R. Li, B. Zhang, B. Wang, and D. Zhao, “Experimental investigations of equivalence ratio effect on nonlinear dynamics features in premixed swirl-stabilized combustor,” *Aerosp. Sci. Technol.*, vol. 1, p. 106601, 2021.
- [32] H. Gotoda, M. Amano, T. Miyano, T. Ikawa, K. Maki, and S. Tachibana, “Characterization of complexities in combustion instability in a lean premixed gas-turbine model combustor,” *Chaos*, vol. 22, no. 4, 2012.
- [33] F. A. Williams, *Combustion Theory*. CRC Press, 1985.
- [34] D. B. Newell and E. Tiesinga, “The international system of units (SI):,” Gaithersburg, MD, Aug. 2019.
- [35] J. W. S. B. Rayleigh, “Investigation of the character of the equilibrium of an incompressible heavy fluid of variable density,” *Proc. London Math. Soc.*, vol. s1-14, no. 1, pp. 170–177, 1882.
- [36] D. Lewis, “The instability of liquid surfaces when accelerated in a direction perpendicular to their planes. II,” *Proc. R. Soc. London. Ser. A. Math. Phys. Sci.*,

- vol. 202, no. 1068, pp. 81–96, Jun. 1950.
- [37] H. W. Emmons, C. T. Chang, and B. C. Watson, “Taylor instability of finite surface waves,” *J. Fluid Mech.*, vol. 7, no. 2, pp. 177–193, Feb. 1960.
- [38] G. R. Baker, D. I. Meiron, and S. A. Orszag, “Vortex simulations of the Rayleigh–Taylor instability,” *Phys. Fluids*, vol. 23, no. 8, p. 1485, 1980.
- [39] C. L. Gardner, J. Glimm, O. McBryan, R. Menikoff, D. H. Sharp, and Q. Zhang, “The dynamics of bubble growth for Rayleigh–Taylor unstable interfaces,” *Phys. Fluids*, vol. 31, no. 3, p. 447, 1988.
- [40] R. D. Richtmyer, “Taylor instability in shock acceleration of compressible fluids,” *Commun. Pure Appl. Math.*, vol. 13, no. 2, pp. 297–319, 1960.
- [41] E. E. Meshkov, “Instability of the interface of two gases accelerated by a shock wave,” *Fluid Dyn.*, vol. 4, no. 5, pp. 101–104, 1972.
- [42] H. J. Kull, “Theory of the Rayleigh–Taylor instability,” *Phys. Rep.*, vol. 206, no. 5, pp. 197–325, 1991.
- [43] P. Clavin and G. Searby, *Gaseous Shocks and Detonations*. 2017.
- [44] C. L. Gardner *et al.*, “A study of chaos and mixing in Rayleigh–Taylor and Richtmyer–Meshkov unstable interfaces,” *Nucl. Phys. B - Proc. Suppl.*, vol. 2, pp. 441–451, Nov. 1987.
- [45] L. D. Cloutman and M. F. Wehner, “Numerical simulation of Richtmyer–Meshkov instabilities,” *Phys. Fluids A Fluid Dyn.*, vol. 4, no. 8, pp. 1821–1830, Aug. 1992.
- [46] F. Liu, A. C. McIntosh, and J. Brindley, “A Numerical Investigation of Rayleigh–Taylor Effects in Pressure Wave–Premixed Flame Interactions,” *Combust. Sci. Technol.*, vol. 91, no. 4–6, pp. 373–386, Jun. 1993.
- [47] T. Tsuruda, M. Harayama, and T. Hirano, “Growth of flame front turbulence,” *J. Heat Transfer*, vol. 108, no. 4, pp. 877–881, 1986.
- [48] C. E. Ebieta, “Dynamics of Premixed Flames in Tube,” 2017.
- [49] G. Joulin and P. Clavin, “Linear stability analysis of nonadiabatic flames:

- Diffusional-thermal model," *Combust. Flame*, vol. 35, no. C, pp. 139–153, 1979.
- [50] G. I. Sivashinsky, "Diffusional-Thermal Theory of Cellular Flames," *Combust. Sci. Technol.*, vol. 15, no. 3–4, pp. 137–145, Jan. 1977.
- [51] P. Clavin, "Dynamic behavior of premixed flame fronts in laminar and turbulent flows," *Prog. Energy Combust. Sci.*, vol. 11, no. 1, pp. 1–59, 1985.
- [52] B. Denet and P. Haldenwang, "Numerical Study of Thermal-Diffusive Instability of Premixed Flames," *Combust. Sci. Technol.*, vol. 86, no. 1–6, pp. 199–221, Nov. 1992.
- [53] C. Kaiser, J.-B. Liu, and P. Ronney, "Diffusive-thermal instability of counterflow flames at low Lewis number," in *38th Aerospace Sciences Meeting and Exhibit*, 2000, no. January.
- [54] A. Clarke, "Calculation and Consideration of the Lewis Number for Explosion Studies," *Process Saf. Environ. Prot.*, vol. 80, no. 3, pp. 135–140, May 2002.
- [55] G. S. Jackson, R. Sai, J. M. Plaia, C. M. Boggs, and K. T. Kiger, "Influence of H<sub>2</sub> on the response of lean premixed CH<sub>4</sub> flames to high strained flows," *Combust. Flame*, vol. 132, no. 3, pp. 503–511, Feb. 2003.
- [56] C. Clanet and G. Searby, "First experimental study of the darrieus-landau instability," *Phys. Rev. Lett.*, vol. 80, no. 17, pp. 3867–3870, 1998.
- [57] P. Clavin, "Dynamics of combustion fronts in premixed gases: From flames to detonations," *Proc. Combust. Inst.*, vol. 28, no. 1, pp. 569–585, 2000.
- [58] F. J. Higuera, "Acoustic response of a lean premixed flame propagating upward in a tube," *Combust. Flame*, vol. 199, pp. 377–386, 2019.
- [59] V. A. Popov, "The initial propagation distance of flames in closed tubes," *Izvest. Akad. Nauk SSSR, Otd. Tekh. Nauk*, no. No. 3, p. 116, 1956.
- [60] C. Clanet and G. Searby, "On the 'tulip flame' phenomenon," *Combust. Flame*, vol. 105, no. 1–2, pp. 225–238, Apr. 1996.
- [61] H. Behrens, "Flame instabilities and combustion mechanism," *Symp. Combust.*, vol. 4, no. 1, pp. 538–545, Jan. 1953.

- [62] P. Clavin, "Premixed Combustion and Gasdynamics," *Annu. Rev. Fluid Mech.*, vol. 26, no. 1, pp. 321–352, Jan. 1994.
- [63] J. Yang, F. M. S. Mossa, H. W. Huang, Q. Wang, R. Woolley, and Y. Zhang, "Oscillating flames in open tubes," *Proc. Combust. Inst.*, vol. 35, no. 2, pp. 2075–2082, 2015.
- [64] S. Kerampran, D. Desbordes, and B. Veyssi re, "Study of the mechanisms of flame acceleration in a tube of constant cross section," *Combust. Sci. Technol.*, vol. 158, no. February 2014, pp. 71–91, 2000.
- [65] C. Mandilas, M. P. Ormsby, C. G. W. Sheppard, and R. Woolley, "Effects of hydrogen addition on laminar and turbulent premixed methane and iso-octane–air flames," *Proc. Combust. Inst.*, vol. 31, no. 1, pp. 1443–1450, Jan. 2007.
- [66] X. J. Gu, M. Z. Haq, M. Lawes, and R. Woolley, "Laminar burning velocity and Markstein lengths of methane–air mixtures," *Combust. Flame*, vol. 121, no. 1–2, pp. 41–58, Apr. 2000.
- [67] H. Edmondson and M. Heap, "The burning velocity of methane-air flames inhibited by methyl bromide," *Combust. Flame*, 1969.
- [68] C. Vagelopoulos, F. Egolfopoulos, and C. Law, "Further considerations on the determination of laminar flame speeds with the counterflow twin-flame technique," ... *Int. Combust.*, 1994.
- [69] F. Halter, C. Chauveau, N. Djeb ili-Chaumeix, and I. G okalp, "Characterization of the effects of pressure and hydrogen concentration on laminar burning velocities of methane–hydrogen–air mixtures," *Proc. Combust. Inst.*, vol. 30, no. 1, pp. 201–208, Jan. 2005.
- [70] D. Bradley, M. Lawes, and R. Mumby, "Burning velocity and Markstein length blending laws for methane/air and hydrogen/air blends," *Fuel*, vol. 187, pp. 268–275, 2017.
- [71] R. H. Herrera, J. Han, and M. van der Baan, "Applications of the synchrosqueezing transform in seismic time-frequency analysis," *Geophysics*, vol. 79, no. 3, pp. V55–V64, 2014.

- [72] M. X. Cohen, *Analyzing Neural Time Series Data*. The MIT Press, 2014.
- [73] C. E. Ebieto, N. A. Amaludin, and R. Woolley, "Methane / Hydrogen / Air Flame Oscillations in Open Ended Tubes," in *Proceedings of the 25th International Colloquium on the Dynamics of Explosion and Reactive Systems*, 2015, vol. 25, no. 99.
- [74] F. Veiga-López, D. Martínez-Ruiz, E. Fernández-Tarrazo, and M. Sánchez-Sanz, "Experimental analysis of oscillatory premixed flames in a Hele-Shaw cell propagating towards a closed end," *Combust. Flame*, vol. 201, pp. 1–11, 2019.
- [75] I. Daubechies, J. Lu, and H. T. Wu, "Synchrosqueezed wavelet transforms: An empirical mode decomposition-like tool," *Appl. Comput. Harmon. Anal.*, vol. 30, no. 2, pp. 243–261, 2011.
- [76] C. Li and M. Liang, "Timefrequency signal analysis for gearbox fault diagnosis using a generalized synchrosqueezing transform," *Mech. Syst. Signal Process.*, vol. 26, no. 1, pp. 205–217, 2012.
- [77] M. Mihalec, J. Slavič, and M. Boltežar, "Synchrosqueezed wavelet transform for damping identification," *Mech. Syst. Signal Process.*, vol. 80, pp. 324–334, 2016.
- [78] P. Ozel, A. Akan, and B. Yilmaz, "Synchrosqueezing transform based feature extraction from EEG signals for emotional state prediction," *Biomed. Signal Process. Control*, vol. 52, pp. 152–161, 2019.
- [79] Y. Hu, X. Tu, and F. Li, "High-order synchrosqueezing wavelet transform and application to planetary gearbox fault diagnosis," *Mech. Syst. Signal Process.*, 2019.
- [80] MathWorks, "Wavelet Synchrosqueezing," 2020. [Online]. Available: <https://uk.mathworks.com/help/wavelet/gs/wavelet-synchrosqueezing.html#bu9sda1-1>. [Accessed: 03-Mar-2020].
- [81] I. Daubechies, *Ten Lectures on Wavelets*. Society for Industrial and Applied Mathematics, 1992.
- [82] I. Daubechies and S. Maes, "A Nonlinear Squeezing of the Continuous Wavelet Transform Based on Auditory Nerve Models," in *Wavelets in Medicine and*

- Biology*, Routledge, 2017, pp. 527–546.
- [83] C. Li and M. Liang, “A generalized synchrosqueezing transform for enhancing signal time–frequency representation,” *Signal Processing*, vol. 92, no. 9, pp. 2264–2274, Sep. 2012.
- [84] “MATLAB.” The MathWorks, Inc., Natick, Massachusetts, United States., 2018.
- [85] K. T. Kim, J. G. Lee, B. D. Quay, and D. A. Santavicca, “The dynamic response of turbulent dihedral v Flames: An amplification mechanism of swirling flames,” *Combust. Sci. Technol.*, vol. 183, no. 2, pp. 163–179, 2011.
- [86] K. C. Schadow, E. Gutmark, T. P. Parr, D. M. Parr, K. J. Wilson, and J. E. Crump, “Large-Scale Coherent Structures as Drivers of Combustion Instability,” *Combust. Sci. Technol.*, vol. 64, no. 4–6, pp. 167–186, Apr. 1989.
- [87] A. Petchenko, V. Bychkov, V. Akkerman, and L. E. Eriksson, “Flame-sound interaction in tubes with nonslip walls,” *Combust. Flame*, vol. 149, no. 4, pp. 418–434, 2007.
- [88] K. R. Mcmanus, T. Poinso, and S. M. Candel, “A review of active control of combustion instabilities,” *Prog. Energy Combust. Sci.*, vol. 19, no. 1, pp. 1–29, 1993.
- [89] S. Hubbard and a. P. Dowling, “Acoustic Resonances of an Industrial Gas Turbine Combustion System,” *J. Eng. Gas Turbines Power*, vol. 123, no. 4, p. 766, 2001.
- [90] S. L. Hahn, *Hilbert Transforms in Signal Processing*. Artech House Signal Processing Library, 1996.
- [91] MathWorks, “Hilbert Transform,” 2020. [Online]. Available: <https://uk.mathworks.com/help/signal/ref/hilbert.html>. [Accessed: 01-Jul-2020].
- [92] J. O. Smith III, “Mathematics of the Discrete Fourier Transform: With Audio Applications,” 2002. [Online]. Available: <https://ccrma.stanford.edu/~jos/mdft/>.



- [93] H. J. Lee, K. T. Kim, J. G. Lee, B. D. Quay, and D. A. Santavicca, "An experimental study on the coupling of combustion instability mechanisms in a lean premixed gas turbine combustor," *Proc. ASME Turbo Expo*, vol. 2, pp. 749–758, 2009.
- [94] P. Pennington, "Flames in Tubes," University of Sheffield, 2009.
- [95] F. Mossa, "Flames in Tubes," University of Sheffield, 2014.
- [96] M. H. Wu, M. P. Burke, S. F. Son, and R. A. Yetter, "Flame acceleration and the transition to detonation of stoichiometric ethylene/oxygen in microscale tubes," *Proc. Combust. Inst.*, vol. 31 II, pp. 2429–2436, 2007.
- [97] Vision Research, "Phantom v210 Data Sheet," Wayne, New Jersey, USA, 2009.
- [98] K. Group, "Type 7261 Low Pressure Transducer," Winterthur, Switzerland, 2010.
- [99] D. Incorporated, "Druck PDCR 800 series," Druck Incorporated, New Fairfield, Connecticut, USA, 2000.
- [100] N. Instruments, "National Instruments myDAQ User Guide," 2016.
- [101] R. J. Kee, F. M. Rupley, and J. A. Miller, "CHEMKIN." Sandia National Labs, Livermore, California, 1987.
- [102] C. Morley, "Gaseq." 2005.
- [103] "Phantom Camera Control." Vision Research, 2016.
- [104] "VirtualDub." 2013.
- [105] D. Bradley *et al.*, "Turbulent burning velocity, burned gas distribution, and associated flame surface definition," *Combust. Flame*, vol. 133, no. 4, pp. 415–430, 2003.
- [106] A. V. Oppenheim, R. W. Schaffer, and J. R. Buck, *Discrete-Time Signal Processing*, Second Edi. Upper Saddle River New Jersey: Prentice Hall, 1999.
- [107] W. van Drongelen, "Continuous, Discrete, and Fast Fourier Transform," in *Signal Processing for Neuroscientists*, Elsevier, 2018, pp. 103–118.
- [108] MathWorks, "Time-frequency ridges from wavelet synchrosqueezing," 2020.

[Online].

Available:

<https://uk.mathworks.com/help/wavelet/ref/wsstridge.html>. [Accessed: 03-Mar-2020].

- [109] T. C. Lieuwen, *Unsteady Combustor Physics*. Cambridge: Cambridge University Press, 2012.
- [110] R. C. Assier and X. Wu, "Linear and weakly nonlinear instability of a premixed curved flame under the influence of its spontaneous acoustic field," *J. Fluid Mech.*, vol. 758, pp. 180–220, 2014.
- [111] H. Jiang, N. A. Amaludin, and Y. Zhang, "Premixed Methane / Air / Hydrogen Flame Oscillations in Horizontal Open End Tubes," in *Proceedings of the 27th International Colloquium on the Dynamics of Explosion and Reactive Systems*, 2019, pp. 1–6.
- [112] M. Gonzalez, "Acoustic instability of a premixed flame propagating in a tube," *Combust. Flame*, vol. 107, no. 3, pp. 245–259, 1996.
- [113] O. J. Teerling, A. C. McIntosh, J. Brindley, and V. H. Y. Tam, "Premixed flame response to oscillatory pressure waves," *Proc. Combust. Inst.*, vol. 30, no. 2, pp. 1733–1740, Jan. 2005.

## APPENDICES

### Appendix A: Rig Volume Calculation

The steps for the rig volume ( $V_R$ ) calculation are as follows:

1. Prepare a syringe containing 50 mL of air.
2. Vacuum the rig.
3. Isolate the rig from the vacuum using the one-way valve, record the pressure reading ( $P_1$ ) and start the stopwatch.
4. Once the time reaches 20 seconds, record the pressure reading ( $P_2$ ) and inject the 50mL ( $V_A$ ) of air into the rig via the fuel injection port.
5. Record the pressure reading ( $P_3$ ) once the 50mL ( $V_A$ ) of air is injected completely.
6. When the time reaches 60 seconds, record the final pressure reading ( $P_4$ ) of the rig.
7. Repeat steps 1-6 a total of 3 times.

3 sets of pressure readings were collected and used in the following equations:

$$V_1 = \frac{P_2 V_2}{P_1} \quad (\text{A.1})$$

$$V_2 = \frac{V_A P_3}{P_2 - P_3} \quad (\text{A.2})$$

$$V_3 = V_A + V_2 \quad (\text{A.3})$$

$$V_4 = \frac{P_3 V_3}{P_4} \quad (\text{A.4})$$

$$V_R = V_4 - V_A \quad (\text{A.5})$$

A known quantity of air needs to be injected into the rig to be incorporated in the equations which consisted of 5 unknown volumes; thus, the injection of  $V_A$  was a vital part of the process. Equation (A.1) was calculated first before solving the other equations. The rig volume calculated from all 3 runs were averaged and used for calculating fuel volume. Table A.1 shows a rig calculation example.

**Table A.1 Rig volume calculation example.**

	Pressure (bar)	Time (s)		Volume (mL)
$P_1$	-0.9481	0	$V_1$	1164.76
$P_2$	-0.9478	20	$V_2$	1168.13
$P_3$	-0.9088	33	$V_3$	1215.13
$P_4$	-0.9083	60	$V_4$	1215.80
	$V_R$			1165.80

## **Appendix B: Fuel Collection Procedure**

Fuel collection from the gas cylinder storage requires a strict procedure to prevent any mishap. The person performing this was required to attend a Gas Cylinder Handling training, Control of Substances Hazardous to Health (CoSHH) online and in-person training. A CoSHH form was drafted for this specific task and submitted to the Departmental Safety and Health Officer (DSO) to be reviewed and revised. The procedure for fuel collection was as follows:

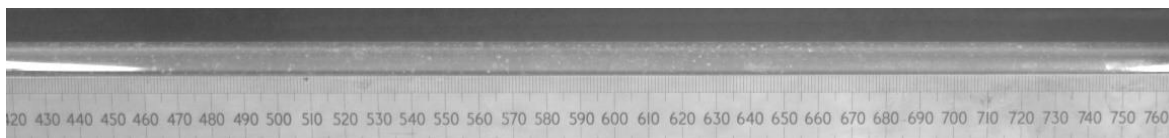
1. Ensure an assigned technician with necessary trainings was present, observing the process.
2. Gas cylinder was examined and ensured to be secured in the holder.
3. The gas cylinder regulator was visually inspected for any signs of damage and has not exceeded its service date.
4. If the regulator was damaged or service date has expired, fuel collection was stopped.
5. Gas storage compound was made sure to be free from any ignition sources.
6. The cylinder gauges were examined to make sure it was reading zero with the regulator and main cylinder valves closed.
7. If the reading of the regulator was non-zero, the main valve of the gas cylinder was closed and the regulator valve was opened to purge any remaining gas inside the regulator.
8. Main cylinder valve was opened, followed by the regulator valve for approximately ten seconds to maintain the purity of the collected gas, purging any air from the cylinder hose.
9. The On/Off valve on the gas sampling bag was opened and attached to the cylinder hose.
10. Only gas sampling bags designated for the gas collected were used to prevent cross contamination.
11. The regulator valve was opened until the bag was filled.
12. Regulator valve was closed, followed by the On/Off valve and the main cylinder valve.

13. The On/Off valve was disconnected from the cylinder hose, followed by opening the regulator valve to purge any remaining gas in the regulator.
14. Gas compound was properly locked before leaving.
15. Gas bag was taken directly to the lab, ensuring there were no significant ignition sources along the path. If any ignition sources were present, an alternative route to the lab was taken.

## Appendix C: Optical Calibration

Optical calibration is an important part of the present work, since any error will directly affect the experimental results. A set of procedures were established to help minimize imaging error and improve the quality of the recordings. The procedures were as follows:

1. The height of the camera was adjusted to the same level as the quartz tube.
2. Focal length of the lens was changed to achieve the desired recording range.
3. Sampling rate of the camera was adjusted to a viewable fps in ambient light.
4. The image resolution was adjusted to fit the recorded part of the tube via the camera software, Phantom Camera Control.
5. The software's horizontal grid display was utilized to align the camera with the tube, making sure the view of the tube was not slanted.
6. A metal wire was inserted inside the quartz tube and the camera focus was adjusted to focus on the metal wire and removing it once focusing was completed.
7. A ruler was placed on the top middle part of the quartz tube and a picture was taken for pixel-distance conversion in post-processing, as shown in Figure C.1.
8. Sampling rate was changed to the desired rate, which was determined by the type of flame tested. This was usually determined by doing a test recording. Sampling rate was increased if the flame was too bright, decreased if flame was too faint.
9. De-noising was done by closing the lens with a lens cap, and performing Current Session Referencing (CSR) in the camera software.



**Figure C.1 Measuring the recorded length of tube.**

## Appendix D: Pressure calibration

The pressure calibration was done through the interface on the Kistler Type 5018 Charge Amplifier. The charge amplifier usually stores the current settings, but if the pressure readings are not logical, it is a good practice to recheck the settings as shown in Figure C.2. The pressure range should be 1.0 bar, sensitivity at -2321 pC/bar (obtained from calibration sheet included with Kistler Type 7261 Pressure Transducer), time constant set to short ( $\tau = 0.42\text{s}$ ), and low pass filter turned off. The pressure signal conversion is shown at the bottom of the screen, which is 0.1 bar/V.

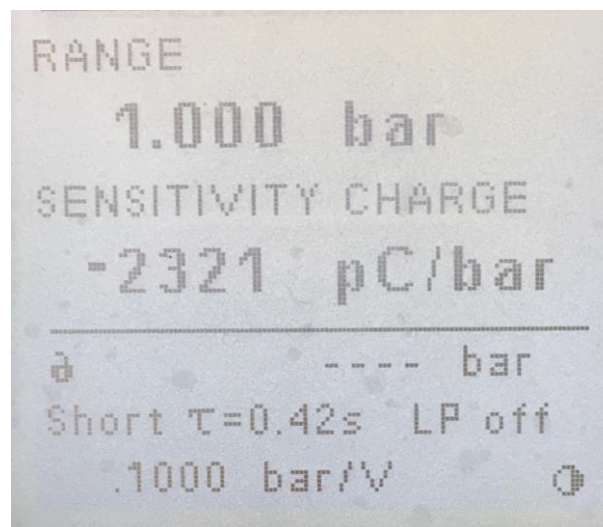


Figure D.1 Kistler Type 5018 Charge Amplifier settings.



## **Appendix E: Experimental Procedures**

Similar to the fuel collection procedure, the experimental procedures are strict. An online and in-person CoSHH training were required to perform the experimental procedures. The procedures are as follows:

1. Equipment and wires were organized to prevent any tripping hazards.
2. Eye protection was worn at all times.
3. The quartz tube was inspected visually for any signs of damage. Quartz tube will be replaced/repaired if damaged.
4. The one-way valve connecting the rig to the vacuum pump was opened.
5. Vacuum was turned on to an approximate pressure of -0.95 bar. Pressure was monitored using the Druck Digital Pressure Indicator 260
6. Either one of the three-way valves was opened to let ambient air into the rig. This was repeated twice to ensure any by-product from a previous combustion was removed.
7. Rig was vacuumed again for the last time and the one-way valve connecting the vacuum pump and rig was closed, leaving the rig under vacuum.
8. A syringe was used to collect the required fuel volume from a gas sampling bag. Gas bag was returned to its designated container and syringe was kept away from any ignition sources.
9. Fuel was injected into the fuel injection port and the needle sheath was replaced on the syringe needle.
10. One three-way valve was opened, allowing ambient air to enter the rig. The valve opening was kept at minimum to reduce dust particles entering the rig, which may cause the flame to have small red spots during combustion.
11. The three-way valve was closed once the pressure reading rises to ambient pressure, approximately 0 bar.
12. Mixing fans were turned on and left running for three minutes to create a homogenous mixture.
13. Mixing fans were turned off, and tube ends were cleared from any objects to prevent fire.

14. Lights were turned off to remove any source of ambient light from the recording, which improves the recording quality. Occupiers of the lab were alerted before turning the lights off.
15. Both three-way valves were turned, isolating the quartz tube section from the main mixing loop.
16. Ignition port was opened.
17. Camera trigger was pressed, pilot flame was used to ignite the mixture via the ignition port and followed by releasing the trigger button once the flame finished propagating.
18. Lights were turned on followed by turning all the valves back to their original positions.

## Appendix F: Flame Tracking Code

```
%% Flame Tracker

folder    = '(Replace with folder directory)';
pattern   = fullfile(folder, '*.bmp'); %detects file extension, change
type according to pic type, jpeg,bmp etc.
images    = dir(pattern); %lists files that matches the pattern
ps1       = 50; %5)pixel size for hole filler. Change to larger if
multiple spots appear
ps2       = 300 %50)
mlength   = 0.477 %measured length of tube
staen     = 8 %3(1.2 RH0.2)
thr       = 0.7 %99(1.2 RH0.2)
strelsize = 1 %1)
findp     = 0.85
ek        = length(images)

for k = 1:ek
j = 1
cframe    = images(k).name;
bgstaframe = images(j).name;
cframeim  = fullfile(folder, cframe);
bgstaframeim = fullfile(folder,bgstaframe);
currentarray = imread(cframeim);
bgstaarray   = imread(bgstaframeim);
stadiff      = (currentarray);%1. Background subtraction(stop
background substitution for now)
tdiff        = (stadiff*staen);%2.Background difference enhancement
bwtdiff      = im2bw(tdifff, thr); %3.Binary conversion.
bwclean     = bwareaopen(bwtdiff,ps1); %4.First pixel removal
se          = strel('disk',strelsize);
bwstrel     = imclose(bwclean,se);%5.Structuring element to join
separated flame front
bwfill      = imfill(bwstrel,'holes') %6.Gap filling
bwclean2    = bwareaopen(bwfill,ps2);%7. Second pixel removal.
blobcc      = bwconncomp(bwclean2, 8); %declare blobs as connected
components %8.Coordinate based noise removal.
blobstats   = regionprops(blobcc, 'Area', 'Centroid'); %Obtain stats of
blobs
bloblabel   = labelmatrix(blobcc); % Create label matrix
totalblob   = length(blobstats)% Find total number of blobs

    for u      = 1:totalblob %Convert centroid structure into double
centroidx(u)=blobstats(u).Centroid(:,1); %Obtain only x-coordinate
end

[ypixel, xpixel] = find(bwclean2); % Coordinates of all the white
pixels.
ylast            = numel(ypixel); %find the index for last y
coordinate(rightmost)

    if ylast>1
        xsort = xpixel(ylast); %find the corresponding x coordinate
        if totalblob >= 2
            ind_x = find(centroidx >= xsort*findp); %find index of x
coordinate +/- 90%
```

```

        bwsorted = ismember(bloblabel, ind_x);
    else
        bwsorted = bwclean2;
    end

imshow(bwsorted)
[x,y] = size(bwsorted);
columnsum = sum(bwsorted,1);
FT = find(columnsum >5);
front = max(FT);
tail = min(FT);
thickness = front-tail;
fsize = sum(FT);
yn = (1:y);
distribution = (bwsorted).* (yn);
vectdist = distribution(:);
vectdist(vectdist==0) = [];
median = nanmedian(vectdist);
mean = floor(nanmean(vectdist));
lconv = mlength/y;
aconv = (lconv*lconv);
cfront(k) = front*lconv;
ctail(k) = tail*lconv;
cthickness(k) = thickness*lconv;
cmedian(k) = median*lconv;
cmean(k) = mean*lconv;
csize(k) = fsize;

else
    cfront(k) = 0;
    ctail(k) = 0;
    cthickness(k) = 0;
    cmedian(k) = 0;
    csize(k) = 0;
end

end

```

## Appendix G: Data Extractor Code

```
%% Data Extractor

for i = 1:197

    fr      = MethaneRHFront{1,i}
    p       = MethaneRHPressure{1,i}
    dsample = MethaneRHDelay{1,i}
    lbv     = MethaneRHLBV{1,i}
    resfreq = MethaneRHResFreq{1,i}

    slength = length(fr)
    if dsample>0 %compensate pressure lead
        fr      = fr(1+dsample:slength)
        p       = p(1:slength-dsample)
    end

    if dsample<0 %compensate pressure lag
        fr      = fr(1:slength+dsample)
        p       = p(1-dsample:slength)
    end

    np      = 4; % Envelope sensitivity
    psstp   = 35; % pressure SST Penalty
    psstafr = 35; % Amplitude Front SST Penalty
    lo200p  = 200;
    hi200p  = 260;
    lo400p  = 440;
    hi400p  = 550;
    lo200afr = 200;
    hi200afr = 260;
    lo400afr = 440;
    hi400afr = 550;
    R       = 40; % number of ridges
    fsx     = 1500; %sampling rate
    dtx     = 1/fsx; %time per frame
    fsp     = 1500; %pressure sample rate
    dtp     = 1/fsp; %time per sample

    tx = 0:dtx: numel(fr)*dtx-dtx; %generates the time data for the
    experimental data set
    tf = max(tx)
    pbf = 26; % 71 126 157 165 % Passband frequency for filter
    pbr = 1; % % Passband ripple for filter
    sbf = 204 %150 150 230 256 % Stopband frequency
    sba = 55 % Stopband attenuation
    lpFilt = designfilt('lowpassfir',... % Filter design
        'PassbandFrequency',pbf,...
        'Stopbandfrequency',sbf,...
        'StopbandAttenuation',sba,...
        'PassbandRipple',pbr,...
        'SampleRate',fsx);
    ffr = filtfilt(lpFilt,fr); %%filtered front
    afr = fr-ffr; %%front amplitude
    hvfr = diff(afr)/dtx; %% High pass velocity
    vfr = diff(ffr)/dtx; %%low pass front velocity
    nvfr = vfr/lbv;
    rvfr = diff(fr)/dtx %% raw velocity
```

```

accfr = diff(vfr)/dtx;
tv = tx(2:end)
ta = tx(3:end);

mpd = 0.0015
mphp = (0.15)*(max(p))
[pkp,lpp]=findpeaks(p,tx,'MinPeakDistance',mpd,'MinPeakHeight',mphp,'sort
str','descend');
pfirst5 = pkp(1:5)
pavg = mean(pfirst5);

mphaf = (0.15)*(max(afr))
[pkafr,lpafr]=findpeaks(afr,tx,'MinPeakDistance',mpd,'MinPeakHeight',mpha
fr,'sortstr','descend');
afrfirst5 = pkafr(1:5)
afravg = mean(afrfirst5);

tp = 0:dtp:numel(p)*dtp-dtp; %pressure time
lenp = floor(0.2*(length(p))); %pressure extension length
pext = wextend('1D','sym',p,lenp)% pressure extension
[sstp,fp] = wsst(pext,fsp); %sst on extended pressure
[fridgep,iridgep] = wsstridge(sstp,psstp,fp,'NumRidges',R);% pressure
ridge detection
precon = iwsst(sstp,iridgep); %reconstructed pressure signal
array
[pupext,~] = envelope(pext,np,'peaks'); %envelope for extended
pressure
pup = pupext(lenp+1 : end-lenp); %cropping extended
pressure envelope

tafr = 0:dtp:numel(afr)*dtx-dtx;
lenafr = floor(0.2*(length(afr)));
afrext = wextend('1D','sym',afr,lenafr)
[sstafr,fafr] = wsst(afrext,fsx);
[fridgeafr,iridgeafr] = wsstridge(sstafr,psstafr,fafr,'NumRidges',R);
afrrecon = iwsst(sstafr,iridgeafr);

[~,afrcol200] = find(frigeafr>lo200afr & frigeafr<hi200afr,1)
[~,afrcol400] = find(frigeafr>lo400afr & frigeafr<hi400afr,1)
[~,pcol200] = find(frigeap>lo200p & frigeap<hi200p,1)
[~,pcol400] = find(frigeap>lo400p & frigeap<hi400p,1)

p200 = (precon(:,pcol200));
[p200upext,~] = envelope(p200,np,'peaks');
p200up = p200upext(lenp+1 : end-lenp);
p200 = p200(lenp+1 : end-lenp);
instfp200ext = fridgep(:,pcol200)
instfp200 = instfp200ext(lenp+1 : end-lenp);

afr200 = (afrrecon(:,afrcol200));
vfr200 = diff(afr200)/dtx;
[afr200upext,~] = envelope(afr200,np,'peaks');
[vfr200upext,~] = envelope(vfr200,np,'peaks');
afr200up = afr200upext(lenafr+1 : end-lenafr);
vfr200up = vfr200upext(lenafr+1 : end-lenafr);
afr200 = afr200(lenafr+1 : end-lenafr);
vfr200 = vfr200(lenafr+1 : end-lenafr);
instfafr200ext = fridgeafr(:,afrcol200)
instfafr200 = instfafr200ext(lenafr+1 : end-lenafr);

```

```

p400          = (precon(:,pcol400));
[p400upext,~] = envelope(p400,np,'peaks');
p400up        = p400upext(lenp+1 : end-lenp);
p400          = p400(lenp+1 : end-lenp);
instfp400ext  = fridgep(:,pcol400)
instfp400     = instfp400ext(lenp+1 : end-lenp);

afr400        = (afrrcon(:,afrcol400));
vfr400        = diff(afr400)/dtx;
[afr400upext,~] = envelope(afr400,np,'peaks');
[vfr400upext,~] = envelope(vfr400,np,'peaks');
afr400up      = afr400upext(lenafr+1 : end-lenafr);
vfr400up      = vfr400upext(lenafr+1 : end-lenafr);
afr400        = afr400(lenafr+1 : end-lenafr);
vfr400        = vfr400(lenafr+1 : end-lenafr);
instfafr400ext = fridgeafr(:,afrcol400)
instfafr400    = instfafr400ext(lenafr+1 : end-lenafr);

speedratio = vfr200up./vfr

mphp200 = (0.15)*(max(p200))
[pkp200,lpp200]=findpeaks(p200,tx,'MinPeakDistance',mpd,'MinPeakHeight',m
php200,'sortstr','descend');
p200first5 = pkp200(1:5)
p200avg = mean(p200first5);

mphp400 = (0.15)*(max(p400))
[pkp400,lpp400]=findpeaks(p400,tx,'MinPeakDistance',mpd,'MinPeakHeight',m
php400,'sortstr','descend');
p400first5 = pkp400(1:5)
p400avg = mean(p400first5);

mphafr = (0.15)*(max(afr))
[pkafr,lpafr]=findpeaks(afr,tx,'MinPeakDistance',mpd,'MinPeakHeight',mpha
fr,'sortstr','descend');
afrfirst5 = pkafr(1:5)
afravg = mean(afrfirst5);

mphafr200 = (0.15)*(max(afr200))
[pkafr200,lpafr200]=findpeaks(afr200,tx,'MinPeakDistance',mpd,'MinPeakHei
ght',mphafr200,'sortstr','descend');
afr200first5 = pkafr200(1:5)
afr200avg = mean(afr200first5);

mphvfr200 = (0.15)*(max(vfr200))
[pkvfr200,lpvfr200]=findpeaks(vfr200,tv,'MinPeakDistance',mpd,'MinPeakHei
ght',mphvfr200,'sortstr','descend');
vfr200first5 = pkvfr200(1:5)
vfr200avg = mean(vfr200first5);
nvfr200avg = vfr200avg/lbv;

mphafr400 = (0.15)*(max(afr400))
[pkafr400,lpafr400]=findpeaks(afr400,tx,'MinPeakDistance',mpd,'MinPeakHei
ght',mphafr400,'sortstr','descend');
afr400first5 = pkafr400(1:5)
afr400avg = mean(afr400first5);

```

```

mphvfr400 = (0.15)*(max(vfr400))
[pkvfr400,lpvfr400]=findpeaks(vfr400,tv,'MinPeakDistance',mpd,'MinPeakHeight',mphvfr400,'sortstr','descend');
vfr400first5 = pkvfr400(1:5)
vfr400avg = mean(vfr400first5);
nvfr400avg = vfr400avg/lbv;

vsub = vfr200-vfr
vfrstaavg = mean (vfr(1:5))
vfrendavg = mean (vfr(end-5:end))
vfrpeak = max (vfr)
if vfrpeak < vfrendavg +0.5
    vfrpeak = 0
end
nvfrpeak = vfrpeak/lbv;
nvfrstaavg = vfrstaavg/lbv;
nvfrendavg = vfrendavg/lbv;

trough = -(rvfr)
[sortedtroughvfr,timetrroughvfr]=findpeaks(trough,tv,'MinPeakDistance',mpd,'MinPeakHeight',0,'sortstr','descend');
[nonsortedtroughvfr,indicestroughvfr]=findpeaks(trough,'MinPeakHeight',0);
;
troughtotal = length(indicestroughvfr); %total number of reversal
timerev = tx(indicestroughvfr);
frrev = fr(indicestroughvfr); %location of flow
reversals
frev = instfp200(indicestroughvfr); %frequency of
oscillation during reversal
prev = p200up (indicestroughvfr); %pressure during
reversal

if trougtotal>5
    troughvfravg = mean(sortedtroughvfr(1:5)) ;
    lengthrevstart = frrev(1);
    lerrev = frrev(end) - frrev(1);
    cyclenumber = 1:1:troughttotal;
    durrev = timerev(end) - timerev(1);
end

if (troughttotal<=5) && (troughttotal>=1)
    troughvfravg = max(sortedtroughvfr);
    lengthrevstart = frrev(1);
    lerrev = frrev(end) - frrev(1);
    cyclenumber = 1:1:troughttotal;
    durrev = timerev(end) - timerev(1);
end

if trougtotal<1
    troughvfravg = 0;
    lengthrevstart = 0;
    durrev = 0;
    frrev = 0; %location of flow reversals
    frev = 0; %frequency of oscillation during reversal
    prev = 0; %pressure during reversal
    cyclenumber = 0;
    timerev = 0;
    lerrev = 0;
end

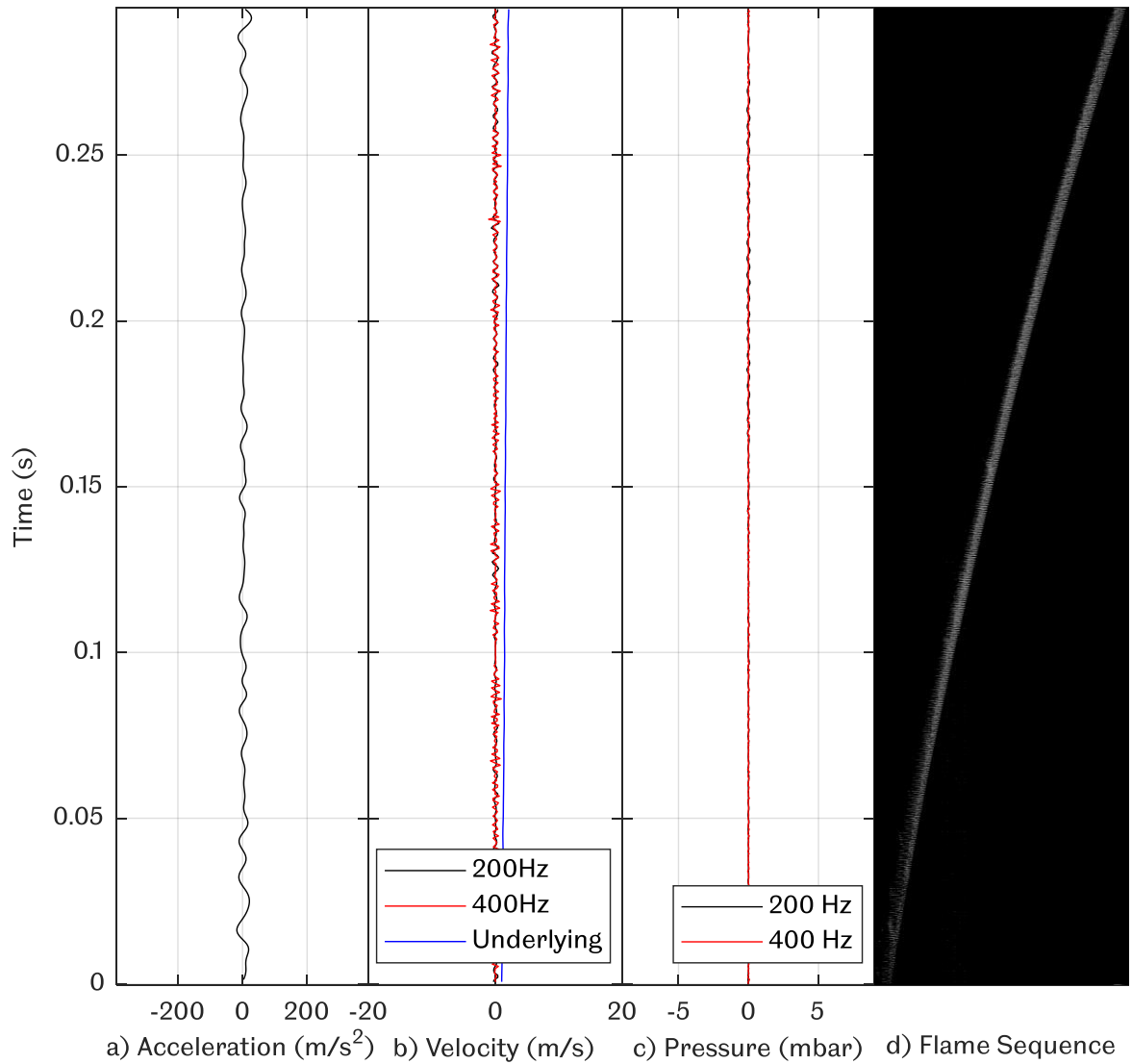
```



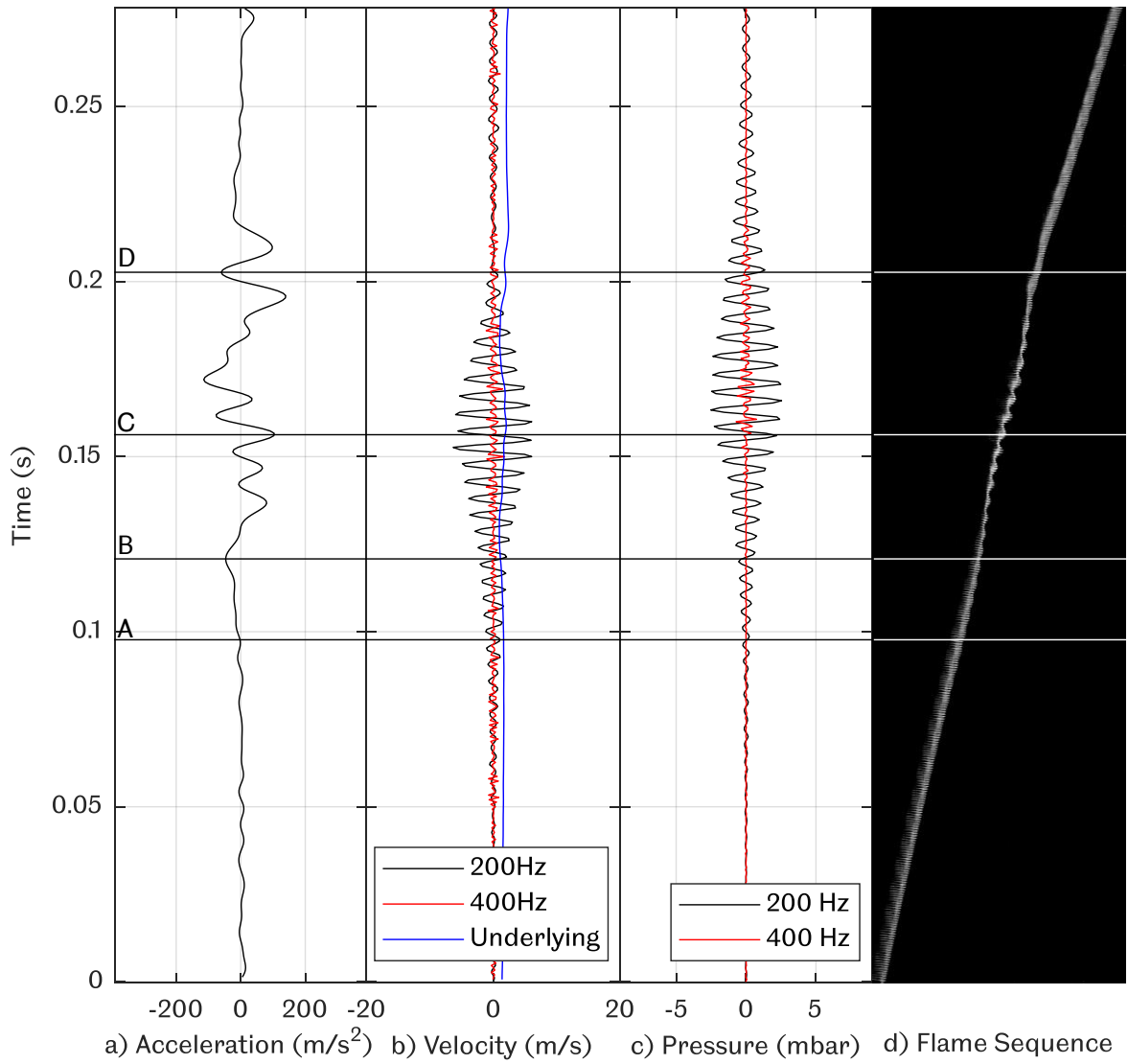
```
vtable(i,:) = [pavg, p200avg, p400avg, afravg, afr200avg, afr400avg,  
vfrstaavg, vfrendavg, vfr200avg, vfr400avg, troughvfravg, lengthrevstart,  
durrev, trougtotal,lerrev,vfrpeak, nvfrpeak, nvfr200avg, nvfr400avg,  
nvfrstaavg, nvfrendavg]
```

```
end
```

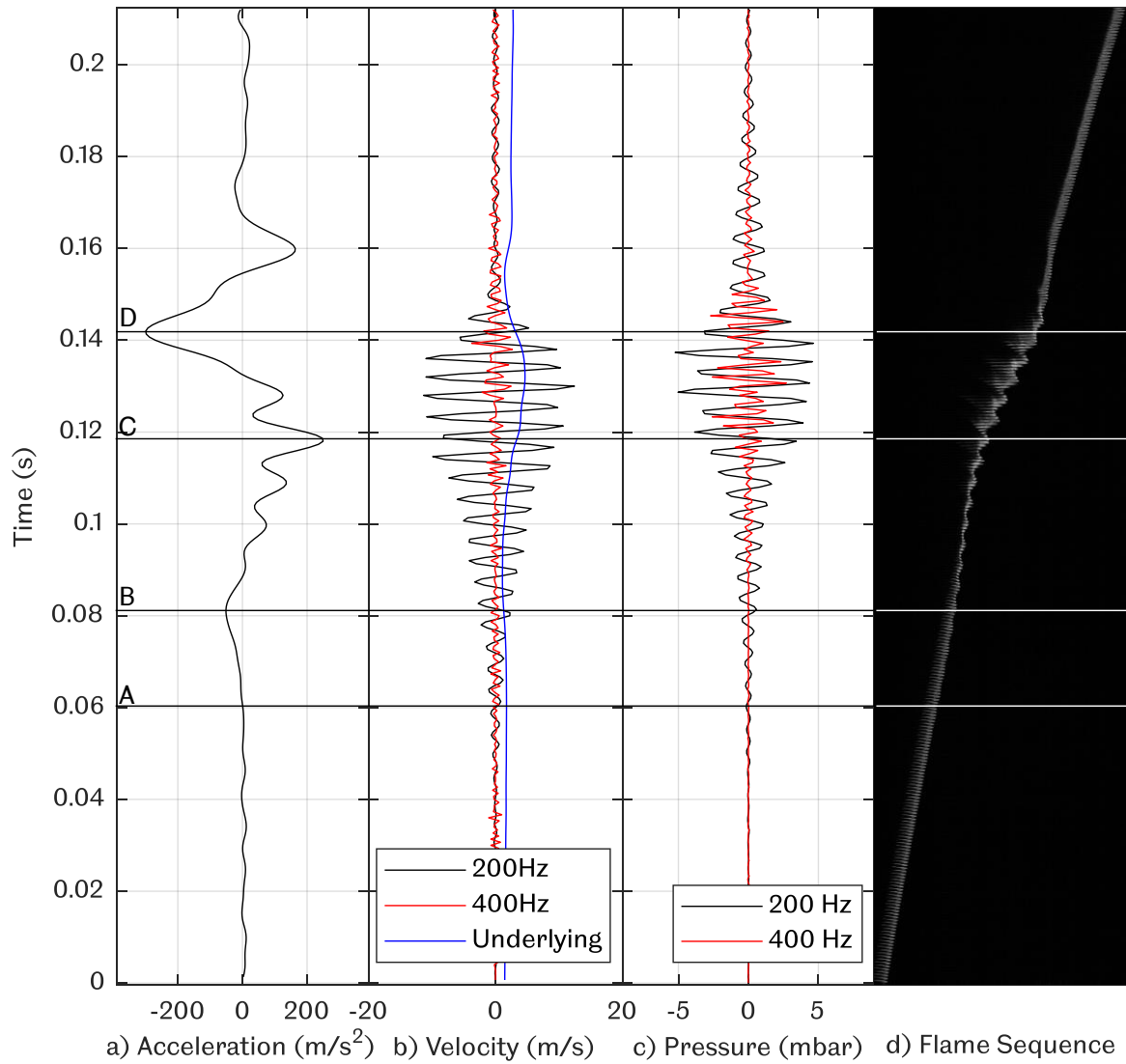
## Appendix H: Whole Flame Propagation (Equivalence Ratio Effect)



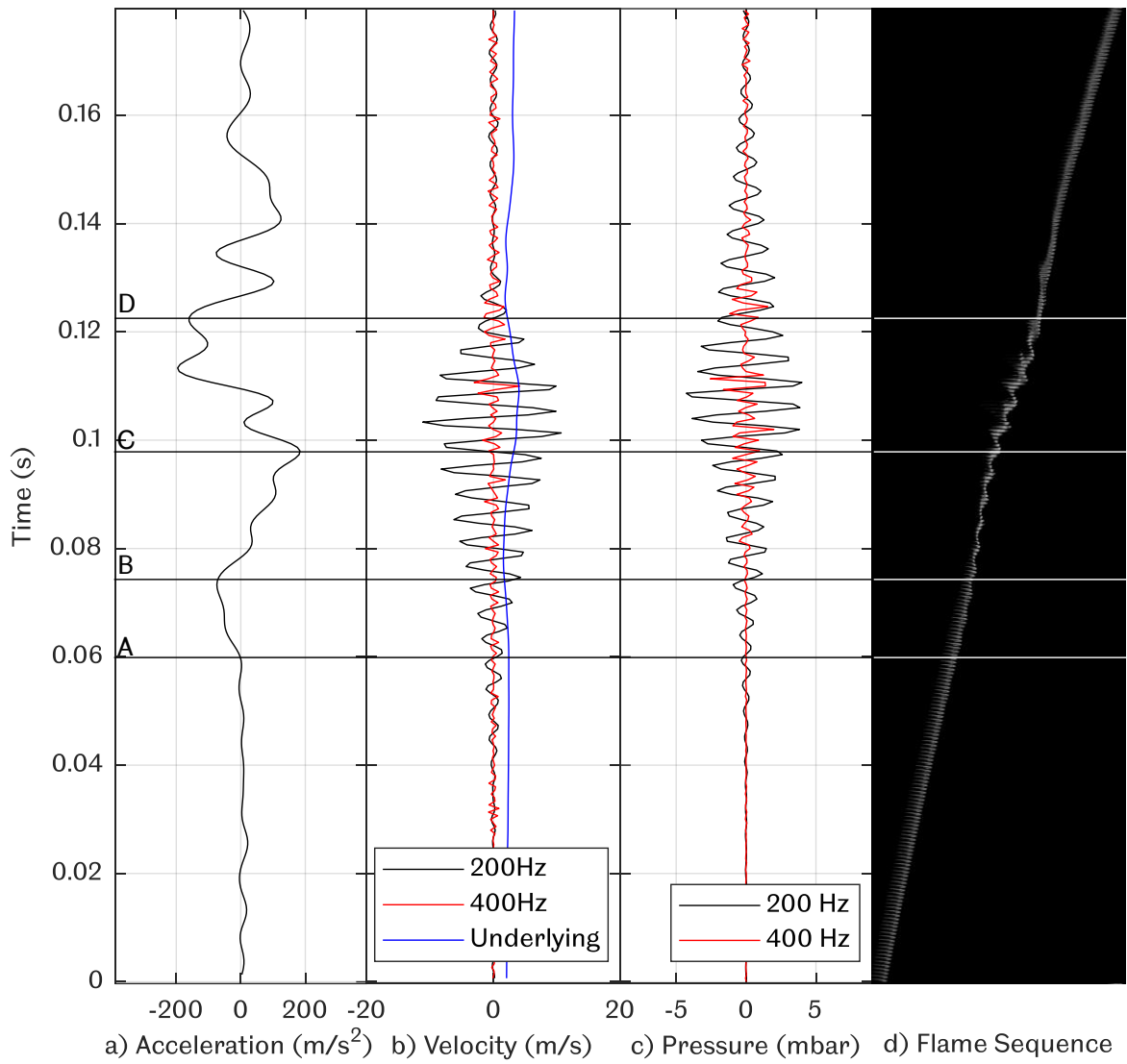
**Figure H.1 Propagation of a  $R_H = 0.1$ ,  $\phi = 0.8$  methane flame with a) underlying acceleration, b) decomposed velocity, c) decomposed pressure and d) flame sequence.**



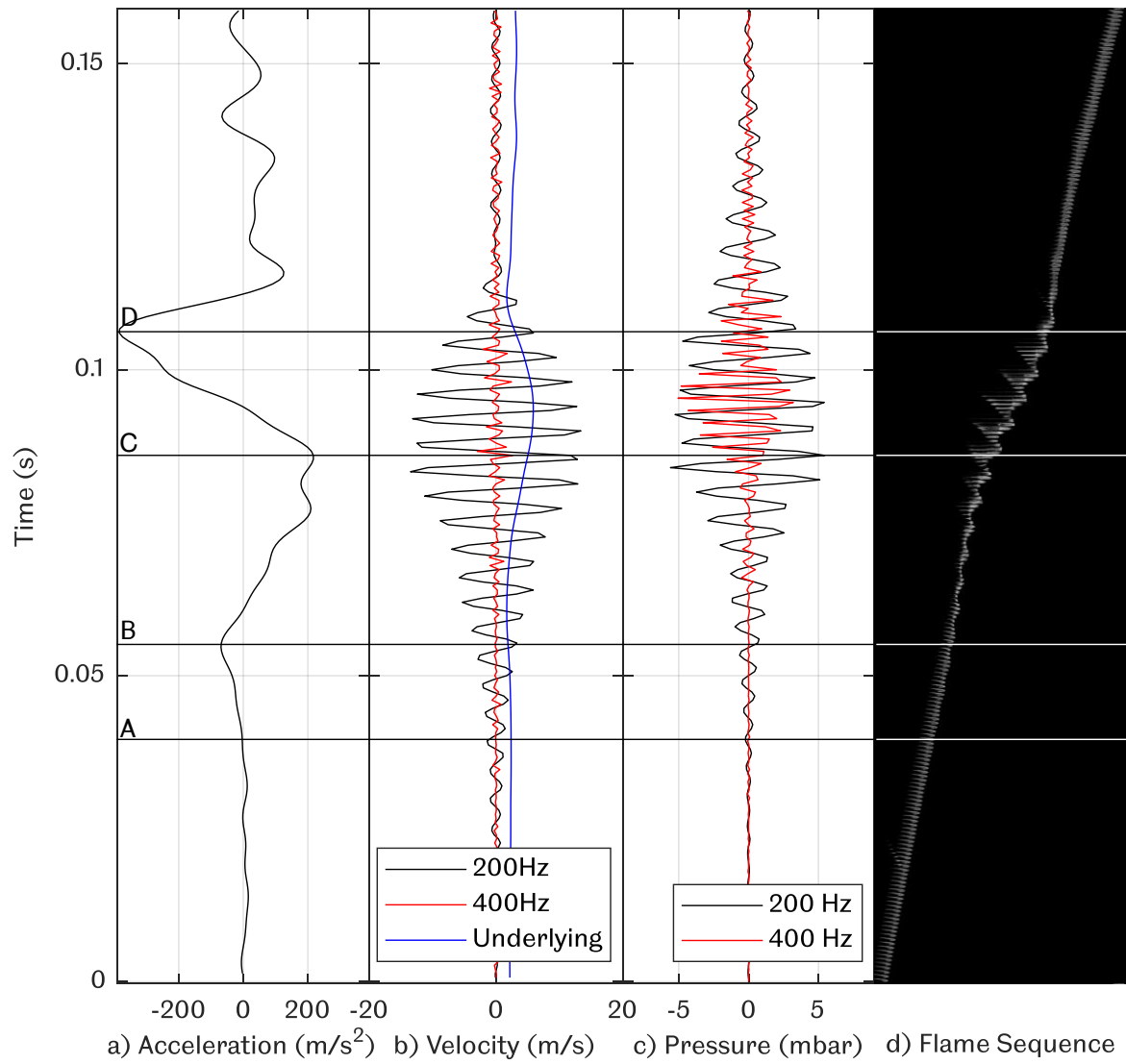
**Figure H.2 Propagation of a  $R_H = 0.1$ ,  $\phi = 0.9$  methane flame with a) underlying acceleration, b) decomposed velocity, c) decomposed pressure and d) flame sequence.**



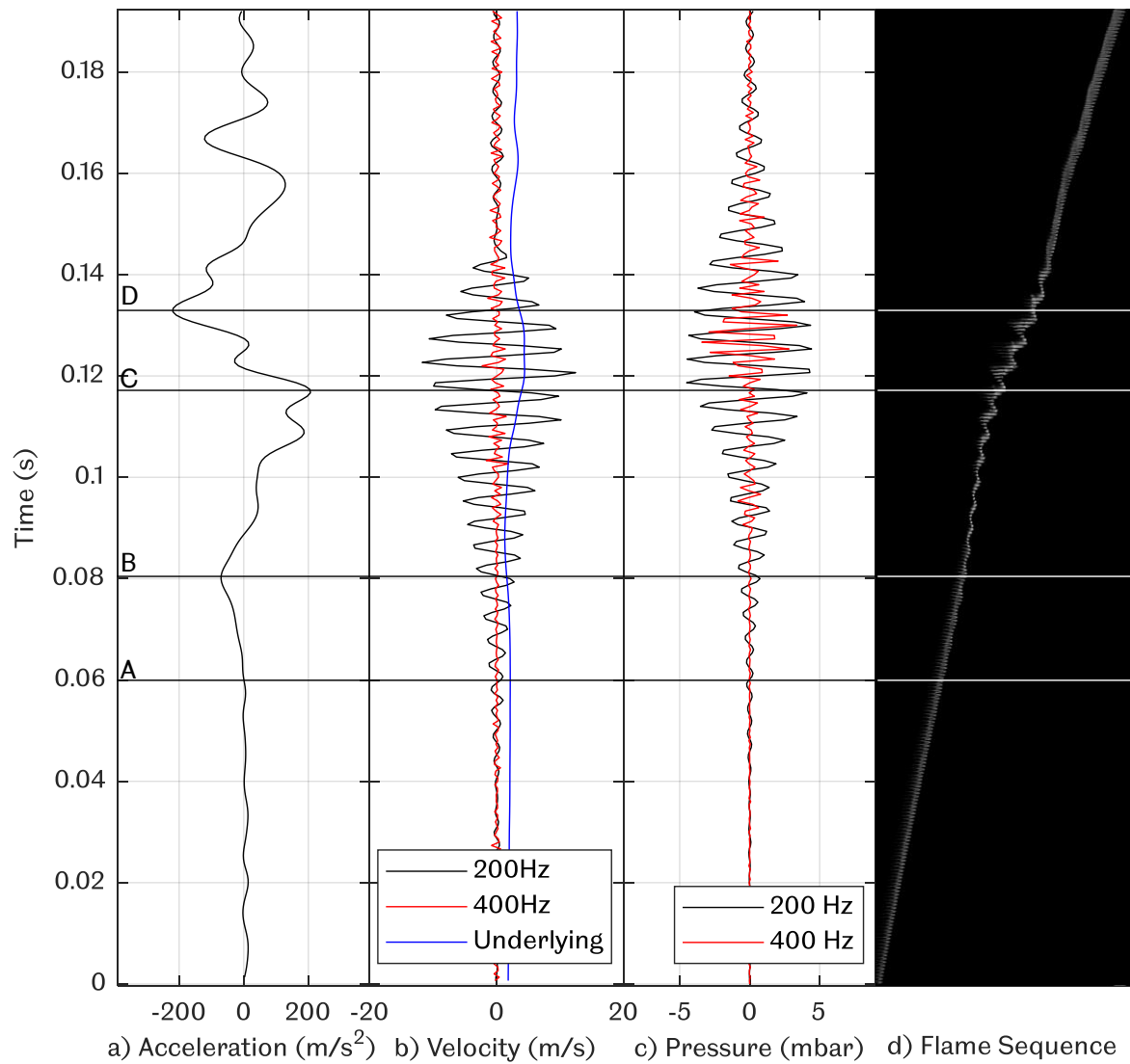
**Figure H.3 Propagation of a  $R_H = 0.1$ ,  $\phi = 1.0$  methane flame with a) underlying acceleration, b) decomposed velocity, c) decomposed pressure and d) flame sequence.**



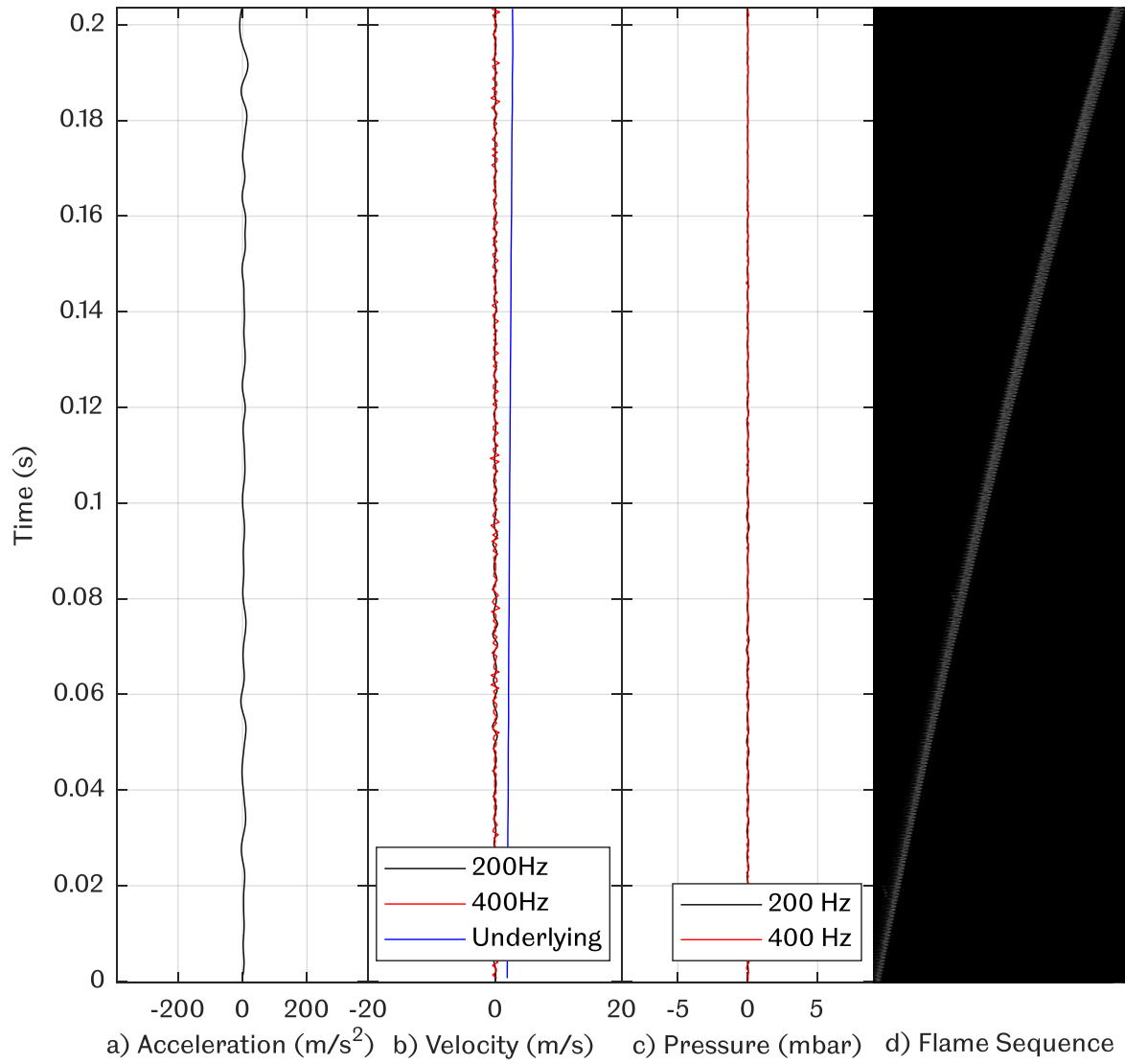
**Figure H.4 Propagation of a  $R_H = 0.1$ ,  $\phi = 1.1$  methane flame with a) underlying acceleration, b) decomposed velocity, c) decomposed pressure and d) flame sequence.**



**Figure H.5 Propagation of a  $R_H = 0.1$ ,  $\phi = 1.2$  methane flame with a) underlying acceleration, b) decomposed velocity, c) decomposed pressure and d) flame sequence.**

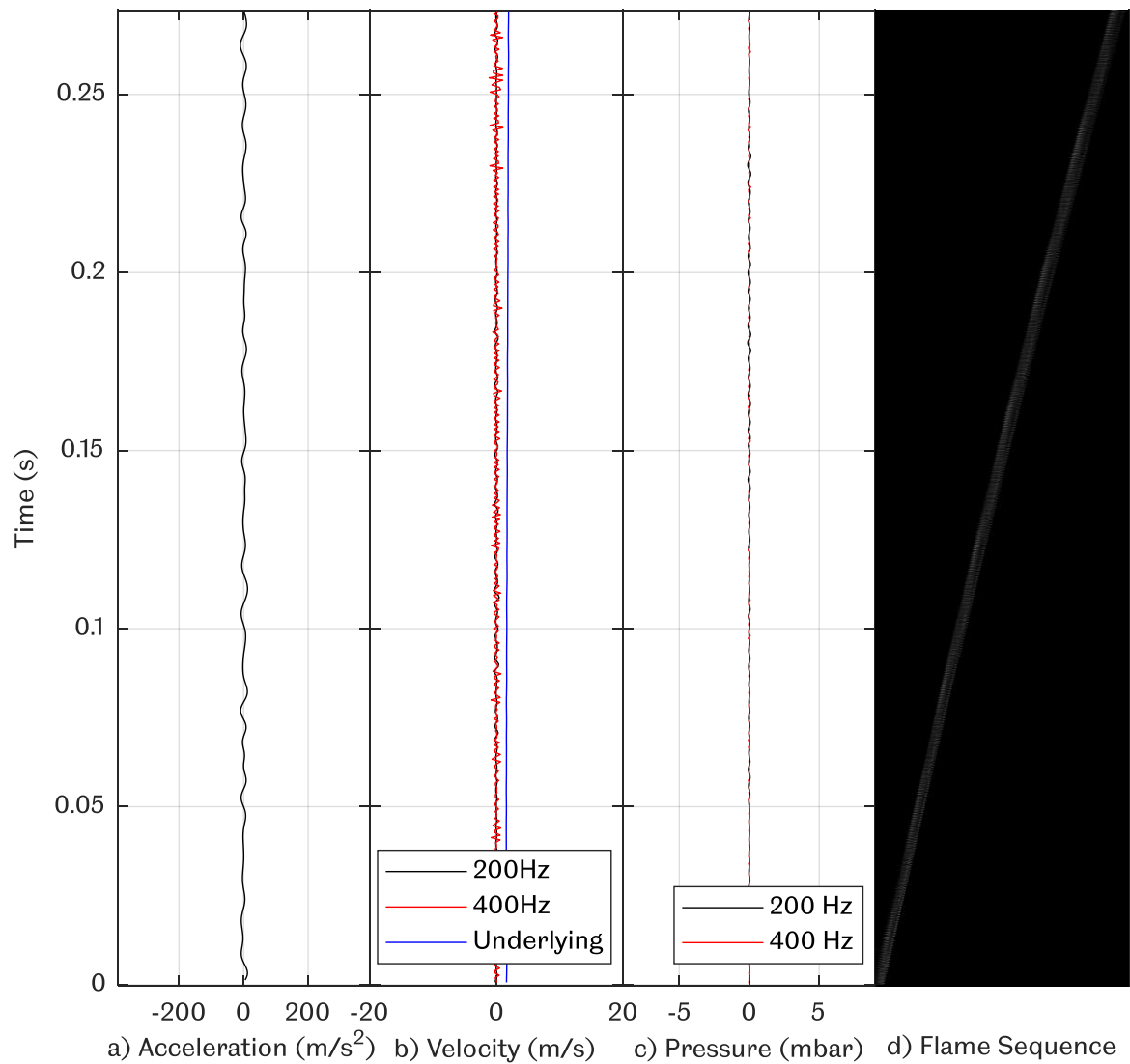


**Figure H.6 Propagation of a  $R_H = 0.1$ ,  $\phi = 1.3$  methane flame with a) underlying acceleration, b) decomposed velocity, c) decomposed pressure and d) flame sequence.**



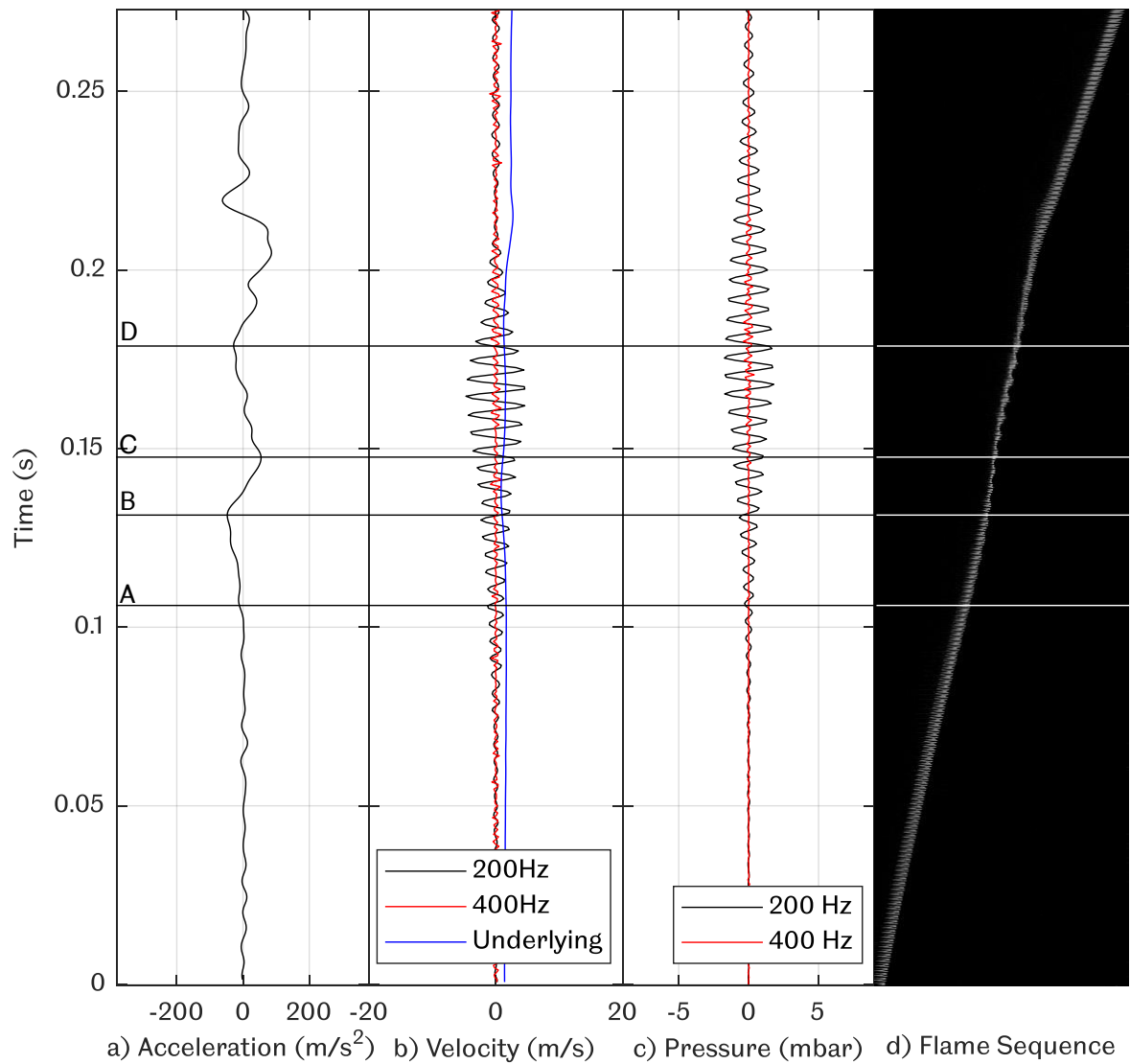
**Figure H.7 Propagation of a  $R_H = 0.1$ ,  $\phi = 1.4$  methane flame with a) underlying acceleration, b) decomposed velocity, c) decomposed pressure and d) flame sequence.**



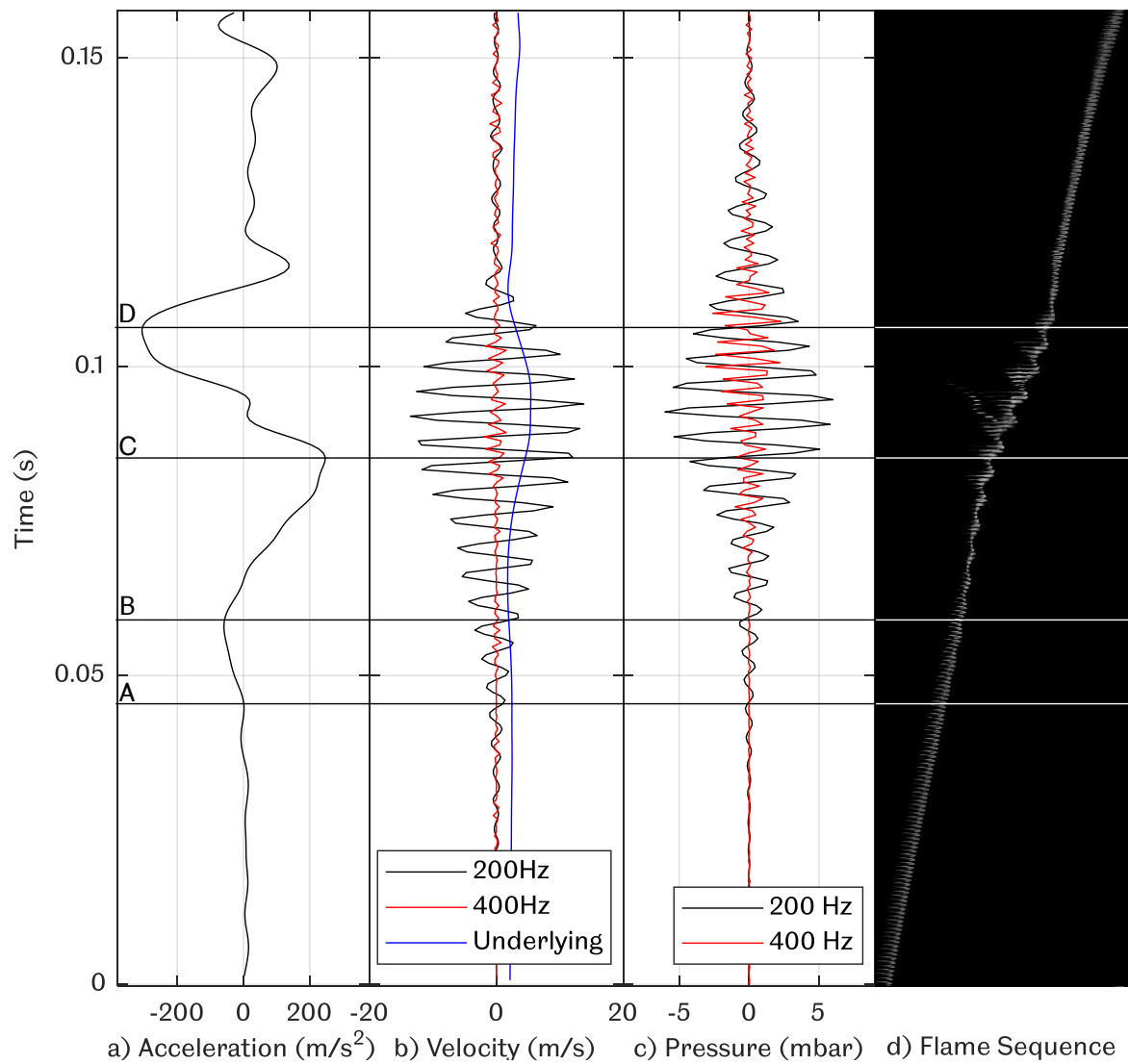


**Figure H.8 Propagation of a  $R_M = 0.1$ ,  $\phi = 1.5$  methane flame with a) underlying acceleration, b) decomposed velocity, c) decomposed pressure and d) flame sequence.**

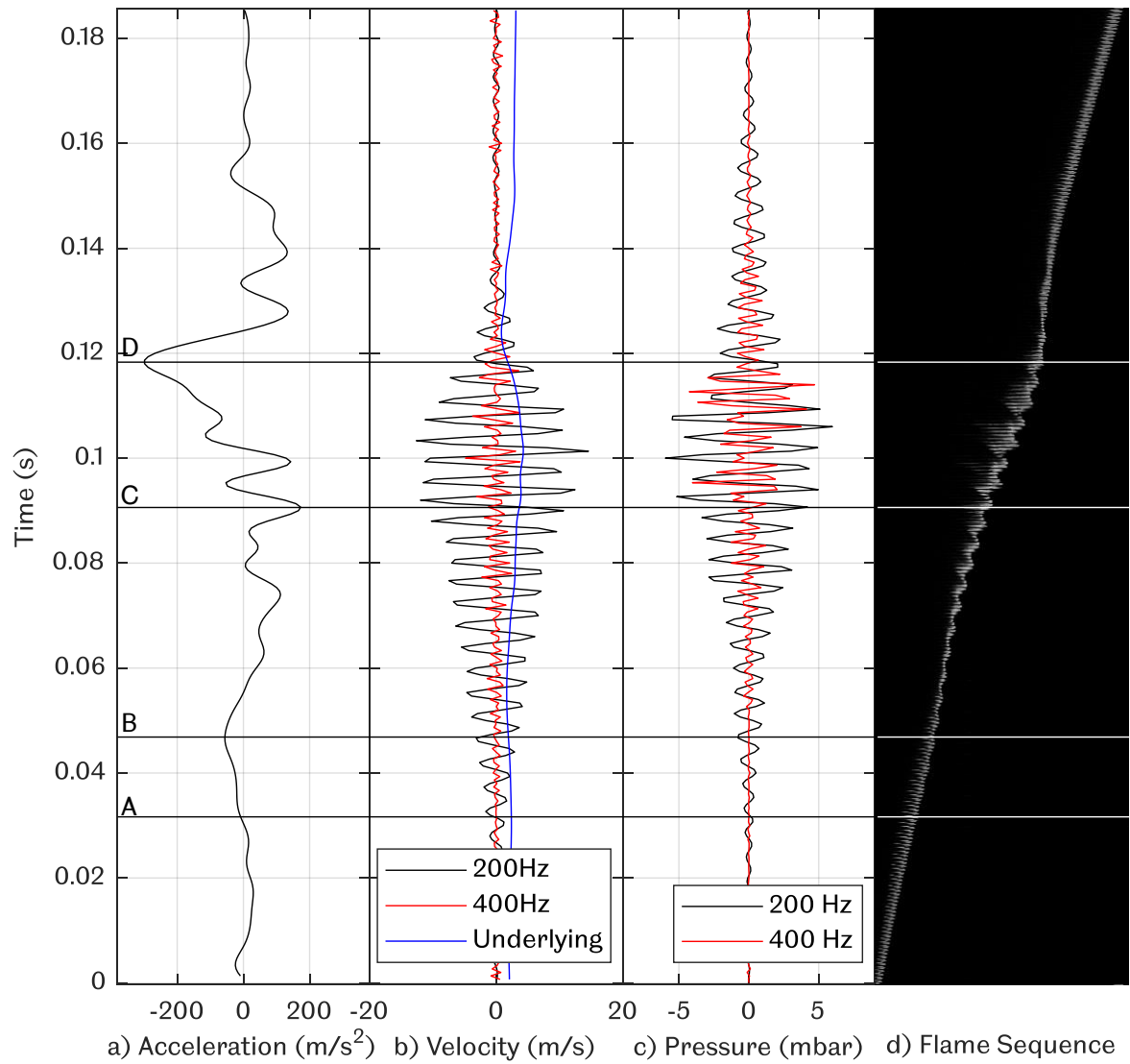
## Appendix I: Whole Flame Propagation (Hydrogen Addition Effect)



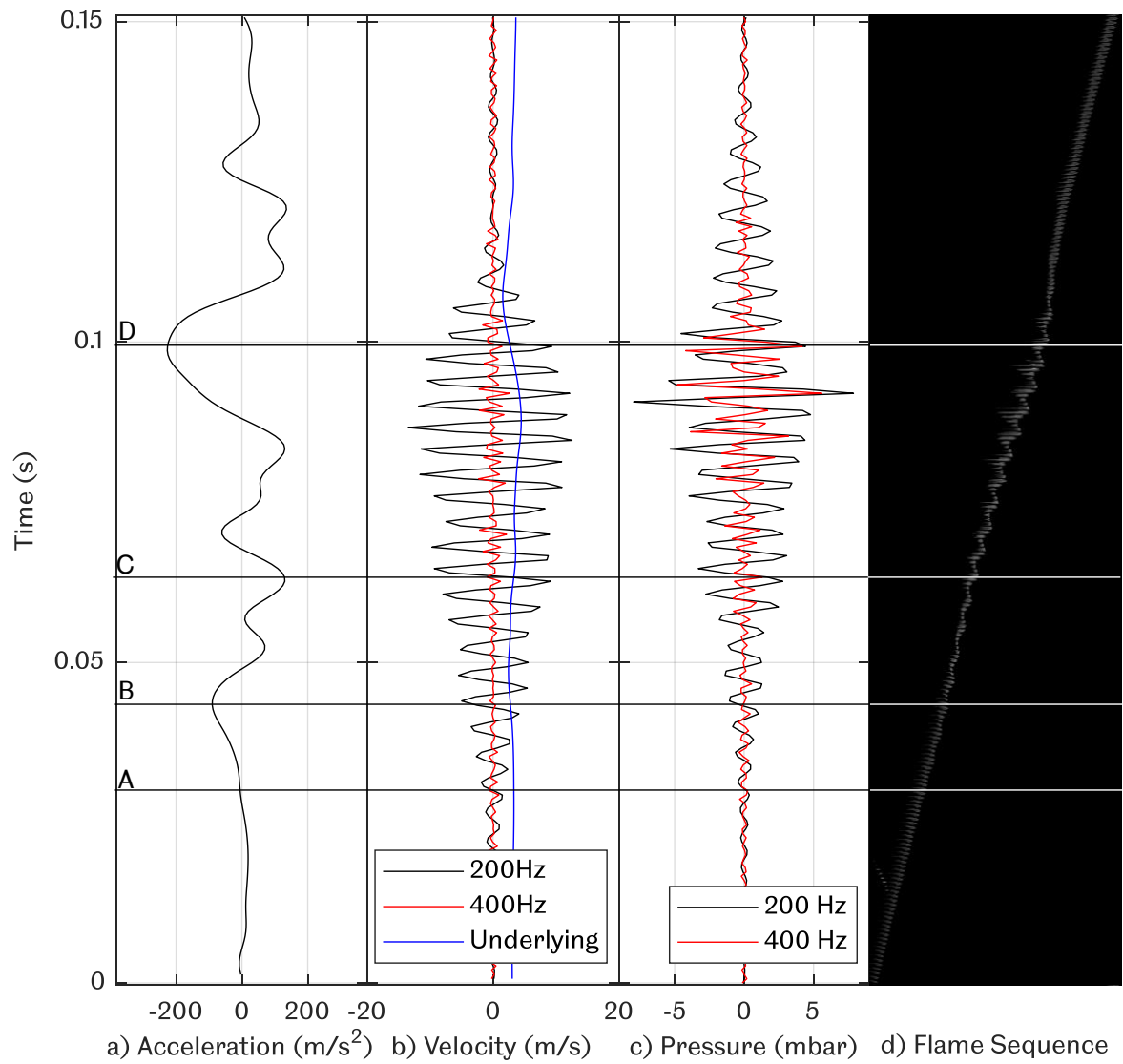
**Figure I.1 Propagation of a  $R_H = 0$ ,  $\phi = 1.1$  methane flame with a) underlying acceleration, b) decomposed velocity, c) decomposed pressure and d) flame sequence.**



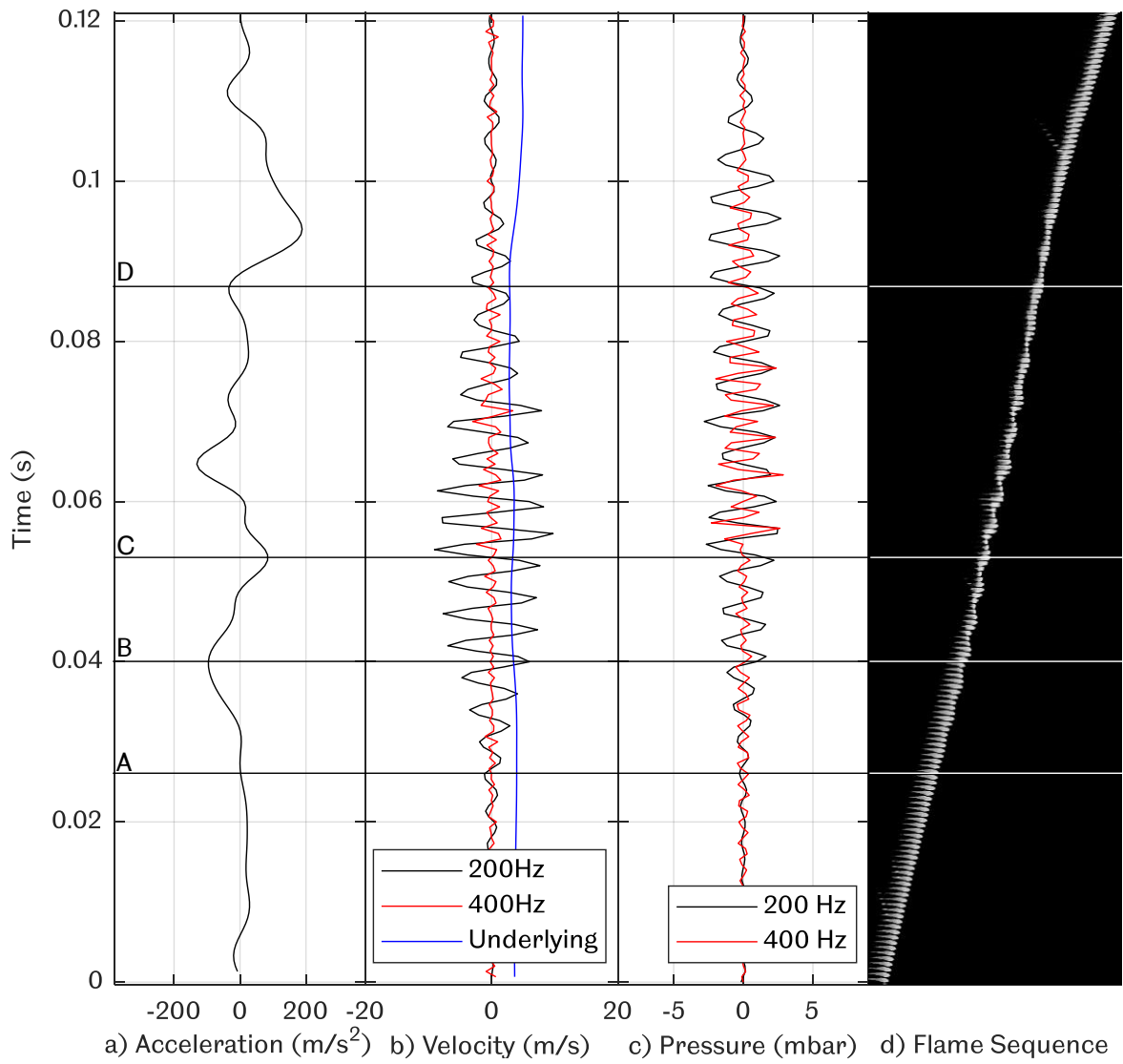
**Figure I.2 Propagation of a  $R_H = 0.1$ ,  $\phi = 1.1$  methane flame with a) underlying acceleration, b) decomposed velocity, c) decomposed pressure and d) flame sequence.**



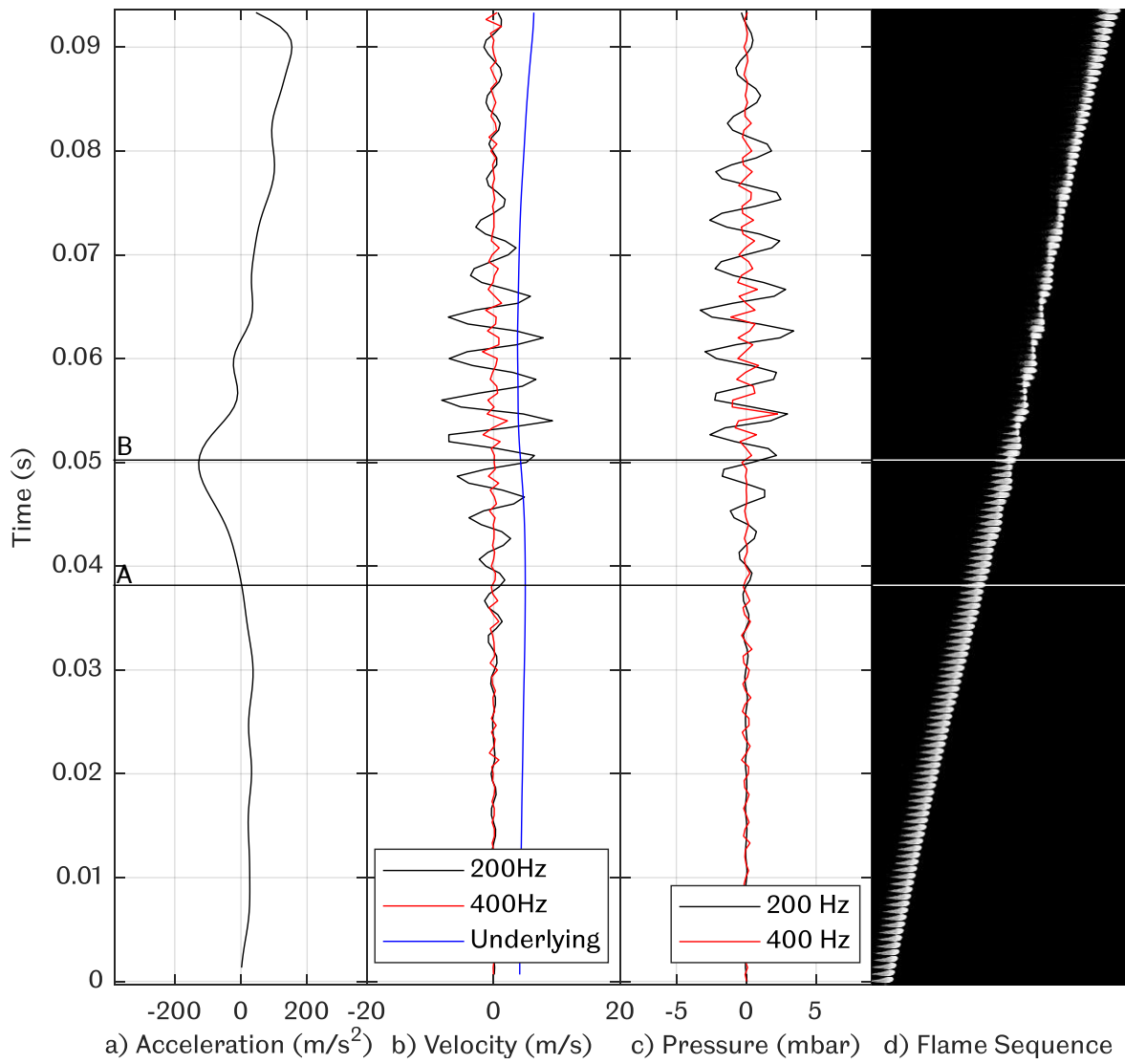
**Figure I.3 Propagation of a  $R_H = 0.2$ ,  $\phi = 1.1$  methane flame with a) underlying acceleration, b) decomposed velocity, c) decomposed pressure and d) flame sequence.**



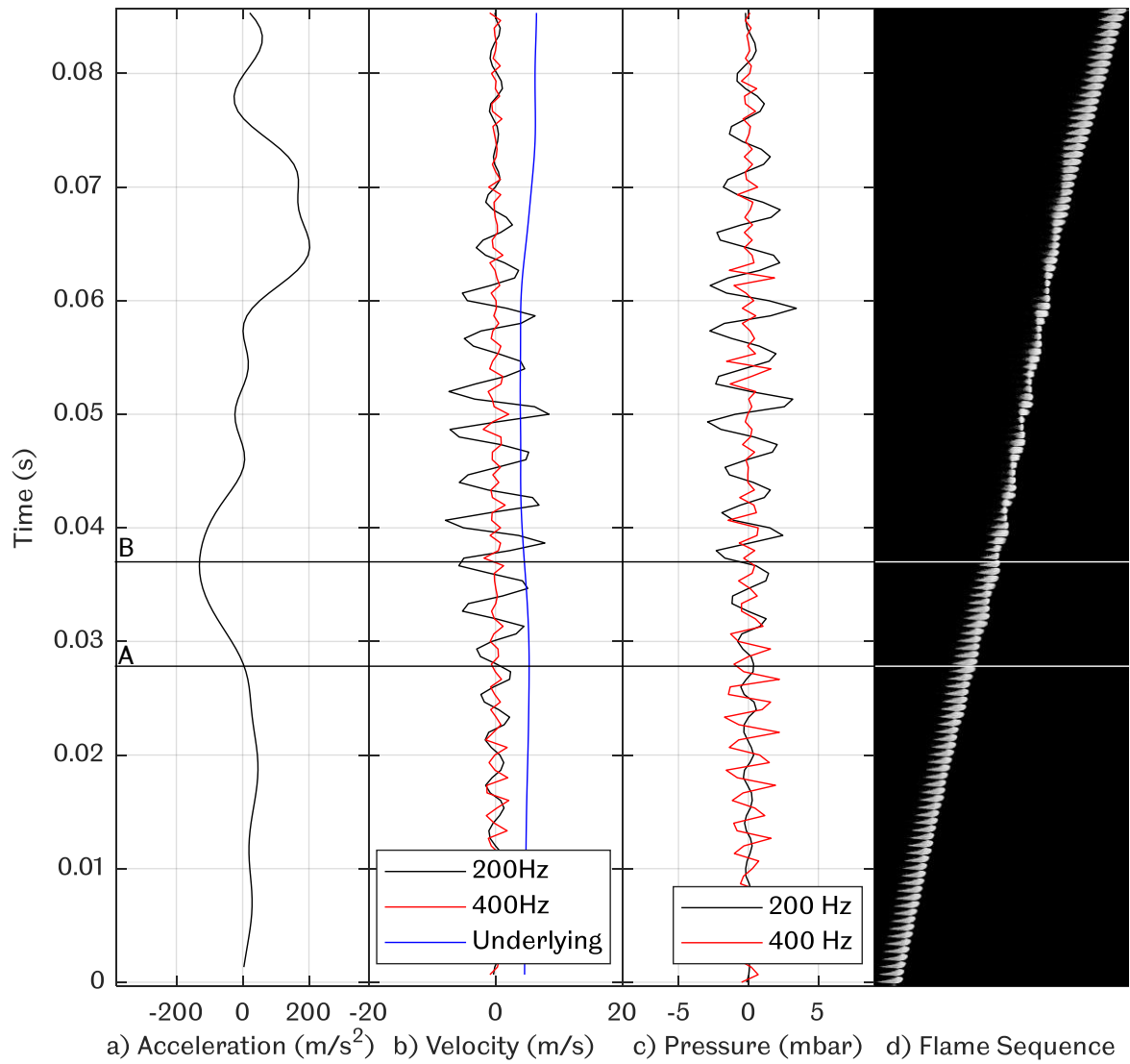
**Figure I.4 Propagation of a  $R_H = 0.3$ ,  $\phi = 1.1$  methane flame with a) underlying acceleration, b) decomposed velocity, c) decomposed pressure and d) flame sequence.**



**Figure I.5 Propagation of a  $R_H = 0.4$ ,  $\phi = 1.1$  methane flame with a) underlying acceleration, b) decomposed velocity, c) decomposed pressure and d) flame sequence.**

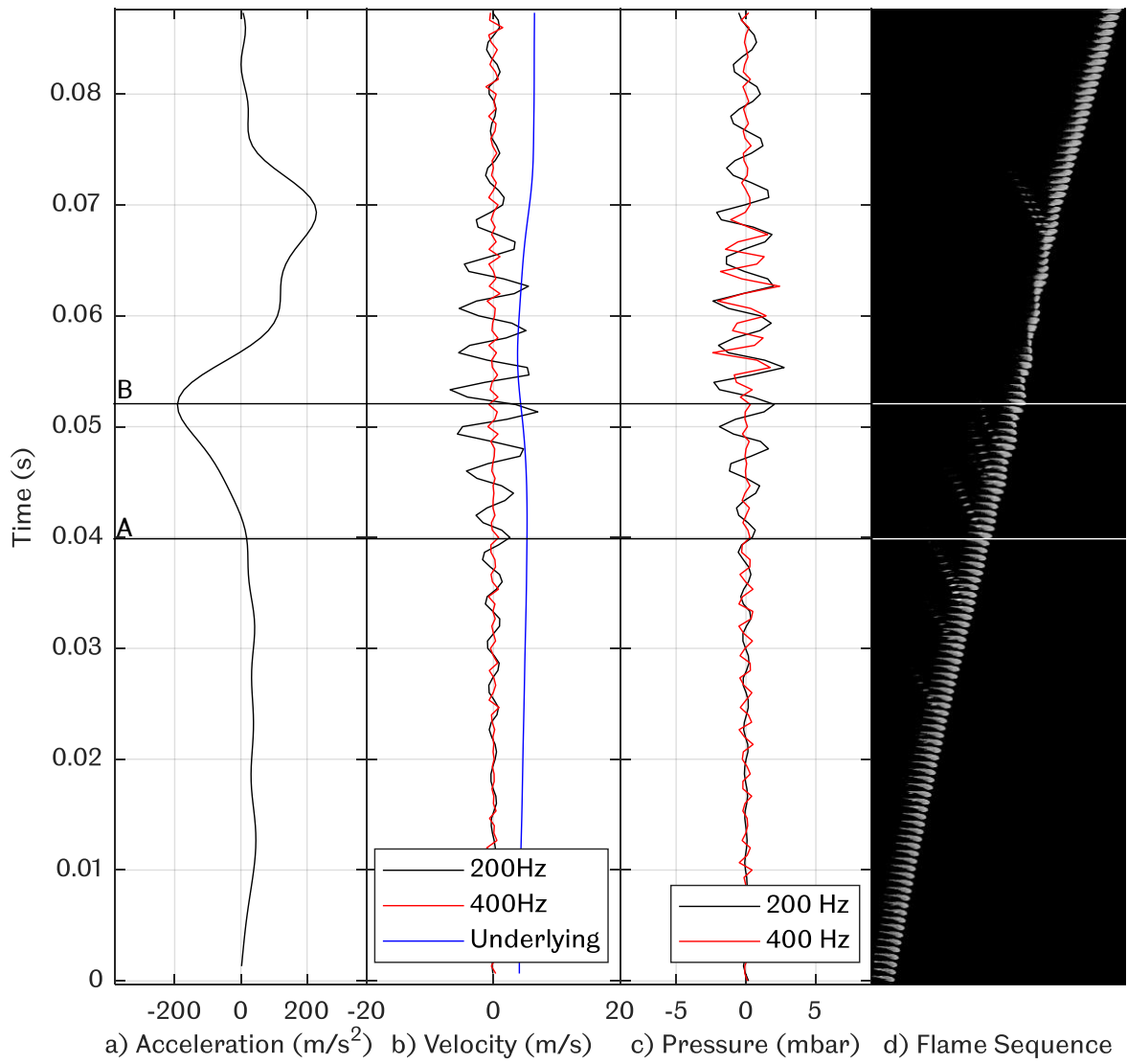


**Figure I.6 Propagation of a  $R_H = 0.5$ ,  $\phi = 1.1$  methane flame with a) underlying acceleration, b) decomposed velocity, c) decomposed pressure and d) flame sequence.**

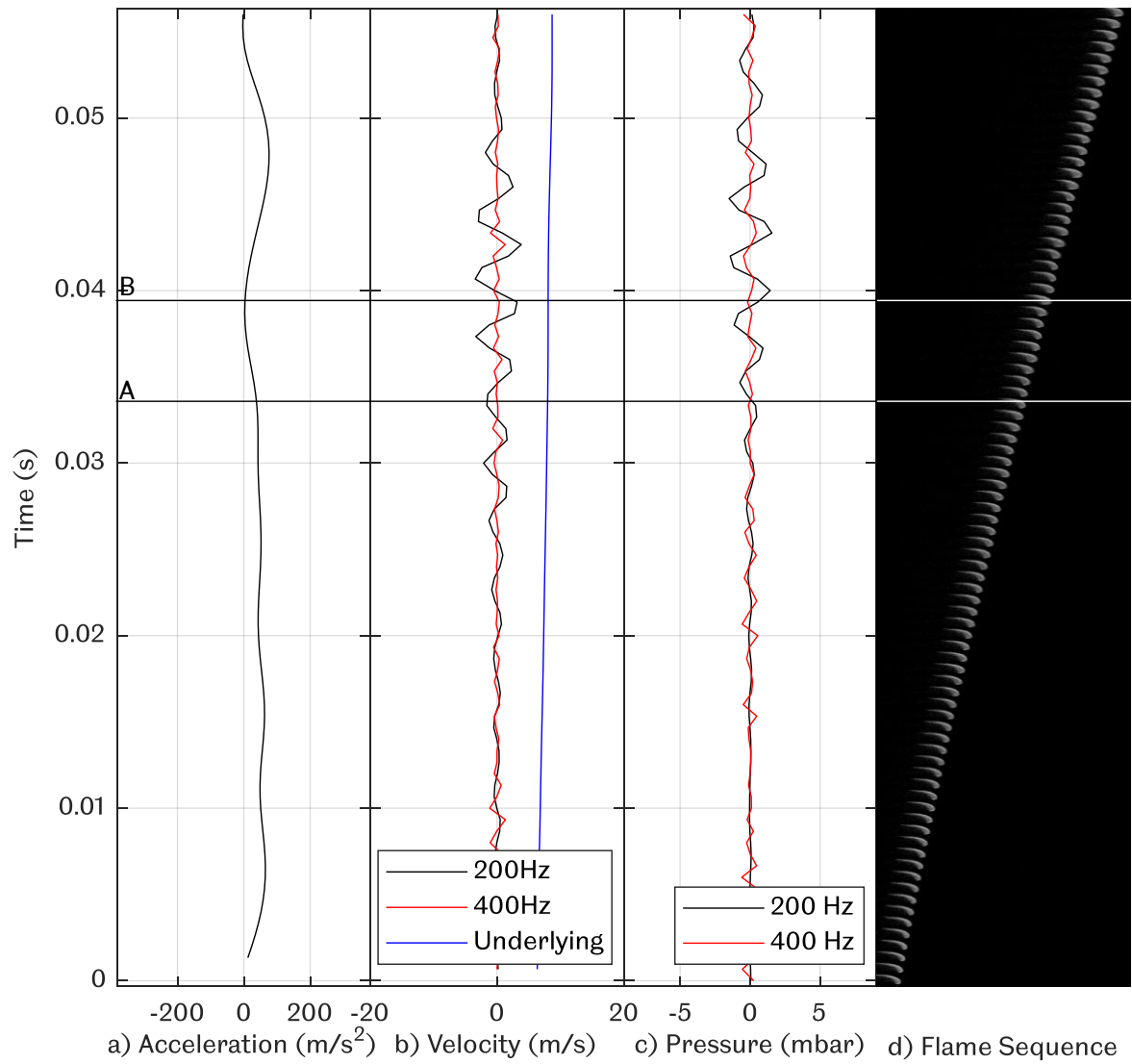


**Figure I.7 Propagation of a  $R_H = 0.6$ ,  $\phi = 1.1$  methane flame with a) underlying acceleration, b) decomposed velocity, c) decomposed pressure and d) flame sequence.**



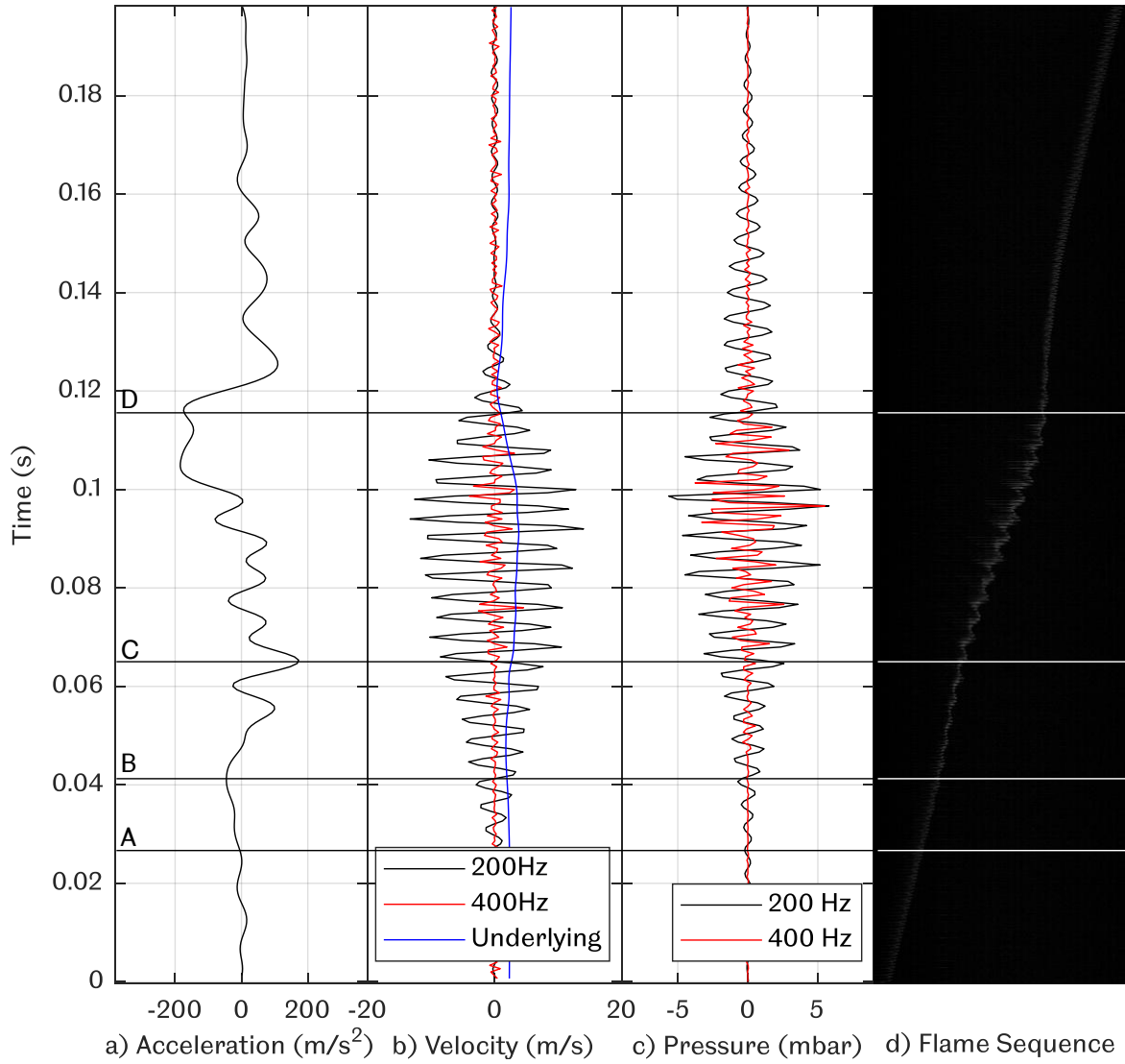


**Figure I.8 Propagation of a  $R_H = 0.7$ ,  $\phi = 1.1$  methane flame with a) underlying acceleration, b) decomposed velocity, c) decomposed pressure and d) flame sequence.**

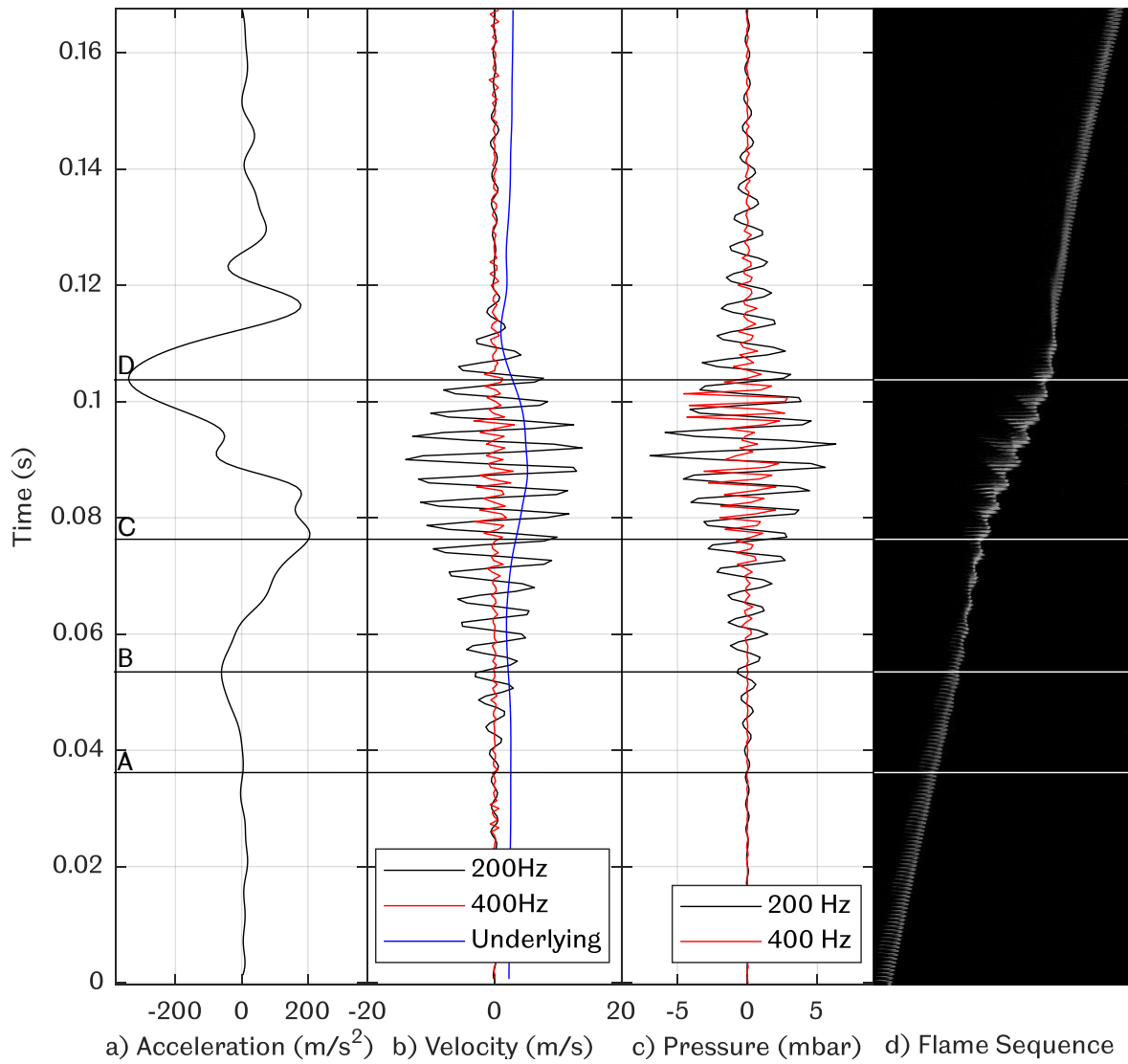


**Figure I.9 Propagation of a  $R_H = 0.8$ ,  $\phi = 1.1$  methane flame with a) underlying acceleration, b) decomposed velocity, d) decomposed pressure and d) flame sequence.**

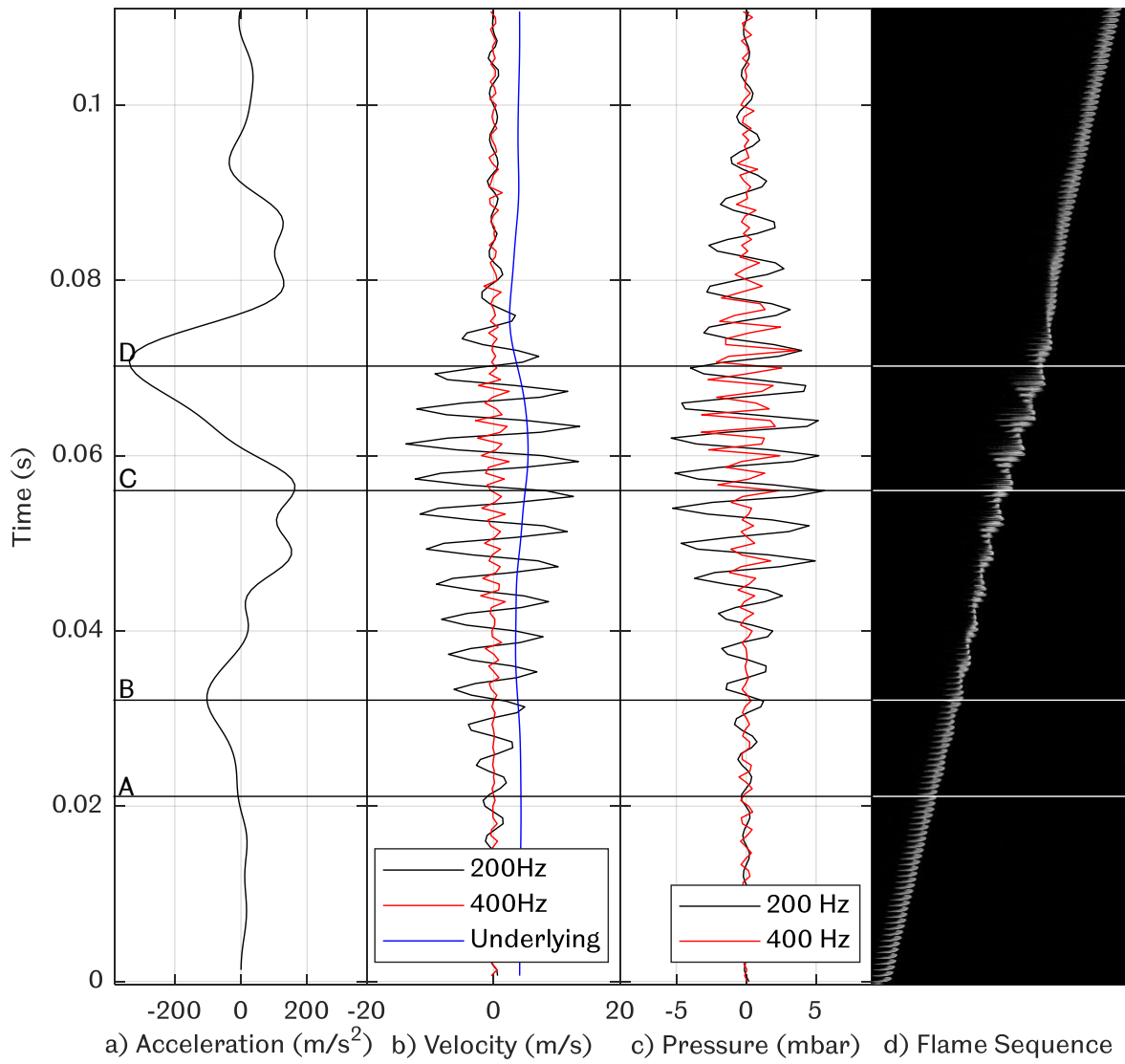
## Appendix J: Whole Flame Propagation (Constant Laminar Burning Velocity)



**Figure J.1 Propagation of a  $R_H = 0.3$ ,  $\phi = 0.8$  methane flame with a) underlying acceleration, b) decomposed velocity, c) decomposed pressure and d) flame sequence.**




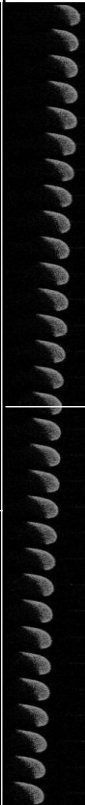



**Figure J.2 Propagation of a  $R_H = 0.2$ ,  $\phi = 1.0$  methane flame with a) underlying acceleration, b) decomposed velocity, c) decomposed pressure and d) flame sequence.**







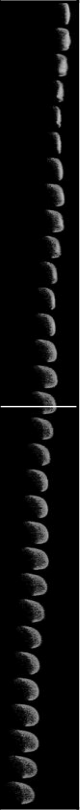
**Figure J.3 Propagation of a  $R_H = 0.4$ ,  $\phi = 1.4$  methane flame with a) underlying acceleration, b) decomposed velocity, c) decomposed pressure and d) flame sequence.**

## Appendix K: Flame Shape Analysis (Equivalence Ratio Effect)

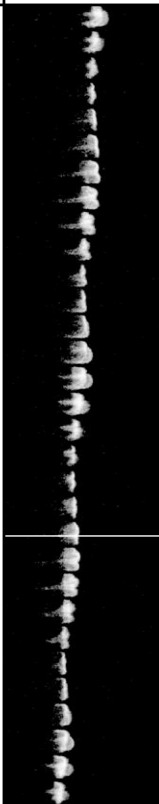
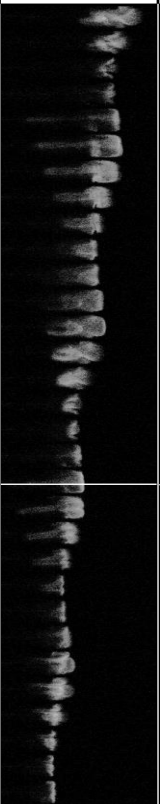
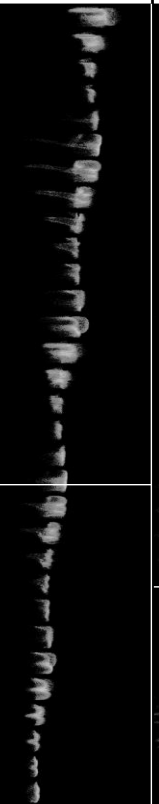
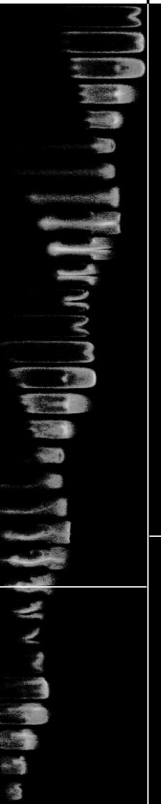
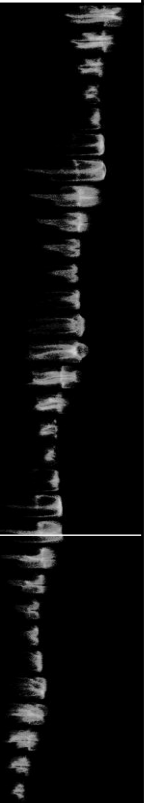
Table K.1 Flame sequence at point A (white line) for methane flames at constant hydrogen addition,  $R_H = 0.1$ , with increasing equivalence ratio,  $\phi = 0.9 - 1.3$ . Interval of 1/1500 seconds increment for every frame upwards.

Equivalence Ratio, $\phi$	0.9	1.0	1.1	1.2	1.3
Hydrogen Addition, $R_H$	0.1	0.1	0.1	0.1	0.1
Flame Sequence					

**Table K.2 Flame sequence at point B (white line) for methane flames at constant hydrogen addition,  $R_H = 0.1$ , with increasing equivalence ratio,  $\phi = 0.9 - 1.3$ . Interval of 1/1500 seconds increment for every frame upwards.**


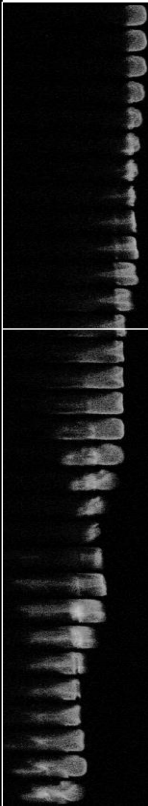
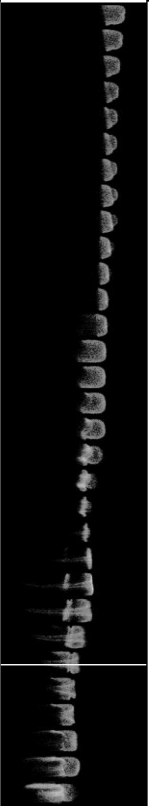


Equivalence Ratio, $\phi$	0.9	1.0	1.1	1.2	1.3
Hydrogen Addition, $R_H$	0.1	0.1	0.1	0.1	0.1
Flame Sequence					

**Table K.3 Flame sequence at point C (white line) for methane flames at constant hydrogen addition,  $R_H = 0.1$ , with increasing equivalence ratio,  $\phi = 0.9 - 1.3$ . Interval of 1/1500 seconds increment for every frame upwards.**

Equivalence Ratio, $\phi$	0.9	1.0	1.1	1.2	1.3
Hydrogen Addition, $R_H$	0.1	0.1	0.1	0.1	0.1
Flame Sequence					

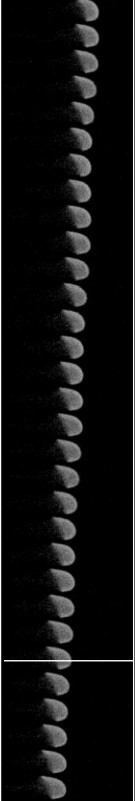

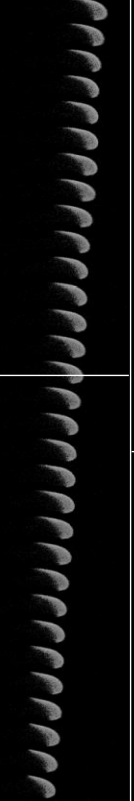

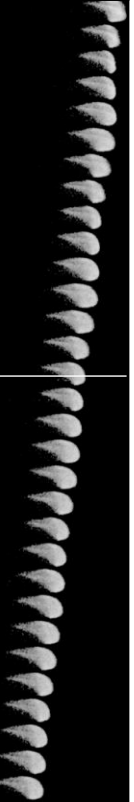


**Table K.4 Flame sequence at point D (white line) for methane flames at constant hydrogen addition,  $R_H = 0.1$ , with increasing equivalence ratio,  $\phi = 0.9 - 1.3$ . Interval of 1/1500 seconds increment for every frame upwards.**

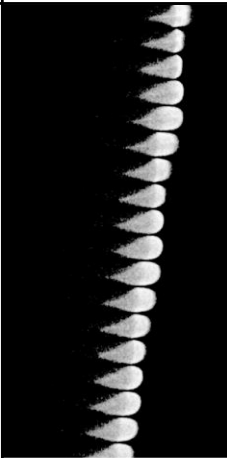

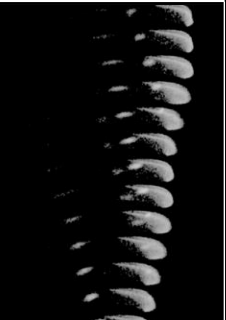
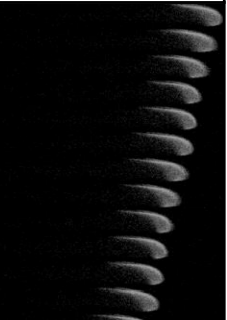
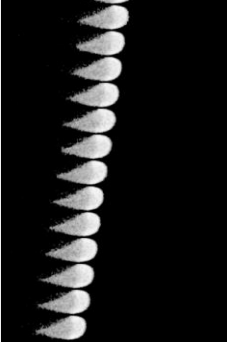


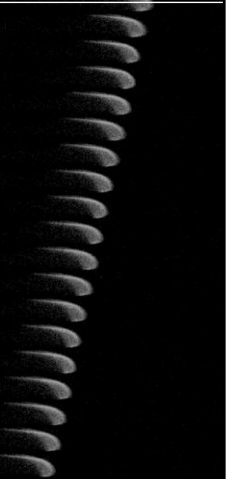
Equivalence Ratio, $\phi$	0.9	1.0	1.1	1.2	1.3
Hydrogen Addition, $R_H$	0.1	0.1	0.1	0.1	0.1
Flame Sequence					

## Appendix L: Flame Shape Analysis (Hydrogen Addition Effect)


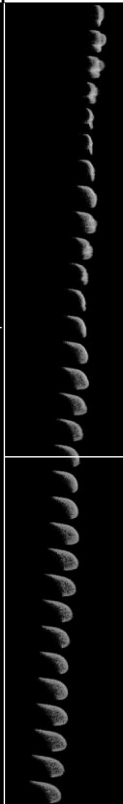
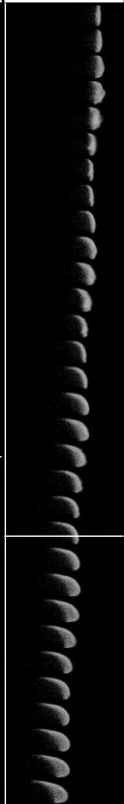


**Table L.1** Flame sequence at point A (white line) for methane flames at constant equivalence ratio,  $\phi = 1.1$ , with increasing hydrogen content,  $R_H = 0 - 0.4$ . Interval of 1/1500 seconds increment for every frame upwards.

Equivalence Ratio, $\phi$	1.1	1.1	1.1	1.1	1.1
Hydrogen Addition, $R_H$	0	0.1	0.2	0.3	0.4
Flame Sequence					

**Table L.2 Flame sequence at point A (white line) for methane flames at constant equivalence ratio,  $\phi = 1.1$ , with increasing hydrogen content,  $R_H = 0.5 - 0.8$ . Interval of 1/1500 seconds increment for every frame upwards.**

Equivalence Ratio, $\phi$	1.1	1.1	1.1	1.1
Hydrogen Addition, $R_H$	0.5	0.6	0.7	0.8
Flame Sequence				
				

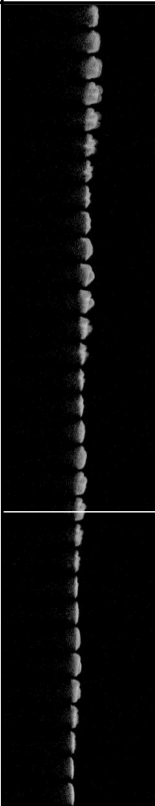

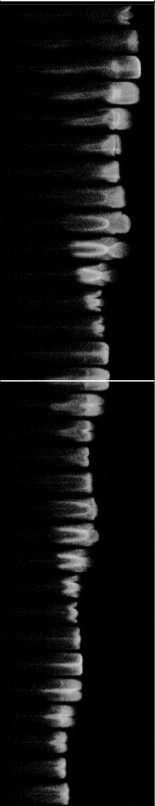


**Table L.3 Flame sequence at point B (white line) for methane flames at constant equivalence ratio,  $\phi = 1.1$ , with increasing hydrogen content,  $R_H = 0 - 0.4$ . Interval of 1/1500 seconds increment for every frame upwards.**

Equivalence Ratio, $\phi$	1.1	1.1	1.1	1.1	1.1
Hydrogen Addition, $R_H$	0	0.1	0.2	0.3	0.4
Flame Sequence					

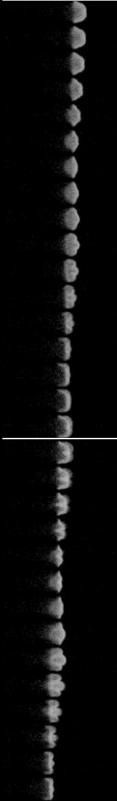

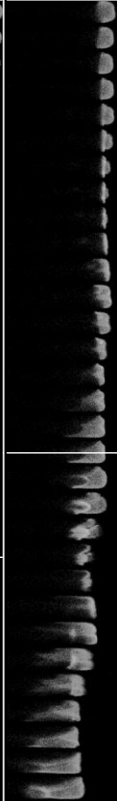
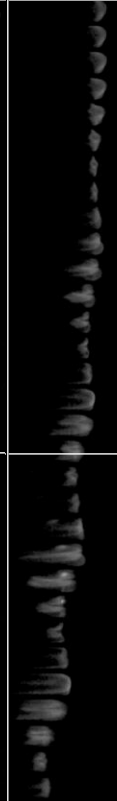
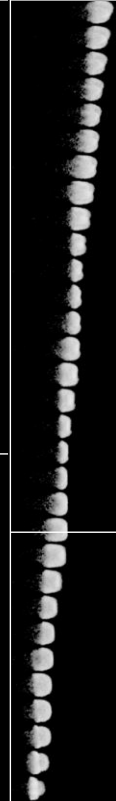
**Table L.4 Flame sequence at point B (white line) for methane flames at constant equivalence ratio,  $\phi = 1.1$ , with increasing hydrogen content,  $R_H = 0.5 - 0.8$ . Interval of 1/1500 seconds increment for every frame upwards.**

Equivalence Ratio, $\phi$	1.1	1.1	1.1	1.1
Hydrogen Addition, $R_H$	0.5	0.6	0.7	0.8
Flame Sequence				

**Table L.5 Flame sequence at point C (white line) for methane flames at constant equivalence ratio,  $\phi = 1.1$ , with increasing hydrogen content,  $R_H = 0 - 0.4$ . Interval of 1/1500 seconds increment for every frame upwards.**

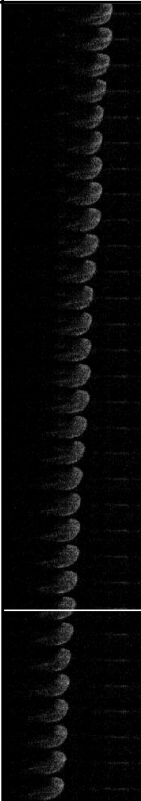
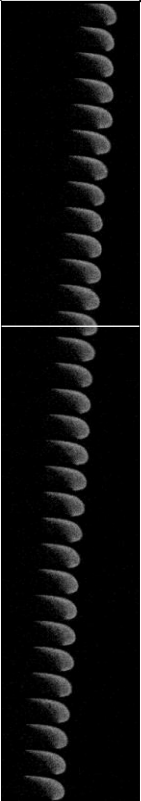
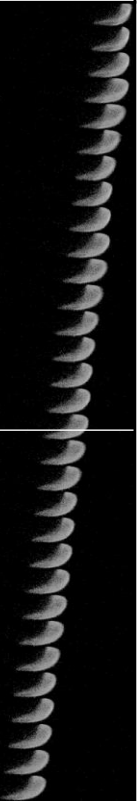
Equivalence Ratio, $\phi$	1.1	1.1	1.1	1.1	1.1
Hydrogen Addition, $R_H$	0	0.1	0.2	0.3	0.4
Flame Sequence					

**Table L.6 Flame sequence at point D (white line) for methane flames at constant equivalence ratio,  $\phi = 1.1$ , with increasing hydrogen content,  $R_H = 0 - 0.4$ . Interval of 1/1500 seconds increment for every frame upwards.**

Equivalence Ratio, $\phi$	1.1	1.1	1.1	1.1	1.1
Hydrogen Addition, $R_H$	0	0.1	0.2	0.3	0.4
Flame Sequence					




## Appendix M: Flame Shape Analysis (Constant Laminar Burning Velocity)

**Table M.1** Flame sequence at point A (white line) for methane flames with similar laminar burning velocity,  $\phi = 0.8$ ,  $R_H = 0.3$ ,  $\phi = 1.0$ ,  $R_H = 0.2$ , and  $\phi = 1.4$ ,  $R_H = 0.4$ . Interval of 1/1500 seconds increment for every frame upwards.

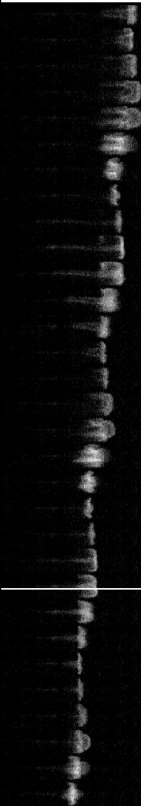
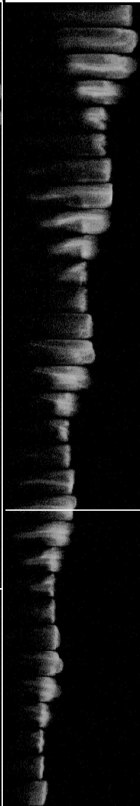

Equivalence Ratio, $\phi$	0.8	1.0	1.4
Hydrogen Addition, $R_H$	0.3	0.2	0.4
Flame Sequence			



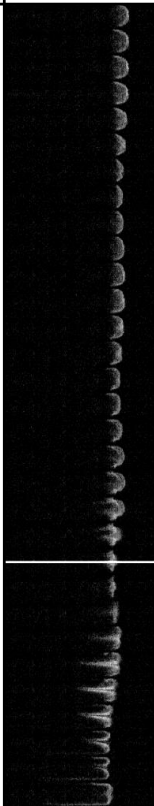

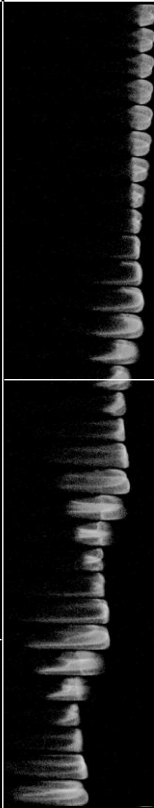
**Table M.2 Flame sequence at point B (white line) for methane flames with similar laminar burning velocity,  $\phi = 0.8$ ,  $R_H = 0.3$ ,  $\phi = 1.0$ ,  $R_H = 0.2$ , and  $\phi = 1.4$ ,  $R_H = 0.4$ . Interval of 1/1500 seconds increment for every frame upwards.**

Equivalence Ratio, $\phi$	0.8	1.0	1.4
Hydrogen Addition, $R_H$	0.3	0.2	0.4
Flame Sequence			

**Table M.3 Flame sequence at point C (white line) for methane flames with similar laminar burning velocity,  $\phi = 0.8$ ,  $R_H = 0.3$ ,  $\phi = 1.0$ ,  $R_H = 0.2$ , and  $\phi = 1.4$ ,  $R_H = 0.4$ . Interval of 1/1500 seconds increment for every frame upwards.**

Equivalence Ratio, $\phi$	0.8	1.0	1.4
Hydrogen Addition, $R_H$	0.3	0.2	0.4
Flame Sequence			

**Table M.4 Flame sequence at point D (white line) for methane flames with similar laminar burning velocity,  $\phi = 0.8$ ,  $R_H = 0.3$ ,  $\phi = 1.0$ ,  $R_H = 0.2$ , and  $\phi = 1.4$ ,  $R_H = 0.4$ . Interval of 1/1500 seconds increment for every frame upwards.**

Equivalence Ratio, $\phi$	0.8	1.0	1.4
Hydrogen Addition, $R_H$	0.3	0.2	0.4
Flame Sequence	 <p>The image shows a vertical sequence of flame frames for <math>\phi = 0.8</math> and <math>R_H = 0.3</math>. The flame is relatively stable and shows a regular, periodic oscillation pattern. A white horizontal line is present in each frame, indicating the position of point D.</p>	 <p>The image shows a vertical sequence of flame frames for <math>\phi = 1.0</math> and <math>R_H = 0.2</math>. The flame exhibits a more pronounced oscillatory behavior compared to the <math>\phi = 0.8</math> case. A white horizontal line is present in each frame, indicating the position of point D.</p>	 <p>The image shows a vertical sequence of flame frames for <math>\phi = 1.4</math> and <math>R_H = 0.4</math>. The flame shows significant oscillatory behavior, with larger amplitude and more irregular patterns than the other two cases. A white horizontal line is present in each frame, indicating the position of point D.</p>